Pathological Mineralisation

Elena Tsolaki

Department of Medical Physics and Biomedical Engineering

University College London

A thesis submitted in fulfilment of the requirements for the degree of

Doctor of Philosophy

June 2020

Declaration

'I, Elena Tsolaki confirm that the work presented in this thesis is my own. Where information has been derived from other sources, I confirm that this has been indicated in the thesis.'

Signature

……

Acknowledgements

Firstly, I would like to thank my supervisor Dr Sergio Berazzo for his continued support, always being available for discussions, sharing his knowledge, and providing constant motivation throughout the last four years.

I would also like to thank Dr Lajos Csincsik and Dr Imre Lengyel for their assistance, support, and sharing their expertise on immunofluorescence staining and confocal microscopy. I also extend my gratitude to Dr Ecaterina Ware, Dr Tom Gregory, and Mark Turmaine for their patience whilst teaching me different aspects of electron microscopy and also Dr Shweta Agarwal for sharing her knowledge on electron diffraction analysis. I am also grateful to Professor Inge K. Hermann for the on-going collaborative work and her support.

I also cannot thank my emotional support team enough; my UCL friends, Negar, Chloe and Ayushi for going through the PhD experience together, my life friends, Lucy, and Ben for always being there, as well as Gavriella and Christina for the motivational pep talks. My Kypros, Loukia, and Marios for being a constant source of entertainment on good and bad days and my parents, Andreas and Miriam, for their continuous support and sacrifices which allowed me to pursue a PhD.

Finally, the biggest thank you goes to my partner in life, Zisis, whose support kept me going throughout this journey and made every single day better.

Abstract

Pathological mineralisation is a well-known phenomenon in the medical field as it relates to a wide range of diseases, including cancer, neurodegenerative diseases, aortic valve stenosis, and atherosclerosis. Despite this, the direct study of pathological minerals has been rare, as most research focuses on the study of the organic components of these pathologies and the microenvironment the minerals are observed in. Even though material science methods have been used for the study of biomaterials, hard tissues, and other biological systems; they have not been widely used in the research of pathological mineralisation. This work is, subsequently, concentrating on the direct study of the minerals found in cardiovascular, breast, and brain tissues aiming to provide a full physicochemical characterization. The presence of inorganic material in these soft tissues has been long observed in relation to several diseases, but the relationship between their properties and specific pathologies is not fully understood. Therefore, through the direct investigation of the minerals present, this study aims to provide new insights into the association of unique mineral properties to specific disease characteristics. In addition, the data on the mineral properties will then be evaluated to gain information on the mineral formation processes, in order to identify proteins, cells, or vesicles, which might be involved. Finally, a range of biochemical assays will be used, aiming to directly investigate the presence of biological markers in the inorganic material to give new insights on the mineralisation mechanisms.

Impact statement

In this work, minerals found in cardiovascular, breast, and brain tissues are studied, all of which are associated with major pathologies that affect a large proportion of the world population, including Alzheimer's disease, breast cancer, and many cardiovascular diseases. Research advances made in recent years have provided many fundamental insights into the disease mechanisms. However, contemporary research has not delved much into the inorganic component of these diseases, even though minerals in the soft tissues have recently been accepted to be, in most cases, active players in the development of the related pathologies. Therefore, the results of this work aim to provide information on the properties and potential origins of pathological minerals, which will be used to provide new insights into the disease microenvironment, increasing our understanding of the pathologies themselves. Subsequently, such information will trigger further research initiatives to comprehend better the processes involved in the development and progression of the associated diseases and the exact role pathological minerals have in these.

Other than that, this work will also have an impact on the broader society. It has been estimated that by 2050, Alzheimer's disease will affect 115 million people (1), breast cancer 3.2 million (2) while calcific cardiovascular diseases are projected to affect close to a billion people (3). In addition to the life-changing effects, these diseases have on affected individuals, they also present the leading cause of death for a large percentage of the population every year (4), as none of them has a definitive treatment. Therefore, understanding these pathologies will improve public health in general as new prevention methods will emerge and advances on new and current treatment options will be made, decreasing their mortality rates.

Other than the dire effects on many individuals' and their families' health and lives, currently, these pathologies also cause a huge financial burden on the patients, their families, and the community. All of these diseases have been shown to require an increased health expenditure from governments, but also require costly procedures and treatment methods or caring facilities that in many cases are covered by the immediate family (5-7). Similarly, to reduce the health impact of these diseases in the wider society, for the minimisation of the economic impact they have, new inexpensive treatment and prevention methods need to be developed.

Therefore, an all-encompassing comprehension of the disease components, including a more detailed study of the minerals, is essential to understand these diseases, which will in return alter for the best the lives of many people worldwide.

Scientific output

Publications

1. Bohmer N, Demarmels N, **Tsolaki E**, Gerken L, Keevend K, Bertazzo S, Lattuada M & Herrmann, IK, Removal of Cells from Body Fluids by Magnetic Separation in Batch and Continuous Mode: Influence of Bead Size, Concentration and Contact Time, ACS Applied Materials & Interfaces, 9(35): 29571-29579 (2017).

2. Noimark SM, Colchester RJ, Poduval RK, Maneas E, Alles EJ, Zhao T, Zhang EZ, Ashworth M, **Tsolaki E**, Chester AH, Latif N, Bertazzo S, David AL, Ourselin S, Beard PC, Parkin IP, Papakonstantinou I & Desjardins AE, Polydimethylsiloxane (PDMS) composites for optical ultrasound generation and multi-modality imaging, Advanced Functional Materials, 28(9) (2018).

3. Keevend K, Panzarasa G, Starsich FHL., Zeltner M, Spyrogianni A, **Tsolaki E**, Fortunato G, Pratsinis SE, Bertazzo S & Herrmann IK, Facile meltPEGylation of Flame-made Luminescent Tb3+-doped Yttrium Oxide Particles: Hemocompatibility, Cellular Uptake and Comparison to Silica, Chemical communications, 54(23): 2914-2917 (2018).

4. Ryabova AV, Keevend K, **Tsolaki E**, Bertazzo S, Pominova DV, Romanishkin ID, Grachev PV, Makarov VI, Burmistrov IA, Vanetsev AS, Orlovskaya EO, Baranchikov AE, Rähn M, Sildos I, Sammelselg V, Loschenov VB & Orlovskii YV, Visualization of ND3 + -doped LaF3 nanoparticles for near infrared bioimaging via upconversion luminescence at multiphoton excitation microscopy, Biomedical Photonics, 7(1): 4-12 (2018).

5. Wald DS, **Tsolaki E**, Berwick JP & Bertazzo S, Scanning electron microscopy for blood micro-crystals in aortic stenosis patients, PLoS one, 13(8): e0202282 (2018).

6. Loaiza S, Ferreira SA, Chinn TM, Kirby A, **Tsolaki E**, Dondi C, Parzych K, Strange AP, Bozec L, Bertazzo S, Hedegaard M, Gentleman E, & Auner H W, An engineered, quantifiable in vitro model for analysing the effect of proteostasis-targeting drugs on tissue physical properties. Biomaterials, 183: 102–113 (2018).

7. Tan ACS, Pilgrim MG, Fearn S, Bertazzo S, **Tsolaki E**, Morrell AP, Li M, Messinger JD, Dolz-Marco R, Lei J, Nittala MG, Sadda SR, Lengyel I, Freund KB & Curcio CA, Calcified nodules in retinal drusen are associated with disease progression in age-related macular degeneration. Science translational medicine, 10(466):eaat4544 (2018).

8. **Tsolaki E**, Didierlaurent L, Latif N, Muller E, Rottmar M, Chester AH, Herrmann IK & Bertazzo S, Electron microscopic characterization of minerals formed by in vitro cell culture. bioRxiv (preprint) (2019).

9. **Tsolaki E** & Bertazzo S, Pathological mineralization: an overlooked materials science field. Materials, 12(19):3126 (2019).

10. Anthis AHC*, **Tsolaki E***, Didierlaurent L, Staubli S, Zboray R, Neels A, Dietrich D, Manser P, Desbiolles LM, Leschka S, Wildermuth S, Lehner S, Chavette-Palmer P, Jochum W, Wick P, Dommann A, Bürki-Turnherr T, Fischer T, Hornung R, Bertazzo S & Herrmann IK, Nano-analytical Characterization of Placental Tissue Reveals Distinct Types of Minerals, Analyst, 114(23): 6850-6857 (2019). * These authors contributed equally as first authors.

11. Iacoviello F, Kirby A, Moeendarbary E, Javanmardi Y, Shabanli M, **Tsolaki E**, Sharp A, Hayes M, Keevend K, Li JH, Brett D, Shearing P, Olivo A, Herrmann IK, Evans S, Moazen M & Bertazzo S, The multiscale hierarchical structure of osteoderms defines their distinct mechanical properties and functions, Acta Biomaterialia, 107: 194-203 (2020).

12. **Tsolaki E**, Doran W, Magnani L, Olivo A, Herrmann IK & Bertazzo S, Invasive breast tumors are characterized by the presence of crystalline nanoparticles, bioRxiv (preprint) (2020).

13. Matter MT, Li JH, Lese I, Schreiner C, Bernard L, Scholder O, Hubeli J, Keevend K, **Tsolaki E**, Bertero E, Bertazzo S, Zboray R, Olariu R, Constantinescu M, Figi R & Herrmann IK, Multi-scale Analysis of Metal Oxide Nanoparticles in Tissue: Insights into Biodistribution and Biotransformation, Advanced Science (2020).

14. Rogers MA, Buffolo F, Schlotter F, Lee LH, Halu A, Blaser MC, **Tsolaki E**, Higashi H, Atkins SK, Bouten C, Singh SA, Bertazzo S, Aikawa M & Aikawa E, Annexin tethers extracellular vesicles and promotes human cardiovascular calcification. Science Advances (2020).

15. **Tsolaki E**, Csincsik L, Xue J, Lengyel I, Bertazzo S, Association of cellular and subcellular calcification with phosphorylated tau in the brains of Alzheimer's disease patients, bioRxiv (preprint) (2020).

Book contributions

1. Tsolaki E, Bertazzo S. Electron Microscopy for the Characterization of Soft Tissue Mineralization. In: Aikawa E, Hutcheson JD, editors. Cardiovascular Calcification and Bone Mineralization. Cham: Springer International Publishing; 2020. p. 219-34.

Poster presentations

1. **Tsolaki E**, Dean MN, Smith K, Chester AH & Bertazzo S, Ubiquity of whitlockite micro-crystals in vascular tissues of amniotes, 8th Biennial Heart Valve Biology & Tissue Engineering Meeting 2018, London (UK).

2. **Tsolaki E**, Csincsik L, Lengyel I & Bertazzo S, Calcified structures on Alzheimer's disease patients and aged brains, Tenth Annual Alliance for Healthy Aging Conference 2019, Newcastle (UK).

Oral presentations

1. **Tsolaki E,** Didierlaurent L, Latif N, Chester AH, Herrmann IK & Bertazzo S, Cell culture mineralization: Similarities and differences to bone, ESVS Spring meeting 2019, London (UK).

Table of Contents

List of Figures

List of Tables

Chapter 1: Introduction

1.1 Background and motivation

Animals (8) and humans (9) experience biological mineralisation processes in different tissues and contexts. Mineralisation is an important biological process that, under physiological conditions, is responsible for the generation, growth, and healing of hard tissues, such as bone (10) and teeth (11). Animals and humans also experience another mineralisation process, sometimes overlooked, but with a significant impact on their health: pathological mineralisation (12). Pathological mineralisation has been reported in a large number of soft tissues, in connection to a large number of underlying diseases (Table 1.1). A range of minerals have been reported, including calcium phosphates (13, 14) calcium carbonates (15), and calcium oxalates (16, 17); all of which are referred to as calcifications due to their calcium content.

The origins of these soft-tissue calcifications were for years attributed to passive processes with no clinical significance; however, in recent years, they have been increasingly recognized as an important and active component of diseases. Many molecular mechanisms have since been proposed in the literature to be possibly leading to the mineral formation. For calcium phosphate minerals, due to having the same elemental composition as bone, the most common assumption is that osteogenic processes are responsible for their presence. Recent studies have although indicated that soft tissue minerals might be a result of other unique mechanisms involving proteins and cells other than those involved in bone formation.

Despite, in the majority of cases, the exact causes and full formation mechanisms of the minerals are not entirely understood. A possible reason for this is that the research on pathological mineralisation has been firmly rooted in the indirect study of the mineral component, through the study of surrounding tissues and cells (18-21). Additionally, many of the studies developing mineralisation models *in vitro* do not take into account the full physicochemical properties of the minerals as observed *in vivo*, as identified through their direct analysis using material characterization methods. Even more importantly, the majority of the studies on pathological mineralisation models do not provide a comparison between the properties of the minerals observed *in vivo* and *in vitro*, but rather only focus on the ability of the model to form a mineral of similar elemental composition.

Table 1.1: *List of some of the pathologies associated with pathological mineralisation along with information on the affected tissues and chemical composition of the observed minerals as reported in the literature (12).*

Disease	**Mineralisation Site**	**Mineral**
Breast cancer	Breast	Hydroxyapatite, calcium oxalate, magnesium-substituted calcium phosphate (22-25)
Prostate cancer	Prostate	Calcium carbonate phosphate, hydroxyapatite, calcium oxalate monohydrate, calcium oxalate dehydrate, whitlockite (26-29)
Chronic kidney disease	Vascular tissue	Hydroxyapatite, calcium phosphate (30, 31)
Benign prostatic hyperplasia	Prostate	Hydroxyapatite, calcium oxalate monohydrate, calcium oxalate dehydrate (32, 33)
Pancreatic cancer	Pancreas	Calcite (34, 35)
Ovarian cancer	Ovaries	Calcium phosphate (36, 37)
Thyroid cancer	Thyroid	Carbonated calcium phosphate, hydroxyapatite, amorphous carbonated, calcium phosphate apatite, octacalcium phosphate pentahydrate, brushite, whewellite, weddellite, caoxite (38, 39)
Fahr's syndrome	Basal ganglia	Calcium phosphate, calcium carbonate (40, 41)
Systemic sclerosis (scleroderma)	Connective tissue	Hydroxyapatite (42, 43)
Calcific tendonitis	Tendons	Calcium carbonate apatite, hydroxyapatite (44-48)
Kidney stones (renal calculi)	Kidneys	Magnesium ammonium phosphate, hydroxyapatite, whewellite, weddellite, struvite, urate, cystine (17, 49-51)
Urinary stasis	Bladder	Whewellite, struvite, ammonium urate, cystine, carbapatite (52-54)
Hypoparathyroidism	Basal ganglia	Calcium phosphate (55, 56)
Atherosclerosis	Cardiovascular tissue	Hydroxyapatite, whitlockite (57, 58)
Calcific aortic valve disease	Aortic valve	Hydroxyapatite (13)
Age-related macular degeneration	Eyes	Apatite, whitlockite (14)
Alzheimer's disease	Brain	Iron oxide, calcium salts (59, 60)
Tuberculosis	Lungs	Calcium phosphate (61)
Meningioma	Brain	Calcium salts (62)
Salivary stones	Saliva glands	Carbonated apatite, whewellite, weddellite, brushite, struvite (63)
Pulp stones	Dental pulp	Calcium phosphate (64)

Material characterization techniques have extensively been used in biological research, leading to a better understanding of organisms and biological processes. These methods include scanning and transmission electron microscopy, which in the

past allowed the visualization of infected cells (65, 66), and a large number of viruses (65, 67), respectively, leading to important discoveries. Likewise, spectroscopic methods, such as Raman spectroscopy (68), together with X-ray diffraction, have contributed to the discovery of the structure of DNA (69-71). These same methods have also been invaluable in expanding our understanding of hard tissues (72-74). For example, thermal analysis, infrared spectroscopy, and electron microscopy with energy dispersive X-ray spectroscopy have been combined to provide fundamental information on the structure of bone, as we know it today (75-79).

Although this research approach has proven successful many times and has added to our understanding of many biological systems, it has been restricted for many years to specific biological fields such as hard tissues, biomaterials, and marine biology systems. The realisation that minerals in the soft tissues have an active role in many diseases led however, to a need for a better comprehension of these inorganic components to understand the associated pathologies fully. Application of material characterisation methods in the study of pathological mineralisation has emerged therefore, in recent years as an alternative way to study minerals that play a key role in the associated mineralising disease. One such example being cardiovascular calcification, which is now considered an active component of several related cardiovascular diseases leading to millions of deaths annually (4).

Nevertheless, it has been yet to be accepted that the physicochemical properties of the minerals (such as their composition, crystallinity, phase, and morphology) are as important as the information about cells and extracellular matrix. Mineral properties can provide evidence of unique formation mechanisms for different types of pathological minerals. For example, distinct mineral phases, including amorphous calcium phosphate and apatite (80, 81), can be easily formed *in vitro*, under specific and controlled conditions, such as at a specific temperature or pH (how acidic or basic a solution is) (82, 83). However, the formation or transformation of these same minerals in biological systems is much more complex, due to the presence of a large number of proteins and cells affecting the mineralisation processes and favouring the formation of specific mineral phases.

In the formation of bone mineral, for instance, it is well known that cells such as osteoblasts are responsible for the formation of the bone matrix and its regeneration (84, 85). Additionally, acidic phosphoproteins, such as bone sialoprotein (86, 87) and collagen molecules (88) have also been found to play a major role in the nucleation of the mineral. Moreover, the presence of a calcium-containing mineral such as that in bone indicates an abundance of calcium ions in the microenvironment, either in the extracellular matrix or due to the presence of specific cells. The needed calcium for

the nucleation of bone mineral, for example, is suggested to originate from osteoblasts, which were found to contain substantial amounts of calcium (89). On the other hand, the nucleation of gallbladder stones, for instance, is believed to be a result of an increase in the concentration of specific ions in the extracellular environment (90).

Such conclusions are partly due to mineral properties such as internal structure and crystallinity, which can hint on the origins and provide insights on the biochemical pathways leading to mineral formation and development. For example, amorphous minerals observed in kidney stones are believed to be the result of supersaturation mechanisms (91). On the other hand, crystalline minerals are more likely to be the product of mechanisms guided by cells and proteins that can control crystallinity. For example, minerals diffracting as single crystals, even though rarely found in the human body might be a result of highly controlled protein systems, similar to those reported in oyster shells (92) and sea urchin spines (93, 94). Moreover, crystallinity alterations can also give information on the mineral nature. Bone and teeth (enamel and dentin) minerals are formed by polycrystalline arrays of hydroxyapatite crystals (95, 96) but undergo physiological and pathological related crystallinity changes over the years (97-100). For instance, knowledge on bone mineral crystallinity changes (from amorphous to polycrystalline) has given insights in time depended changes leading to the formation of the final mineral form and ultimately lead to a better understanding of why and how these changes occur (81, 101).

As with human hard tissues and mineral structures observed in animals and plants, the presence of pathological minerals in soft tissue is also a result of complex biochemical mechanisms, the complete understanding of which can only be achieved through the study of all components involved, both organic and inorganic. Pathological minerals should not be assumed as a single entity nor completely independent events. Therefore, this work focuses on providing a better understanding of minerals that are either a fundamental component or are associated with pathologies and adverse health outcomes. Gaining information on different pathological minerals, some of which are believed to play a role in the development of disease while others to be a by-product of a specific pathology or ageing tissues, will contribute significantly to the understanding of pathological mineralisation in general.

Three types were studied; cardiovascular, breast, and brain minerals, which have been associated with calcific cardiovascular diseases including atherosclerosis, benign and malignant breast diseases, and neurodegenerative diseases such as Alzheimer's disease, respectively. These minerals are present in anatomically and biologically different locations and are considered to have different pathological significance. Therefore, knowledge of their physicochemical properties will allow the evaluation of whether a shared formation process is responsible for their presence or the

mineralisation mechanisms are tissue and disease-specific. Subsequently, this data will also allow for a better comprehension of the role of tissue microenvironment in mineral formation, which will provide a more 'global' understanding of soft tissue mineralisation. Such information can then be used to propose mineralisation mechanisms but also to understand the effects of these minerals in individual diseases and tissues, which will subsequently lead to a better understanding of the development, diagnosis, and treatment of the associated pathologies.

1.2 Aims and objectives

The main aim of this work is to provide the physicochemical characterisation of soft tissue minerals in different anatomical locations and to use this data to extract information on the possible origins of these minerals.

As the work is concentrated on minerals found in three different anatomical locations, it is divided into three individual projects: cardiovascular, breast, and brain mineralisation, all of which share the same objectives.

1. F*ull physicochemical characterisation of the minerals observed in the brain, breast, and cardiovascular tissues of both healthy and diseased individuals.* For the physicochemical characterisation, electron microscopy will be used as it allows for the visualisation of minerals directly in the tissue environment, at the nanoscale, and for in-depth chemical analysis. Both healthy and diseased tissues will be analysed where appropriate to be able to gain general information on the mineral profile and to pinpoint in which tissue microenvironments these occur.

2. S*pecific correlations between mineral phenotypes and clinical information were identified.* Clinical information includes specific details on clinical diagnosis such as type of disease, stage, and clinical outcome. This will allow the identification of relationships between specific minerals and subcategories of diseases and subsequently to distinguish which minerals will be further studied.

3. Identification of the specific biological and anatomical location of the minerals observed. Achieving a deep understanding of the mineral microenvironment will be the main aim of this stage, as it will lead to gaining knowledge on cells, cell products, extracellular matrix, and proteins that could take part in the mineralisation processes.

4. Mechanisms of mineral formation to be proposed. Work will be carried out to test arising hypotheses, which will include the use of biological assays such as immunofluorescence staining. These methods will be used to test the presence of specific proteins and cell markers in the minerals or their microenvironment, the results of which will give new insights into the mechanisms of mineral formation.

1.3 Thesis Outline

Chapter 2 The essential background knowledge to understand the contents of the experimental work will be discussed. Information on the anatomical location, anatomy, and cellular components of the tissues of interest, namely; cardiovascular, breast, and brain, will be provided to enable an understanding of the tissues studied. A brief discussion on the pathophysiology of the mineral associated conditions (calcific cardiovascular diseases, breast cancer, and Alzheimer's disease) will also be included. Finally, a literature review on the data available to date on the minerals to be studied will be provided.

Chapter 3 This chapter will focus on the application of several techniques to the study of pathological calcification and will discuss the optimised sample preparation methods used for the needs of this work, the study of minerals. The basic principles of scanning and transmission electron microscopy and what information these methods can provide on pathological minerals will be discussed. Optimised sample preparation protocols used in this work for the physicochemical characterisation of pathological minerals directly in the tissue will be provided. Similarly, the principles of some biochemical methods used for protein identification, such as immunofluorescence staining and blotting methods will also be included. The most suitable sample preparation protocols for mineral protein identification will be discussed.

Chapter 4 The possible origins of the magnesium containing calcium phosphate nanoparticles previously observed in cardiovascular calcification are studied. A brief electron microscopy mineral characterisation is carried out on cardiovascular tissues to confirm the results previously reported in the literature. Following, the majority of the chapter focuses on the identification of the possible origins of these calcific particles by blotting methods and immunofluorescence staining.

Chapter 5 Electron microscopy physicochemical characterisation of minerals found in the breast tissue of healthy donors and patients with a benign or malignant breast disease diagnosis is presented. The association of these minerals to specific malignancies and grades of tumours is evaluated, and the diagnostic potential of the minerals is presented. Finally, possible mechanisms of formation of these minerals are discussed.

Chapter 6 The results of the electron microscopy analysis on the identification and characterisation of minerals observed in the brain of healthy young donors, elderly donors, and Alzheimer's patients are presented. Based on the results, the association

of these minerals to Alzheimer's disease pathology is evaluated. Finally, the role of one of the hallmarks of the pathology; the presence of increased amounts of phosphorylated tau protein in the brain, with the minerals is also investigated through the use of immunofluorescence staining.

Chapter 7 This is the final chapter providing a brief overview of the results, as well as a summary of the limitations and scientific contribution of the research. A small discussion on the future work will also be provided.

Appendices In **appendix A**, the work on pregnancy-induced placenta calcification carried out in collaboration with the group of Professor Inge K. Hermann (ETZ Zurich and Swiss Federal Laboratories for Materials Science and Technology (Empa)) is presented. This work was done in parallel with the work discussed in this thesis. Only the results carried out solely by the author of this thesis are discussed. The outcomes of the project as a whole have been published in a peer-reviewed paper (102).

Chapter 2: Background

2.1 Cardiovascular mineralisation in cardiovascular diseases

2.1.1 Cardiovascular system

As a whole, the cardiovascular system consists of the heart and blood vessels. Blood vessels are divided into two types; arteries and veins. Arteries are carrying oxygen-rich blood away from the heart to the rest of the body, and veins carry oxygen-depleted blood back to the heart (103). Small arteries are called arterioles, and similarly, small veins are called venules. The smallest blood vessels in the body are called capillaries, and they transfer blood between arterioles and venules.

Other than the difference in their function, structurally, veins, and arteries also slightly differ. The wall of both consists of three layers (Figure 2.1); next to the lumen the tunica intima is found, followed by the tunica media and the outer layer, called the tunica adventitia (103). The tunica intima of the arteries consists of endothelial cells and connective tissue with its outer layer being wrapped in an elastic fibre layer called the internal elastic membrane (Figure 2.1). This membrane is however, absent in veins (103) (Figure 2.1). In the tunica media, both arteries and veins contain vascular smooth muscle cells organised among elastic fibres; the number of these is much lower in veins thus this layer is much thinner in veins than in arteries (103). Finally, the tunica externa is similar in both veins and arteries, consisting of connective tissue made of collagen fibres and fibroblasts. However, the tunica externa of arteries also includes the external elastic membrane.

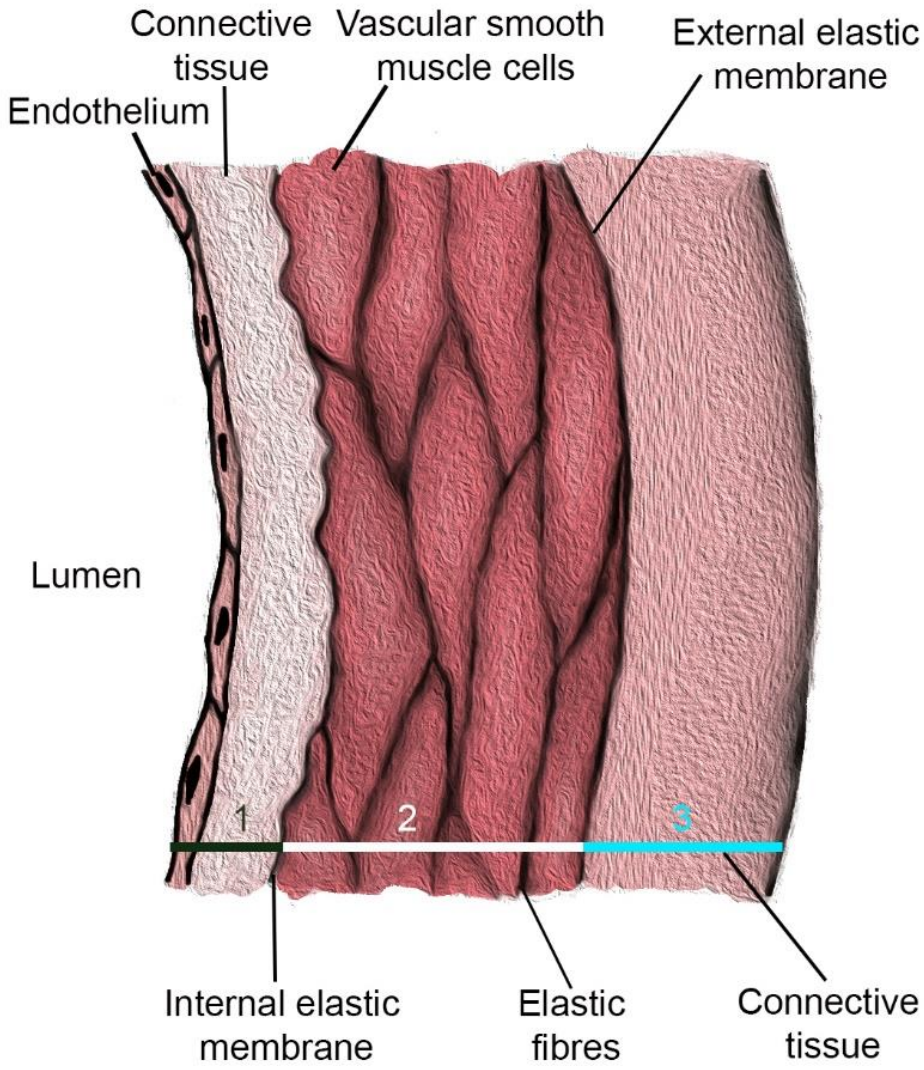

Figure 2.1: Graphic illustration of the arterial wall. ***(1)*** *The tunica intima (black line) is made of a linen of endothelial cells called the endothelium, connective tissue, and the internal elastic membrane.* ***(2)*** *The tunica media (white line) is mainly composed of vascular smooth muscle cells surrounded by elastic fibres.* ***(3)*** *The tunica externa (blue line) consists of the external elastic membrane and connective tissue.*

Similarly, to blood vessels, the heart also consists of three layers; the endocardium, myocardium and epicardium. The internal part of the heart is also divided into four chambers; right atrium, left atrium, right ventricle, and left ventricle (104) (Figure 2.2). As the blood from the venous system enters the right atrium through two vessels; the inferior and superior vena cava the myocardium contracts such that the blood is pumped into the lungs through the pulmonary artery. The blood is then re-oxygenated in the lungs and is pumped back into the heart to be pumped out to the rest of the body through the aorta (104) (Figure 2.2). To enable the correct blood flow through the body, the heart also contains four valves; the tricuspid, pulmonary, mitral, and aortic valve (104) (Figure 2.2). Finally, the outer lining of the heart that consists of several arteries

providing blood supply to the heart. There are four such arteries, referred to as the coronary arteries (104).

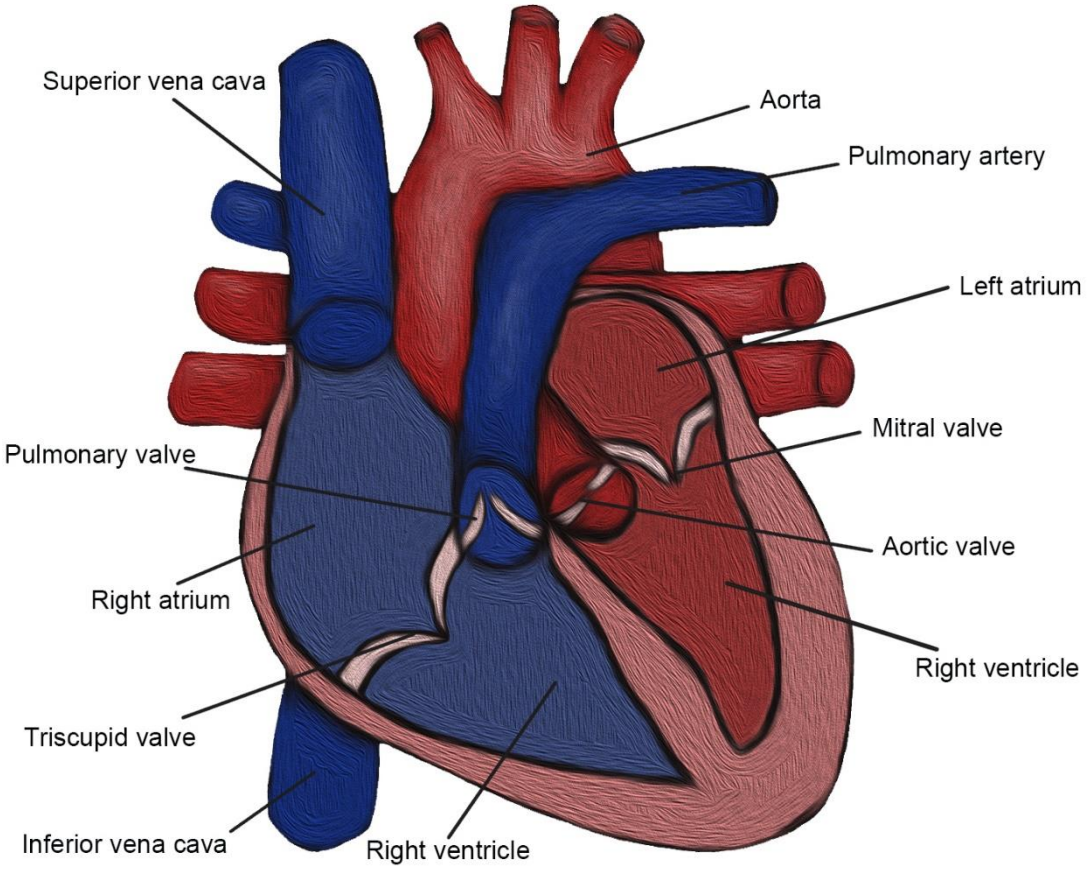

Figure 2.2: Graphic illustration of the heart showing the atriums, ventricles, valves, and main vessels. *The venous side of the heart is indicated with blue and the arterial side with red. The exterior part of the heart is pained pink.*

Circulation of the blood to the heart and other organs is essential for the function of the body as it is responsible for the transportation of nutrients and oxygen. A sudden cut to the blood supply to any organ can be fatal; for example, if the blood supply feeding the heart is restricted, it can lead to heart failure and subsequent death.

The blood of a healthy adult mainly contains red and white blood cells, as well as megakaryocytes (105, 106). Red blood cells are anucleate cells, responsible for the transportation of oxygen and are the most abundant type of blood cell (105, 106). White blood cells, on the other hand, are responsible for the immune response of the body (105, 106) and are divided into two main categories; granulocytes and mononuclear cells (106). There are three types of granulocytes; neutrophil, eosinophil, and basophil, and two types of mononuclear cells; lymphocytes (B lymphocytes, T lymphocytes, and natural killer lymphocytes) and monocytes (macrophages) (106). Granulocytes are involved in allergic and inflammatory responses as well as to control parasitic

infections and destroy foreign bodies. Lymphocytes also have similar functions; however, these cells are also responsible for the production of antigens (106). Finally, megakaryocytes are cells originating from the bone marrow (106). Their fragmentation gives rise to platelets (106), which circulate in the blood and are responsible for haemostasis. Platelets are also involved in coagulation, a response to vascular injury, which leads to platelet activation and aggregation to the site of injury, forming a layer to prevent blood leakage (107).

2.1.2 Calcific cardiovascular diseases

Cardiovascular diseases (CVD) are a group of blood vessel and heart diseases affecting the function of the heart. The long list of such diseases includes arrhythmia, coronary artery disease, heart failure, heart attack, stroke, heart valve disease, and rheumatic heart disease. It is predicted that by 2030 almost 44% of the US adult population alone will at least have one type of CVD (108). Smoking, obesity, high blood pressure, and cholesterol are all considered to be risk factors for CVD (109). Therefore, a healthy diet and active lifestyle are considered a significant part of the prevention, management, and treatment of CVD.

Unfortunately, when it comes to treatment, for most CVD in which cardiovascular mineralisation is observed such as; atherosclerosis (110), aortic valve stenosis (111) and coronary artery disease (112) the only viable choices involve surgical interventions. Coronary artery revascularization bypass surgery, percutaneous coronary intervention (angioplasty), transcatheter aortic valve replacement, and surgical aortic valve stenosis are costly procedures usually used (113). For these diseases, there is no definitive pharmaceutical treatment, even though drugs such as anti-inflammatories (114) and antithrombotics (115) are used for their management. A major obstacle in the development of successful non-invasive treatment of these diseases is the presence of calcified material, the formation of which is not entirely understood and subsequently cannot be prevented.

Biologically, what is known is that atherosclerosis is a disease that affects the lumen of large and medium-size arteries (116). It involves the deposition of lipoproteins such as cholesterol within the intimal layer of the arterial wall (117) which then triggers a chronic inflammatory response of the endothelium with the recruitment of monocytes, macrophages, and T lymphocytes (118). The recruitment of macrophages and a range of phenotypic changes of vascular smooth muscle cell result in foam cell formation (118)l which frequently become mineralised through the deposition of calcium deposits (119). Deposition of minerals is also found in the medial layers of arteries which can be triggered even in the absence of lipids deposition due to phenotypic changes of vascular smooth muscle cells to osteoblast-like cells (120).

Calcified plaques can be found in a variety of arteries such as the aorta, carotid, and coronary arteries. When the plaques are located in the coronary arteries, the corresponding disease is called coronary artery or coronary heart disease. Over time, plaques in the coronary arteries restrict the blood flow to the heart or can even rapture, resulting in a blood clot and a sudden heart attack (121). Likewise, aortic valve stenosis is the result of the deposition of lipids and minerals on the leaflets of the aortic valve (122). Similarly to coronary heart disease, the deposition of minerals on the aortic valve or aorta can, over time, affect the natural blood flow and lead to fatal outcomes.

2.1.3 Cardiovascular mineralisation

The presence of cardiovascular calcification has also been associated to increased mortality rates and worse prognosis not only in patients with a diagnosis of cardiovascular diseases but also in patients prompt to the development of calcification due to chronic kidney disease, diabetes, hypertension and other (123, 124). Despite the large number of proposed mineralisation mechanisms in the literature, the exact processes leading to the minerals observed in cardiovascular tissue are still unclear (21, 111, 120, 125-130). These include suggestions that cardiovascular calcification is a result of the transdifferentiation of vascular smooth muscle to bone cells (120), or due to the release of extracellular vesicles from macrophages that serve as mineral nucleation sides (131). It has for many years also being argued that the mineralisation of cardiovascular tissues is a consequence of osteogenic processes (132), a suggestion mainly based on the elemental composition of the minerals and the presence of biological bone markers in the affected tissue.

Studies have, however, identified a number of minerals present in cardiovascular tissues suggesting a more complex mineralisation process involving several distinct mechanisms. An early study using scanning electron microscopy and X-ray diffraction pattern analysis of minerals in atherosclerotic aortic tissue showed the presence of several structures including spheres, irregularly shaped particles, fibres forming networks and flat plates with a chemical composition of calcium apatite of varying calcium to phosphorous ratios and carbonate contents (133). These results came in agreement with another study also using a range of spectroscopic methods; which reported heterogeneity amongst the structures observed and also the presence of trace minerals such as sodium and magnesium in the apatite minerals (134).

A more refined study, although showed the presence of magnesium-containing beta-tricalcium phosphate in the media layers of the aorta, while hydroxyapatite was mostly observed in the intima instead suggesting different origins (135). However, no morphological information on the magnesium-containing minerals was included. Interestingly though, the presence of calcification in the intima and media of arteries

has been found to correlate to different underlying pathologies; with calcification of the intima being observed in atherosclerosis while chronic kidney disease and diabetes result in calcification of the media layers (136, 137). Observations further supporting different origins for these two types of minerals, even though the two can also co-exist.

Similarly, characterisation of calcified aortic and mitral valves reported the presence of nodules, nanoparticles and large minerals on the valve leaflets (138). The study also reports a chemical composition of calcium phosphate with varying carbonate contents and calcium to phosphorus ratio (138). Another study also reports the presence of spherical deposits and large poorly crystalline hydroxyapatite in the valves, whose calcium to phosphorus ratio was fount to be increasing as the disease is progressing (139).

A more detailed electron microscopy study (13, 140) on vascular calcification in the aortic and mitral valves, coronary arteries and aorta, indicated that the minerals observed can be divided into three distinct structures, despite anatomical location and underlying disease: mineralized fibres (Figure 2.3 (a)), calcific particles (Figure 2.3 (b, c)), and a large mineral with no defined morphology (Figure 2.3 (d)).

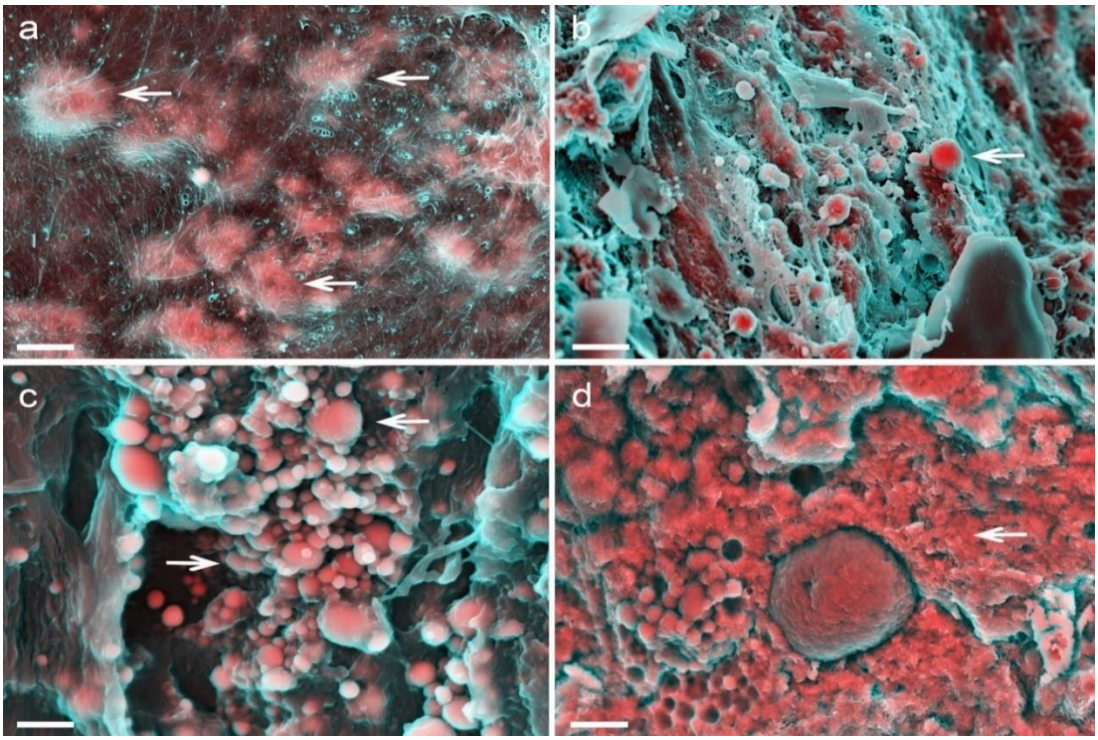

Figure 2.3: Density-dependent colour - scanning electron micrographs (DDC-SEM) of calcification observed in cardiovascular tissue (12)*. Red and pink indicate inorganic and turquoise (blue/green) indicates organic material.* ***(a)*** *Calcified fibres indicated by arrows. Scale bar = 2 µm.* ***(b)*** *Calcific particles (arrow). Scale bar = 5 µm.* ***(c)*** *Aggregates of calcific particles (arrows). Scale bar = 1 µm.* ***(d)*** *Large mineral of no defined morphology (arrow). Scale bar = 2 µm.*

The same study shows the presence of distinct magnesium-containing calcium phosphate particles (13), while it also highlights differences in mineral crystallinity, with the large mineral diffracting as a polycrystalline mineral (13), while the particles as a single crystal (13). Interestingly the particles were observed even in tissues with no macroscopic calcification and with no other form of mineral present, suggesting that they are the first to be deposited (13). On the other hand, the large minerals and mineralised fibres were only observed in patients with a diagnosis of a calcific cardiovascular disease confirmed through the macroscopic presence of calcification in the tissue (13). The uniqueness of the magnesium-containing particles was also confirmed through indexing of electron diffraction patterns obtained, which showed that they are formed by crystalline whitlockite rather than hydroxyapatite (141). This information on the morphology, elemental composition, crystallinity and timeline at which the cardiovascular minerals are observed, further supports several mineralisation mechanisms being involved, with the whitlockite particles possibly having a role in the development of the other minerals.

Furthermore, comparing the properties of the cardiovascular minerals reported to the bone mineral, they were found to be remarkably different. In bone, the calcium/phosphorus ratio most commonly reported is below 1.7 (75, 142-144). In contrast, the ratio in cardiovascular mineralisation (determined by infrared spectroscopy and atomic absorption spectroscopy) has been most frequently reported as 1.7 or above (134, 135, 139). Additionally, even though magnesium is present in bone, it is only considered a trace element, unlike cardiovascular minerals where it corresponds to a considerable percentage of the inorganic component (134, 135, 145). At the same time, the presence of crystalline whitlockite nanoparticles suggests a unique mechanism other than an osteogenic processe as such crystallinity has never been reported in the bone.

Subsequently, these findings highlighted the need for new mineralisation origins and pathways to be identified and mineralisation models to be developed (20, 21, 146, 147). However, many studies using cell culture models to reproduce these minerals do not carry out a detailed mineral characterisation, focusing only on confirming the presence of calcium phosphate or osteogenic markers. For example, in the study of valvular calcification, the presence of apatite in the produced mineral was reported in cell mineralising models using vascular smooth muscle cells (to study calcification in the media layers of arteries), and macrophages (to study calcification in the intima layers of arteries) (148, 149), even though the mineral was not characterised. Few studies do although include a mineral characterisation, with a study using extracellular vesicles isolated from vascular smooth muscle cells showing the formation of calcium phosphate particles in the mineralising model used; the properties of which are similar

to the apatite mineral found in native tissues (20). Similarly, mineralising cell culture models using valvular intestinal cells to understand valvular calcification (150) report the production of calcium phosphate but do not give detailed information on the minerals reported (151-153).

As with cell culture models, a large number of animal models have also been developed focusing on the induction of calcification in cardiovascular tissues (154). The presence of calcium phosphate and osteogenic markers in a variety of cardiovascular tissues has been reported in both small (e.g. mice and rats) and big (e.g. horses and cows) animal models (154). However, again no detailed characterisation of the minerals is carried out to confirm that these are the same structures observed in humans; while most of the animal models used also have other biological, anatomical and pathophysiological differences to humans (154). For example, mice, (even though they are the most frequently used animal for the study of atherosclerosis and aortic valve stenosis) do not develop calcification naturally, while the models used to induce calcification do not report deposition in the coronary and carotid arteries, something widespread in humans (154). Arterial calcification has, on the other hand, been reported in horses; thus, they are argued to be a more suitable model (155). However, characterization of the minerals present only reported the presence of hydroxyapatite (155), with magnesium or whitlockite not been mentioned.

Taken all together, the results of a large number of studies using mineralising models could indeed give insights on the presence of the apatite minerals in cardiovascular tissues. Despite, none of these studies concentrates on the identification of the exact minerals formed, nor they compare these to what is found in native human tissues. Finally, all studies on cardiovascular calcification have to date dismissed the presence of magnesium in the mineral; subsequently, the mechanisms responsible for the presence of the whitlockite nanoparticles are yet undefined.

2.2 Breast mineralisation in breast cancer

2.2.1 Breast anatomy

In humans, the breasts are anatomically located on the anterior part of the thorax on top of the pectoralis major muscle and the ribs (156, 157) (Figure 2.4). Their shape and size vary between individuals as they depend on, amongst others, racial and genetic factors (156). On the exterior of the main bulk of the breasts lays the nipple and the areola (Figure 2.4) (156). Under the skin and the nipple-areola complex lies a layer of subcutaneous fat (adipose tissue) which covers the fibrous (ligaments and stroma (connective tissue)) and glandular tissue (156). That is divided into around 20

ducts, which start from the lobe and converge to the nipple (Figure 2.4). Each lobe is made up of up to several lobules which are made of alveoli (Figure 2.4). The lobules are surrounded by connective tissue called stroma from both the inside and the outside (Figure 2.4). However, the stroma outside the lobules is formed by collagen fibres; thus, it is substantially denser than that found on the inside, which is predominantly formed by loose adipose tissue (156). The stroma extents to surround all lobules and ducts providing structural support.

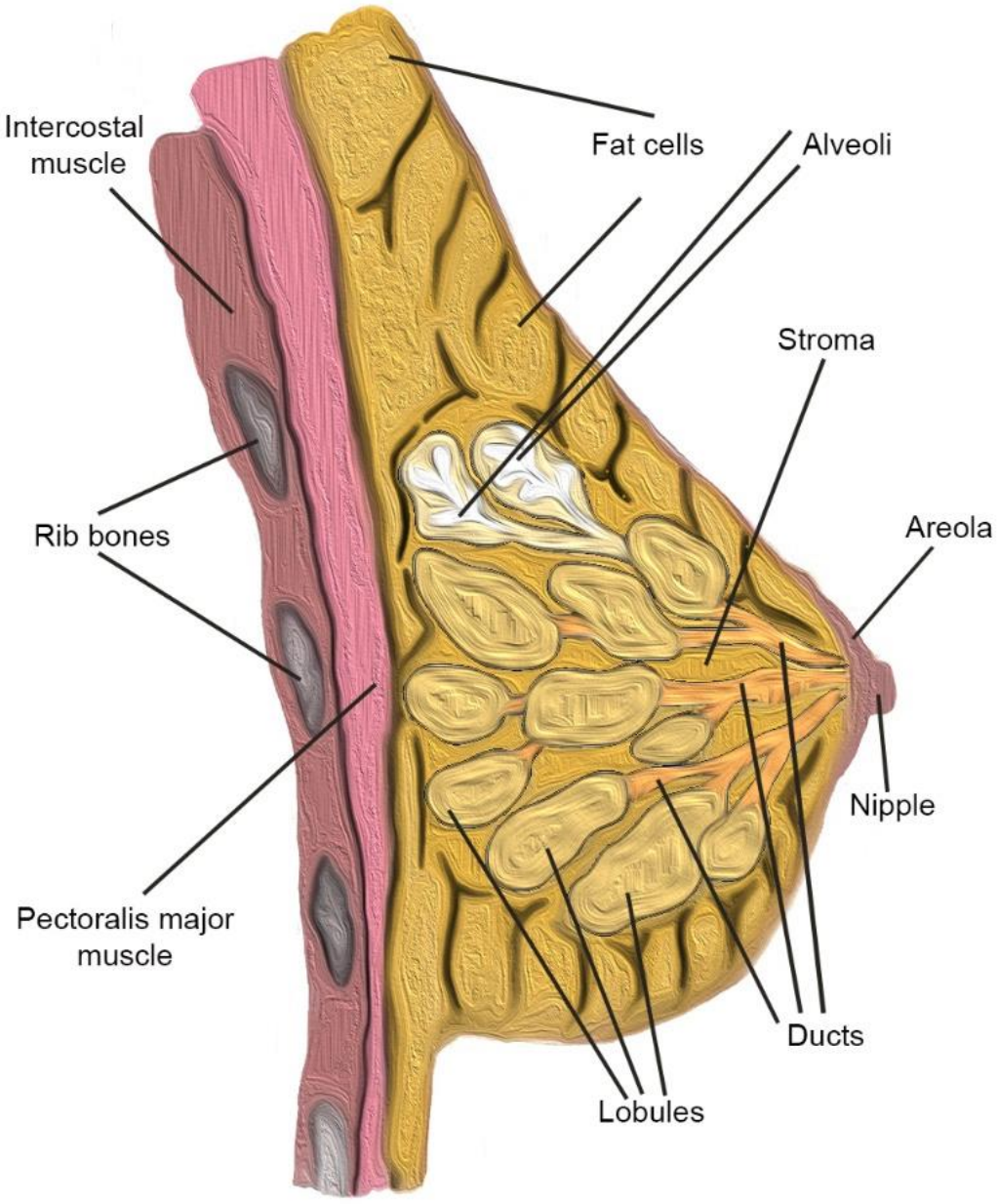

Figure 2.4: Graphic illustration of the breast. *The rib bones, intercostal muscle, and the pectoralis major muscle, which are located at the posterior of the breast, and the different structures and tissues forming the breast: fat (adipose tissue), stroma (connective tissue), ducts, lobules, and nipple-areola complex are shown.*

2.2.2 Breast cancer

Breast cancer is the most common type of cancer in women (158) and refers to several diseases. The main challenge in the diagnosis and treatment of these diseases is their heterogeneity (159). The development of each breast tumour depends on the types of cancer cells present (160, 161), their alterations during disease progression (161, 162), and also the tumour microenvironment (161).

Different types of breast diseases affect different breast structures. Benign breast tumour diseases include; fibrocystic changes, benign phyllodes tumour, hamartomas, papillary lesions, and Paget's disease. Fibrocystic changes include the formation of cysts (abnormal cells accumulating together to form a 'bubble' filled with fluids (163)) in the stroma, ducts or lobules, non-sclerosing adenosis (enlargement of the lobules (163)) and fibrosis (damages to the connective tissue) (164). Usually, these changes lead to breast lumps, however, are considered to be associated with hormonal changes and menopause (165) and to not contribute to an increase of the risk of a breast malignancy (166). Simple fibroadenomas, a type of fibroepithelial lesions (a growth of epithelial and stromal cells) (167) formed in the lobules (163), are also considered fibrocystic changes and harmless (166). Harmless are also considered some benign tumours (166) including; benign phyllodes tumour (another type of fibroepithelial lesions (167, 168)), hamartomas (lesions formed by glandular epithelial cells (epithelial cells covering the mammary glands), fibrous and adipose tissue) and papillary lesions (benign tumours forming in the ducts (163)). On the other hand, sclerosing adenosis and sclerosing papillary lesions are suggested to increase the risk of malignancy (166). Finally, Paget's disease (cancerous lesions on the nipple and the areola (169)) is rarely encountered in the breast tissue and is usually associated with other underlying breast diseases, in many cases malignant (170).

Malignant breast diseases are divided into non-invasive and invasive. The most common invasive breast carcinoma is the ductal carcinoma in situ (DCIS) (171), which involves the growth of cancer cells within the ducts. Even though the disease is non-invasive, it increases the possibility of developing an invasive ductal carcinoma (171). Invasive ductal carcinoma (IDC) is the most common among invasive breast tumours; anatomically starting from the ducts and over time infiltrating into other breast tissues and body parts (172). The second most common invasive breast cancer is invasive lobular carcinoma (ILC) (172), which begins in the lobules and similarly to IDC spreads to other parts of the breast and the body. Other malignant diseases accounting for only a small percentage of malignant breast tumours include; malignant phyllodes tumours and invasive cribriform carcinoma (ICC), which refers to tumour growth with a nest-like shape (173) in the breast stroma.

2.2.3 Breast mineralisation

Mineralisation of the breast tissue has been suggested to be a result of tissue necrosis as a consequence of injury or a range of diseases, such as chronic kidney disease (174) and hypertension (175). Additionally, microscopic mineral deposits (known as microcalcifications) found in breast tissue are a crucial component in the indication of underlying breast carcinomas (176). Microcalcifications are also regularly used as mammographic features in the differentiation between malignant and benign diseases (176-178). For example, multiple similar calcification clusters (appearing as bright white spots on the mammograms) spread over one or both breasts are considered to be concomitant of benign diseases, while variability in their appearance suggests a malignant cause (176).

This association of breast mineralisation to cancer has led to many research initiatives aiming to identify specific differences between benign and malignant mineralisation (179-181). Through electron and light microscopy, X-ray diffraction, and microprobe analysis, two chemically different types of minerals were associated with breast carcinomas: calcium oxalate (25, 179, 182) and hydroxyapatite (22, 24, 25, 179, 182). Calcium oxalate has been identified mostly in the context of benign diseases (25, 182), although some more recent studies do not report its presence (183, 184). On the other hand, hydroxyapatite has been recorded widely in studies using spectroscopic and diffraction methods, in both benign and malignant cases (23, 179). Recent studies, using Raman and energy dispersive x-ray spectroscopy, have also pointed out the presence of magnesium-substituted apatite and whitlockite in malignant cases (22, 24, 182). No clear correlation has been found, however, between the levels of magnesium in tissue and malignancy (24, 183). Changes in the crystallinity of hydroxyapatite, were although reported to correlate with disease classification with an increased crystallinity associated with invasive tumours (185). Furthermore, studies where Fourier transform infrared (FTIR) and Raman spectroscopy were used found that a decrease in the concentration of carbonate and protein context in the mineral is concomitant to an advanced malignancy (23, 179).

Despite, most of these studies do not provide detailed information about the morphology of breast minerals in the microscale and how these are related to malignancy. An exception to this are studies also incorporating scanning electron microscopy in their workflow. An early study showed the presence of pyramid calcium oxalate crystals and calcium phosphate minerals in the form of structures of no defined shape, spherical particles and rod-like crystals (25). More recent studies, on the other hand, only report the presence of large minerals of no defined shape on electron micrographs in all types of tissues used (Figure 2.5) (22, 24). The presence of whitlockite particles

was also reported in an invasive malignant breast tumour case, although only one sample was used in the analysis; therefore, no definite correlation was noted (22).

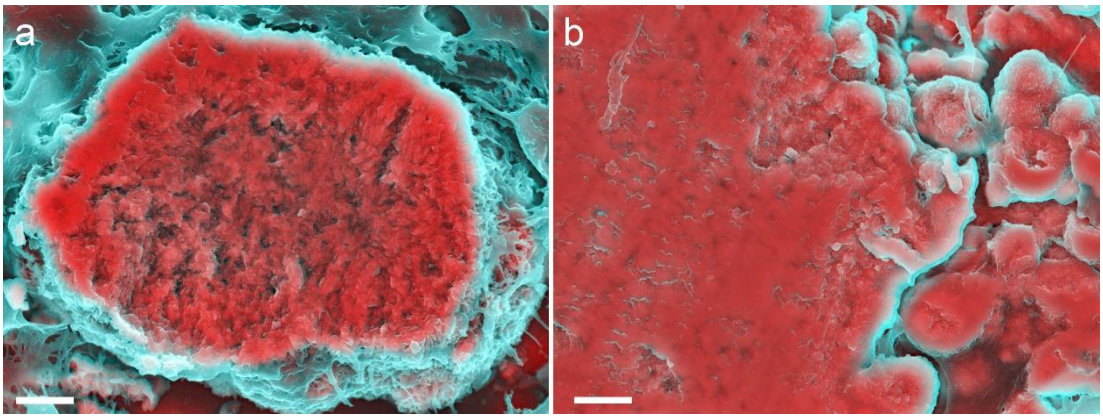

Figure 2.5: Density-dependent colour - scanning electron micrographs (DDC-SEM) of calcifications observed in breast tissue (12)*. Red and pink indicate inorganic and turquoise (blue/green) indicates organic material.* ***(a)*** *Electron micrograph of smaller apatite mineral observed in breast tissue.* ***(b)*** *Electron micrograph of large apatite mineral observed in breast tissue. Scale bar = 2 µm.*

Other than their diagnostic capacity, the physicochemical properties of minerals in breast cancer are of growing interest due to their potential in providing insights on the prognosis of the disease (186, 187). It has been reported that breast cancer patients with small minerals have a lower survival rate than patients who present more extensive deposits (188), and the presence of minerals in ducts increases the risk of cancer recurrence (187). Studies have also reported that the presence of apatite in breast cancer cell cultures can enhance mitosis processes (19) and also the migration of tumour cells (189). The exact origins of these apatite minerals are still yet unknown, due to probably the common belief that mineralisation had no biological significance and was just only a by-product of cell death.

More recent studies, however, indicate an active cellular process, with *in vitro* experiments showing that tumourigenic mammary cells can produce hydroxyapatite, in contrast to non-tumourigenic cells, which do not mineralize (18). Detailed characterisation of the mineral morphology was not although carried out; even though, raman spectroscopy was used to confirm the chemical composition of the mineral. This capability of breast tumour cells to form such minerals has been attributed to the fact that such cells express bone-associated proteins (190, 191). It has been therefore suggested that, as a consequence, osteogenic-like processes might be leading to the formation of hydroxyapatite minerals in the mammary tissue (192). Despite, a comparison between the minerals found *in vivo* to those produced *in vitro* is still missing for a definite conclusion to be made.

2.3 Brain mineralisation in Alzheimer's disease

2.3.1 Brain anatomy

The human brain consists of the brainstem, cerebrum, and the cerebellum (193) (Figure 2.6 (a)). The brainstem is located just above the spinal cord and consists of three regions, the midbrain, the medulla, and the pons (193). Behind the brainstem, at the back of the head, the cerebellum is located. On top of the brainstem and the cerebellum lays the cerebrum, the largest part of the brain (193). The surface of the cerebrum is called the cerebral cortex; which has a folded structure forming gyri and sulci (Figure 2.6 (b)) all of which are named based on their location. Internally, the cerebral cortex is also divided into regions of grey and white matter (Figure 2.6 (b)). Grey matter itself contained neural cell bodies, while white matter contains neural projections (the axons).

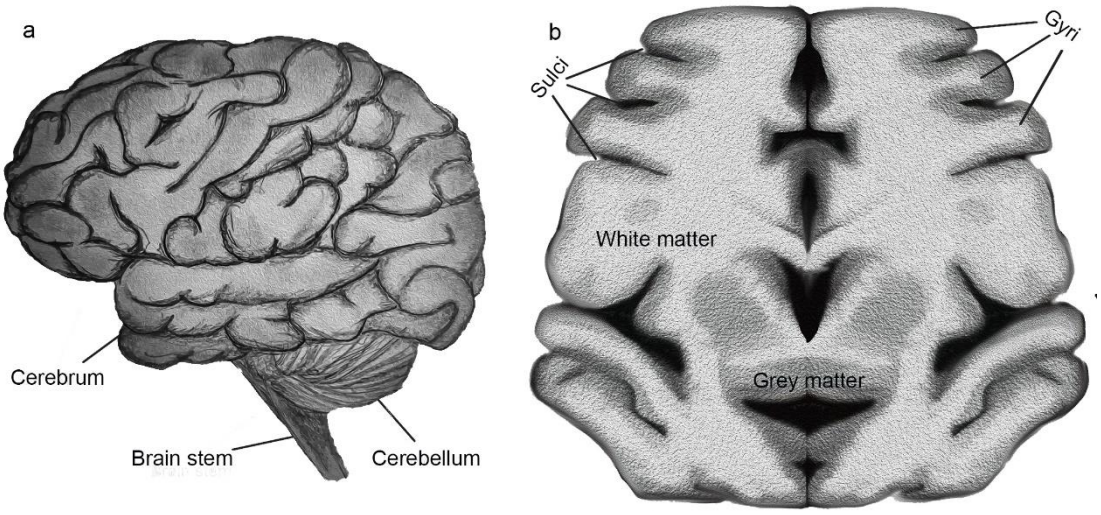

Figure 2.6: Graphic illustration of the brain. (a) *Whole-brain schematic indicating the cerebrum, brain stem, and cerebellum.* ***(b)*** *Coronal view of the brain indicating the grey matter with dark grey and the white matter with off white-grey. The gyri and the sulci of the brain are also indicated, which are the folds and gaps found on the brain, respectively.*

Four lobes, the frontal, temporal, parietal, and occipital (Figure 2.7) further divide the cortex; based on their specific functions (194). The frontal lobe is associated to socioemotional behaviour, cognitive, behavioural, and motor functions (194), the temporal lobe to sensory functions, language and emotions (194), the occipital lobe to vision (194), and the parietal lobe to the processing of incoming somatosensory signals as well as to the perception of external space, body image and attention (194).

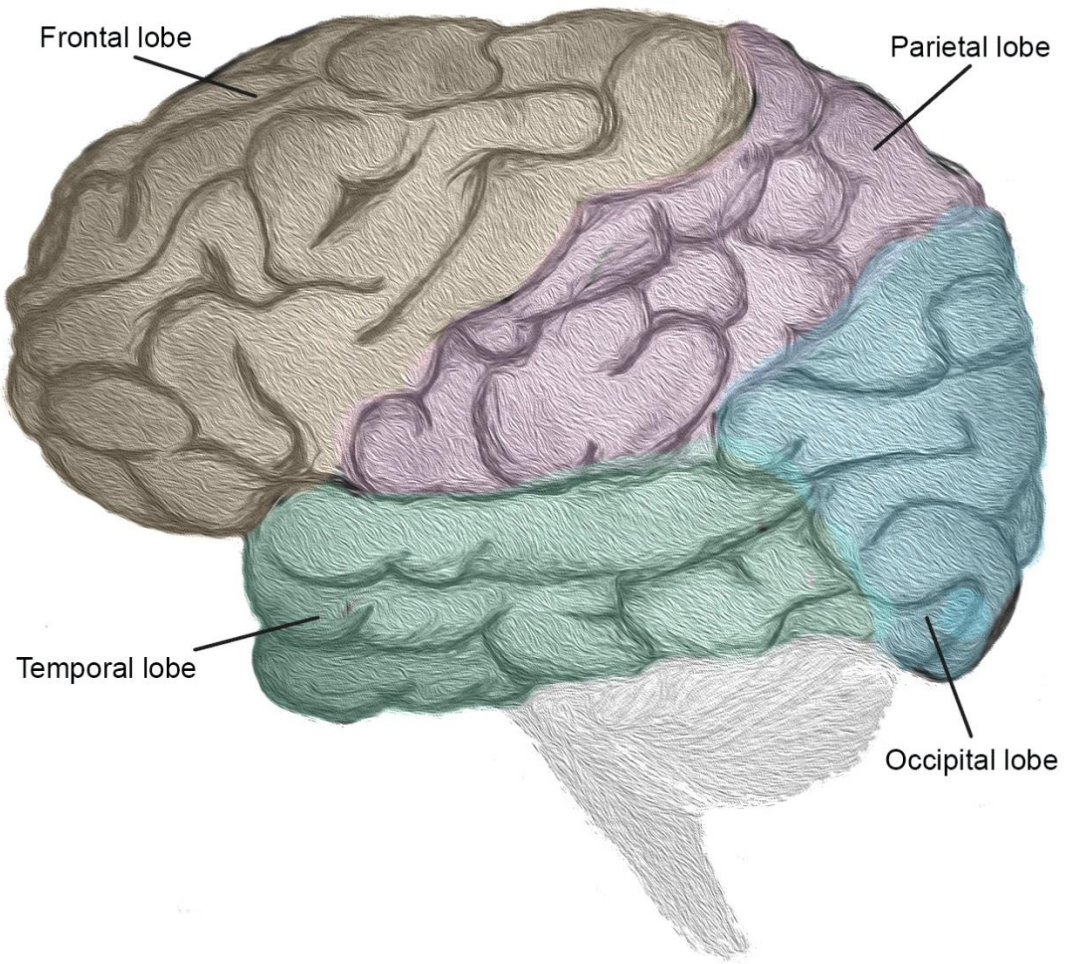

Figure 2.7: Brain illustration indicating the four lobes in different colours. *The frontal lobe is indicated with yellow, the parietal lobe with pink, the temporal lobe with green, and the occipital lobe with blue.*

Deep into the cerebral cortex, with functions strongly connected to individual lobes, a group of subcortical structures is located. These include, amongst others; the hippocampus and basal ganglia (194). The basal ganglia consists of a group of brain nuclei, including the caudate nucleus, putamen, substantia nigra claustrum, and globus palidus (195). As a whole, the basal ganglia is involved in cognitive and emotional operations as well as motor function control (195). However, individual nuclei are associated with specific functions; for example, the putamen is associated with motor function while the caudate nucleus to cognitive function. The hippocampus is, on the other hand, responsible for the formation and storage of memories, allowing for fasts and events to be recalled (194).

At the cellular level; the brain mainly consists of neurons (196) and glial cells (197). Several different neuronal species exist, all of which have different morphologies and functions (196). Morphologically, there are unipolar, bipolar, pseudo unipolar, and multipolar neurons, with the latter being the most common in the human brain (198). Despite their differences, all neurons are formed by a cell body (soma), an axon with axon terminals and dendrites (199). Axons and dendrites are both used for neuronal communications; with axons being responsible for signal output, while dendrites for signal input (199). The signalling between neurons is done at synaptic points (synapses) between axons and dendrites, through a bioelectrochemical process that is controlled by neurotransmitters; chemicals such as dopamine and serotonin (198).

As previously mentioned, neuronal bodies are located in the grey matter of the brain and the axonal projections in the white matter. In the cerebral cortex, the outer grey matter layer called the neocortex is also divided into six different cellular layers. Each of these layers contains a different number and type of neurons which receive and send signals to specific parts of the brain. Studies showed that these cellular layers are substantially different based on their location in the cortex, which led to the separation of the brain lobes into smaller distinct areas; the Brodmann areas (198, 200). The structural differences in these areas are believed to be due to the associated functions; thus, each Brodmann area is considered responsible for that function (200).

Glial cells are fundamental for the correct function of neurons and include amongst others; oligodendrocytes, astrocytes, and microglia. Oligodendrocytes are responsible for the production of myelin; an insulating layer surrounding the axons fundamental for their function (197). Astrocytes are divided into two types: fibrous and protoplasmic. Fibrous astrocytes are found in white matter, while protoplasmic astrocytes in grey matter. Both types have however similar functions; including regulation of brain blood flow, homeostasis within the nervous system, proper synaptic function, and brain metabolism (201). Finally, microglia cells are involved in immune responses and are responsible for the clearance of pathogens (197). These cells, have different resting and activated states; thus, their morphology can give information on the occurrence of insults in the brain (202).

2.3.2 Alzheimer's disease

Neurodegenerative diseases include a number of pathologies leading to cognitive impairment and movement disorders (203). One such disorder is Alzheimer's disease (AD), affecting about 30 million people worldwide (204). The disease is char-

acterised by severe memory loss as well as impairments in motor functions and cognition (205). Down to the cellular level, neurofibrillary tangles and amyloid plaques are the two primary landmarks of the pathology, always observed in AD brains (206).

Amyloid plaques are an accumulation of amyloid β peptides (205). Their formation is believed to be due to structurally altered amyloid β monomers being released, leading to the formation of soluble amyloid β oligomers. Protofibrils are then formed through the attachment of new monomers to the oligomers. Aggregation of these protofibrils leads to fibrils that subsequently accumulate to form plaques promoting further deposition of amyloid β oligomers (205, 207, 208). High concentrations of amyloid β oligomers have been proven toxic, having a catastrophic effect on neuronal cells. Synaptic damage (205) is observed soon after the levels of oligomers increase (207, 209, 210). Additionally, the presence of amyloid plaques leads to an inflammatory response of microglial cells (205, 207, 210, 211), while the presence of amyloid β oligomers has been shown to affect the function of tau protein (207).

Tau protein is a microtubule protein primarily located in axons that under normal conditions, interact with tubulin for microtubule stabilization (212). The protein mainly functions through well-controlled phosphorylation events (213, 214) but under pathological conditions, they are found to hyperphosphorylate into helical filaments (215). Hyperphosphorylated tau leads to the formation of neurofibrillary tangles (216) and succeeding functional loss of neuronal cells. However, it is yet not entirely clear whether the unfavourable effects of tau on cells is due to these aggregates, or due to the formation of insoluble or soluble oligomers following hyperphosphorylation (217).

Despite that, the development and spreading of tau pathology is related to brain regions associated with cognitive impairment, with the spreading pattern to be an important part of the Braak stages used for the clinical evaluation of AD (218). Braak staging states that in the early onset of the disease changes affect the transentorhinal region of the cerebral cortex, while later on the subcortical nuclei, the hippocampus, and medial temporal lobe regions. In the late stages of the disease, the changes spread to other regions, including the medial occipitotemporal gyrus, temporal neocortex, superior temporal gyrus, and parts of the visual cortex (219).

Other than damages on neurons, AD pathology has more recently also been correlated to changes in glial cells, even though it is not entirely understood whether these are a result of the pathology or are contributing factors (220). For example, it has been observed that the presence of amyloid plaques can have a toxic effect on microglial cells, causing them to degenerate (202). Additionally, the increase in degenerating microglia cells has been associated with the presence of an increased amount of neurofibrillary tangles (202). Astrocytes have also been observed to un-

dergo compromises in AD pathology, with astrocyte atrophy affecting the synaptic connectivity, brain homeostasis, and subsequent neuronal function (221). Neuronal communication has also been observed to be compromised due to myelin degeneration resulting from dysfunctional oligodendrocytes in AD pathology (221). Thus, even though not all parts of AD pathology are fully understood, it is clear that it does not only involve neuronal cells but instead has an effect on all cellular components of the brain.

2.3.3 Brain mineralisation

Alzheimer's disease has also been previously associated with brain mineralisation, mainly in the form of intracranial vascular calcification in brain regions affected by the disease (222). Vascular calcification has been observed in the caudate nucleus, putamen, globus pallidus, and cerebellum (222) while in the hippocampus, it has been associated with neural cell death (222). These minerals were observed through Von Kossa staining suggesting a calcium-containing mineral in the form of calcified nodules and large mineral plates (223). Another study also reports the association of intracranial vascular calcification with the presence of amyloid plaques (224); while it also reports the presence of mineralised plaques outside the vasculature, although the nature of these was not further investigated (224). Additionally, atherosclerotic brain calcification, as observed on magnetic resonance images, has been correlated to low cognitive scores and thus is believed to lead to cognitive impairment (225). However, it is not clear if the minerals have a role in the development and progression of AD pathology as such.

Mineralisation of the brain was initially believed to be a result of calcium abnormalities in the body, but it was later suggested that iron and dopamine metabolism abnormalities play a significant role as well (226, 227), often associated with psychotic pathologies (228). Additionally, the presence of minerals in brain structures has also been related to other pathologies. Case studies suggest that the vascular non-atherosclerotic mineralisation of structures such as the cerebral cortex, basal ganglia, and cerebellum is related to Fahr’s disease (40). An electron microscopy study of the minerals observed showed that they were of mostly spherical morphology and contained both calcium and iron (229). Furthermore, calcifications are present in meningioma tumours (228); while intracranial arterial calcification has also been proven to increase the probability of ischemic stroke in patients with chronic kidney disease (230).

Although most of these pathologies have been associated with calcium-containing minerals, and more specifically calcium phosphate due to the knowledge already available on vascular calcification in other anatomical parts of the body, other

mineral properties are yet unknown. One of the limitations in the research of brain mineralisation is that most of the studies found in the literature are using macroscopic methods of mineral characterization (231-233). Such macroscopic methods are used to provide information on the anatomical location of the minerals in the brain, but no information is collected at the nanoscale. As a result, it is still not clear whether brain mineralisation is a passive process, due to ageing, or an active one, nor it is clear whether these minerals affect the progression of any of the associated pathologies.

Chapter 3: Experimental methods

3.1 Electron microscopy in the study of pathological minerals

The most widely used electron microscopes are scanning and transmission electron microscopes. Both types have been used countless times in the study of cells, biological structures, and tissues, providing valuable information on these systems. The most apparent advantage of electron microscopes over light microscopes is their high resolution. State-of-the-art scanning electron microscopes (SEM) have a resolution of around 0.4 nm (234). Conventional SEMs usually have a resolution limit of about 1 nm (235), which is at least a hundred times higher than that obtained by conventional optical microscopes (236). Transmission electron microscopy (TEM), on the other hand, can achieve a resolution of angstroms (237) allowing information on delicate biological structures to be obtained and even the visualisation of individual atoms within crystals.

Electron microscopes have allowed the visualisation of bone ultrastructure, with a large part of the knowledge we have today on bone mineral originating from electron microscopy studies (72). Moreover, several researchers have shown the importance of using electron microscopy in the study of pathological mineralisation (13, 14). SEM aided the identification and provided detailed structural information on the minerals observed, amongst others, in cardiovascular (13), kidney (238), and ocular (14) tissues. Even though the most widely reported in physiological (10) and pathological minerals are usually formed by calcium phosphates, SEM visualisation of these minerals has indicated significant differences and allowed the identification of distinct mineral structures (13, 14, 74).

Similarly, TEM imaging has also proven to be particularly useful in the understanding of the formation mechanisms of biological minerals, as it enables the localization of minerals in relation to cells, cell organelles, and extracellular matrix. Energy-dispersive X-ray spectroscopy (EDS) and selected area electron diffraction (SAED) tools can also provide data on the chemical composition, phase, and crystallinity of the minerals present. Information incredibly valuable in the identification of the mineralisation processes taking place as differences in the phase and crystallinity can hint that different mechanisms are responsible for the presence of minerals. SAED has been employed in the study of pathological minerals and has given insights on their origins (13, 14).

3.2 Electron microscopes overview

Electron microscopes, unlike optical microscopes which use light, employ interactions between an electron beam and a sample for image formation. As previously mentioned, the two most common types (Figure 3.1) are scanning and transmission electron microscopes (239). Scanning electron microscopes rely on reflected products of the interactions (240) to produce an image of the sample surface, while on the other hand, transmission electron microscopes, use primarily the ability of the electron beam to penetrate through the sample (240).

Despite the functional differences, in both microscopes, the electrons are produced by an electron gun. In general, two types of electron guns are most widely used; thermionic and field emission (241). Thermionic guns typically consist of a tungsten filament that is heated using an electric current, providing the needed energy for electrons to escape the surface of the filament (241). Field emission guns, on the contrary, use a sharp tungsten crystal instead with a high electric field applied near the tip of the crystal, causing electrons to tunnel out (241). As both types of guns are rather sensitive, to avoid contamination, all traditional electron microscopes operate under high vacuum (242). Operating under high vacuums also eliminates the scattering of electrons on air particles, allowing for a uniform electron beam to be formed (243). An exception to this, are some SEMs that operate at variable pressure; with the electron source and column maintained at high vacuum and the specimen chamber at different pressures (243), however, no such microscopes were used in this work.

Following the formation of the initial electron beam, the electrons are accelerated through an electric field towards the anode and focused through electromagnetic lenses called condenser or objective lenses (Figure 3.1) (240, 242). Condenser lenses are used to alter the beam size, while objective lenses adjust the angle of the beam and subsequently the focus point (242). In a SEM these electromagnetic lenses are only used for the formation of the final electron beam, while in a TEM electromagnetic lenses are also used for image formation (244). Apertures are also used in both microscope types to modify the beam size by blocking electrons travelling at larger angles (244).

Once the primary electron beam interacts with the atoms in the sample, a range of charged particles originating from the primary beam, secondary charged particles, and photons (239) are generated, which are collected to form an image, a chemical spectrum, or an electron diffraction pattern (245). In the SEM, detection happens by specific detectors, usually using indirect methods of detection and image formation. Scintillator or semiconductor detectors are usually used. One example of a scintillator detector is the Everhart–Thornley detector. This detector is composed of a positively

charged Faraday cage to attract the electrons and a scintillator which converts the electron signal into photons (244). The photons then enter a photomultiplier tube that converts them back to electrons, which are then multiplied through interactions that generate secondary electrons. These electrons are then captured to form an image. For the TEM, direct detection and image visualisation can also be employed through the use of a phosphorescence screen (246). The images can then be recorded on photographic films and in more recent years on charged coupled devices which allow visualisation on a computer screen (246).

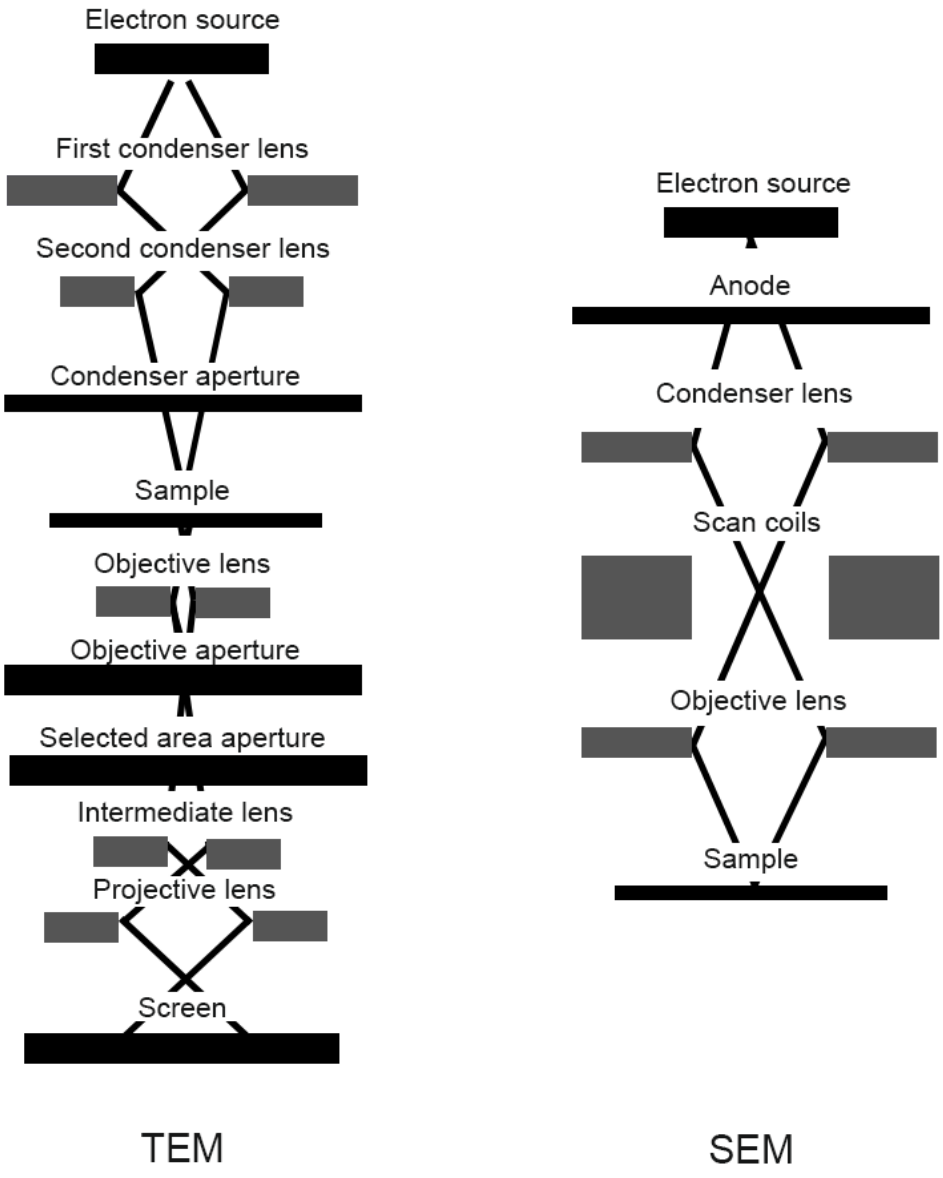

Figure 3.1: Diagrams of the electron beam path in a transmission electron microscope and a scanning electron microscope (247).

3.2.1 Electron – matter interactions

When an electron beam interacts with a material, elastic and inelastic electron scattering is observed. In elastic scattering, the electrons do not lose kinetic energy through the interaction with the sample surface; however, their direction is altered (248). On the contrary, in inelastic scattering electrons experience energy changes due to interactions with the electrons and nuclei of the atoms within the sample. As a result, these electrons can be reflected, transmitted through, or come to rest within the sample (248, 249).

Inelastic collisions can, therefore, give rise to backscattered electrons, which result from electromagnetic forces between the negatively charged primary beam and the positively charged nucleus of the atoms found in the sample, which cause primary electrons to be deflected back (249) (Figure 3.2). The portion of incident electrons that get backscattered (backscatter coefficient) was found to be related to the atomic number of the elements present in the specimen (244, 249). Higher atomic numbers are correlating to a higher number of backscattered electrons and therefore, a higher backscatter coefficient (244).

Secondary electrons are another result of inelastic scattering. They are called secondary as they do not originate from the primary electron beam but are instead a result of the interaction between the electron beam and the sample surface. They are generated through energy transferred between the incoming primary electrons and the electrons within the electron energy levels of the sample atoms (249) (Figure 3.2). When enough energy is transferred, these electrons can escape the atoms and the sample surface (250) (Figure 3.2). Secondary electrons were found to provide topographic information (239) as spikes and edges present in the specimen allow more electrons to escape the surface at different angles leading to differences in the brightness of the resulting image (electron number effect) (244, 249). Additionally, the amount of detected secondary electrons also depends on the angle in which the specimen is located in relation to the detector which also results in brightness differences in the end image (trajectory effect) (244).

Another secondary product of the interaction between the primary beam and the atoms of the sample are photons emitted, referred to as characteristic x-rays (249). Characteristic x-rays are a by-product of the generation of secondary electrons (Figure 3.2), which as they escape leave behind an electron vacancy in the corresponding electron energy level of that atom (Figure 3.2). A higher energy electron then fills this vacancy by losing some of its energy in the form of a photon (Figure 3.2). The photon energy corresponds to the difference in the energy between the two electron levels

(249). As this energy difference is a property specific to each chemical element, analysing the energy of the emitted photon can lead to the identification of the atoms present in the sample (249).

Finally, in cases where the sample is thin enough, the primary beam electrons can penetrate the sample. These electrons have interacted with the specimen atoms and therefore, also carry information on the sample morphology and chemical composition (249). Both elastically and inelastically transmitted electrons carry information of the elemental composition of the sample, as the amount of electrons passing through is inversely proportional to the atomic number of the elements present.

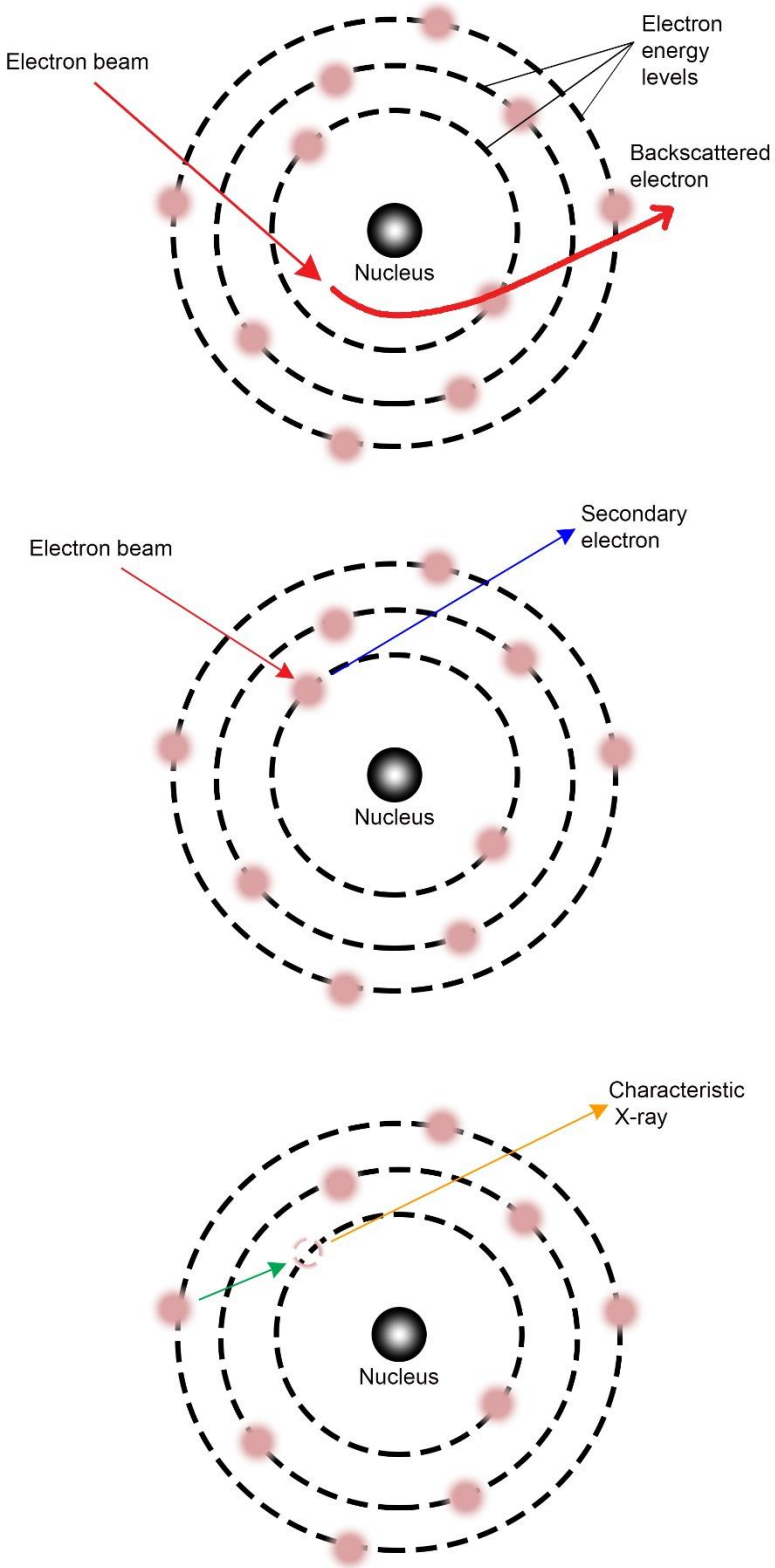

Figure 3.2: Graphical representation of the generation of backscattered electrons, secondary electrons, and characteristic X-rays.

3.2.2 Electron – crystal interactions

In the case of pathological minerals, it is also essential to consider how the electron beam interacts with crystalline structures, as electron behaviour is specific to the crystallinity and lattice of minerals.

A crystalline structure is one in which atoms are arranged in a regular, geometric way (249). For example, the simplest crystal has a unit cell in the shape of a tube, which has eight edges corresponding to eight atoms (Figure 3.3). The full crystal consists of repetitions of this unit cell forming a three-dimensional arrangement of atoms (called the crystal lattice) at specific planes (called the lattice planes) (249) at a specific distance apart (*d* spacing) (249). Each lattice plane is represented by the Miller indices (h,k,l) which essentially indicate the location of a plane in the lattice; h represents the x-axis, k the y-axis, and l the z-axis (Figure 3.3) (249).

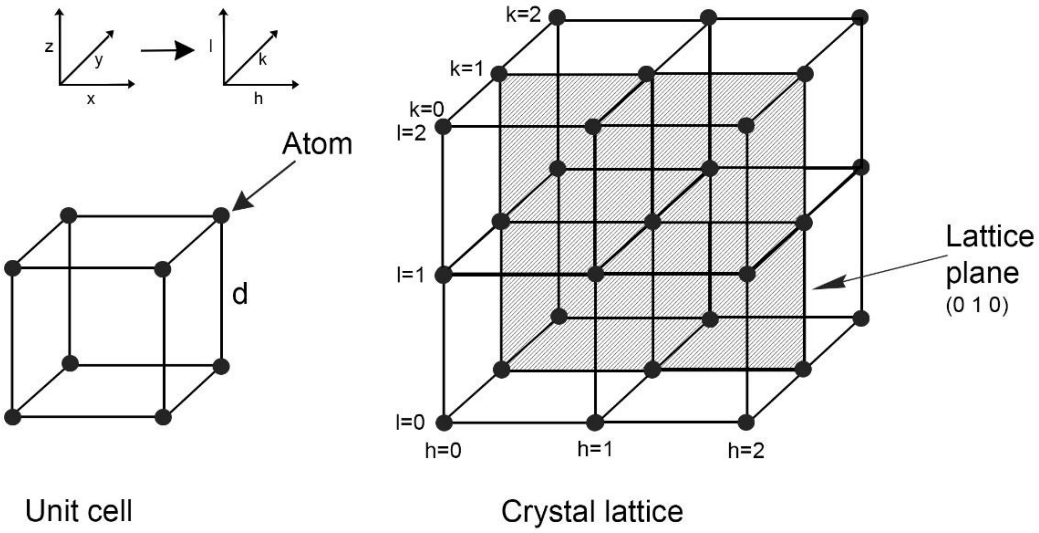

Figure 3.3: Representation of a cubic unit cell and the corresponding crystal lattice. *Spheres indicate the atoms and lines the d spacing between them. An example of the lattice plane with Miller indices (0 1 0) is represented by the shaded area in the crystal lattice.*

This atom orientation in crystals allows the scattering of radiation waves in a specific way, which is described by Bragg's equation (249, 251):

$$2d\ sin\theta = n\lambda \quad (1)$$

Where *d* is the d spacing of the crystal, *θ* the angle of incidence of the radiation wave (Figure 3.4), *n* is an integer, and *λ* the wavelength of the wave.

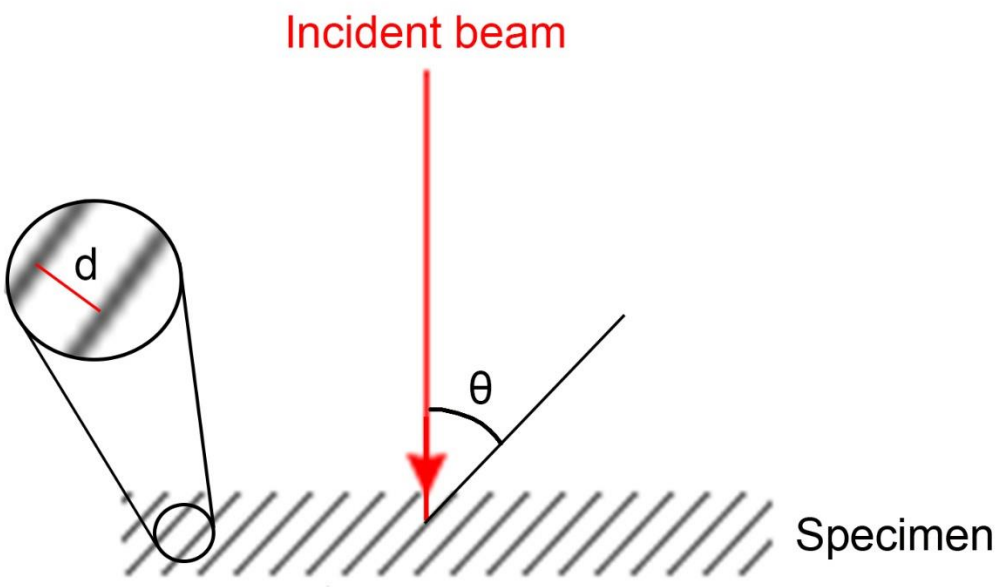

Figure 3.4: Schematic showing the angle of incidence and the d spacing of the crystal lattice.

The relationship is also valid when electrons are used, with the only difference being that electrons have a much shorter wavelength than other types of radiation resulting in much smaller angles needed for scattering to take place (249, 251). Therefore, the equation can be simplified to:

$$2d\,\theta \approx n\lambda \qquad (2)$$

As sin *θ* at small angles is approximately equal to *θ.*

At a specific angle, the result of Bragg's equation gives an *n* value higher than zero, which means that the waves add up, a phenomenon called constructive interference (251). On the other hand, when the *n* value is zero, the waves cancel each other out, leading to destructive interference (251). Based on Bragg's equation when the wavelength of the incident beam is known, and the incident angle can be found the d spacing of the crystal lattice can be found which allows the identification of the crystal itself (251). This principle is used in the analysis of electron diffraction patterns obtained by TEM, which will be discussed further later on.

3.3 Scanning electron microscopy and pathological minerals

3.3.1 Imaging

Secondary electron images are the most common and well-recognised SEM images (Figure 3.5 (a, b)). Two types of detectors can be used for secondary electron images. The in-lens detector is inbuilt in the path of the primary electron beam of modern SEMs. It detects electrons emitted from a very small volume near the surface of the sample at large angles (252), which as previously mentioned, carry specific topographic information of the imaged area, resulting in high-resolution images (Figure 3.5 (a)). The resolution of the in-lens images increases at low voltages, as shorter penetration depths are achieved, allowing for more electrons to be able to escape the surface and reach the detector (253). Most widely used, although, is the secondary electron (SE) detector, which can be found on all SEMs. This detector collects secondary electrons emitted from the interaction point at a wider range of small angles, therefore from a larger volume and depth. As a result, the final images are of lower resolution compared to the in-lens detector, with some information on the sample surface being lost (Figure 3.5 (b)).

The backscattered electron (BSE) detector, on the other hand, is not widely used for the imaging of biological samples, due to its lower resolution. The backscattered signal is invaluable; however, when information on the atomic number is required. A higher atomic number results in higher backscattered coefficients and subsequently, to a higher signal (240); therefore, the difference in the number of backscattered electrons generated by different materials produces high contrast differences. BSE images are for that reason useful in the study of biological minerals; as inorganic material can easily be identified in the organic matrix during imaging. In the case of pathological calcification in general, the elemental composition of the mineral is calcium phosphate. As calcium is a larger atom than carbon, (the main element of organic material), it appears as white (Figure 3.5 (c)) in a dark background. BSE imaging can, therefore, be used as a tool for an easy initial assessment of the presence of minerals in organic tissues.

The image quality of both detection modes depends strongly on the operational variables of the SEM, including working distance, voltage, current, and aperture size. It was mentioned above that a lower voltage would result in higher resolution due to a decrease in the interaction volume resulting in higher resolution images of the surface of the sample. On the other hand, a higher voltage will result in a smaller beam diameter, which will increase the beam brightness and subsequently, the resolution (244). Beam brightness also depends on the electron gun used; with field emission guns

having a higher electron brightness than thermionic guns (241, 244). The operation current should also be considered, which also has a positive linear relationship to beam diameter. However, one should also take into account that for a high-resolution image to be formed, enough electrons need to be generated to distinguish small features (244). Working distance and aperture also affect the resolution as they affect the depth of field of the microscope (the maximum distance between two objects in an image such that both are in focus). Smaller aperture size results in a higher depth of field as it reduces the beam current and can also decrease the noise (244). A long working distance also increases the depth of field; however, decreases resolution as it reduces the ability of the lenses to focus (244). Lastly, astigmatism of the lenses should also be 'fixed' for a high-quality image. Astigmatism is the inability of the lens to focus, due to differences in the electromagnetic field of the lens; resulting in stretched features on the images (244). At high magnifications, lens astigmatism is noticeable and therefore, should be fixed before capturing an image.

All these parameters should be tested and adjusted for the best resolution and image quality to be achieved. Subsequently, the electron micrographs presented in this work, are captured using optimised parameters for each case to achieve the best image quality.

3.3.2 Density Dependent Colour – Scanning Electron Microscopy (DDC-SEM)

As a biological system, pathological mineralisation requires the understanding of mineral components and the biological features associated with them to achieve a deeper understanding of the complex mineralisation processes.

The DDC-SEM method uses micrographs obtained by the different detectors (13), which are then added artificial colours and are manipulated into one final image. Any image manipulation software can be used to overlay the electron micrographs and to assign colours to the greyscale SEM images used. Due to differences between the contrast of the in-lens, SE, and BSE micrographs, each colour on the final image carries specific information (Figure 3.5 (a, b, c)). Dual colour images can be produced using the SE (or in-lens) and BSE micrographs, and in cases where all three detectors are available, multicolour images can be produced. The most common images are dual colour images (13, 20, 140, 238); for example, where the green channel is assigned to the SE (or in-lens) image, and the red channel to the BSE image. Thus, DDC-SEM images of minerals in soft tissue are produced where the mineral appears as red-orange (information originating from the BSE micrograph) and the less dense material, the organic matrix, appears as green (information on which originates from

the in-lens or SE detector) (Figure 3.5 (d)). Other colour combinations can also be used (Figure 3.5 (e, f)).

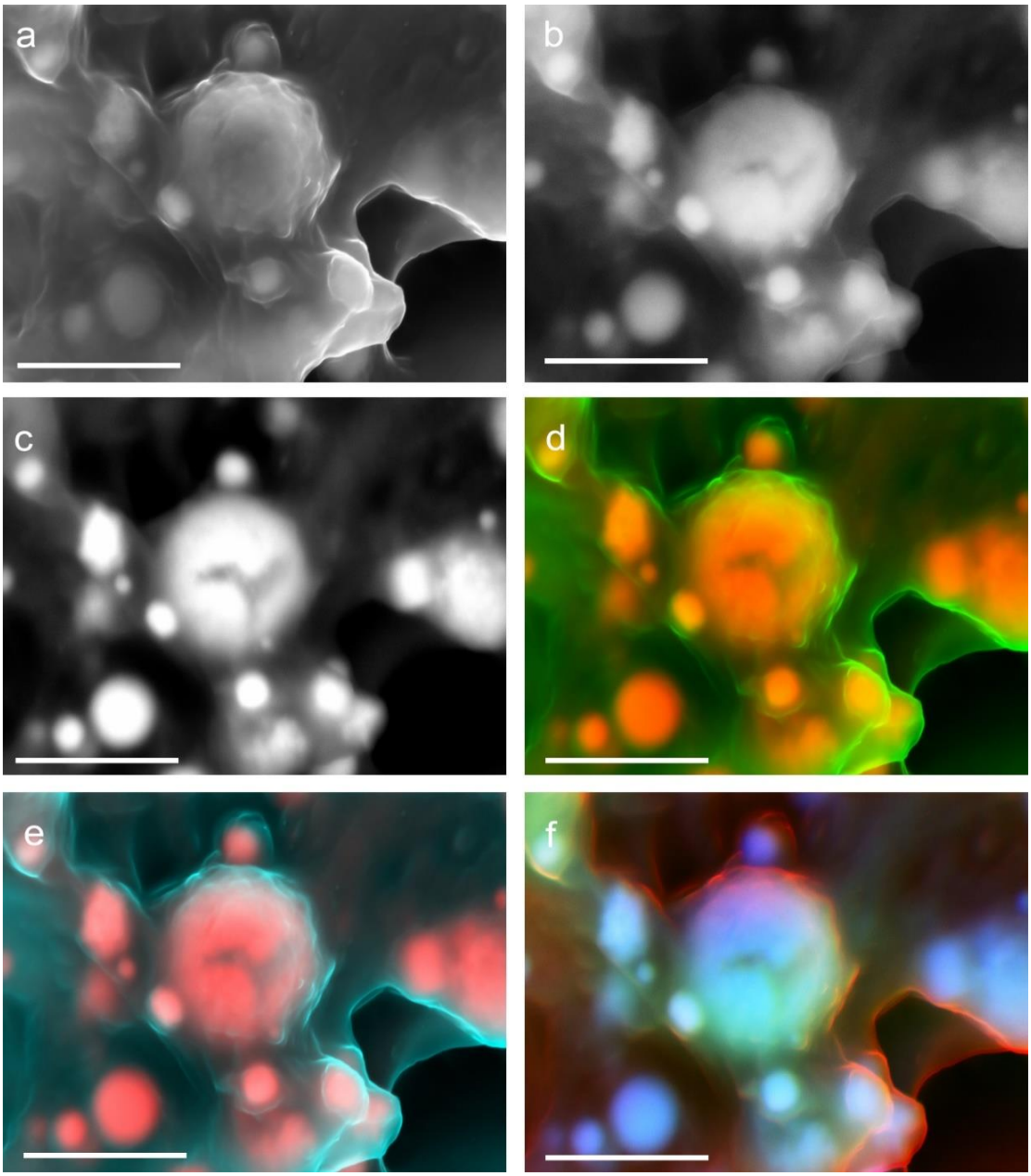

Figure 3.5: Electron micrographs of inorganic particles in organic material. (a) *In-lens electron micrograph.* ***(b)*** *SE micrograph.* ***(c)*** *BSE micrograph (organic material (black) and inorganic material (white)) (247).* ***(d)*** *DDC-SEM micrograph, where the in-lens electron micrograph was assigned the green channel and the BSE micrograph the red channel. Inorganic material appears as orange and organic material as green (247).* ***(e)*** *DDC-SEM micrograph with the in-lens micrograph being assigned the green and blue channel and the BSE micrograph the red channel. Inorganic material appears as red-pink and organic material as turquoise.* ***(f)*** *DDC-SEM micrograph with the in-lens micrograph being assigned the red channel, the SE micrograph the green channel, and the BSE micrograph being assigned the blue channel. Inorganic material appears as blue-green and organic material red-orange. Scale bars = 1 µm.*

3.3.3 Chemical analysis - Energy Dispersive X-ray spectroscopy (EDS)

Scanning electron microscopes coupled with an Energy Dispersive X-ray spectroscopy (EDS) detector are also commonly used in pathological mineralisation research (240). The detector is used to gain chemical data on the material under investigation through the detection of the characteristic X-rays originating from the sample surface. The detector is most widely used in the study of archaeological and hard materials, as is also useful in the identification of unknown materials in samples. For that reason, it is also a valuable tool in the study of biological minerals. During imaging, a specific point or area in the tissue is chosen for analysis (Figure 3.6 (a)) and a spectrum (Figure 3.6 (b)) or an elemental map (Figure 3.6 (c)) can be produced respectively. This can aid the fast identification of inorganic material in soft tissues, eliminating misinterpretation of any sample preparation artefacts. In this work, at the voltages used and as most pathological mineralisation is made of calcium phosphate; some peaks of interest are calcium (Ca) at 3.692 keV, magnesium (Mg) at 1.253 keV, phosphorus (P) at 2.013 keV, and oxygen (O) at 0.525 keV (Figure 3.6) (254). It is worth keeping in mind that each atom can release more than one type of characteristic x-rays as these can be originating from electrons getting knocked from different electron energy levels (254). Thus multiple peaks of the same chemical element might be observed; for example, calcium can appear both at 3.692 keV and 4.038 keV (255) (Figure 3.6 (b)).

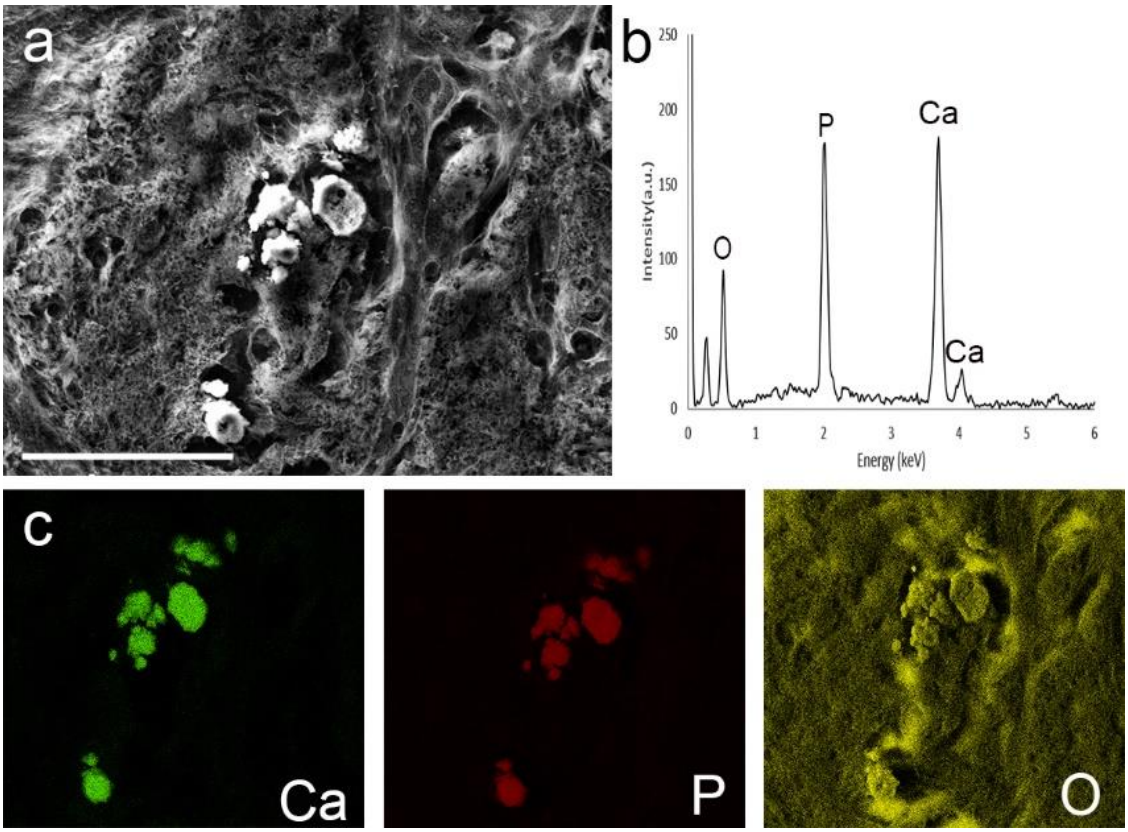

Figure 3.6: Chemical analysis of a pathological mineral in soft tissue (247). (a) *SE micrograph of the area of interest. Scale bar = 50 µm**. (b)** An EDS spectrum obtained from the area. **(c)** Maps of the distribution of calcium (Ca), phosphorous (P), and oxygen (O) in the area of interest.*

3.3.4 SEM sample preparation of biological material

Imaging biological material using electron microscopes can be challenging due to the un-physiological conditions required. Biological tissues are full of water, and conventional microscopes operate under vacuum; therefore, several preparation steps must be followed for successful imaging. Firstly, samples must be dehydrated and dried carefully for their ultrastructure to be preserved. Furthermore, to achieve good image quality, coating, and painting of the biological sample is required to build a conductive layer.

The first step of sample preparation involves glutaraldehyde or formaldehyde fixation, used to preserve sample morphology, and to prevent autolysis (256). The choice of fixative and percentage used depends on the samples and the purpose of sample preparation. The two most widely used fixatives are formaldehyde and glutaraldehyde. Formaldehyde (CH_2O) is usually used at ~3.7% concentration, a solution which is also referred to 10% neutral buffered formalin (sometimes also containing 1% methanol, however in this work none of the fixative solutions contained methanol)

(257), at a pH that should be maintained between 6.8 – 7.2. That is because a more acidic pH indicates oxidisation resulting in the formation of formic acid, which can lead to tissue artefacts (258).

The fixative properties of formaldehyde are due to its crosslinking activity (259) as it can react with amino acids on proteins to form a methylene bridge (a CH_2 bond) (260). Additionally, it has been shown to also react at a low degree with unsaturated lipids (which have more than one double bond between to carbon atoms); however, other solvents remove these unless more suitable fixatives are used such as osmium tetroxide. The samples should stay in the fixative for a period of 24 to 48 hours at room temperature, as for complete crosslinking at least 24 hours are required (257). The time required also varies with the thickness of the sample, thus for the fixative to penetrate the tissue quickly; it should be cut in small pieces of a couple of millimetres if possible (261). It is also imperative to not over fix the samples, especially in cases where immunostaining might be employed (261). For the same reason, formaldehyde was preferred in this work over glutaraldehyde even though the latter is widely used in electron microscopy, as it has been found that glutaraldehyde fixation results to decreased antibody binding and increases tissue immunofluorescence (262, 263).

Following fixation, dehydration is the subsequent step of sample preparation. Tissue samples can be dehydrated through a series of increased ethanol graded solutions. Other dehydration agents, such as acetone can alternatively be used. The time required for dehydration must be adjusted depending on the size of the sample of interest; larger samples require more prolonged time intervals. Thus, similarly to fixation, the samples should be cut down to a few millimetres for better infiltration of the dehydrating agent at a shorter time.

The dehydration step is particularly important in cases where critical point (264) and hexamethyldisilazane (HMDS) (265) drying are used, as these require the presence of a dehydrating agent. It may, however, be omitted when the sample is simply air-dried. Critical point and HMDS drying are widely used methods for biological tissues because they avoid sample shrinkage, preserving its ultrastructure (Figure 3.7 (a)). Critical point drying is based on the substitution of the dehydration agent by carbon dioxide. Once carbon dioxide has thoroughly infiltrated, it is then brought to its gas phase. As a result, the sample dries without the presence of capillary forces (266). For HMDS drying, the sample is immersed in HMDS after dehydration and then left to air dry (267).

These methods were found unsuitable for the study of pathological minerals directly in tissues, as it is challenging to identify them when they are covered by organic material. It was observed that in cases where the ultrastructure of the tissue is preserved, the electron beam interacts with a large amount of organic material before

reaching the inorganic material beneath it, resulting in reduced contrast differences between the two (Figure 3.7 (b)). HMDS and critical point dried samples might, therefore, produce misleading results and lead to the omission of the inorganic material. Consequently, for the imaging of pathological minerals in this work, all samples were simply air-dried. Allowing the sample to air dry creates capillary forces in the tissue, causing the organic matrix to collapse in on itself. Such forces do not, however, apply to the mineral, which does not collapse. This difference in behaviour between the organic and inorganic material can be used for easier identification of pathological minerals in tissues. The electron micrographs of the air-dried samples provide very little information on the ultrastructure of the organic matrix but allow for high contrast with the inorganic material (Figure 3.7 (c)).

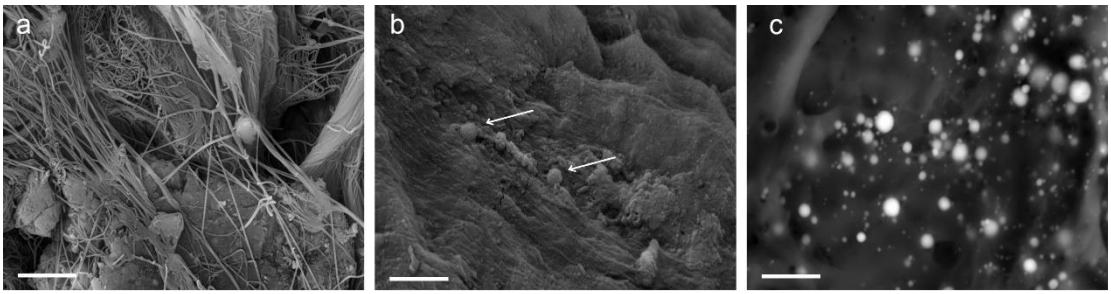

Figure 3.7: Electron micrographs of biological tissues prepared with HMDS, compared to conventional air-drying (247). (a) *SE micrograph of collagen fibres in cardiovascular tissue preserved with HMDS drying.* ***(b)*** *BSE micrograph of a HMDS prepared sample with potential calcified particles indicated by arrows. Some differences in colour, indicating different densities, can be seen. It is, however, not certain whether these are mineralised.* ***(c)*** *BSE micrograph of air-dried samples where the organic material has collapsed on itself, allowing for clear identification of mineral particles. Scale bars = 1 µm.*

3.3.4.1 Coating and silver painting

Another challenge of using an electron beam in the imaging of biological samples is the build-up of electrons on their surface. As insulators, biological tissues do not allow electrons to escape their surface, leading to sample damage and poor quality, including distorted images. To eliminate this, the sample must be attached to an aluminium stub, and a conductive coating must be applied. The coating can be, amongst others, carbon, gold, or platinum, and should usually have a thickness between 5-15 nm, depending on sample roughness. However, when chemical analysis of the samples is needed, coating composition must be carefully considered, to avoid the overlapping of energy peaks. Such information can be obtained by identifying the

energy values of the characteristic X-rays emitted by each element. In the case of cardiovascular calcification, for instance, at voltages higher than 5 kV, phosphorous has an energy X-ray peak of 2.013 keV, and carbon, gold, and platinum have energy peaks at 0.277 keV, 2.123 keV, and 2.051 keV respectively (254). Thus, platinum is not the most suitable coating to use as its peak can mask the phosphorus peak. Carbon, on the other hand, can be used as its energy peak cannot mask other peaks of interest including; calcium, phosphorus, and oxygen.

In addition to the coating, it is also essential to maintain good conductivity between the sample surface and the aluminium stub, such that any charge build-up may be eliminated. This can be done by applying a silver paint layer around the sample. Application of the silver paint before coating ensures that both the sample and the silver paint are dry before entering the electron microscope chamber.

3.3.4.2 SEM sample preparation protocol

Based on the information obtained through literature research and the results of different protocols, the SEM sample preparation protocols used for all samples analysed in this work are as follows. Tissue samples were cut down to small pieces (Figure 3.8) of two to five millimetres and put in 4% formaldehyde (10% formalin) (Figure 3.8) for at 24 hours at room temperature or for longer periods at 4°C. The samples were then washed three times with distilled water, for 5 minutes each time. Dehydration steps followed using ethanol at concentrations of 20%, 30%, 40%, 50%, 60%, 70%, 80%, 90% for 10-minute intervals, and three 10-minute intervals at 100% ethanol changes (Figure 3.8). The samples were then left in an open petri dish to dry (Figure 3.8).

For paraffin-embedded histological slides, the paraffin wax was removed by immersing the slides in pure xylene for two 10-minute intervals. The slides were simply left to air dry. Tissue pieces or histological slides were then secured on SEM aluminium stubs (Figure 3.8) using conductive carbon adhesive tape. The mounted samples are silver painted thoroughly, and the paint is left to dry. A carbon 10 nm thick layer was then applied to all samples before imaging (Figure 3.8).

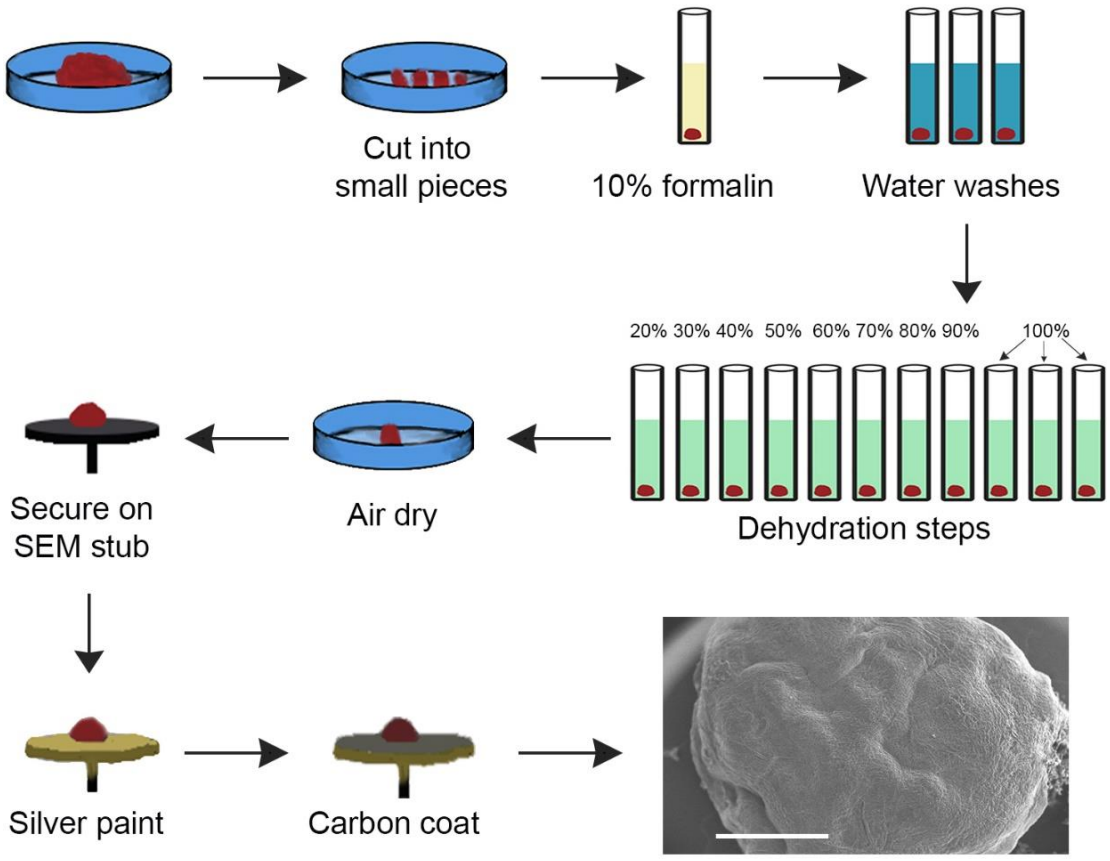

Figure 3.8: Visual representation of the sample preparation procedure of tissue pieces for SEM imaging. *The tissue should be cut into small pieces, fixed in 10% formalin, washed, dehydrated through a series of ethanol solutions 20 – 100%, and left to air dry. The sample is then secured on an SEM stub, silver-painted, carbon-coated, and image on the SEM. Scale bar = 1 mm.*

3.4 Transmission electron microscopy and pathological minerals

3.4.1 Imaging

In modern TEMs, imaging the transmitted beam is done digitally with a camera system. Density differences in the sample are the primary source of the contrast on the resulting images, while the brightness depends on the intensity of the transmitted beam (241). Phase dependent contrast can also be captured in cases where a periodic structure is observed that causes points of constructive and destructive interference. Additionally, diffraction dependent contrast can also be employed, which is particularly useful in the study of crystalline materials (241). As previously mentioned for diffraction to take place the incident beam needs to be at a specific angle to the crystal lattice planes, thus diffraction generated contrast also changes with angle which can be altered by tilting the sample within the TEM (241).

Conventional TEM micrographs can be captured in both the bright and dark field. Bright-field images use the transmitted beam and are the most common. In the resulting image, the darker areas correspond to denser regions in the sample while less dense areas with higher transmission signals appear brighter (Figure 3.9 (a)). Darkfield images, on the other hand, omit the transmitted beam to form an image where the colours are reversed with darker areas indicating less dense areas (241).

3.4.2 Selected area electron diffraction

Diffracted electrons are also used as an analytical tool rather than for simple sample imaging. This TEM mode is widely used for capturing electron diffraction patterns of crystals, selected area electron diffraction (SAED) (Figure 3.9). For the creation of the patterns, the diffracted beam is focused on the back-focal plane of the objective lens and enlarged, forming a reciprocal lattice image of the crystal (241). Interpretation of these diffraction patterns, therefore, provides information on both the crystallinity and chemical phase of the minerals present. The diffraction pattern appears as spots (Figure 3.9 (a_1)) in cases where the material diffracts as a symmetric single crystal (251), whereas for polycrystalline materials rings are observed which are a result of many crystals randomly orientated (Figure 3.9 (a_2)) (251). Finally, diffuse broad rings are indicative of amorphous materials. For the chemical phase to be identified, further indexing of the spots or rings observed is needed.

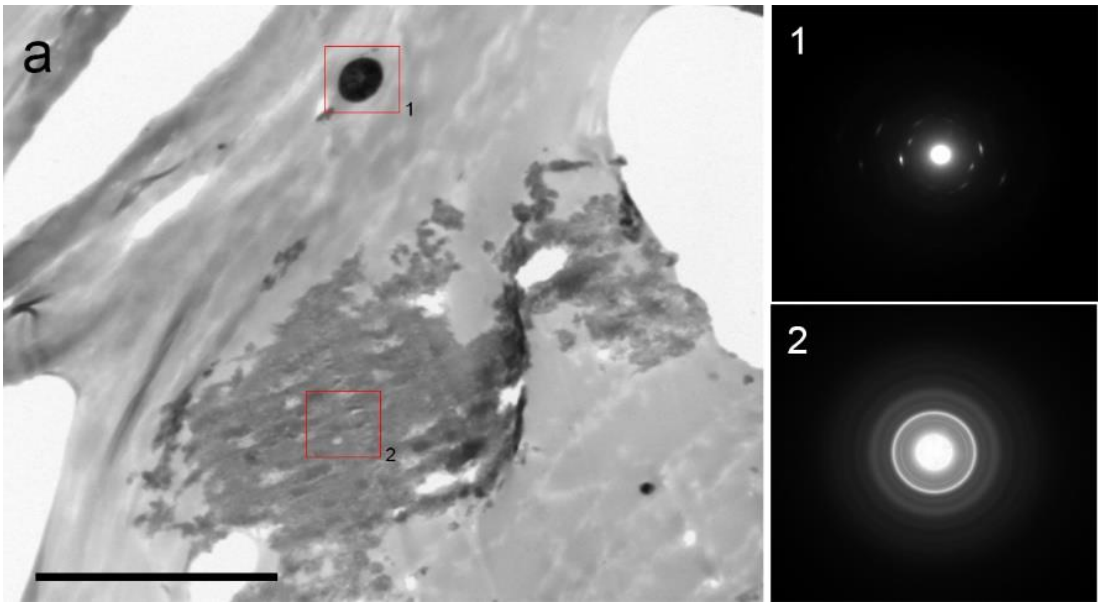

Figure 3.9: TEM micrograph showing minerals (darker areas marked with rectangles) observed in cardiovascular soft tissue (light grey area) along with their electron diffraction patterns (247). (a) *TEM micrograph of a cardiovascular tissue sample, where calcified particles marked by **1** are denser and diffract as a single crystal, based on their electron diffraction pattern. Larger calcification marked by **2** appears less dense and has an amorphous structure. Scale bar = 2 µm.*

Recalling Bragg's equation *(Section 3.2.2)*, knowing the incident angle *θ* and the wavelength λ of the beam it is possible to calculate the *d* spacing of the crystal planes such that:

$$2d\,\theta \approx n\lambda \tag{3}$$

For TEM analysis, this relation can be rewritten using laws of trigonometry (249, 251) (Figure 3.9), such that:

$$\tan 2\theta = \frac{r}{L} \approx \theta \tag{4}$$

Where L is the distance between the crystal and the camera and r the distance between the incident and diffracted beams (Figure 3.10).

Therefore, the final relationship can be approximated to:

$$\lambda L = rd \tag{5}$$

Based on this formula the *d* spacing of the crystal can be calculated as the wavelength *λ* can be calculated from the accelerating voltage used, *L is by the operator and r* can be calculated from the SAED pattern (249, 251).

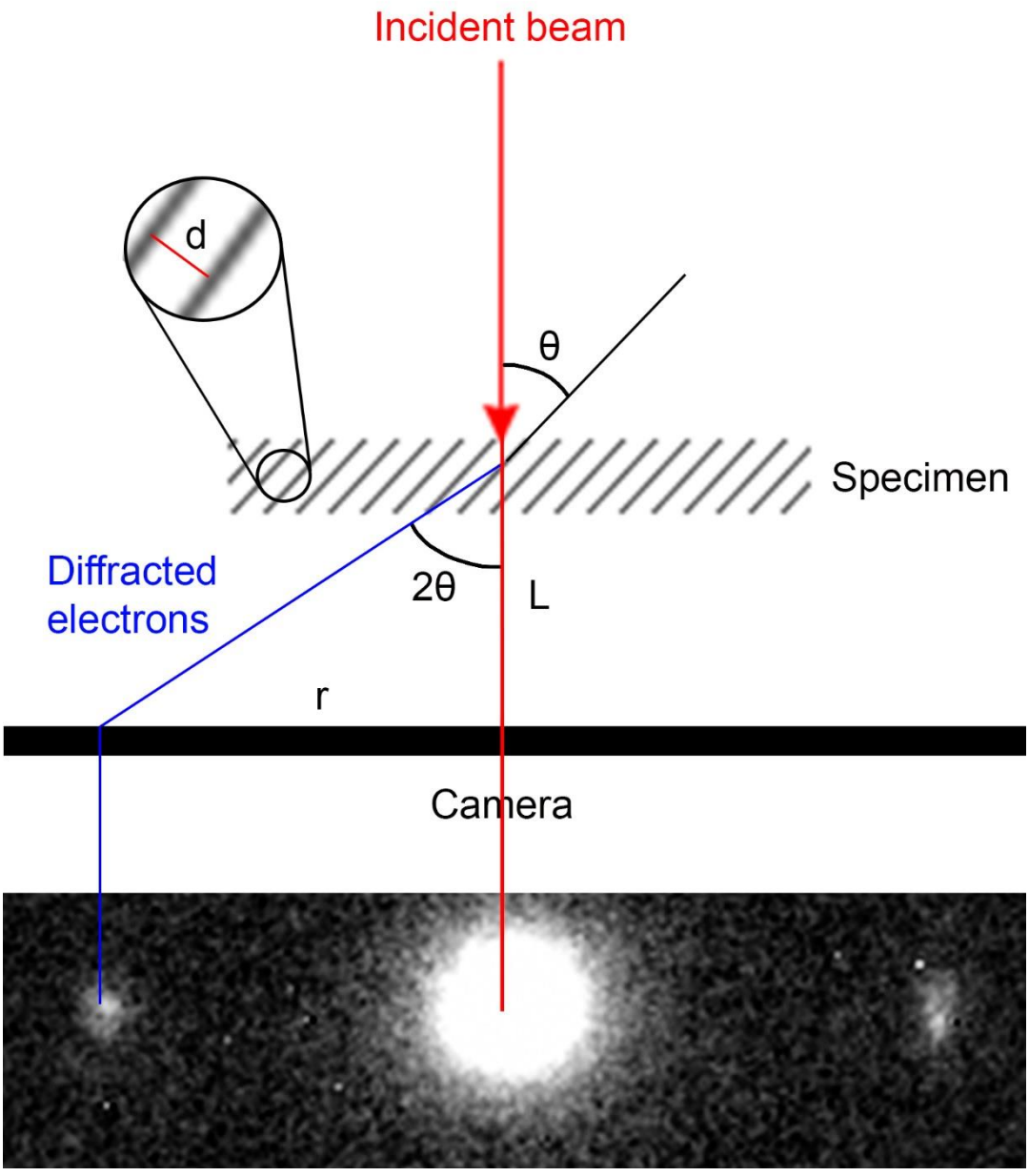

Figure 3.10: Diagram showing the incident and diffracted beam and how these translate on a SAED pattern.

As *λL* is a constant, *d* is inversely proportional to *r,* with *r* being the reciprocal distance and therefore the scale bar of the SAED pattern has a unit of nm^{-1}. Measuring the distance differences between the diffracted spots and the angles forming between them allows as a result, the indexing of the crystal with readily available online data-bases. SAED pattern indexing becomes easier when the elemental composition is also known; which can be obtained through EDS analysis; also available on TEMs.

3.4.3 TEM sample preparation of biological material

Similarly to SEM, a number of steps are required for TEM images of good quality to be acquired from biological samples (268). As these are non-crystalline samples, TEM imaging relies on density differences. Biological tissues are, however, mainly made of carbon with no significant density variations; therefore, contrast agents must be employed to enhance image contrast.

Such agents include; osmium tetroxide (269), lead citrate (270), and uranyl acetate (271), among others. Osmium tetroxide attaches to lipids, resulting in cell membrane staining (Figure 3.11 (a)). It is used before sample dehydration as a contrast agent, but also as a fixative, as it can stabilize lipids when attached to them. In addition to osmium tetroxide, uranyl acetate is also widely used. The latter stains for proteins due to its ability to react with phosphate and amino groups (Figure 3.11 (b)); however, it does not stain for lipids (Figure 3.11 (b)). Uranyl acetate can, therefore, be applied along with osmium tetroxide staining to enhance image quality and contrast. Finally, lead citrate may be employed to enhance the previous staining with either osmium tetroxide or uranyl acetate for its ability to react with both. This chemical is, however, difficult to handle, due to its very fast precipitation when in contact with air or water.

However, in the case of imaging mineralised tissues, no artificial contrasting is necessary to visualise the minerals, on the contrary when contrast agents are used the minerals cannot be visualised as clearly and sometimes cannot be identified. Therefore, in the TEM preparation of all of mineralised tissues used in this work, contrasting was unnecessary.

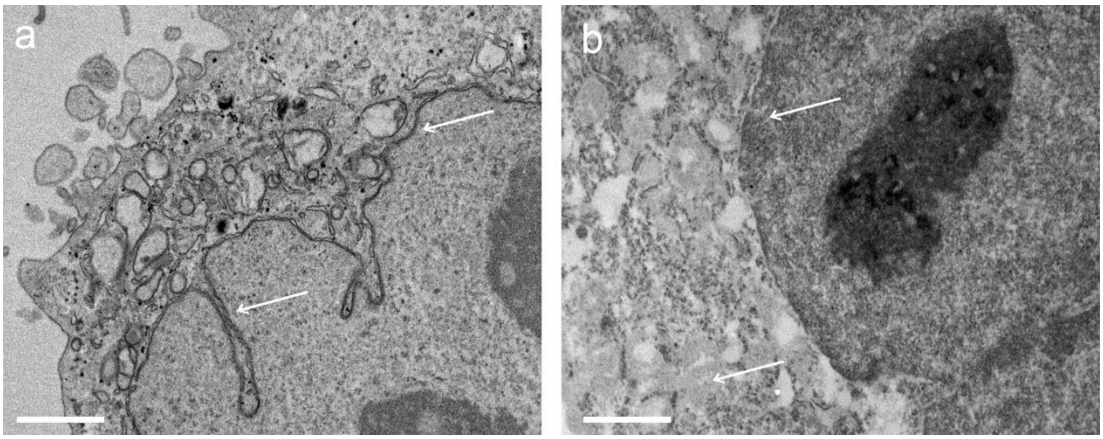

Figure 3.11: TEM micrographs of resin embedded samples with added contrast agents (247). (a) *Cross-section of epoxy resin embedded HeLa cell with osmium tetroxide staining; the double membrane of the nucleus is visible (arrows).* ***(b)*** *Cross-section of epoxy resin embedded HeLa cell with uranyl acetate staining; although the nucleus is still visible, the double membrane and membranes of intracellular organelles are not seen (arrows). Scale bars = 1 µm.*

3.4.3.1 Focused Ion Beam – Scanning electron microscope

Other than contrast, TEM imaging requires samples of a thickness of less than 100 nm. For such thickness to be achieved, samples may be resin embedded and sectioned either using an ultra-microtome or a Focused Ion Beam (FIB) milling (272). For biological samples, resin embedding followed by ultra-microtome sectioning is usually preferred. Resin embedding is faster and cheaper than FIB milling, and the contrasting steps allow for visualisation of cell organelles and other biological structures. These sections can also be SEM imaged in cases where TEM analysis is not necessary.

Despite its many advantages, ultra-microtome sectioning is only suitable for demineralised samples or tissues containing minerals measurable in a few nanometres, but in cases where the sample contains more substantial amounts of mineral, the method is usually not employed. This is due to possible damage to the knives used during sectioning of resin blocks but most importantly, due to damages to the mineral itself. FIB sectioning can, therefore, be proven more suitable as it allows mineral sectioning with minimal damage (Figure 3.12 (a)). In cases where ultra-microtomy is used, the minerals are usually fractured (Figure 3.12 (b)) or pushed out of their original location. Finally, another advantage of FIB-SEM machines is that they enable more targeted sectioning, as it allows large samples to be imaged, and subsequently for more targeted sectioning at high spatial accuracy. As a result, for all TEM analysis of mineralised tissues in this work, the samples were FIB prepared.

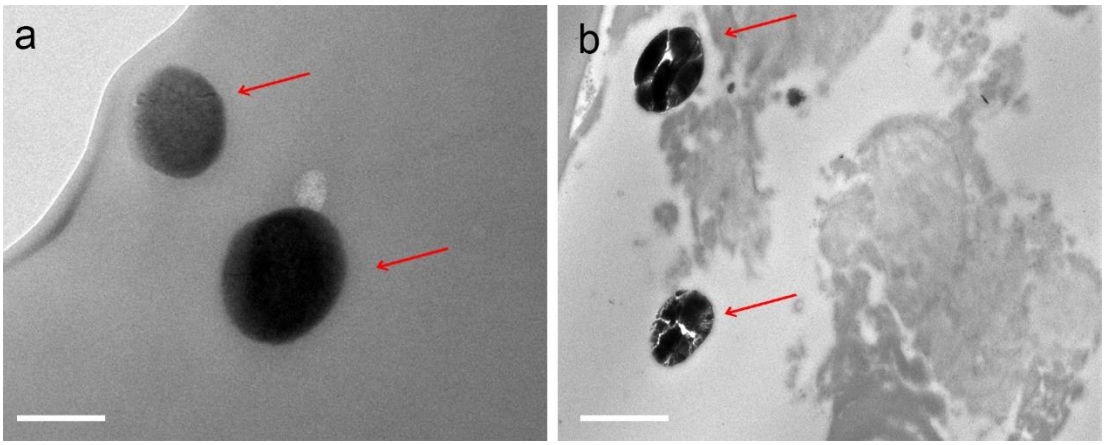

Figure 3.12: TEM microscopy of cardiovascular tissue containing minerals (247). ***(a)*** *FIB sectioned sample where the minerals (arrows) are intact. Scale bar = 200nm.* ***(b)*** *Resin embedded sample sectioned by ultra-microtome. The mineral in the sample is visibly damaged (arrows) and cracks can be seen. Scale bar = 1 µm.*

FIB-SEMs are similar to simple SEMs, with the difference that a second column is added, which consists of a gaseous plasma or a metal with a low melting point such as gallium (273). Gallium atoms are much bigger than electrons; however, similar effects to those observed in electron-matter interactions; such as elastic and inelastic interactions are observed (274). For FIB milling, elastic interactions are employed that result in energy transfer from the ion beam to the sample, which, when higher than a specific value causes the sample atoms to be removed (274). This effect is called sputtering and can be used for different time intervals and at different energies for the desired material to be removed from the sample creating a 'milling' effect.

However, the effect can also have a damaging result to the sample due to transfer of heat causing sample damage, deflection of the beam which can result in drifting and subsequently milling of the area of interest and re-deposition of the removed atoms to the surrounding area (274). To reduce material re-deposition, a reactive gas can be used that attaches to the removed atoms making them volatile, allowing for their clearance through a pumping unit (274). Another way to protect the sample and enhance the milling process is through the deposition of platinum at the surface of the area to be milled (274). Platinum deposition and gallium milling are also alternatively used to enable the removal of the milled side of interest from the sample onto a grid for TEM analysis. The detailed protocol is discussed in the next section.

3.4.3.2 FIB milling protocol for the preparation of TEM samples

Initially, the sample must be secured on an aluminium stub, coated and silver-painted carefully and thoroughly. Poor sample preparation allows for sample movement and produces a 'charging effect', which might result in inaccurate FIB cutting. In this work, the area of interest was identified before FIB sectioning through SEM imaging which allowed for BSE mode imaging for the easy identification of the mineral as the FIB-SEM used was not equipped with the BSE detector. The same area was identified in the sample using the SE electron detector before cutting.

The following milling protocol was carried for all samples analysed in this work. A platinum layer is deposited on top of the area of interest (Figure 3.13 (a)). Following, low currents (93 pA- 2.8 nA) are used for gallium milling. The material in front and behind the sample was milled first, followed by the area on the right-hand side and the area immediately below the area of interest (the lamella), to allow for easier detaching from the rest of the sample (Figure 3.13 (a)). The lamella is then shaped and thinned down to around 100nm (Figure 3.13 (b)) and is then attached to a needle probe (Figure 3.13 (b)) through the deposition of platinum. The needle is then used to transfer the lamella to a TEM grid (Figure 3.13 (c)). The lamella is then attached to the grid through platinum deposition (Figure 3.13 (d)) and is released from the probe through gallium milling (Figure 3.13 (d)). Finally, the lamella is cleaned and thinned down to about 50 nm. The sample can then be transferred to the TEM for imaging and analysis.

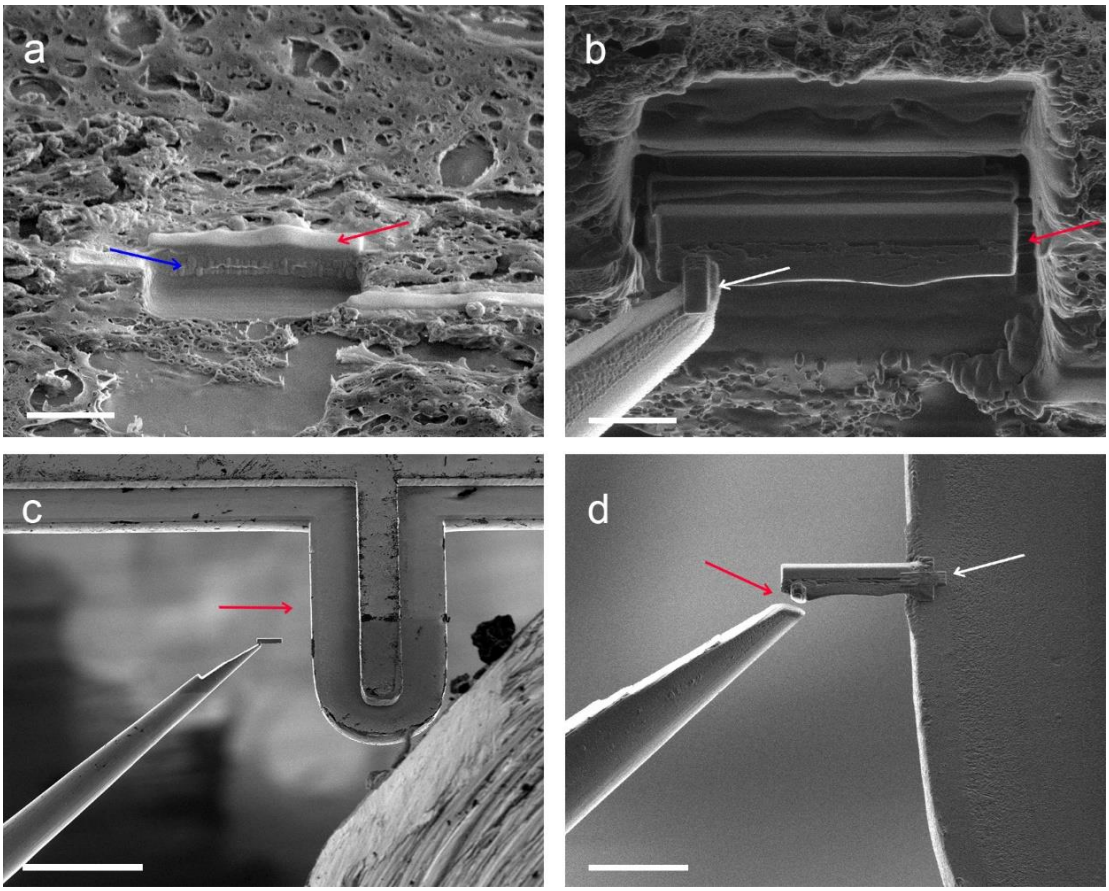

Figure 3.13: FIB micromachining sequence (247). (a) *A platinum layer must be deposited for protection of the target area (red arrow) before the gallium ion beam is used for milling (blue arrow).* ***(b)*** *The section is attached to the probe through platinum deposition (white arrow) and milled to be released from the sample (red arrows). Scale bar = 300 nm.* ***(c)*** *The section is transferred to the carbon grid (arrow) by the needle. Scale bar = 100 µm.* ***(d)*** *The section is then attached to the grid through platinum deposition (white arrow). Once the section is secured onto the grid (white arrow), its attachment to the probe is cut (red arrow). Scale bars = 10 µm.*

3.5 Biochemical assays for pathological mineralisation

Biochemical assays include amongst other, immunostaining and blotting methods. Even though such techniques are routinely used in biological research; it is challenging to apply them to the direct study of mineralised tissues. For example, in hard tissue research, such as bone, a complete understanding of its protein profile is usually compromised by the methods needed for the removal of its inorganic component (275, 276). That is due to the unfavourable effects of demineralisation procedures on protein yield and stability (275, 276). Different methods have been proposed to overcome these issues; however, all methods have reported some drawbacks such as low protein yields, limitations on which proteins can be detected, and on the extraction of whole proteins (275-278).

Additionally, for immunostaining which allows identification of proteins directly in tissues and also can give localisation information on proteins, sample preparation procedures again require removal of the inorganic component (279). Mineralised tissues are usually demineralised prior to processing to avoid damaging of equipment and the surrounding tissue. Even if the minerals are preserved during the initial sample processing, the use of multiple solutions needed for successful staining usually results in mineral alterations.

Unfortunately, these limitations have also a negative effect on research on pathological minerals. Protein extraction yields being one of the main challenges. This is because unlike bone which can be obtained in significant quantities for enough proteins to be extracted for analysis and proteomics profiling, pathological minerals are observed in much smaller quantities. Thus, substantial amounts of soft tissues need to be processed for a few milligrams of these minerals to be obtained, something not always achievable. Another limitation that mainly arises in the use of optical and fluorescence microscopy is that minerals cannot be observed in the tissue without some sort of staining. Commercially available stains for minerals have, however, their drawbacks as it is not always that the resulting staining represents the mineral in its natural state. Furthermore, alterations of the minerals during sample preparation procedures are also a challenge as not all pathological minerals are stable enough to be even partially preserved.

3.6 Immunofluorescence staining

Immunofluorescence (IF) is a staining technique that allows for the detection and visualisation of antigens in tissues and cells (280). This is achieved through the use of antibodies tagged with fluorophores; molecules that absorb and emit light at specific wavelengths (281). The procedure involves many different steps, all of which

can affect the quality of the staining and therefore, should be optimised accordingly based on the type of sample and antibodies used.

3.6.1 Antibodies

Antibodies, also known as immunoglobulin proteins (Ig), are glycoprotein molecules formed by a carbohydrate group attached to a protein (an amino acid chain). The carbohydrate group can be attached to either a nitrogen or an oxygen atom. Naturally, they are produced by B lymphocytes (282). In detail, a foreign substance (an antigen) that is not recognised by the immune system generates an immune response which leads to the production of specific antibodies which then bind to the antigen (282). In immunofluorescence staining, this ability of antibodies to bind to antigens is used to detect antigens within cells and tissues.

There are five types of antibody classes, with the most common being immunoglobin G (IgG) because of its ability to stay in circulation longer due to slower clearance. IgG antibodies also have subclasses (e.g. IgG1, IgG2) found in different animal species. Despite the subtype, all antibodies are formed by one or more copies of the same structure (Figure 3.14) formed by two light and two heavy polypeptide chains (amino acid chains) connected by disulphide bonds (two sulphur atoms attached) (282). The light chains of the antibodies are the ones binding to antigens (Figure 3.14), with their specificity to do that depending on their amino acid sequence (282).

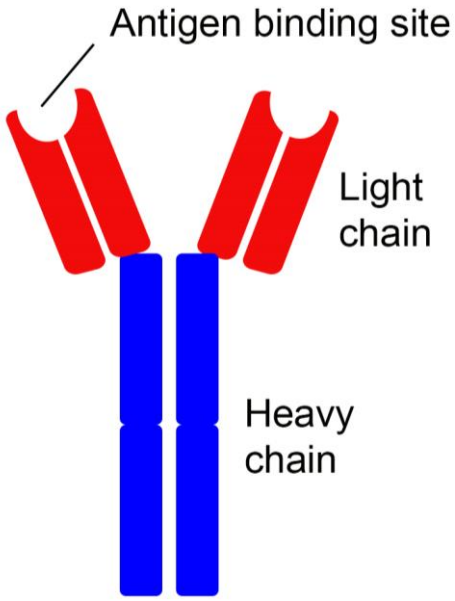

Figure 3.14: Representation of the general antibody structure. *The heavy chains (blue), light chains (red), and the antigen-binding site are indicated.*

For IF staining, the ability of antibodies to attach to specific antigens also depends on how they were produced. Proteins exist in different forms; their native three dimensional folded (tertiary) structure which is usually found *in vivo* and its primary structure usually resulting due to biochemical processes that denature the protein, breaking the bonds forming the tertiary structure (282). In IF staining, antibodies raised to recognise native protein structures are more suitable; however, sample preparation might lead to protein alterations; thus, antibodies need to be chosen and optimized for individual applications.

Production of antibodies for specific biochemical research applications is usually done with specific peptides as antigens. Peptides are preferred over other antigens (for example cells) as they are easy to produce and can also be used to produce specific antibodies that can recognise post-translational protein alterations such as phosphorylation (282). However, peptide antigen produced antibodies might be less able to recognise native protein forms as the epitope (part of the protein) they can bind to might not be accessible if the protein remains in its tertiary form. Thus the peptide antigen needs to be chosen depending on the most accessible protein part (282), any possible modification the protein might have gone through, and its cross-reactivity with other proteins. Following, these antigens are injected into the host animal, triggering an immune response producing antibodies.

Two types of antibodies are currently commercially available; polyclonal and monoclonal (282). Polyclonal antibodies, even though easier and cheaper to produce, have a significant drawback. Their quality depends on the immune response of the host animal; therefore, they vary from batch to batch (282). However, due to different immune responses, polyclonal antibodies consist of a mixture of different antibodies each of which can recognise different epitopes of the protein of interest, leading to more antibody binding and therefore higher staining ability. On the other hand, monoclonal antibodies are produced through a more complex process as instead of extracting the antigens from individual animals, the B lymphocytes of the host animal themselves are extracted (282). These B lymphocytes are then cultured with cancerous cells to produce hybrid cells that produce antibodies, which are specific to one protein epitope (282). Even though these antibodies only recognise one epitope, there is little variance from batch to batch as all antibodies originate from the same B lymphocytes allowing for better experiment reproducibility.

In biochemical assays, the monoclonal or polyclonal antibodies that attach to a specific protein are called primary antibodies. Secondary antibodies that bind to primary antibodies are also used for visualisation purposes; for example, in IF staining the secondary antibody contains a fluorophore (282) allowing for visualisation using a

fluorescence microscope. The way secondary antibodies attach to the primary is similar to the way the primary antibody attaches to the protein of interest, however, instead of being raised against a specific protein they are raised against the host and immunoglobulin type of the primary antibody (282).

The use of both a primary and a secondary antibody for the IF staining is called indirect labelling. Direct labelling can also be employed where a single primary antibody attached to a fluorophore is used (283). Even though direct labelling resolves problems of secondary antibody specificity, indirect labelling is usually preferred as it allows for the binding of multiple secondary antibodies to the same primary antibody leading to signal amplification (283). Direct labelling might also be useful in multiple staining where two antibodies are used for simultaneous labelling of different proteins as it eliminates cross-reactivity between the two primary and secondary antibodies needed for indirect labelling. For both methods, however, different fluorophores (emitting at two different wavelengths) must be used to distinguish the proteins of interest (283).

Other than the choice of primary and secondary antibodies based on their production method; their reactivity should also be considered. A primary antibody should be able to recognise the protein of interest in the specific animal from which the sample (cells or tissue) originates. This animal needs to be different from the host species to avoid unspecific binding of the antibody to other proteins. For the same reason, secondary antibodies should also have a host animal different from that of the sample. In cases where multiple antibodies are used; the secondary antibodies should be raised in a different host animal to that of all primary antibodies.

3.6.2 Fluorescence detection

As previously, mentioned IF uses fluorophores for the visualisation of the targeted proteins. Fluorophores are molecules that when illuminated by a light source, absorb photon (light waves) (284) energy. The energy absorbed leads to the molecule entering an 'excited' state (100); which means that some electrons in the atoms' electron energy levels have higher energy (Figure 3.15) than that in their ground (natural) state causing them to enter an 'excited' state (100). When returning to their natural state, these electrons emit a photon that has an energy corresponding to the difference between the excited and ground state (100, 285) (Figure 3.15). This absorption - emission cycle is called the Stokes shift and can be repeated multiple times (100).

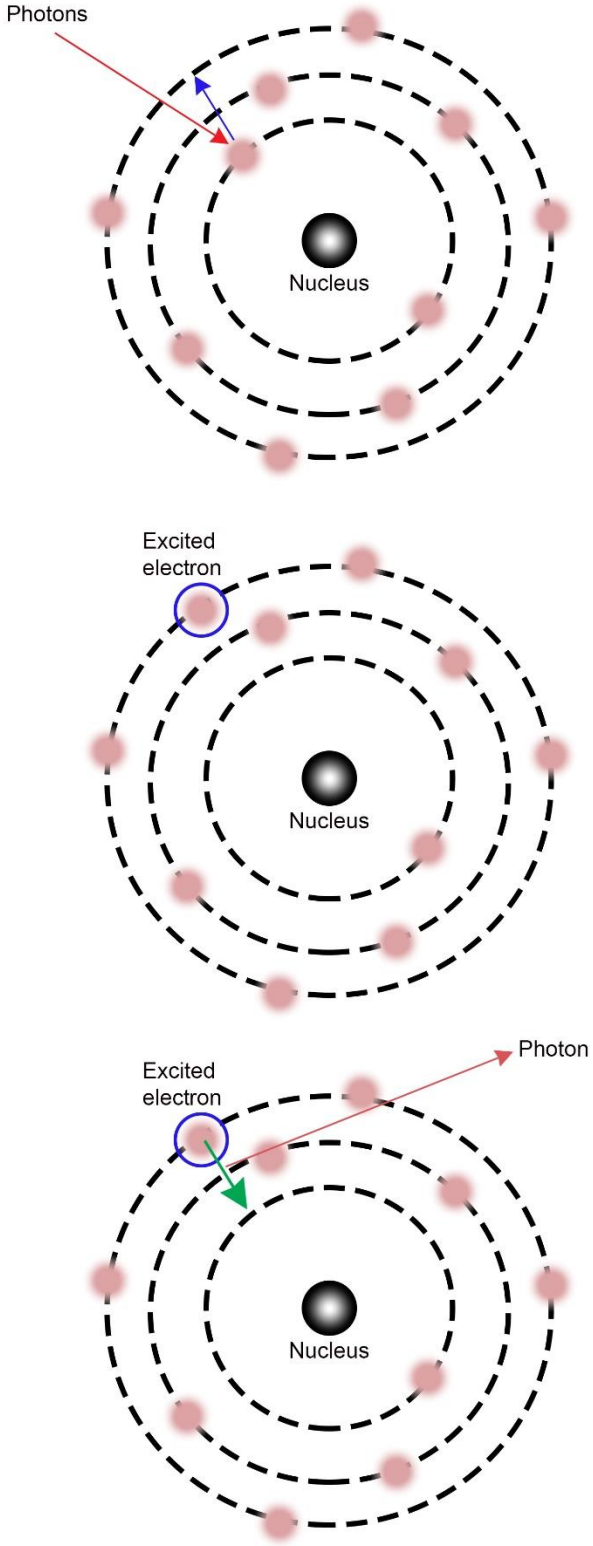

Figure 3.15: Representation of the mechanisms through which fluorophores absorb and emit light.

Fluorophores used for IF staining are usually organic molecules as these are characterized by strong emission in the visible light spectrum (286). Additionally, these compounds have a high quantum yield which could theoretically reach even 100%; meaning they can emit the same amount of photons they absorb (286). Commercially, there is a large number of such antibodies available that are attached to fluorophores emitting light in a range of wavelengths; from 380 nm up to near-infrared at 900 nm. Fluorophores in the near-infrared range have been shown to have a higher quantum yield as they have a higher penetration depth than visible wavelengths, thus are usually preferred (287). However, in multi-labelling procedures, the wide range of choice allows suitable antibodies to be chosen, as it should be avoided to use antibodies that have overlapping absorption or emission spectrums as that would lead to misleading results and unspecific background in the resulting images.

3.6.3 Tissue auto-fluorescence

One drawback of using fluorescence detection in soft tissue samples is that most types of tissue usually have some auto-fluorescence that can mask the antibody labelling. For example in aortic tissue; collagen and elastic fibres tend to be auto-fluorescence at specific wavelengths (288) while in aged brain tissue pigments formed by lipids and misfolded proteins called lipofuscin pigments also auto-fluoresce, interfering with the staining (289). Therefore, fluorophore selection should also be, where possible, done such that the wavelengths in which the tissue auto-fluorescence are avoided.

3.6.4 IF procedure background

3.6.4.1 Sample preparation

Other than a correct choice of antibodies, sample preparation is also rather crucial for good quality IF staining. The first step of sample preparation is fixation. Fixation is essential to prevent the degradation of the sample and to preserve its morphology, such that the antigens remain accessible and well preserved for antibody attachment (280). As previously mentioned, the most common fixatives used are glutaraldehyde and formaldehyde; however, in the case of IF glutaraldehyde fixation was found to result in weak staining and high background fluorescence (262, 263). Thus formaldehyde is usually the fixative of choice, which however should also be used appropriately to avoid over or under fixing, which will also result in reduced staining and badly preserved tissue structure respectively (261). Following fixation, the samples are dehydrated and embedded in paraffin wax to allow for cutting into thin slices,

usually about 4 µm thick, using a tissue processor (290). The slices are then placed onto glass slides (290).

3.6.4.2 Antigen retrieval

An antigen retrieval step can be used if needed to 'reverse' the effects of fixation on tissue antigenicity to unmask antigenic sites (291). The most widely used method is heat-induced antigen retrieval (292) which is based on the principle that the fixation crosslinking can be reversed through treatment with various solutions and use of head (292). However, in cases where minerals are to be studied, antigen retrieval is avoided as it results in mineral alterations and dissolution.

3.6.4.3 Blocking agents

Blocking agents are used prior probing the tissue with antibodies, in order to reduce the amount of unspecific antibody binding due to specific endogenous enzymes, biotin, and receptors present on the tissue which can be recognised by either the primary or secondary antibodies (293). Usual blocking agents involve serum, bovine serum albumin (BSA), cold-water fish gelatine, and dry milk (293). To avoid unspecific binding of the secondary antibody to the tissue, serum from the same host origin as that of the secondary antibody is usually used (294). The serum can then bind to endogenous sides that could also be recognised by the antibody, reducing background staining.

3.6.4.4 Washing buffers

Washing between all steps of the IF procedure is also vital to remove one solution prior application of the next one. For washing, phosphate-buffered saline (PBS) or tris buffered saline (TBS) can be used. Detergents including triton X-100 or tween 20, which increase cell membrane permeability (295) and bovine serum albumin (BSA) for its blocking effect can also be added in the washing buffers. The most widely used in IF are PBS or TBS solution with added 0.1% triton X-100 and 0.5% BSA that are referred to as PBT and TBT respectively.

3.6.4.5 Counterstaining

Other than antibody staining, counterstains can also be used to label biological structures. The most widely used is 4′,6-diamidino-2-phenylindole (DAPI), which is a nuclear stain used to visualise cell nuclei (296) due to its ability to bind to deoxyribonucleic acid (DNA). It is typically applied at low concentrations (down to even 1:100000) and has an absorption of 358 nm and an emission of about 462 nm (296).

3.6.5 IF staining protocol for mineralised tissues

For this work, all samples to be IF stained were fixed as quickly as possible following surgical removal using 10% formalin for at least 24 hours or were immediately processed to be cut into histological slides (Figure 3.16). Samples were then dehydrated and embedded in paraffin wax before being cut into 4 – *5* µm thick slices and placed on histological glass slides (Figure 3.16). Following, the samples were dewaxed through three, five-minute interval pure xylene changes and rehydrated using a series of solutions of decreasing ethanol concentration; 100%, 90%, 70% for 3 minutes each followed by immersion in distilled water for 5 minutes (Figure 3.16). A hydrophobic pen was used to mark the area surrounding the tissue to minimise the solutions needed in the next steps. The tissue was then blocked using 5% goat, horse serum, or BSA for 1 hour at room temperature diluted in the washing buffer, of choice (PBS/TBS/PBT/TBT) (Figure 3.16). Using the same washing buffer, the tissue was washed several times and is incubated at the appropriate primary antibody concentration (Figure 3.16) for 1 hour at room temperature or overnight at 4 ºC. The concentration and incubation time of the primary antibody were optimised for each experiment. Higher concentrations of antibodies than needed can result in unspecific binding, high background, and antibody agglomerates. Following the primary antibody incubation, the tissue was rewashed several times and incubated for another hour at room temperature using the appropriate concentration of secondary antibody (Figure 3.16). Through and after this point, the samples are always kept in the dark. Washing follows again, and the samples are incubated for 15 minutes with a DAPI solution at a concentration of 1:1000 (Figure 3.16). DAPI is always diluted in either PBS or TBS without any additives. Finally, the tissue was rewashed and mounted using an aqueous mounting medium containing glycerol and a coverslip (Figure 3.16). The coverslip was sealed using traditional nail polish.

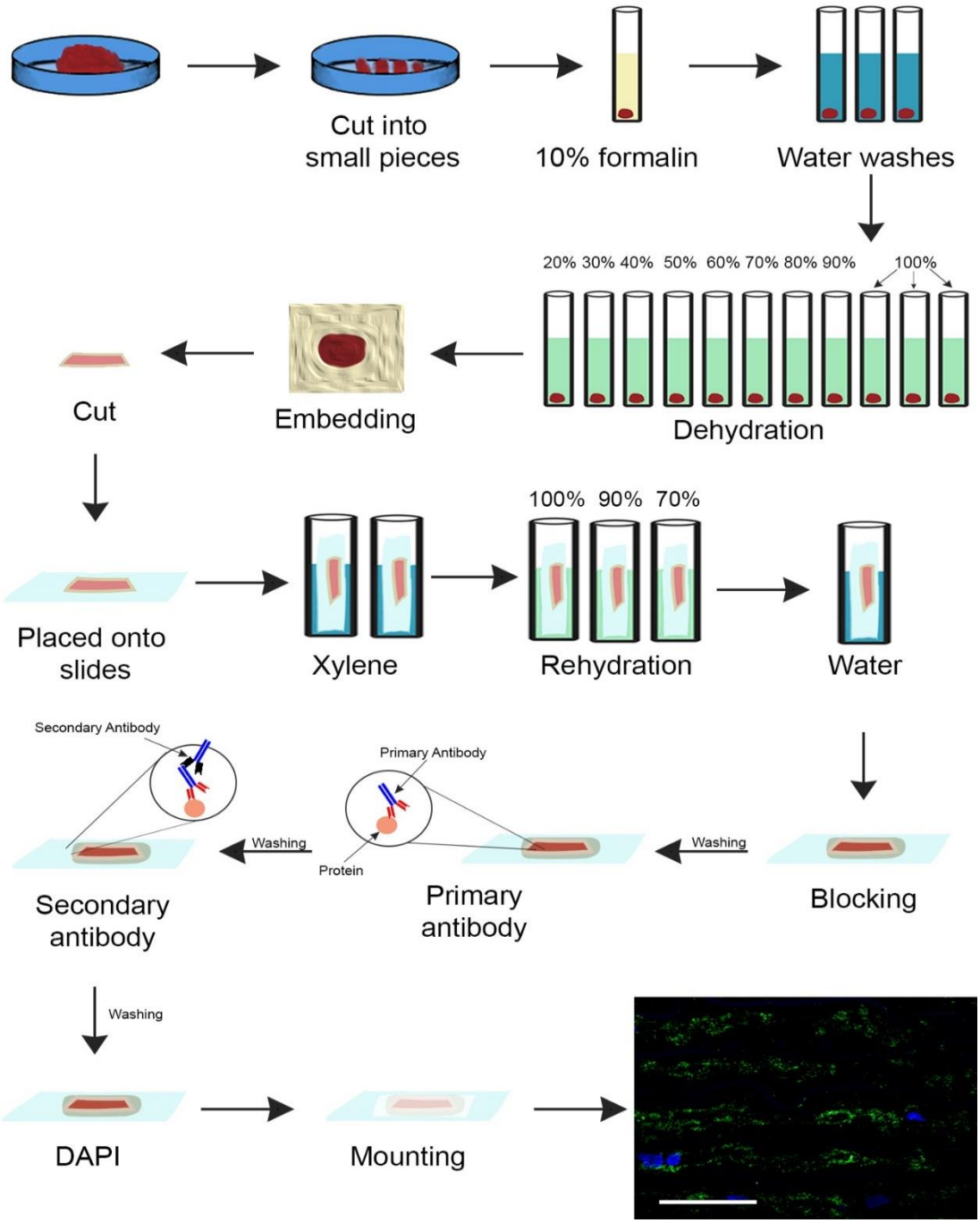

Figure 3.16: Visual representation of the sample preparation and IF procedure for mineralised tissues. *For the initial sample preparation, the tissue should be cut into small pieces and fixed using 10% formalin. Samples are then washed using distilled water, dehydrated, embedded in paraffin wax, cut into thin slices, and placed on histological slides. The IF procedure involves removal of the paraffin wax using xylene, rehydration of the tissue, blocking using 5% BSA or goat serum, incubation with primary and secondary antibodies, and staining using DAPI. Between all steps, the tissue is washed using a buffer. Finally, the tissue is mounted and imaged. Scale bar = 40 µm.*

3.7 Correlative microscopy for the study of pathological minerals

Correlative light electron microscopy (CLEM) refers to the use of both light and electron microscopy for the study of a biological system (297, 298). It is usually used in research where both the presence of specific proteins needs to be identified, but also structural information needs to be obtained. Both scanning and transmission electron microscopy can be employed depending on the biological structures under investigation. However, the technique has rarely been used in the study of pathological minerals (184).

As discussed several times, in this work, the primary aim is the direct study of the minerals; correlative microscopy was therefore also considered. The method was tested for its ability to enable the identification of associated mineral proteins by fluorescence microscopy and mineral visualisation by electron microscopy. To be able to do that the experimental workflow was first optimised, by examining the most suitable order in which the two techniques can be used.

The effect of the immunofluorescence staining procedure on the minerals was initially tested. As previously mentioned, it was identified by both our work and the work of other researchers that antigen retrieval results in the dissolution of the minerals. Thus, we also examined the effect of the whole procedure, omitting the antigen retrieval, to the minerals. SEM imaging of the samples prior (Figure 3.17 (a)) and post (Figure 3.17 (b)) the immunofluorescence staining procedure showed mineral alterations. The backscattered electron micrographs post-processing indicate changes that affect mineral density and appearance (Figure 3.17 (c, d)). The observation led to the conclusion that to observe the natural form of the minerals and precisely correlate them to the IF signal, the SEM imaging needs to be done before the staining procedure.

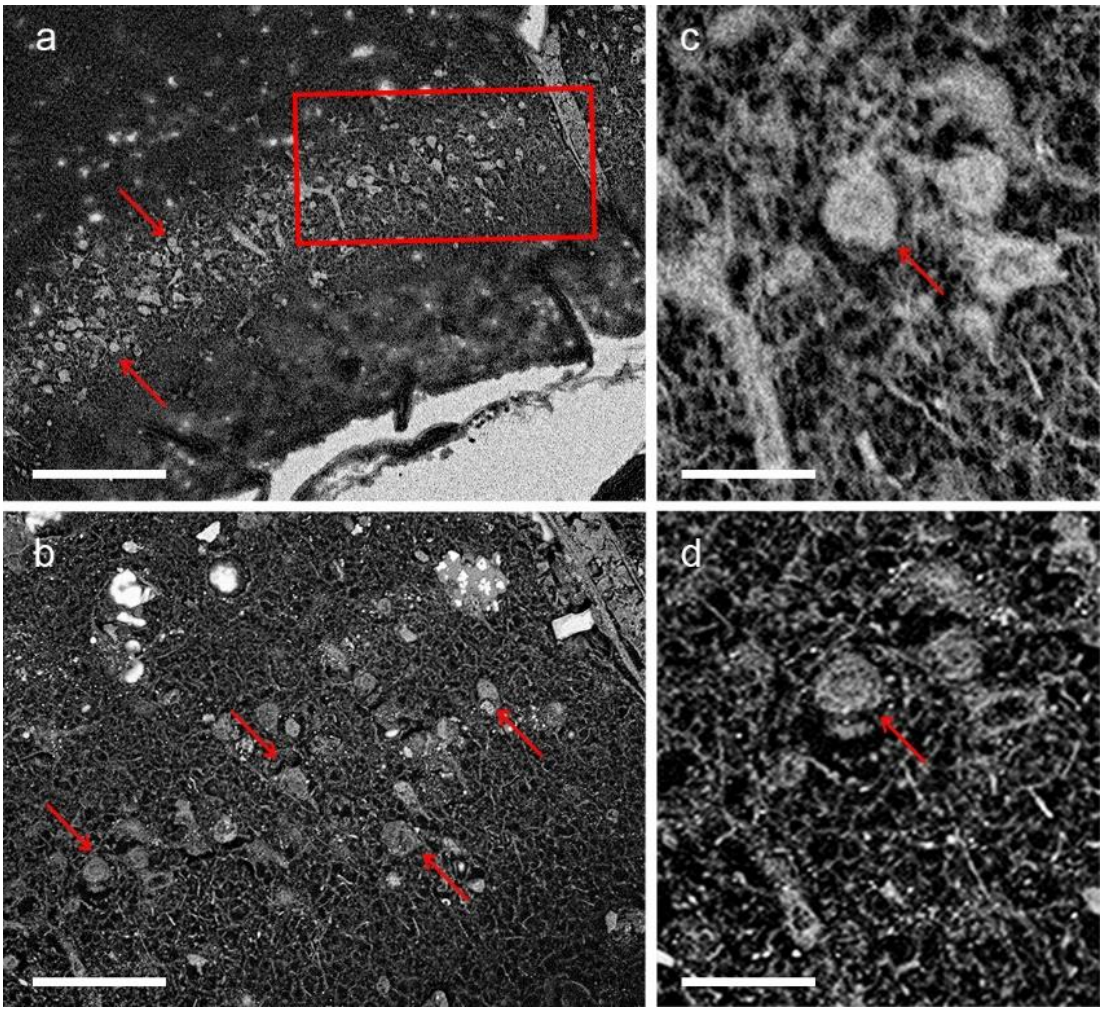

Figure 3.17: Backscattered electron (BSE) micrographs of the same sample prior and post the immunofluorescence (IF) staining procedure. (a) *BSE micrograph of a sample before the IF staining procedure where the mineral (arrows) can be distinguished clearly even at low magnifications. Scale bar = 100 µm.* ***(b)*** *BSE micrograph of a sample post the IF staining procedure, of the same area indicated by a red box in* ***a,*** *where the mineral does not appear as dense as in* ***a*** *(arrows). Scale bar = 50 µm.* ***(c)*** *BSE micrograph at higher magnification showing clearly the presence of calcification (arrow) before the IF staining. Scale bar = 25 µm.* ***(d)*** *BSE micrograph at higher magnification showing the same calcification as in* ***c*** *(arrow) post the IF staining. The calcification appears less dense and more porous, indicating that the procedure causes the mineral to dissolve. Scale bar = 25 µm.*

Therefore, the SEM imaging effect on the quality of the IF staining was examined, at both high and low magnifications, and at different image acquisition times. It was observed that the use of high magnifications and long image acquisition times (to obtain high resolution and low noise images), the electron beam led to a 'burning' effect (Figure 3.18 (a)) on the tissue. The region that had been SEM imaged (Figure 3.18 (b)) before the staining procedure showed no fluorescence signal of neither the DAPI

dye nor the antibody staining (Figure 3.18 (c)). Additionally, the regions in close proximity (approximately within 50 *µm)* to the SEM imaged area also showed reduced fluorescence signal in comparison to the areas further away. Interestingly, even though within the SEM imaged area there was, almost no auto-fluorescence in the surrounding areas there was an increase in tissue auto-fluorescence that in combination to a lower fluorescence signal of the staining lead to poor image quality. Taking these findings into account, it was therefore concluded that SEM sample preparation and imaging do not affect the whole sample but rather the areas directly imaged at high magnifications and long acquisition times.

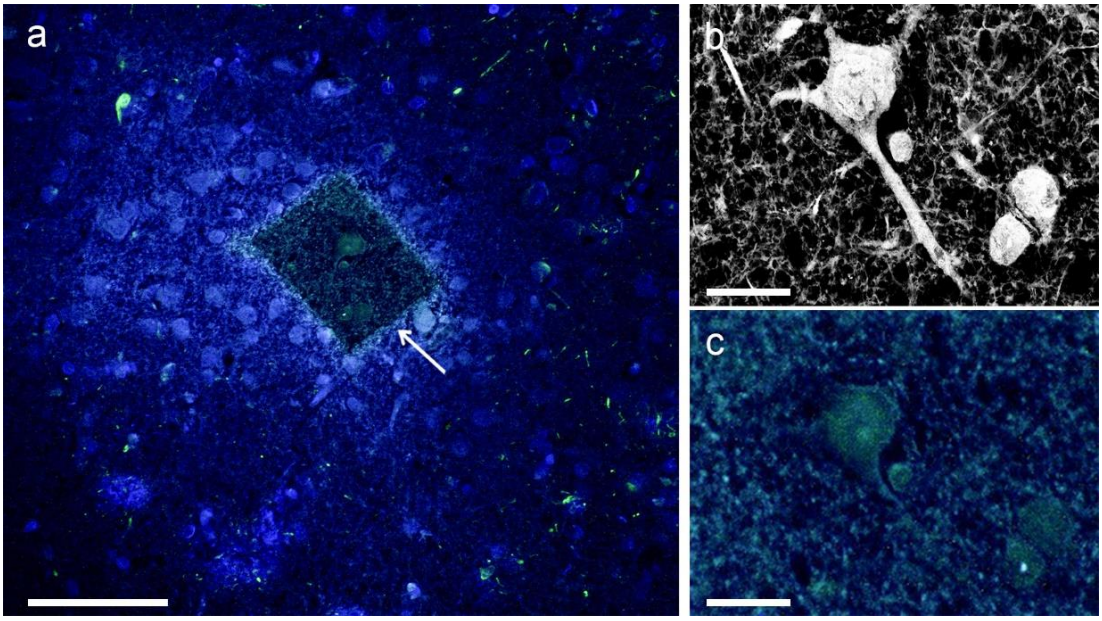

Figure 3.18: Effect of SEM imaging at high magnification and slow image acquisition on IF staining and image quality. (a) *Fluorescence image of a sample stained with DAPI dye (blue) and a phosphorylated tau antibody (green) showing that the SEM imaging had a 'burning effect on the area directly imaged by the electron beam. It can also be observed that the surrounding area shows poor staining and an increase in tissue autofluorescence. Scale bar = 70 µm.* ***(b)*** *BSE micrograph taken at high magnification and slow image acquisition time, showing the same region with the calcification appearing as white. Scale bar = 10 µm.* ***(c)*** *Higher magnification fluorescence image of the area shown in* ***b*** *in which the calcification can still be distinguished, however, no staining is observed. Scale bar = 10 µm.*

On the contrary, in the case of SEM imaging at lower magnifications and shorter image acquisition times (Figure 3.19 (a)), it was observed that the effect of the electron beam was reduced. The results show that the exposure was not as damaging with both the DAPI dye staining and the antibody staining being visible (Figure 3.19 (b)). However, for this work, lower magnification images could not provide the desired

structural information on the mineral but instead could be used to confirm its presence. Another problem with low magnification images was also found to be that in cases where the mineral was not dense enough, it can be misinterpreted with organic material.

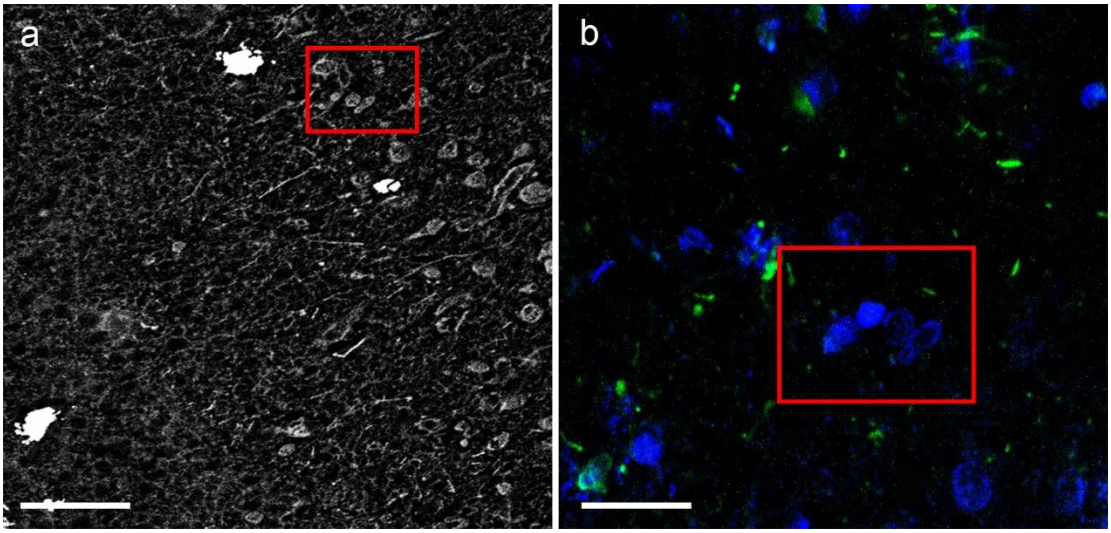

Figure 3.19: Effect of SEM imaging at high magnification and slow image acquisition on IF staining and image quality. (a) *BSE micrograph taken at low magnification and short image acquisition time, showing a region with calcification appearing as grey. Scale bar = 40 µm.* ***(b)*** *Fluorescence image of a sample stained with DAPI dye (blue) and a phosphorylated tau antibody (green) where the staining is visible. Scale bar = 20 µm.*

Based on the results, it was concluded that it was not feasible to carry out correlative work on the same histological slide in which both the mineral and the staining can be sufficiently observed. The IF staining procedure was found to affect the mineral structure leading to misleading results on both the mineral structure and its correlation to any staining. On the other hand, the effect of the electron beam at high magnifications and long acquisition times is damaging to the fluorescence signal and image quality. Despite the minimal effect, the electron beam has at low magnifications, and short image acquisition times, the images do not enable the clear visualization of the minerals therefore in cases where the minerals are of dimensions below few millimetres the method is unsuitable. Lastly, at lower magnifications, a correlation between the SEM and fluorescence images becomes challenging due to the low image quality. As a result, other ways to visualize the minerals were explored, such as dyes.

3.8 Stains for the visualization of calcium phosphate minerals

3.8.1 Von Kossa staining

The von Kossa technique for staining of minerals in tissues was first described by Gyula Kossa (299). It was initially believed that it employs a unique reaction between silver nitrate and calcium salts such as calcium phosphates and calcium carbonate by replacing the calcium ions (300). During incubation with silver nitrate, the tissue is also illuminated to aid the reaction and then incubated by sodium thiosulfate for the protection of black silver deposits (301).

However, other researchers found that the reaction can take place in the presence of ions other than calcium such as strontium, barium, iron, and copper (301). It was also found that the illumination is needed not for the reaction to take place but rather for the production of the black silver precipitates that are insoluble to sodium thiosulfate, as the reaction does take place without the presence of light, producing yellow or brown precipitates (302). Additionally, it was also observed that in a beaker, with or without illumination or incubation with sodium thiosulfate, in the case of calcium phosphates, the resulting silver phosphate precipitates are always yellow (302). Black or dark brown, silver precipitates resulting from calcium phosphates were only observed in the presence of proteins (Figure 3.20) (302). Therefore these precipitates usually observed in tissues (Figure 3.20) are not an indication of calcium phosphate but rather a byproduct of the reaction due to the organic material also present (302).

The specificity of the technique to calcium phosphates in soft tissues originates from the fact that most of these minerals are not present in soft tissues. Furthermore, for minerals such as calcium carbonate and calcium oxalate which have been observed in tissues; it was found that sodium carbonate precipitates can be formed and visualized, but they dissolve in the presence of sodium thiosulfate (302). Calcium oxalates, on the other hand, do not produce visible precipitates, when stained in the traditional von Kossa method (303), a precipitate only forms in the presence of hydrogen peroxide which causes calcium oxalate to transform to calcium carbonate (303).

Subsequently, from a chemical perspective, von Kossa staining can be used to indicate the presence of calcium phosphates in tissues; however, the exact elemental composition of the minerals should always be confirmed through another technique.

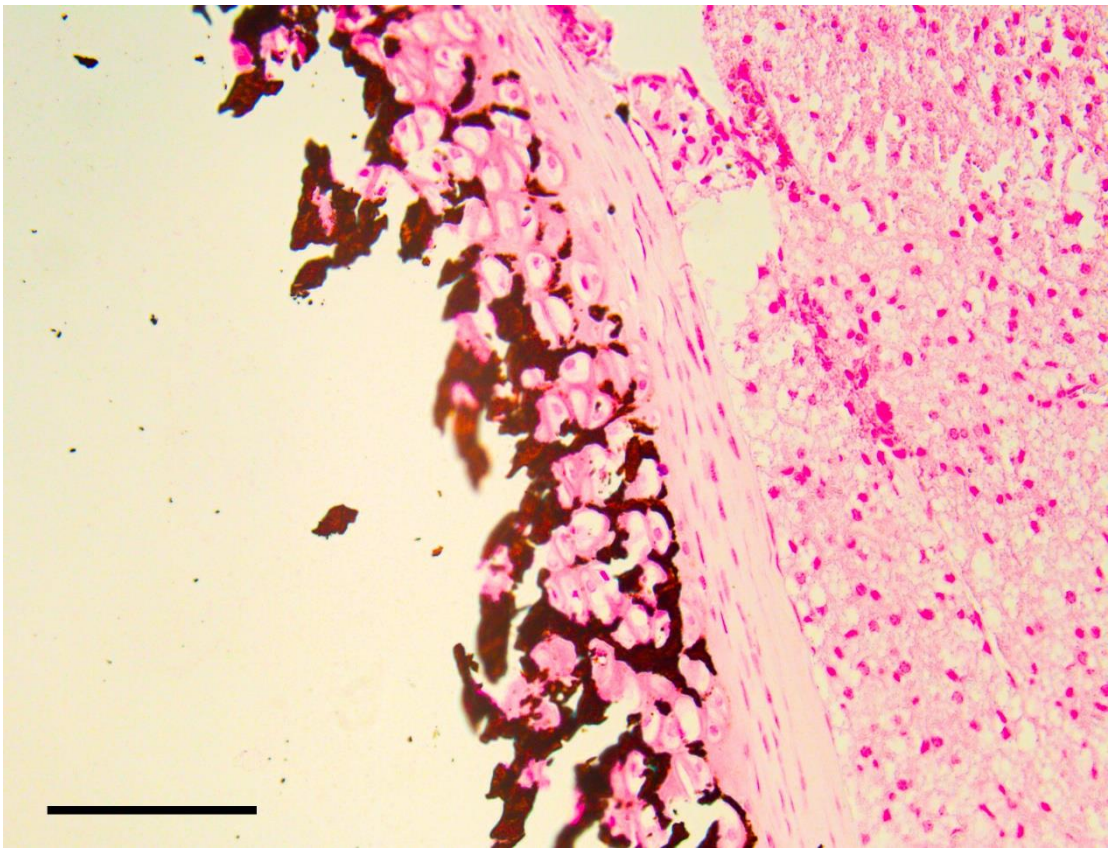

Figure 3.20: Von Kossa stained mouse ribs showing a black-brown precipitate which indicates the presence of calcium phosphate.

In this work, the suitability of the von Kossa staining for correlative methods was also investigated. The precision of the staining in relation to the natural state of calcium phosphate minerals was examined. The results indicated that even though von Kossa staining is sufficient to stain parts of the minerals present (Figure 3.21), some of the minerals observed through SEM imaging (Figure 3.21 (a)) did not present any staining (Figure 3.21 (b)). Thus, it was concluded that even though von Kossa staining is efficient to indicate the presence of a mineral, it should be used in line with SEM imaging for a complete set of information on the minerals present.

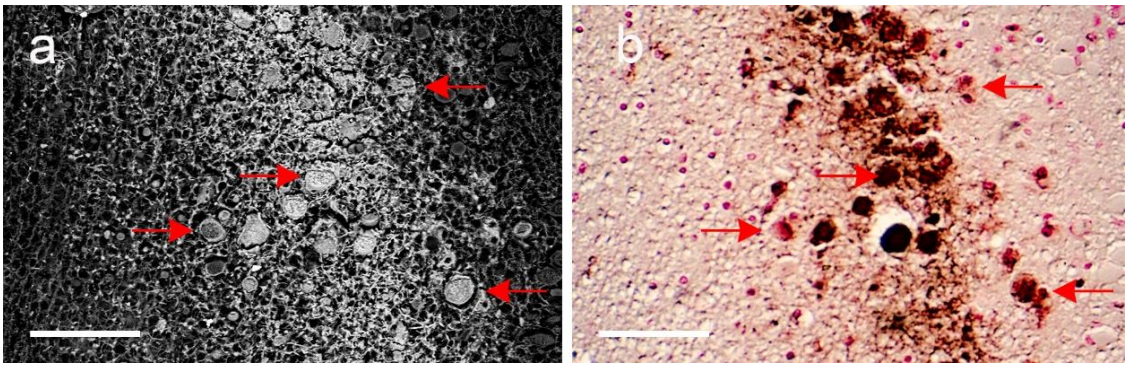

Figure 3.21: Comparison of calcium phosphate minerals as observed through SEM and von Kossa staining. (a) *BSE micrograph of calcium phosphate mineral where brighter regions indicate the inorganic material (arrows).* ***(b)*** *Optical micrograph of the von Kossa staining of the same region, it can be observed that even though some of the minerals are indeed stained (arrows), the staining is not an exact representation of the mineral observed using the SEM. Scale bars = 50 µm.*

3.8.2 OsteoSense staining

Another dye that can be used for the staining of calcium phosphate minerals is called OsteoSense (20, 304, 305). OsteoSense dyes are fluorescent dyes emitting in the near-infrared range (600 - 900 nm), usually used for *in vivo* studies however it was also found to work on formalin-fixed paraffin-embedded tissues (14, 306). The dye is made of a bisphosphonate, a synthetic phosphate that can bind to apatite (307).

Comparing the OsteoSense staining of calcium phosphate minerals to the minerals observed in SEM imaging (Figure 3.22 (a)), it was found that the dye can stain most of the mineral observed naturally (Figure 3.22 (b)). Thus, OsteoSense images were considered to give enough information for correlation purposes between the mineral and other stains (Figure 3.22 (c)) making it the dye of choice in this work for reliable representation of the mineral context in fluorescence images.

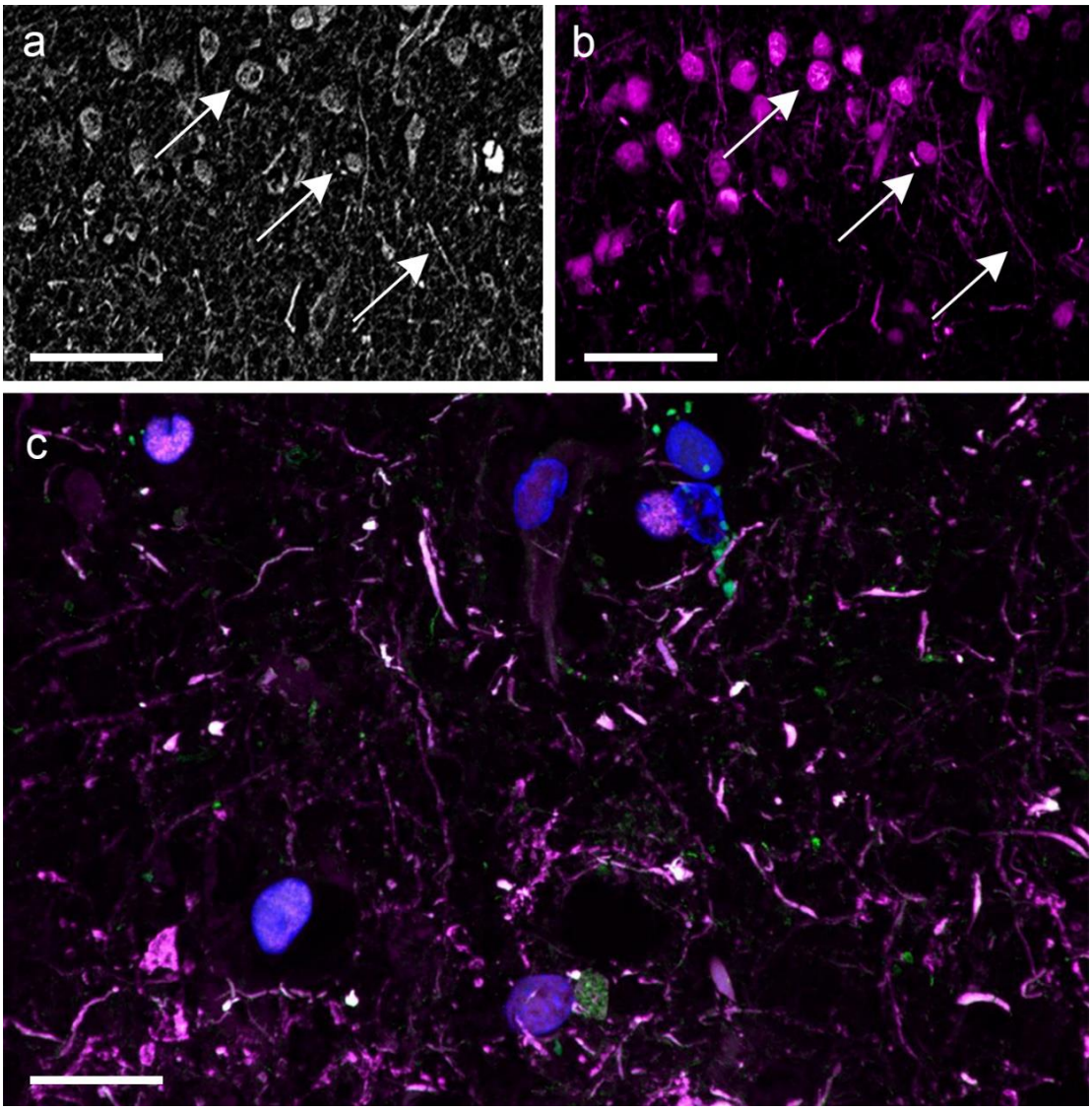

Figure 3.22: Comparison of calcium phosphate minerals as observed through SEM and OsteoSense staining. (a) *BSE micrograph of calcium phosphate mineral where brighter regions indicate the inorganic material (arrows).* ***(b)*** *Fluorescence micrograph of the same region stain with OsteoSense. It can be observed that the mineral is stained (arrows) with high precision. Scale bars = 15 µm.* ***(c)*** *Fluorescence micrograph showing calcification stained with OsteoSense (magenta), nuclei stained using DAPI (blue), and pTau antibody staining (green). Scale bar = 5 µm.*

3.9 Protein blotting methods

Protein blotting methods such as dot blot and western blot are methods that use the extraction of proteins from samples and their transfer to membranes to enable protein identification (308). Dot blot is a simple method that involves the direct deposition of proteins on a membrane, while western blot uses electric currents to transfer proteins from a gel onto a membrane (308). These proteins have been previously separated through the use of electric currents through a method called gel electrophoresis (308).

3.9.1 Gel electrophoresis

Even though other techniques for protein separation exist (such as liquid chromatography), gel electrophoresis is by far the most widely used. The technique uses differences in molecular mass or isoelectric points (or both) of proteins to achieve separation (309). In cases where one of the two parameters is used, the gel electrophoresis is called one dimensional (1D) while when both parameters are used, two-dimensional (2D). Gel electrophoresis can also vary based on the nature of the proteins; whether these are in their native form or denaturated (310). Molecular mass separation of denaturated proteins is the most commonly used 1D gel electrophoresis method, also called sodium dodecyl sulfate (SDS) polyacrylamide gel electrophoresis (PAGE). Separation of native proteins is called native PAGE; however, in this work, this was not used.

SDS PAGE is based on the principle that the size of a molecule is inversely proportional to the speed at which it can migrate in a gel (Figure 3.23), assuming that the size of the proteins is proportional to their molecular mass and charge (309). Therefore, the native tertiary structures of the proteins cannot be used, as they do not satisfy these assumptions. SDS is used during sample preparation to denaturate the proteins into their linear form and to add the necessary negative charges needed for the proteins to move in the electric field (proteins cannot contain both positive and negative charges as they usually do in their native form) (309, 310). These denaturated proteins are then loaded onto the wells of polyacrylamide gels; which are used due to their porosity, allowing for a network of 'tunnels' to be formed through which protein molecules can travel through when an electric field is applied (Figure 3.23) (309).

The electric field causes the negatively charged proteins to move towards the positively charged electrodes; with smaller proteins being able to travel faster than bigger ones resulting in a mass-depended separation (Figure 3.23) (309). The current and voltage used for the separation should be optimised based on the mass of the proteins of interest such that it separates effectively concentrating at a specific point.

To aid the visualisation of the transfer, a dye of low molecular mass (bromophenol blue) as the individual protein bands are invisible (Figure 3.23). Following the separation, the bands can be stained using dyes or metals for visualisation.

Silver staining is usually used for the direct visualisation of protein bands on gels due to its high sensitivity, enabling staining of low amounts of proteins (311, 312). The staining is based on the use of silver nitrate, which can bind on negatively charged proteins. Following, a reduction reaction is carried out through the use of formaldehyde that results in visible silver grains (313). The staining enables both the visualisation of the number of bands but can also aid the visualisation of proteins in a sample against a standard solution containing molecules of known mass in kilo Dalton (kDa) called the 'ladder' (Figure 3.23). This gives information on the molecular mass of the proteins present.

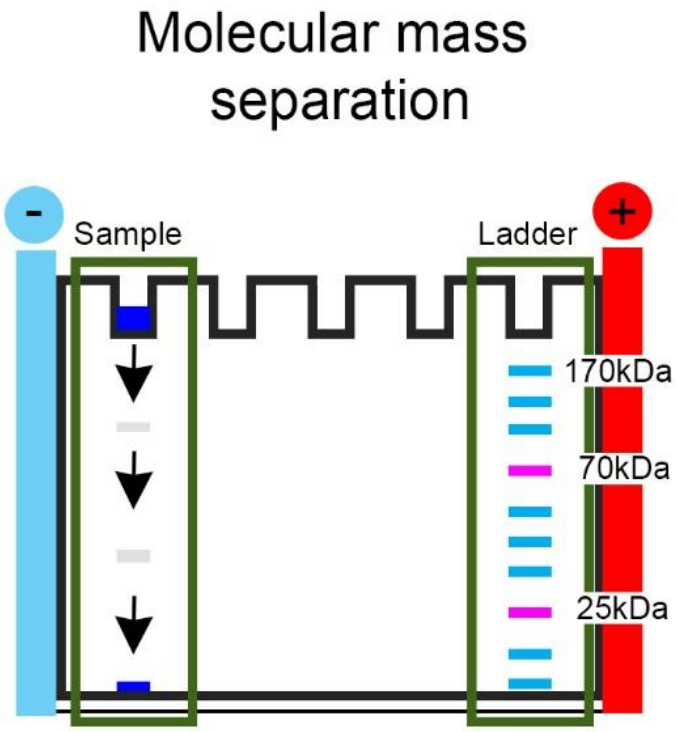

Figure 3.23: Graphic illustration showing 1D gel electrophoresis for protein separation based on molecular mass. *The protein mass affects the speed at which they move in an electric field, with larger proteins moving slower and smaller proteins moving faster. The molecular weight of the proteins can also be identified by a standard 'ladder', which contains molecules of known masses.*

Even though SDS PAGE is sufficient to evaluate the proteins present, to compare the protein contexts of individual samples, and to gain information on molecular masses, it is possible that several proteins with similar molecular mass can be present

thus have not separated and cannot be identified. These proteins can be resolved with the use of 2D gel electrophoresis. Following the molecular mass separation, an isoelectric point gel electrophoresis can be done which uses a pH gradient (Figure 3.24), that is proportional to the isoelectric points of the proteins causing them to separate horizontally (309) (Figure 3.24). However, this method was not used in this work.

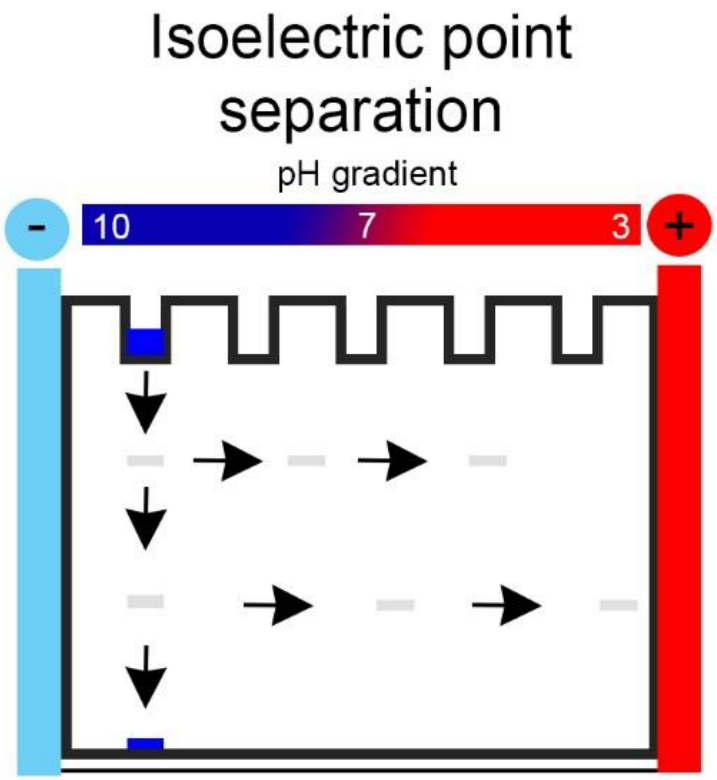

Figure 3.24: Graphic illustration showing 2D gel electrophoresis for protein separation based on isoelectric point following separation using molecular mass. *Isoelectric point separation is based on the isoelectric point of the proteins that is proportional to the pH. A pH gradient is applied on top of the gel, which results in the horizontal movement of the proteins.*

3.9.2 Western blot and dot blot

Another way of protein identification in the individual bands is through antibody staining, which can be employed following protein transferring onto a membrane; called blotting (308). The membranes used for these purposes are microporous and made by, including amongst others nitrocellulose and nylon (308). Nitrocellulose membranes are in general the most commonly used, even though their porous size is big enough to allow small protein molecules to pass through rather than bind to it resulting in weak protein staining (308). The way that protein molecules bind to the nitrocellu-

lose membrane is not fully understood; however, it is believed to be through hydrophobic interactions (308). Furthermore, for western blotting, the addition of methanol in the transfer buffer was found to increase the binding ability of the membrane. Methanol was also found to prevent shrinking of the polyacrylamide gel that can lead to distorted protein bands (308) and enables the transfer buffer to be reused several times (314).

In western blot, the transfer is done through electro-blotting; the use of an electric field to transfer the proteins from a gel to the membrane (308). This can be done through a wet transfer set up, in which the gel and membrane are secured in a 'sandwich' form (Figure 3.25) and immersed fully in the transfer buffer. The choice of voltage, current, and time should be adjusted based on the molecular size of the proteins under investigation. Larger proteins need more time to get 'transferred'; however, this might lead to smaller proteins passing through the membrane (308). For an SDS PAGE gel, the negatively charged proteins are transferred to the membrane (308) as they move towards the anode (close to the membrane).

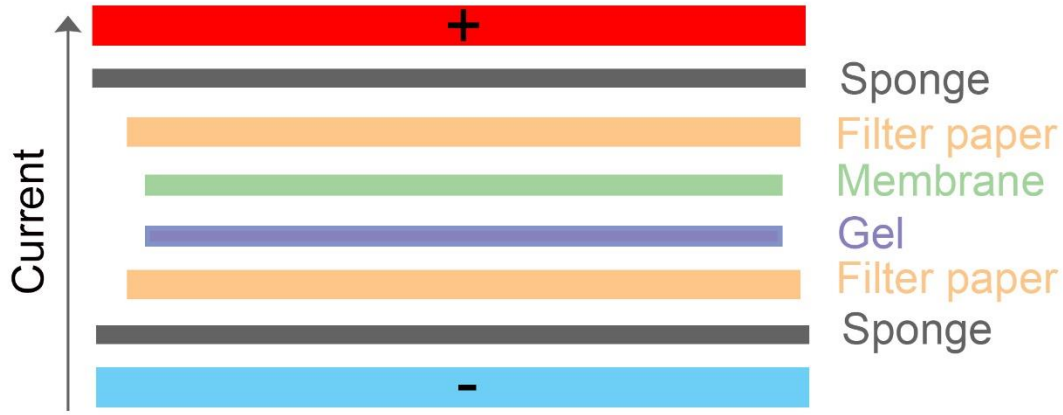

Figure 3.25: Graphic illustration showing the 'sandwich' set up used in a wet western blot transfer.

Following the protein transfer, the membrane can then be stained using the same principle involved in immunofluorescence staining. Blocking has to be optimised; however, in general, the membranes are blocked with 5% nonfat dry milk which attaches to parts of the membrane where there has been no protein binding (during the transfer) such that they are not available to antibody binding (310). Similarly, to immunofluorescence the membrane is then incubated using antibodies; with indirect detection usually performed for signal amplification (using individual primary and secondary antibodies). Detection can be done either through the use of chromogenic (gives a visible precipitate on the protein band), fluorescent or chemiluminescent (a chemical

reaction that produces light which can be detected using specific equipment) probes (310).

Dot blotting, on the other hand, involves the manual deposition of proteins on a nitrocellulose membrane (315), rather than through an electric field as in western blot. Even though it does not give any information on protein mass, it can still be employed for protein identification by immunostaining (316). An advantage of dot blot is that it allows for the concentration of proteins as the sample can be applied at the same spot several times which increases antibody binding and subsequently the signal. Therefore, in the case of mineral protein extraction, it was considered a good tool to determine whether protein concentrations in the samples are high enough to be detected and to increase the protein concentration for staining if needed.

3.9.3 Sample preparation

3.9.3.1 Tissue digestion

The first steps for sample preparation in all immunoblotting methods involve protein extraction (310). Tissues and cells undergo a disintegration process called lysis, which can be achieved both chemically and mechanically (310).

For tissue samples, a mechanical disturbance is usually carried out first through the use of a homogenizer, which essentially 'minces' the tissue. Mechanical disturbance can also be used in cases where the mineral content needs to be isolated as the tissue structure needs to be destroyed for the minerals to be released. Mincing the tissue also aids digestion when digestive enzymes are to be used (317). These are compounds used to break up the extracellular matrix and cell junctions, and subsequently, the structure of the tissue (317). Collagenase is one such compound usually used due to its ability to break the extracellular matrix and also the peptide bonds in collagen (317). As collagen is one of the most abundant proteins in the extracellular matrix present in most tissues, (318) collagenase can sufficiently aid tissue digestion (134).

3.9.3.2 Mineral isolation and demineralisation

Following tissue digestion, for mineralized tissues, full mineral isolation can take place through the use of various methods depending on the purpose for which minerals are needed. For physicochemical characterization of the minerals, hydrazine treatment is usually carried out which was found to remove almost all organic material (134). However, in cases where the protein content of the mineral needs to be preserved, such methods are not suitable. In this work, minerals were instead isolated

through the use of a sucrose density gradient and centrifugation, a technique usually used for the isolation of vesicles and macromolecules (319, 320). The method uses sucrose fractions of different density layers on top of each other to form a density gradient to separate a sample into its different components (319). Applying a centrifugal force on the gradient causes proteins and molecules to move through the gradient at different speeds based on their size, achieving their separation (319).

Optimization of the original method was carried out such that the density of the gradient and centrifugation forces were enough for the mineral content to move to the bottom of the gradient while the organic material did not. The mineral was then washed to remove the sucrose, and SEM imaged to evaluate the efficiency of the method (Figure 3.26). The results of the isolation also depended on the effectiveness of tissue digestion as incomplete tissue homogenization resulted in tissue pieces encapsulating the mineral crystals, which could not be fully isolated (Figure 3.26 (a)). In cases where homogenization was carried out successfully, only a small amount of organic material was found attached to the minerals when the sucrose gradient density was not sufficient for separation (Figure 3.26 (b)). Finally, a successful tissue homogenization and a very dense fraction (70%) at the bottom of the sucrose gradient achieved the removal of most of the organic material and subsequently good isolation of the crystals (Figure 3.26 (c)).

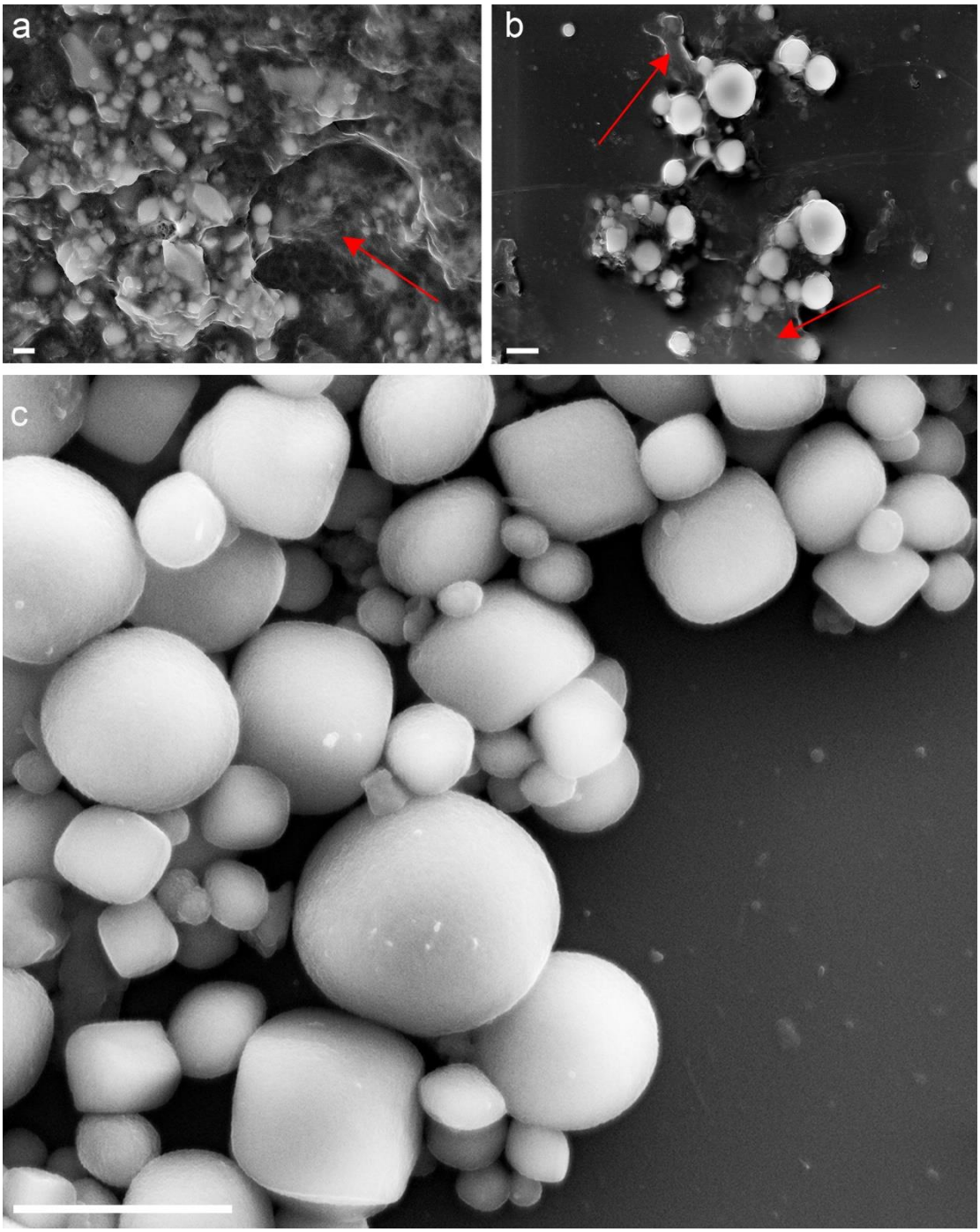

Figure 3.26: SE micrographs of cardiovascular minerals following isolation from the tissue using a sucrose density gradient. (a) *SE micrograph showing organic material (arrow) surrounding the mineral crystals indicating that tissue homogenization was not completed successfully as the mineral crystals are trapped in the organic material.* ***(b)*** *SE micrograph showing some organic material attached to the particles (arrows).* ***(c)*** *SE micrograph of calcium phosphate crystals with no organic material observed. Scale bar = 1 µm.*

Once a sufficient amount of mineral was isolated, demineralisation was carried out for protein extraction. Several studies exist detailing protocols for the extraction of proteins from bones; thus, similar methodologies can also be used for pathological calcium phosphate minerals (275, 276, 321). Demineralisation agents include weak inorganic acids such as formic acid (322) and diluted strong acids such as hydrochloric acid (276). Ethylenediaminetetraacetic acid (EDTA), a chelating agent, is also used (275) due to its ability to react with calcium ions to form a soluble solution (276, 323). Removing the calcium ions from calcium phosphate also results in a solution of phosphate ions leading to complete demineralisation (275). In comparison to other demineralisation agents, EDTA was found to have a more favourable outcome on the protein contents as it does not break them down (275). Following demineralisation, SDS can be used for protein solubilization in the sample preparation for gel electrophoresis and blotting (275). Some studies indicate that SDS is not effective enough in the solubilization of bone proteins; thus, guanidine hydrochloric acid is used instead (275). However, in this study, the use of SDS was considered to produce good results in the subsequent procedures.

Demineralisation methods used for bone also include precipitation or dialysis steps to concentrate the proteins and remove salts (276). Unfortunately, precipitation steps for the concentration of the proteins and separation from the salt contents also result in salt precipitation especially when demineralisation solutions are high in salt such as EDTA (276) thus dialysis is preferred. The amounts of proteins extracted by pathological minerals in this work were deficient; thus, such methods were not employed as they resulted in the loss of the proteins. The downside to this is that EDTA was subsequently not removed which as suggested in the literature (275) resulted in smeared bands on the SDS page

3.9.3.3 Lysis

For tissues and cells, a wide range of lysis buffers can be used following homogenization to break down biological structures further; all of which have the same principle components: a buffering agent, detergents, and protease inhibitors (310). Detergents are used to solubilize proteins; with ionic detergents such as SDS used in cases where the denaturation of the proteins is needed (310). This is determined by the ability of antibodies to detect denaturized proteins. In cases where this is not the case, lysis buffers without detergents are used or non-ionic weaker ones such as Triton X-100 (310). Protease inhibitors include such as leupeptin and pepstatin are usually also added to slow down protein processes that can lead to degradation (324).

Such processes are also slowed down by keeping the lysate at low temperatures. Finally, the choice of the buffer should be made based on its ionic strength, and the effect this has on the protein yield (324). Lysis can also be carried out following protein extraction from minerals to solubilize the proteins further if needed.

To determine the presence or amount of proteins in the resulting lysates, a Bradford protein assay (325) can be used. The technique is based on colour changes resulting from the binding of the amino acids in the proteins to the coomassie brilliant blue dye (326). This binding results in a spectral shift and thus, a colour change of the solution to blue, which determines the presence of proteins (326). This spectral shift can then be analysed using a spectrophotometer which based on the absorbance can give information on the protein concentration when it is compared to a standard of known protein concentration (327).

3.9.3.4 Loading

In gel-electrophoresis, the samples were then mixed with a 'loading' buffer that can also contain SDS for complete denaturation. To enhance protein denaturation, the lysates are usually also boiled for 5 minutes at 95 ºC (310). As previously mentioned in SDS PAGE, SDS is also used to negatively charge the proteins, while in native PAGE, a dye called coomassie blue is used to provide the negative charges needed (310). Coomassie brilliant blue is also used to allow visualization of the protein solution when loaded in the gel and during the separation. The loading buffer also contains a reducing agent to break the disulfide bridges in the proteins to ensure that they are unfolded and therefore are correctly separated during electrophoresis (328). This step can also be carried out before running a dot blot even though; it is not required.

3.9.3.5 Protein extraction from pathological minerals protocol

Protein extraction steps depend on whether tissues, cells, and minerals are to be studied. For the study of pathological minerals, all tissues were initially cut into small pieces (Figure 3.27) and were then mechanically and chemically digested through the use of collagenase (Figure 3.27). Centrifugation was then carried out, and the supernatant was removed (Figure 3.27), eliminating as much organic material as possible, this step was repeated up to three times. The minerals were re-suspended in PBS and added on top of a sucrose gradient (Figure 3.27) containing 40%, 50%, 60%, 70% sucrose following centrifugation. The supernatant was discarded (Figure 3.27), and the minerals were washed before being incubated using 0.5 M EDTA over-night (Figure 3.27). The resulting solution was centrifuged; the supernatant was collected and mixed with the lysis buffer (Figure 3.27) for 30 minutes and centrifuged

again. The supernatant was collected and mixed with the loading buffer (Figure 3.27), boiled for 5 minutes at 95 ºC and spanned down at 16000 rcf (relative centrifugal force) for 1 minute. The supernatant was then used for gel electrophoresis and blotting (Figure 3.27).

The preparation method might need to be adjusted in cases where the minerals are more soluble and would not withstand the extensive use of solutions in the initial steps. In some cases, the minerals could dissolve and thus cannot be isolated; therefore, other biochemical assays might be more suitable.

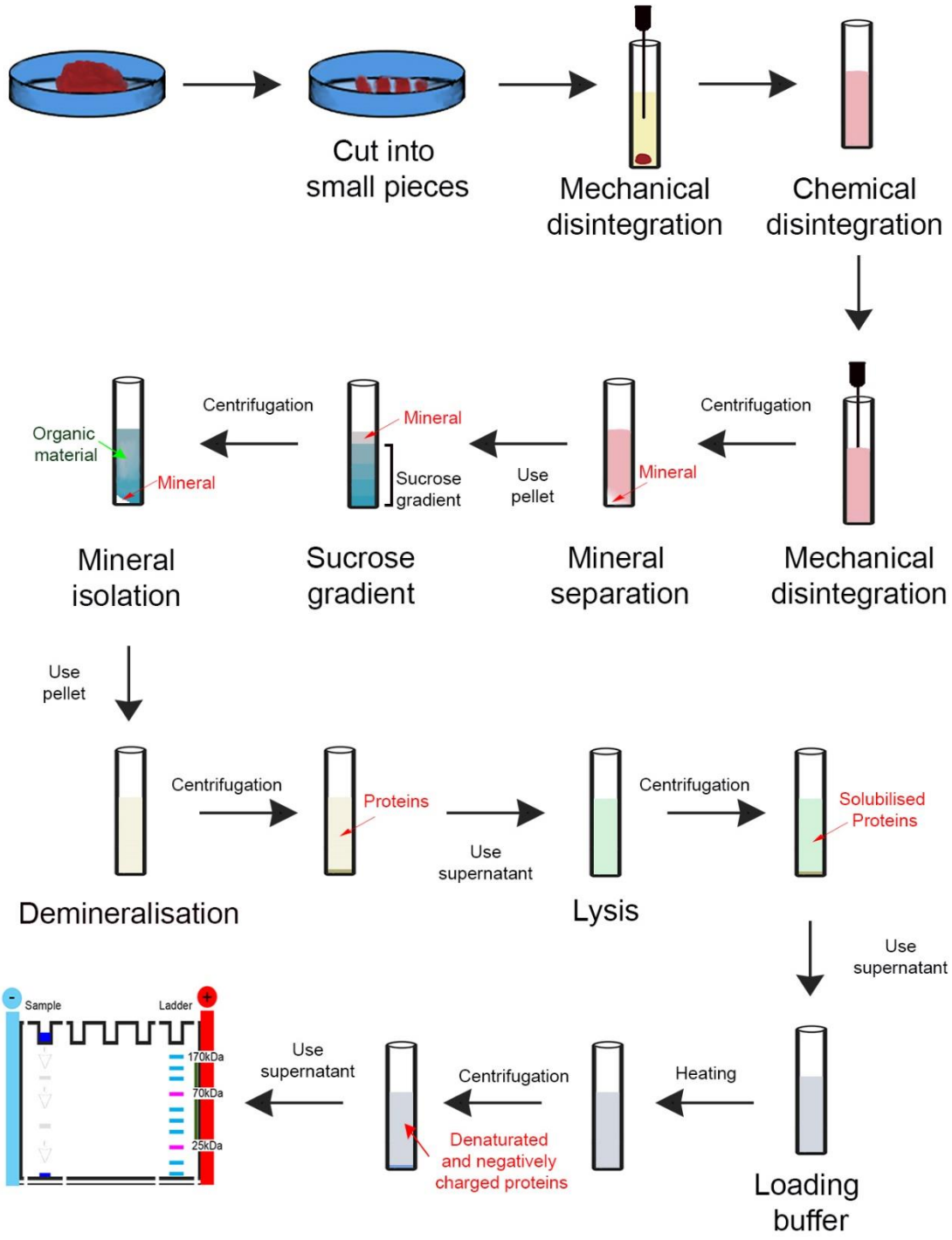

Figure 3.27: Visual representation of the protein extraction from pathological minerals. *The tissue is firstly mechanical and chemically digested such that the organic matrix is broken up and the minerals are released. Centrifugation is then used to separate the mineral content which is then completely isolated through the use of a sucrose gradient. Demineralisation of the mineral takes place for the proteins to be released, followed by lysis for solubilization of the proteins and addition of the loading buffer for complete denaturation and for proteins to be negatively charged as required for gel electrophoresis.*

Chapter 4: Cardiovascular calcification in cardiovascular diseases

4.1 Introduction

As previously mentioned, cardiovascular mineralisation is associated with many diseases, including atherosclerosis and aortic valve stenosis (111). Several competing mineral formation mechanisms can be found in the literature (21, 111, 120, 125-130); however, the exact processes responsible are not entirely understood.

Electron microscopy characterisation of cardiovascular minerals in a range of cardiovascular tissues has shown that there are three distinct minerals present; calcified fibres, calcified particles, and large calcifications (13). The minerals were found to have a chemical composition of calcium phosphate; with the exception of calcified particles composed of whitlockite (a magnesium containing calcium phosphate); which were also found to diffract as a single crystal. The finding suggested that it is possible that more than one mineralisation mechanisms to be responsible for the formation and development of cardiovascular calcification and subsequently, many cardiovascular diseases. Most of the research on cardiovascular calcification, however, focuses on the origins of the apatite minerals (calcified fibres and large calcification) dismissing the presence of the magnesium-containing particles. The shape, composition and crystallinity of which suggest a process yet to be identified, as the mineralisation models found in the literature have not to date reproduce them.

In this chapter, we focus on the investigation of the possible origins of these particles, aiming to identify a possible mineralisation mechanism that can result in the formation of such a unique mineral. Moving away from the proposed mechanisms of formation found in the literature, the possibility that these nanoparticles are originating from blood or blood components was examined. Identifying the origins of the particles can open several pathways to advance our knowledge on their role in calcific cardiovascular disease and in cases where they have unfavourable effects, to allow the development of methods to prevent their formation.

To identify the origins of the whitlockite particles, firstly ***physicochemical characterization of the particles in several cardiovascular tissues was carried out***. Following, ***whether the calcified particles can be found in the bloodstream of patients as independent entities*** were investigated***.*** Finally, ***cells and vesicles, which could play a role in the mineralisation processes*** were identified, and their association to the whitlockite nanoparticles was examined through the use of dot blot and immunofluorescence staining.

4.2 Materials and methods

4.2.1 Samples

4.2.1.1 Human cardiovascular tissues

Fresh human aortic tissue samples from 8 donors obtained from the Oxford Heart Valve Bank (John Radcliffe Hospital, Oxford, UK) after they had been rejected for transplant for various reasons, were used for the biochemical assays carried out in this work. For the SEM analysis, tissue from 32 human aortic valves, 17 mitral valves, 14 coronary arteries, and 22 aortas was used, obtained for the purposes of the original study carried out by Dr Sergio Bertazzo. Samples were collected under approved ethical guidelines with informed consent that allowed the anonymous analysis of the tissues. Ethical approval was obtained from the Health Research Authority - NRES Committee London (10/H0724/18) to research tissue from organ donors.

4.2.1.2 Blood and platelet-rich plasma

Blood was obtained from 69 patients with no cardiovascular diseases to act as the control group and 63 patients with a confirmed diagnosis of aortic valve stenosis patients. The study was approved by the North West Preston Research ethics committee and was carried out in collaboration with Professor David S. Wald (Queen Mary University of London, Barts and The London School of Medicine and Dentistry, Wolfson Institute of Preventive Medicine, London, United Kingdom). Written consent was obtained from all patients. Platelet-rich plasma was also obtained in collaboration with Professor Janice Tsui from NHS blood and transplant biobank after a project ethical approval was obtained by the Proportionate Review Sub-Committee of the North East - Tyne & Wear South Research Ethics Committee (18/NE/-354).

4.2.2 Isolation of calcified particles from tissue

The isolation of the whitlockite nanoparticle was carried out as explained in *chapter 3 section 3.9.4.5*. Initially, fresh aortic tissue was cut into small pieces and was then mechanically digested using a tissue homogenizer until all tissue was broken up. The tissue was then incubated overnight at 37 ºC and constant agitation, in 1 ml of collagenase (10 mg/ml) diluted in 1 ml of PBS, mechanically homogenized again the next day, during which 1 ml of PBS was added. The solution was incubated again overnight at 37 ºC and constant agitation in the solution. The digested tissue was cen-

trifuged, the supernatant was removed along with the tissue pellet on top of the particles. The particle pellet was re-suspended in 500 ml of PBS, and the solution was applied at the top of a sucrose gradient.

4.2.3 Isolation of platelet dense granules

For the isolation of platelet dense granules, methods previously described in the literature were adjusted for the purposes of this study (329). A 200 ml platelet-rich plasma was centrifuged at 2800 rcf for 10 min. The supernatant was removed, and the resulting pellet was re-suspended at 1ml of homogenization buffer per 50ml of platelet-rich plasma originally used. The homogenization buffer was made of 100 mM potassium chloride (KCl), 25 mM sodium chloride (NaCl), 2 mM magnesium sulfate ($MgSO_4$), 12 mM sodium citrate, 10 mM glucose, 25 mM N-2-hydroxyethylpiperazine-N'-2-ethanesulfonic acid (HEPES), 5 mM Adenosine Triphosphate (ATP), 0.35% (w/v) bovine serum albumin (BSA) and protease inhibitors; 0.1 mM 4-(2-aminoethyl) benzenesulfonyl fluoride, 10 µM pepstatin, 10 µM leupeptin, 10 µM trans-epoxysuccinyl L-leucylamido-(4-guanidino) butane, and 10 µM N-α-tosyl-L-lysine chloromethyl ketone. The pH of the buffer was adjusted to 7.0 with 1 M hydrochloric acid (HCl) or 1 M sodium hydroxide (NaOH). Platelets were sonicated, and intact cells were separated by centrifugation at 1000 rcf for 15 min. Sonication and centrifugation were repeated twice with the pellets re-suspended in 0.5 ml of homogenization buffer. The three supernatants were combined and centrifuged at 19000 rcf for 20 minutes. The pellet was re-suspended with 1 ml of lysis buffer and added on top of with a sucrose gradient (30 – 60%). The gradient was centrifuged at 100,000 rcf for 60 min at 4 ºC. The dense granule-rich fraction was then identified using TEM imaging.

4.2.4 SEM sample preparation

Tissue samples were prepared as detailed in c*hapter 3, section 3.3.4.2*. Isolated whitlockite nanoparticles were suspended in deionised water, and 5 µL of the solution were placed onto a clear glass slide and left to dry. The slide was then secured to an aluminium sample holder with carbon tape, which was then silver painted. All samples were carbon-coated using a Quorum K975X coater before imaging.

4.2.4.1 Blood preparation for SEM imaging

Blood samples were centrifuged at 1000 rcf for 10 minutes to separate red blood cells from white blood cells and platelets. Red blood cells were then removed and centrifuged at 3600 rcf for 10 minutes. 5 µl from the bottom of the tube were removed and placed onto microscopic slides and left to air dry.

The samples were then coated with 5 nm of using a Quorum K975X. The backscattered electron detector mode and EDS analysis were used to identify and confirm the presence of whitlockite nanoparticles in the blood.

4.2.4.2 Validation study for nanoparticles in blood

Blood samples from a healthy volunteer were used. Hydroxyapatite microcrystals (Sigma-Aldrich hydroxyapatite nanopowder 693863-5G) were used at concentrations between 0.5 mg/mL and 0.005 mg/mL. All blood samples containing hydroxyapatite nanoparticles were then prepared for SEM imaging, as described in *section 4.2.4.1.*

4.2.4.3 SEM imaging

Samples were imaged using a Hitachi S-3499N and a Carl Zeiss Crossbeam. Voltage, current, aperture, and working distance were adjusted for individual samples and microscope. Density-dependent colour SEM images were obtained as described in c*hapter 3 section 3.3.2*. Energy-dispersive X-ray spectroscopy (EDS) analysis was carried out using Oxford Instruments EDS detectors.

4.2.5 FIB – TEM analysis

A FEI Helios NanoLab 600 DualBeam Focused Ion Beam System was used for cutting, with the assistance of Dr Sergio Bertazzo. Samples extracted and prepared by FIB were imaged and analysed on a JEOL 2100 TEM at an operating voltage 200 kV.

Platelets and platelet dense granules were also imaged by TEM. 10 µl of platelets, and platelet dense granules were applied to a TEM grid and left to dry. The samples were imaged using at 120 kV and 80 kV on a JEOL 2100 TEM and a JEOL 1010 TEM respectively.

TEM electron diffraction patterns were obtained with the help of Dr Ecaterina Ware (Imperial College London). The indexing of the patterns was carried out manually using the measurement tools on Gatan Microscopy Suite 2 software. The image scale bars were used as a reference for calibration. EDS data obtained from the same particles was used as a reference to estimate the chemical profile of the minerals. All data collected was then compared using existing available data on the CrystalWorks Server (https://cds.dl.ac.uk/), for the chemical phase of the minerals to be identified.

4.2.6 Protein extraction

Protein extraction from calcified particles was carried out as detailed in c*hapter 3, section 3.9.4.5.* Particles were incubated in 0.5 M EDTA for 24 hours at room temperature and constant agitation. They were then centrifuged at 20238 rcf for 10 minutes, the supernatant was collected, and the pellet was re-suspended in EDTA for 72 hours at room temperature and constant agitation. The final solution and the 24-hour supernatant were both used in SDS PAGE and dot blot. Following demineralisation, the resulting solution was added to a triton lysis buffer (15 0mM NaCl, 1% Triton X-100 and 50 mM Tris pH 8) was added in one portion (sample-buffer ratio 1:1), which was incubated for 90 minutes at 4 ºC and then centrifuged at 16000 rcf for 10 minutes. The supernatant was collected, and the pellet discarded. To ensure the presence of proteins within the lysates, a Bradford assay was carried out using 50 µl of the sample (325). Following, the demineralised particles were added to 2x laemmli sample buffer (65.8 mM Tris-HCl, pH 6.8, 26.3% (w/v) glycerol, 2.1% SDS (Bio-rad #1610737) with added 50 mM dithiothreitol (DTT)) (sample- buffer ratio 1:1). The solutions were then boiled at 95 ºC for 5 minutes and centrifuged at 16000 rcf for 5 minutes. The supernatant was collected and used immediately or aliquot and stored at - 80 ºC for several months.

For protein extraction from tissue, following homogenisation and separation from the mineral contents, the tissue solution was collected and spin down at 20238 rcf for 10 minutes, the pellet was then collected and re-suspended in triton lysis buffer (see above) (sample-buffer ration 1:4) and incubated for 90 minutes at 4 ºC. The solution was then centrifuged at 16000 rcf for 10 minutes, the pellet was discarded, and the supernatant was added to the laemmli solution, boiled and centrifuged as specified above. Platelets were directly treated with laemmli.

4.2.7 SDS page

For the SDS page, 20 µl of each sample were loaded onto separate wells of a 4-20% gel (Bio-Rad #4561094). For the gel electrophoresis, 10% 10x tris/glycine/SDS buffer (Bio-Rad #1610732) diluted in distilled water was used. The gel was run at 150 V for around 45 minutes.

Following, the gel was incubated in a fixation solution (50% ethanol, 10% acetic acid, and 40% distilled water) for 20 minutes and was then dehydrated using 30% ethanol for 10 minutes. The silver staining was done using a ProteoSilver Silver staining kid (Sigma Aldrich PROTSIL1-1KT). The gel was then washed using distilled water and incubated in 1% sensitizer solution (Sigma Aldrich 3739) for 10 minutes and

washed twice with distilled water for 10 minutes each time. Following the gel was incubated for 10 minutes in 1% silver solution (Sigma Aldrich 3614), was quickly washed for one minute with distilled water, and then was incubated with 5% developer solution (Sigma Aldrich 3864 and Sigma Aldrich 3989) for up to 10 minutes. A stop solution (Sigma Aldrich 4114) was used to end the reaction.

4.2.8 Dot blot

Proteins extracted from platelet and particles were deposited onto a membrane. Five drops of 2 µl were used; each drop was left to dry prior to the addition of the next drop. For the serotonin and collagen controls, pure serotonin (Sigma Aldrich 14927) and collagen I (Sigma Aldrich C3867) samples were used.

The membrane was then blocked using 5% dry milk powder for one hour at room temperature; the drops were changed every 15 minutes to ensure no precipitation of milk was taking place and that the whole membrane was blocked efficiently. The membranes were washed 4 times with PBS for 2 minutes each, incubated with the primary antibodies (rabbit polyclonal to CD41 (abcam® ab63983), goat polyclonal to serotonin transporter (abcam® ab130130), rabbit monoclonal [EPR12735] to serotonin transporter (abcam® ab181034), rat monoclonal [YC5/45] to serotonin (abcam® ab6336), rabbit polyclonal to CD63 (abcam® ab118307), anti-CD62P antibody [EPR1444(2)(B)] (abcam®ab178424), rabbit polyclonal to collagen I (abcam® ab34710)) at a dilution of 1:10 in PBS for one hour. Following, the membranes were rewashed 4 times for 2 minutes each using PBS and were incubated with the secondary antibodies (goat anti-rabbit alexa fluoro 488 (abcam® ab150077), donkey anti-mouse alexa fluoro 568 (abcam® ab175700), anti-rat IgG (H+L) highly cross-adsorbed, CF™ 633 (Sigma Aldrich SAB4600133) or a donkey anti-goat alexa fluor 555 (Thermofisher A-21432)) at a concentration 1:100 in PBS for one hour. Finally, the membrane was rewashed 4 times for 2 minutes each and was imaged using a Leica optical microscope at a 10x magnification, 100 microsecond capture time, and 30% intensity.

4.2.9 Immunofluorescence staining

Samples were prepared as detailed in c*hapter 3, section 3.6.5.* Deparaffinisation and rehydration of the aortic tissue samples took place through a sequence of xylene and ethanol washes. For slight demineralisation of the whitlockite nanoparticles in the tissue, 0.5 M EDTA was applied to the samples for 30 minutes. The samples were then blocked for 1 hour using 5% BSA diluted in PBS. Samples were washed three times with PBS for 3-minute intervals, and incubated with one undiluted primary

antibody (rabbit polyclonal to CD41 (abcam® ab63983), mouse monoclonal to CD41 [M148] (abcam® ab11024) or goat polyclonal to serotonin transporter (abcam® ab130130), rabbit polyclonal to collagen I (abcam® ab34710), goat polyclonal to alpha smooth muscle actin (abcam® ab21027)) for one hour at room temperature. Following, the samples were washed three times with PBS for 3-minute intervals and incubated with the secondary polyclonal antibodies (goat anti-rabbit alexa fluoro 488 (abcam® ab150077), donkey anti-mouse alexa fluoro 568 (abcam® ab175700) or a donkey anti-goat alexa fluor 555 (Thermofisher A-21432)) diluted in PBS to a concentration of 1:10 for 1 hour. The samples were then rewashed three times with PBS for 3-minute intervals and incubated with pure OsteoSense 680EX (PerkinElmer NEV10020EX) for 20 minutes. Two PBS washes, 10 minutes each were then carried out, and the tissue was incubated in DAPI stain (abcam® ab228549) at a concentration of 1:1000 (diluted in PBS) for 15 minutes. The sample was then washed twice using PBS for 3-minute intervals. Finally, the samples were mounted with a coverslip using Fluoroshield mounting medium (abcam® ab104135) and was sealed using nail polish at the edges of the coverslip. All samples were imaged using an Olympus FV1000 and a Zeiss LSM 980 Airyscan confocal microscope. All antibodies were tested for specificity using secondary antibody, and negative controls where appropriate.

Co-localisation analysis was done using the Coloc 2 function of FIJI Image J software, which was obtained as the Mandres' overlap coefficient (330, 331).

4.2.9.1 Statistical analysis

All statistical analysis was done using OriginLab 2019 and GraphPad Prism 8.3.1 software. A Mann-Witney two-tailed unpaired U test (332) was used ($p<0.05$). The test is non-parametric thus; it does not assume that the data points follow a normal distribution. All box blots represent the upper and lower quartiles; the whiskers indicate standard deviation, and the middle line the median value. All data is represented as the average value ± standard deviation.

4.3 Results and discussion

4.3.1 Physicochemical characterisation

Scanning electron microscopy indicated the presence of calcified nanoparticles (Figure 4.1 (a)) in various amounts, despite the outcome of the macroscopic assessment of the samples for the presence of calcification. In accordance with previous work (13), the nanoparticles were observed in samples where no other type of mineral was present, suggesting that they are the first calcified structure present in cardiovascular tissue, and therefore might play a role in the development of the associated diseases. The nanoparticles were present in cardiovascular tissue as distinct entities (Figure 4.1 (b)) with an average diameter of 459 nm ± 314.6 nm and were found to be composed of magnesium, calcium, and phosphorus (Figure 4.1 (c, d)). Additionally, SAED patterns obtained from FIB prepared TEM sections indicated that the particles are diffracting as a single crystal (Figure 4.1 (b)). Indexing of the SAED patterns indicated a chemical phase of magnesium whitlockite (333) (Figure 4.2).

It was noted that these nanoparticles, were always observed as independent entities; thus, it was concluded unlikely that they accumulate over time to grow and transform into the larger apatite calcification observed in the tissues. In addition, the size and shape of the nanoparticles, also suggests a process involving a vesicle which possibly mineralises over time. Therefore, we suggest that a distinct mineralisation mechanism is taking place, leading to the formation of the whitlockite nanoparticles, different from the mineralisation mechanisms associated with the other apatite minerals previously reported in the literature.

As mentioned in *chapter 2* comparison to bone mineral under physiological conditions, which does not present highly crystalline magnesium containing particles (13), indicated that the calcified particles do not follow the same mechanisms of formation as those involved in physiological bone. Osteogenic processes might, however, be triggered due to the presence of these nanoparticles, leading to the formation of the hydroxyapatite minerals. It has been previously reported in the literature that the presence of calcium phosphates promotes osteogenic differentiation of cells (334). Additionally, It has been suggested that the presence of whitlockite rather than apatite induces a higher degree of osteogenic differentiation in mesenchymal stem cells (335). Such observations could explain the countless studies reporting osteogenic markers in cardiovascular and other mineralising tissues of diseased individuals.

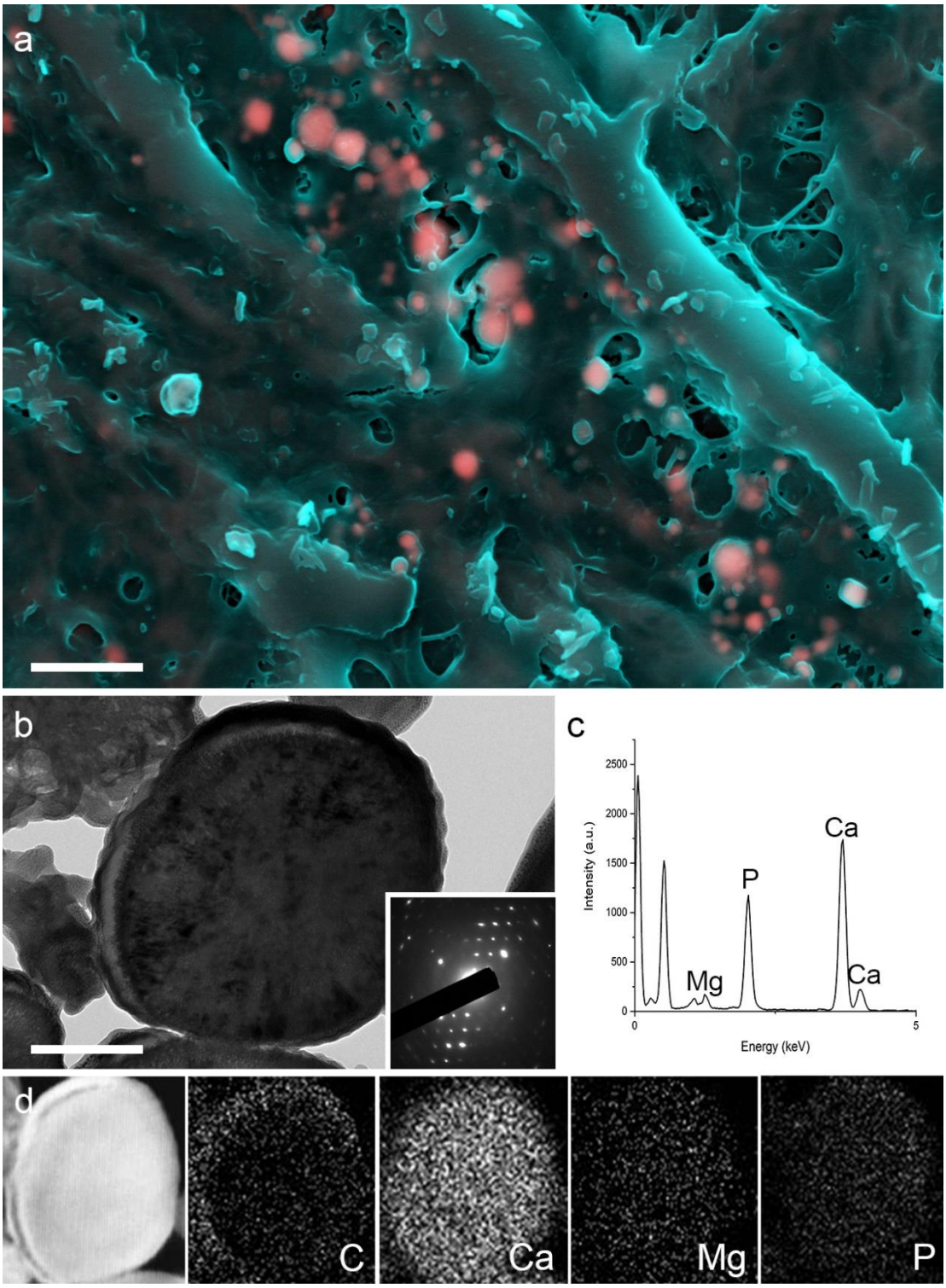

Figure 4.1: Electron microscopy analysis of calcified particles. (a) *DDC-SEM micrograph of calcified particles observed in aortic tissue. Red and pink indicate inorganic and turquoise (blue/green) indicates organic material. Scale bar = 2 µm.* ***(b)*** *TEM micrograph of a FIB prepared section of a nanoparticle with SAED pattern (inset) indicating properties of a single crystal structure. Scale bar = 200nm.* ***(c)*** *EDS spectrum confirming an elemental composition of calcium, phosphate, and magnesium.* ***(d)*** *Scanning TEM mapping of the particle shown in* ***b*** *confirming the presence of calcium, magnesium and phosphorus.*

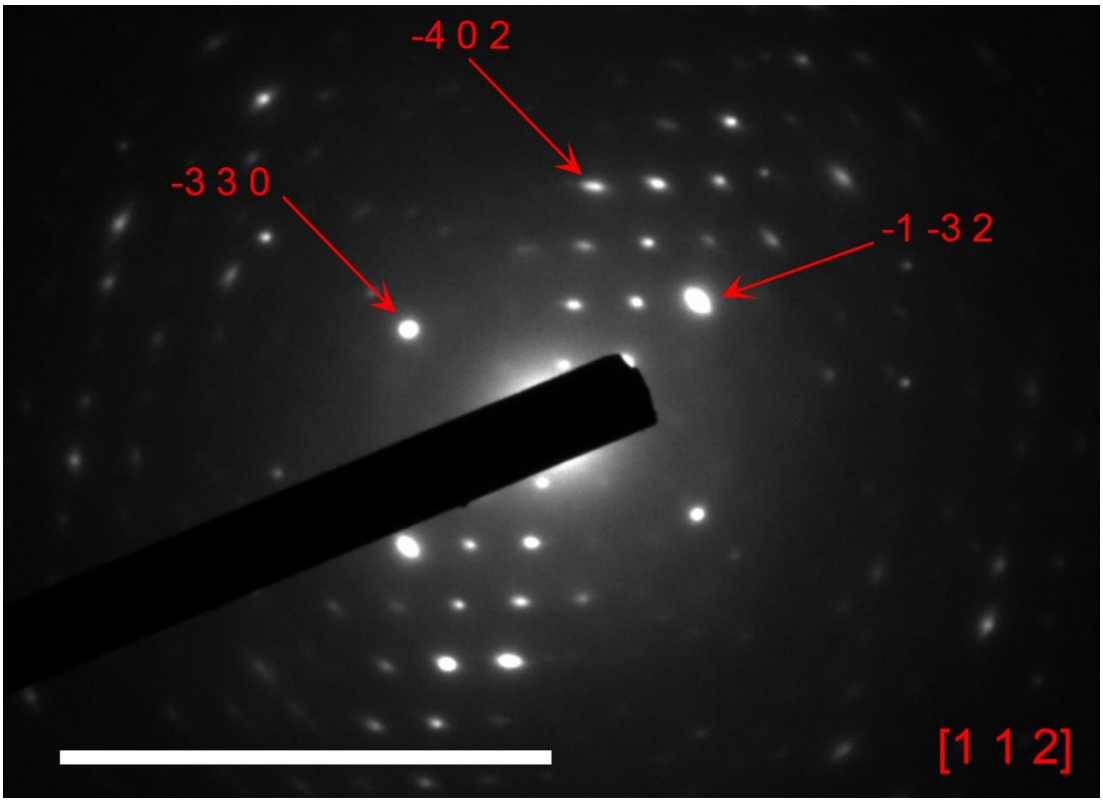

Figure 4.2: Electron diffraction pattern obtained from a nanoparticles showing the vector points (-3 3 0), (-1 3 2) and (-4 0 2), corresponding to the zone axis [1 1 2]. *Scale bar = 10 nm[1].*

In addition, looking at the anatomical location of the whitlockite nanoparticles in the aortic tissue, it was found they accumulate deep into the vascular wall, after the internal elastic membrane, spreading into the tunica media (Figure 4.3). This observation subsequently led to the belief that vascular smooth muscle cells are responsible for the development of medial calcification (120, 336). However, in none of the related studies, vascular smooth muscle cells were able to produce whitlockite nanoparticles, with most mineralizing models reporting the production of apatite mineral.

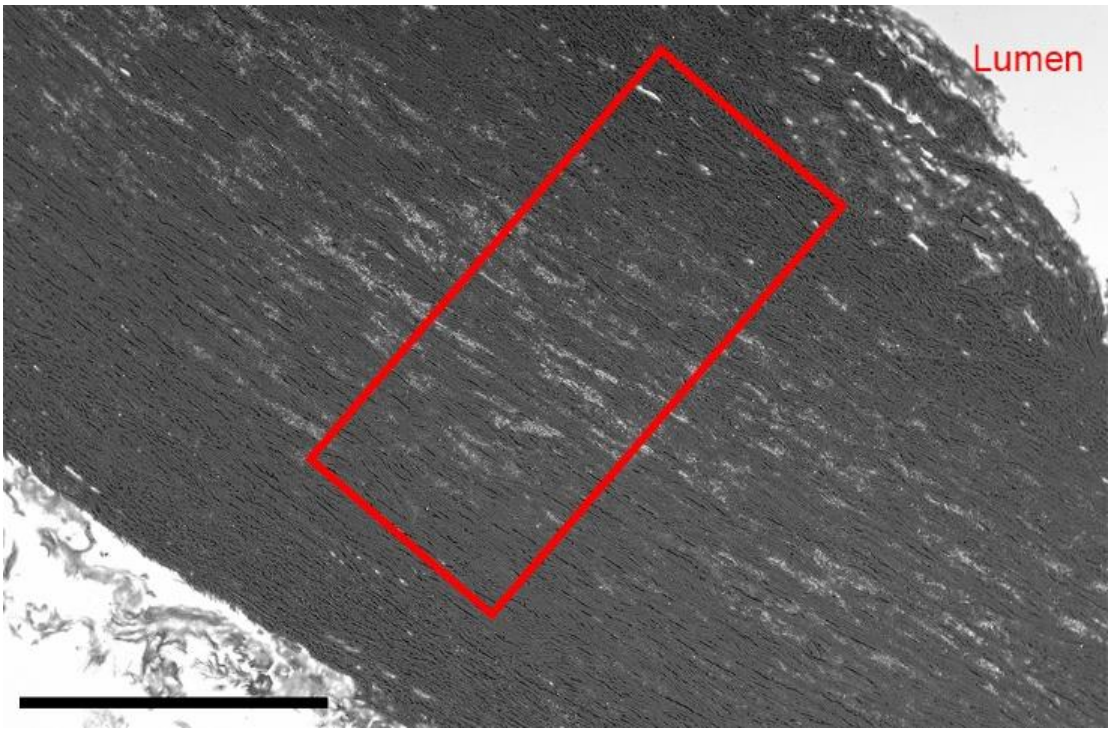

Figure 4.3: Anatomical location of whitlockite particles as observed in aortic tissue where inorganic material is indicated by bright areas and organic material as dark areas. *BSE image of aortic tissue showing that the whitlockite particles (white parts in the red rectangle) are concentrated in the tunica media of the aorta (rectangle). Scale bar = 500 µm.*

Therefore, in this work, it is hypothesized that the nanoparticles originate from mineralization mechanisms other than those already reported in the literature. It is instead proposed, that the whitlockite nanoparticles or their precursors originate from the blood. The hypothesis suggests a mineralization mechanism following similar principles to those employed by nanoparticle delivery for therapeutic purposes which were found to be able to penetrate through the vascular wall into the tunica media and adventitia (337, 338). This could be done through transcytosis, transcellular channels (339, 340), or through the recruitment of specific blood cell types following similar pathways to those leading to the recruitment of lymphocytes in the tunica intima in atherosclerosis (341).

4.3.2 Whitlockite nanoparticle origins

4.3.2.1 Blood circulating calcified particles

Firstly, to understand the origins of the whitlockite nanoparticles, it was examined whether they are present in the blood, a result of a blood-derived precipitation process. For this part of the work, blood from aortic valve stenosis patients was used

as they also present the whitlockite nanoparticles on the valve leaflets (13). Healthy volunteers with no record of cardiovascular diseases were also used as a control group.

A control study was carried out to validate the accuracy of SEM imaging in detecting such particles in blood samples. Blood from a healthy volunteer with added concentrations of synthetic hydroxyapatite nanoparticle crystals was prepared and imaged in the same way as the obtained samples. The hydroxyapatite particles used had the same morphology as the whitlockite particles, and an average size of 200 nm, slightly smaller than the average size of the particles (459 nm). Concentrations between 0.5 mg/mL and 0.005 mg/mL were tested. The SEM results indicated that the hydroxyapatite particles were detectable by SEM in blood samples, down to a concentration of 0.008 mg/mL (Figure 4.4 (a)). No particles were detected at a concentration of 0.007 mg/mL or below (Figure 4.4 (b)). The validation experiments were carried out twice for each tested concentration, with the same results being observed.

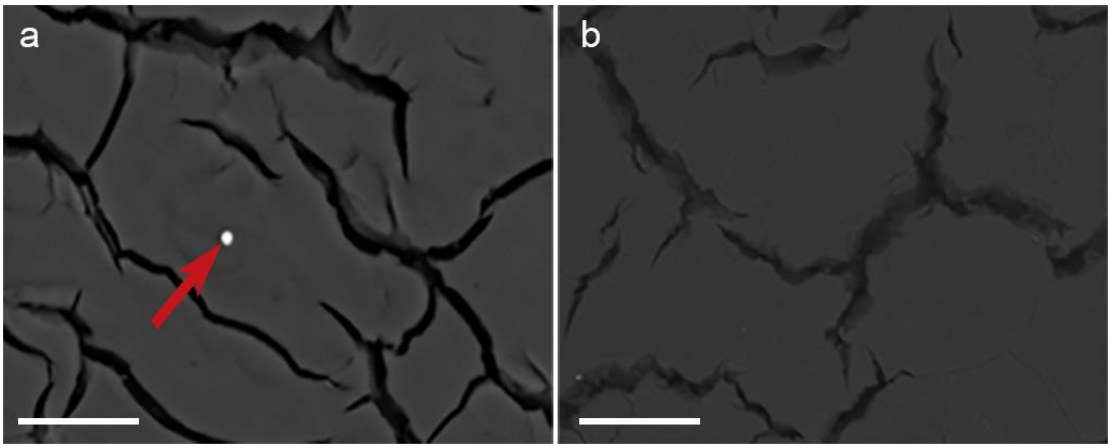

Figure 4.4: Backscattered electron micrographs of blood samples. (a) *Blood sample of a healthy volunteer with hydroxyapatite nanoparticles (arrow) added at a concentration of 0.05 mg/mL.* ***(b)*** *Blood sample of a patient with aortic valve stenosis where no calcified nanoparticles were detected. Scale bars = 5 µm.*

On the other hand, no whitlockite nanoparticles were observed in neither the blood obtained by the volunteers in the control group nor the aortic valve stenosis patient group. The result indicated that the calcified nanoparticles are not present in the bloodstream of neither healthy nor diseased volunteers; or if present, they are at a concentration lower than 0.008 mg/ml. It was therefore concluded that it is unlikely that they are forming and circulating freely in the bloodstream prior to penetrating through the vascular wall.

Analysis on the amount of serum phosphate, serum calcium, and the calcium-phosphate product all of which had been previously associated with aortic valve stenosis (342); was also carried out using blood samples from the same patients by the collaborators of this work for the purposes of the published study (343). No statistical significance was observed in serum calcium values ($p = 0.154$) (343). However, the serum phosphate and the calcium-phosphate product differences between the two groups were found to be statistically significant with p values of 0.011 and 0.005, respectively (343). The results come in agreement with previous studies that identified a correlation between increased phosphorus and calcium-phosphate product levels to an increased risk of developing cardiovascular diseases (344, 345).

Therefore, the serum phosphate and the calcium-phosphate product might have a role in the calcification processes, even though the blood phosphate and calcium are only a small percentage of the total body amounts. Both calcium and phosphate are found in blood either bound to proteins and lipids or in ionic forms (346), the specific location of which could hint on which blood components might play a role in the mineralization processes. Interestingly, increased calcium and phosphate levels in the blood (347, 348) are also observed in patients with platelets of increased mean volume; a factor also correlated to cardiovascular calcification (349).

4.3.2.2 Platelet-derived precursors

Based on these outcomes, the remaining of the work concentrated on the identification of other possible mechanisms of mineral formation and possible blood-derived origins. Special attention was paid to platelets, due to their association with a range of calcific cardiovascular diseases and the development of cardiovascular calcification (349-352). As previously mentioned, platelets originate from megakaryocytes and are responsible for coagulation. Resting platelets have the shape of a small disk and contain a number of granules and organelles (353). There are two types of platelet granules; alpha (α) and delta (δ) granules (also known as dense granules) (353), both of which are storage vesicles which upon platelet activation are released into the extracellular matrix (353). Following platelet activation, several microvesicles, microparticles, and exosomes are released into the extracellular space and circulate in the bloodstream (354).

Activation of platelets takes place mainly as a response to a vascular injury, although in diseases such as atherosclerosis an excessive amount of activated platelets and activation products is thought to contribute to disease progression (351, 355). For example, a number of platelet granular proteins have been found in atherosclerotic

lesions while are absent in healthy vascular tissues (355-357). Additionally, an increased platelet volume has been correlated to coronary artery calcification (349), while platelet activation has been found to promote the development of atherosclerotic lesions (351, 352) and the progression of aortic valve calcification (358). Moreover, increased amounts of circulating platelets vesicles have also been shown to contribute to the development of vascular calcification (359). This is believed to be due to the impact platelet vesicles have, on the function and phenotype of leukocytes, macrophages, and endothelial cells (359).

Interestingly, platelet vesicles have also been found to alter the phenotype of vascular smooth muscle cells (360); phenotypic changes believed to be related to the development of calcification (120). Platelet dense granules involvement in the calcification process was also supported by a study that showed platelet markers overlapping with osteocalcin (a bone formation protein - also expressed in platelet dense granules) close to calcified atherosclerotic plaques (357). In addition, a different study has also indicated the presence of another dense granule marker (14-3-3 zeta) in atherosclerotic plaques (356).

This strong association of platelets and platelet products with calcific cardiovascular diseases led to the hypothesis that platelets might play a direct role in the mineralization processes leading to the formation of the whitlockite nanoparticles. The main aim of the remaining of this work was, therefore, to examine the presence of platelet markers in the whitlockite nanoparticles. To the best of our knowledge, no study had to date investigated a direct correlation of platelet markers (or any other cellular markers) and the whitlockite nanoparticles or any other form of cardiovascular calcification.

The most widely used platelet marker, integrin alpha IIb/beta-3 receptor (CD41) is a membrane protein (361). The protein was identified to be appropriate as it is only expressed on platelets and megakaryocytes (362). Interestingly, the receptor was correlated to atherosclerotic plaques before (357, 363). An observation believed to be due to the adhesion of platelets on the arterial endothelium (363), rather than the mineral itself, or due to the release of osteogenic promoters from platelets that contribute to the mineral formation (357). Either way, the presence of CD41 in atherosclerotic vasculature has been observed, even though the exact causes are yet speculated. Another protein expressed in platelets is the platelet activation marker, P selectin (CD62P) (361). A protein also expressed in platelet alpha granules, activated platelets (364), and Weibel–Palade bodies of endothelial cells (365, 366). The marker has also been correlated to atherosclerotic plaques (364, 365), however endothelial and platelet activation have been accounted for its presence (364, 365).

Serotonin was also considered to be a possible marker as it is abundant in platelets and platelet dense granules (361). Aortic vascular smooth muscle cells have, however, be found to uptake serotonin (250, 367) and possibly synthesize it (368). Serotonin receptors have been found on endothelial cells (367, 368), while serotonin has been reported to increase vascular permeability (369). Limitations on using serotonin as a marker is the small size of the molecule which makes it hard to detect in methods such as conventional SDS PAGE and blotting methods, and its ability to oxidize both inside and outside the body, during sample preparation processes, for example, to become undetectable (370). Thus serotonin transporter markers were considered instead, which are widely expressed in platelets (361, 371) but also vascular smooth muscle cells (368, 372) amongst others. In platelets, serotonin transporter (SERT) is located on platelet membranes and intracellularly for the regulation of serotonin uptake from plasma (373, 374). Other than the vital role these molecules have on serotonin levels, they were also found to play an essential role in the activation and aggregation of platelets and subsequently have a role in disease, as blocking of these receptors changes platelet behavior (375, 376).

Finally, tetraspanin-30 (CD63) and the lysosomal markers (LAMP-1 and LAMP-2) are proteins expressed in platelet granules, vesicles, and microparticles (361, 377), but as general lysosomal granular membrane markers, they are expressed in technically all vesicles despite their cell origin (378). Thus these markers need to be used in addition to other more cell-specific markers. In cardiovascular calcification research, such markers have been used widely to support disease mechanisms involving amongst others platelet, vascular smooth muscle, and macrophage cell vesicles (20, 146, 379).

4.3.2.2.1 SDS PAGE and dot blot

Following marker identification, SDS PAGE and dot blot were carried out to evaluate the presence of proteins in the whitlockite nanoparticles and to identify whether any of the platelet markers mentioned above are present respectively. A Bradford assay was used to identify the presence of proteins in the lysates while SDS PAGE results indicated that all the mineralised nanoparticles presented similar protein bands. Some of the particles observed were found to contain a higher number of distinct protein bands, which could be due to tissue proteins present or a higher amount of protein contents within the particles (Figure 4.5). Comparing to the protein bands observed in platelet and tissue lysates, it could not be determined if the particles originate from platelets even though they shared bands at the same molecular weight (Figure 4.5). Despite this, some of the bands observed were also present in tissue

lysates; thus, it could not be determined if the complete isolation of the whitlockite nanoparticles was successful. As a result, these experiments were only used to determine the presence of protein bands, rather to examine the relationship between the nanoparticles and platelets.

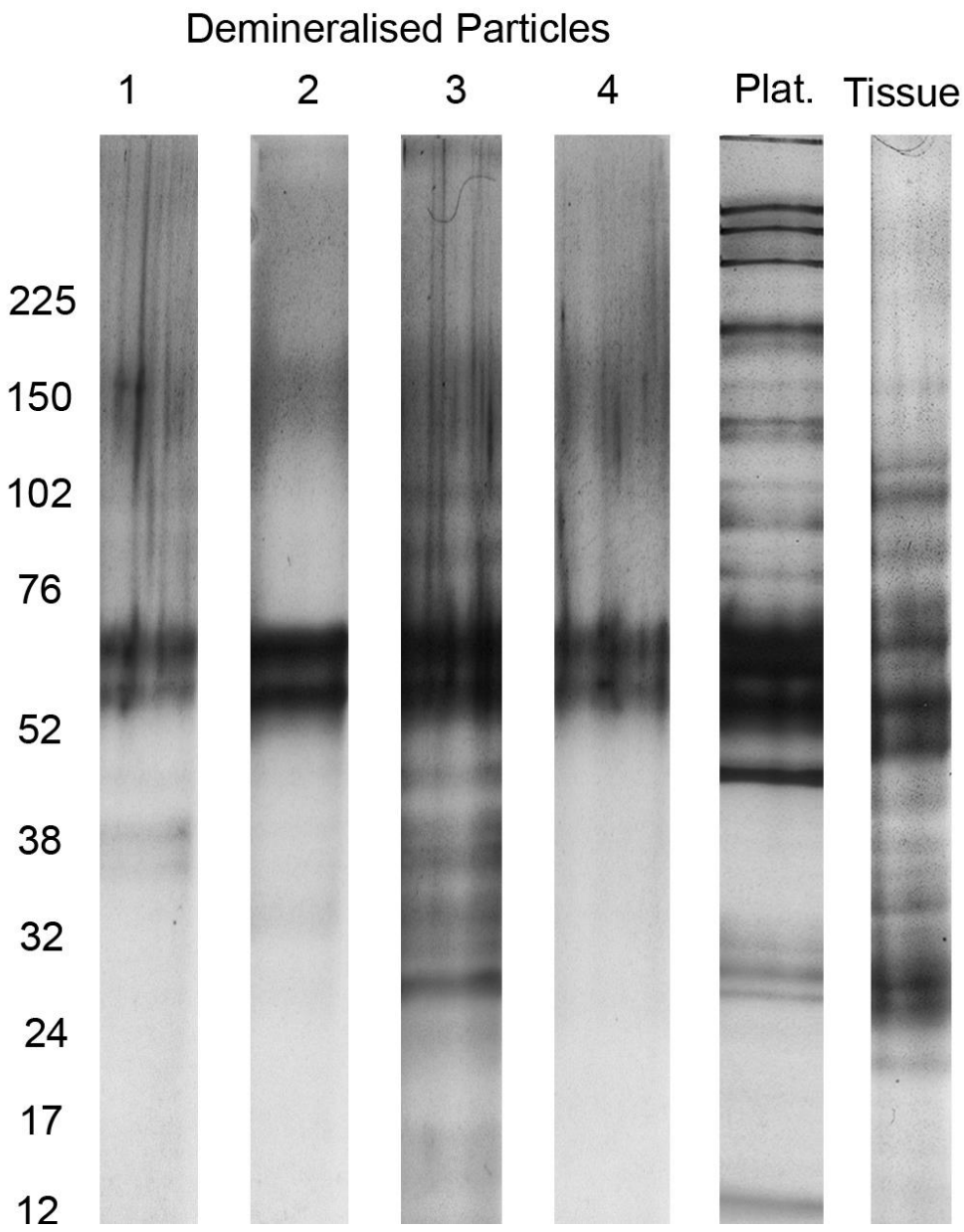

Figure 4.5: Silver stained SDS PAGE gel of demineralized whitlockite nanoparticles of four different patients, whole platelet, and tissue lysate showing the protein bands observed.

Nevertheless, following the extraction of proteins, work towards the evaluation of the presence of platelet markers in the whitlockite nanoparticle solutions was carried out. Both western blot and dot blot were considered. All markers (serotonin

transporter, integrin GPIIb (CD41), p-selectin (CD62P), CD63, and serotonin) identified were used for the control experiments.

The specificity of the staining was initially tested through positive controls using platelet lysates. Positive staining was observed for the CD41 (Figure 4.6 (a)) and the serotonin transporter (Figure 4.6 (b)) antibodies. Some staining was observed for the CD62P (Figure 4.6 (c)); however, this was very faint. High background was observed for the CD63 (Figure 4.6 (d)) antibody, which suggested unspecific binding of the primary antibody to the nitrocellulose membrane. Some staining was also observed in the serotonin antibody (Figure 4.6 (e)), which was also confirmed by the use of pure serotonin as a control (Figure 4.6 (f)). However, these results were not consistent; therefore, it was concluded that the antibody staining was not specific. The specificity of the secondary antibody staining observed was confirmed through the omission of the primary antibody (Figure 4.6 (g)), where no staining was observed indicating no unspecific attachment of the secondary antibody to the nitrocellulose membrane or the lysates. In addition, a collagen antibody was used as a negative control to ensure that the primary antibody binding to the lysates was not due to sample impurities (Figure 4.6 (h)). This was compared through the use of pure collagen as a sample (Figure 4.6 (i)). The results indicated as expected no collagen staining of the platelet lysates (Figure 4.6 (h)).

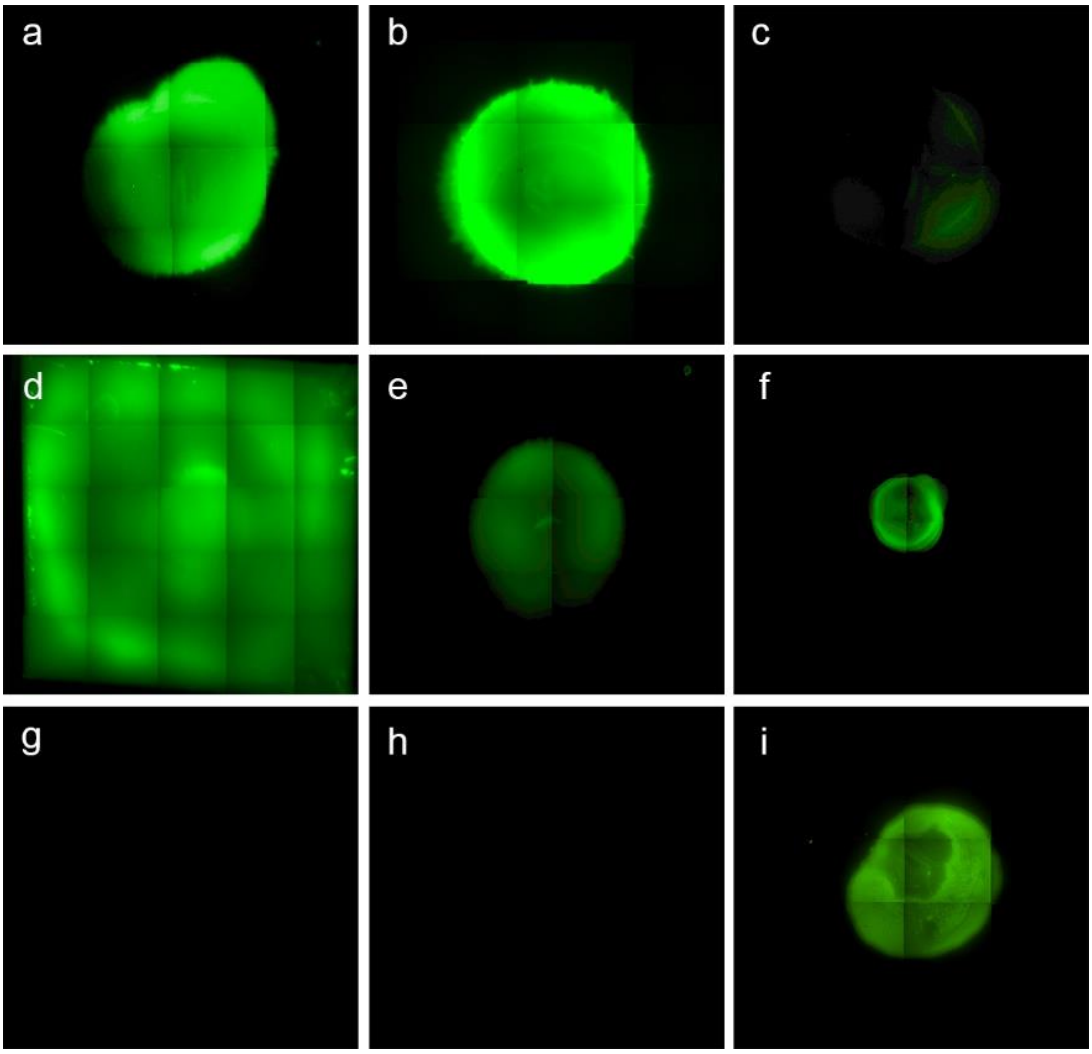

Figure 4.6: Representative dot blot of platelet lysate results. *Platelet lysates were stained for* ***(a)*** *CD41* ***(b)*** *serotonin transporter* ***(c)*** *CD62P* ***(d)*** *CD63 and* ***(e)*** *serotonin.* ***(f)*** *Positive control for the anti-serotonin antibody was carried out using pure serotonin.* ***(g)*** *Secondary antibody controls were carried out where the primary antibodies were omitted, showed no staining.* ***(h)*** *The platelet lysate was also stained using a collagen antibody to ensure that the staining observed was not due to impurities present in the lysates.* ***(i)*** *Positive control for the collagen antibody was also carried out using a sample of pure collagen.*

The specificity of the antibodies was also tested against increasing protein concentrations of the platelet lysates. As expected imaging of the dot blots using the same microscope settings, indicated an increase in the signal with increasing protein concentrations (Figure 4.7). Based on the results, it was concluded that the best markers to evaluate the association of the whitlockite nanoparticles to platelets was through the use of CD41 and serotonin transporter.

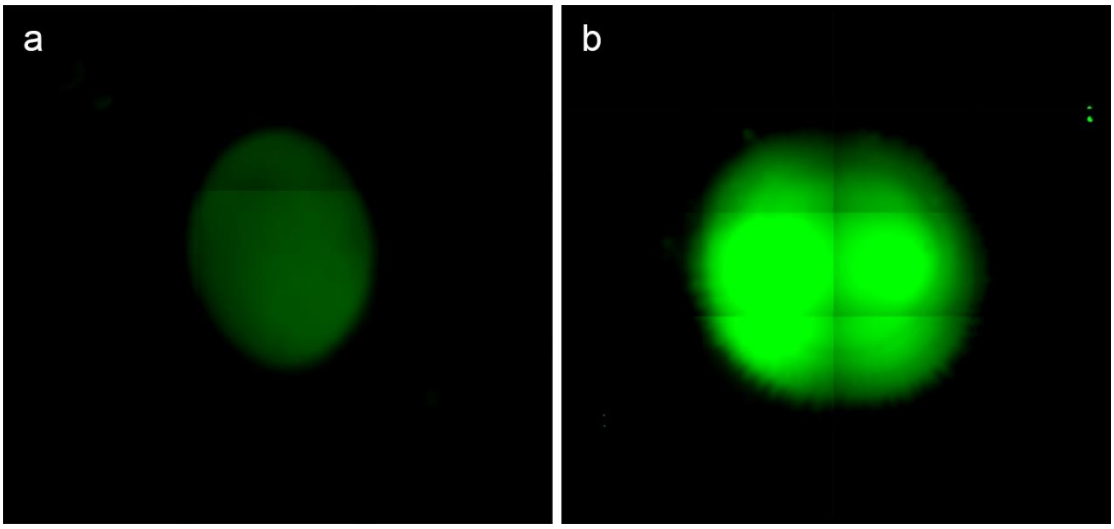

Figure 4.7: Representative dot blot of platelet lysate stained using an anti CD41 antibody. (a) *Low staining intensity was observed after one drop of 2 µl of sample was deposited on the nitrocellulose membrane.* ***(b)*** *Higher staining intensity was observed after the use of 5 drops of 2 µl of sample deposited on the same spot on the nitrocellulose membrane.*

Positive staining for both CD41 and serotonin transporter was observed in the proteins extracted from the whitlockite nanoparticles (Figure 4.8). As expected, a higher intensity fluorescence signal was observed in the platelet lysate (Figure 4.8); however, comparing to the secondary antibody controls both samples showed some amount of staining. Interestingly, not all five nanoparticle samples (isolated from five different patients) presented some staining for the two markers. There was positive staining observed in four out of the five nanoparticle samples for CD41, while only two samples had positive staining for the serotonin transporter. The measurements were repeated several times, indicating the same results.

Furthermore, the fact that not all nanoparticle samples stained for the platelet markers, was indicative of a signal specificity, as all samples were prepared in the same way. Therefore, it is unlikely that the staining was a result of the sample preparation or unspecific staining due to the presence of small crystals, not completely dissolved in the demineralisation processes. A collagen antibody was also used as a control for sample impurities; such as tissue pieces present in the lysates, however, no collagen staining was observed, indicating that no tissue fragments were present but also that the particles did not contain any collagen (Figure 4.8).

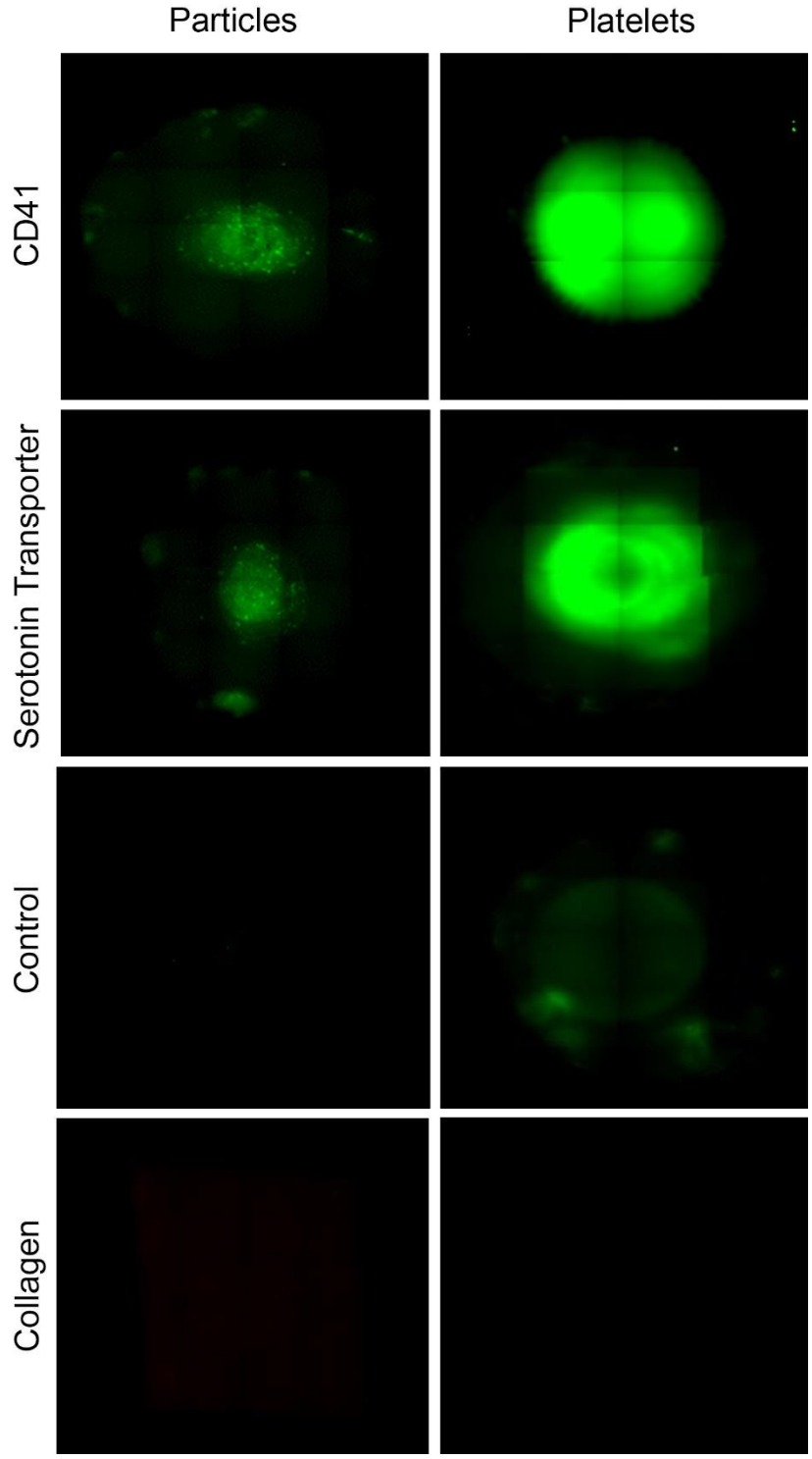

Figure 4.8: Dot blot of whitlockite nanoparticles and platelet lysates*. Positive staining was observed for CD41 and serotonin transporter antibodies. Controls omitting the primary antibodies indicated no staining. Both lysates were also stained for collagen where no staining was observed.*

Even though these results suggested a relation between the whitlockite nanoparticles and platelets, both the SDS PAGE and the dot blot experiments depend on the successful and complete isolation of the particles. Unfortunately, it could not be determined whether the proteins observed in the particle solutions were solely originating from the whitlockite nanoparticles, while similarly it could not be determined if the tissue did not contain any proteins from the precursors. Additionally, even though the majority of the minerals observed in these tissues were found to be whitlockite nanoparticles, it cannot be excluded that other minerals were also observed, which subsequently would lead to the presence of proteins not necessarily associated with the nanoparticles. As a result, it was concluded that a more direct method is needed to ensure the specificity of the staining.

4.3.2.2.2 Immunofluorescence staining

Therefore, to test if the antibody staining was indeed related to the whitlockite nanoparticles and not a result of tissue proteins or unspecific staining, immunofluorescence staining on aortic tissue histological slides obtained from the same five patients was carried out. For this, anti CD41 and serotonin transporter antibodies were used along with DAPI stain for cell nuclei and OsteoSense stain for mineral visualization. The results indicated a co-occurrence of the OsteoSense and CD41 staining widespread over the samples (Figure 4.9, 4.10). On the other hand, the co-occurrence of serotonin transporter with OsteoSense was less frequent (Figure 4.11, 4.12).

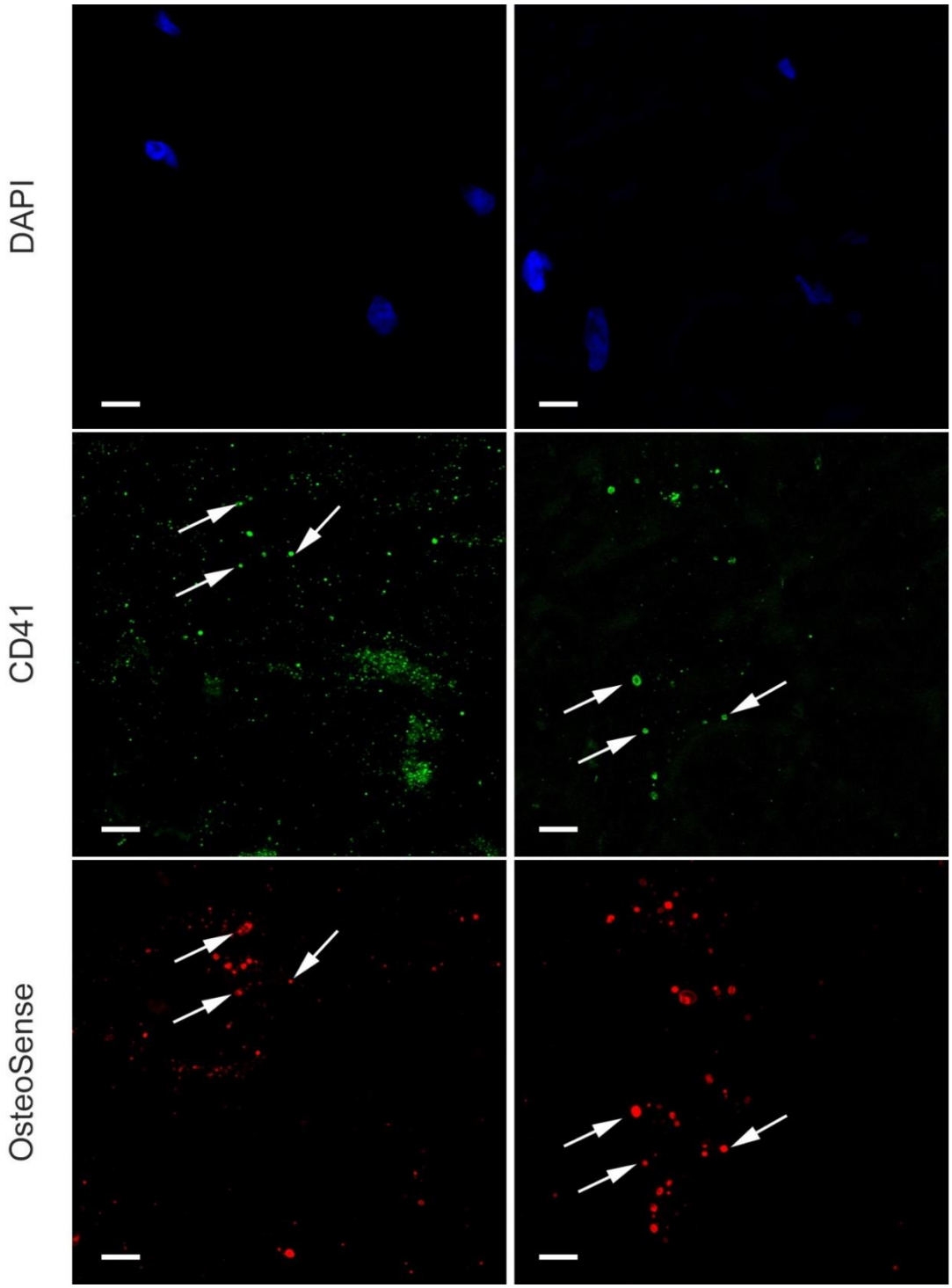

Figure 4.9: Fluorescence images of aortic tissue showing individual channels: DAPI (blue), CD41 (green), and OsteoSense (red). *Scale bars = 5 µm.*

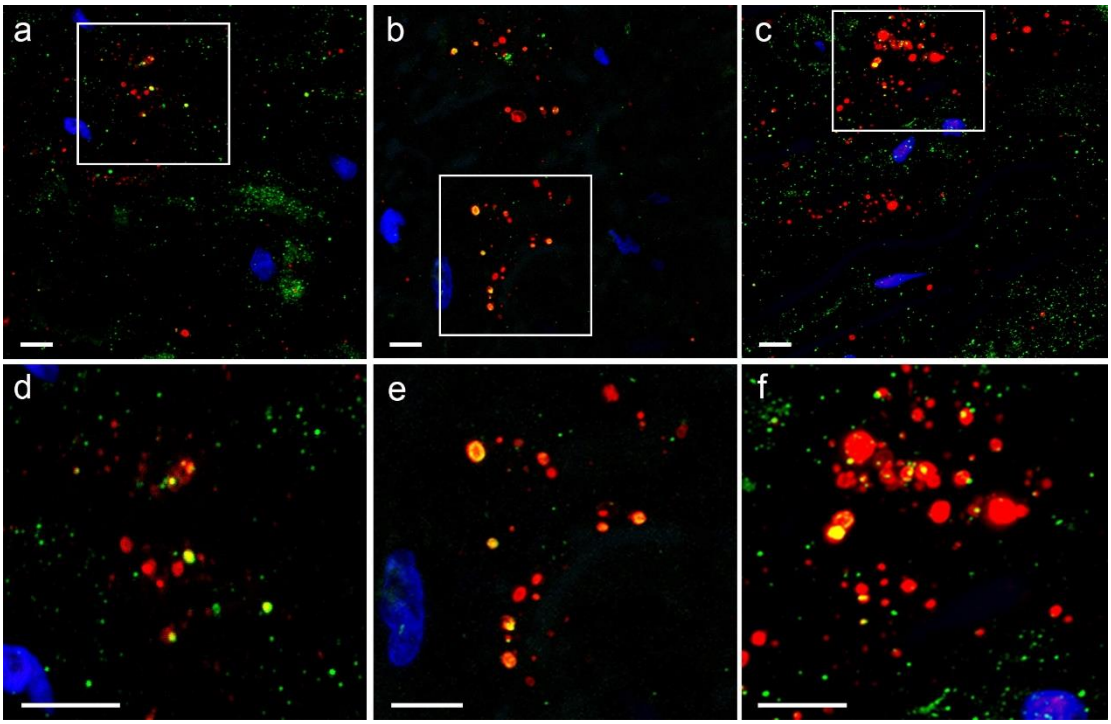

Figure 4.10: Fluorescence images of aortic tissue showing DAPI (blue), CD41 (green), and OsteoSense (red). (a), (b), (c) *Low magnification images and* ***(d), (e), (f)*** *high magnification images showing the regions indicated with white rectangles in* ***a, b*** *and* ***c*** *respectively. A resulting yellow colour indicated co-occurrence of OsteoSense and CD41 staining. Scale bars = 5 µm.*

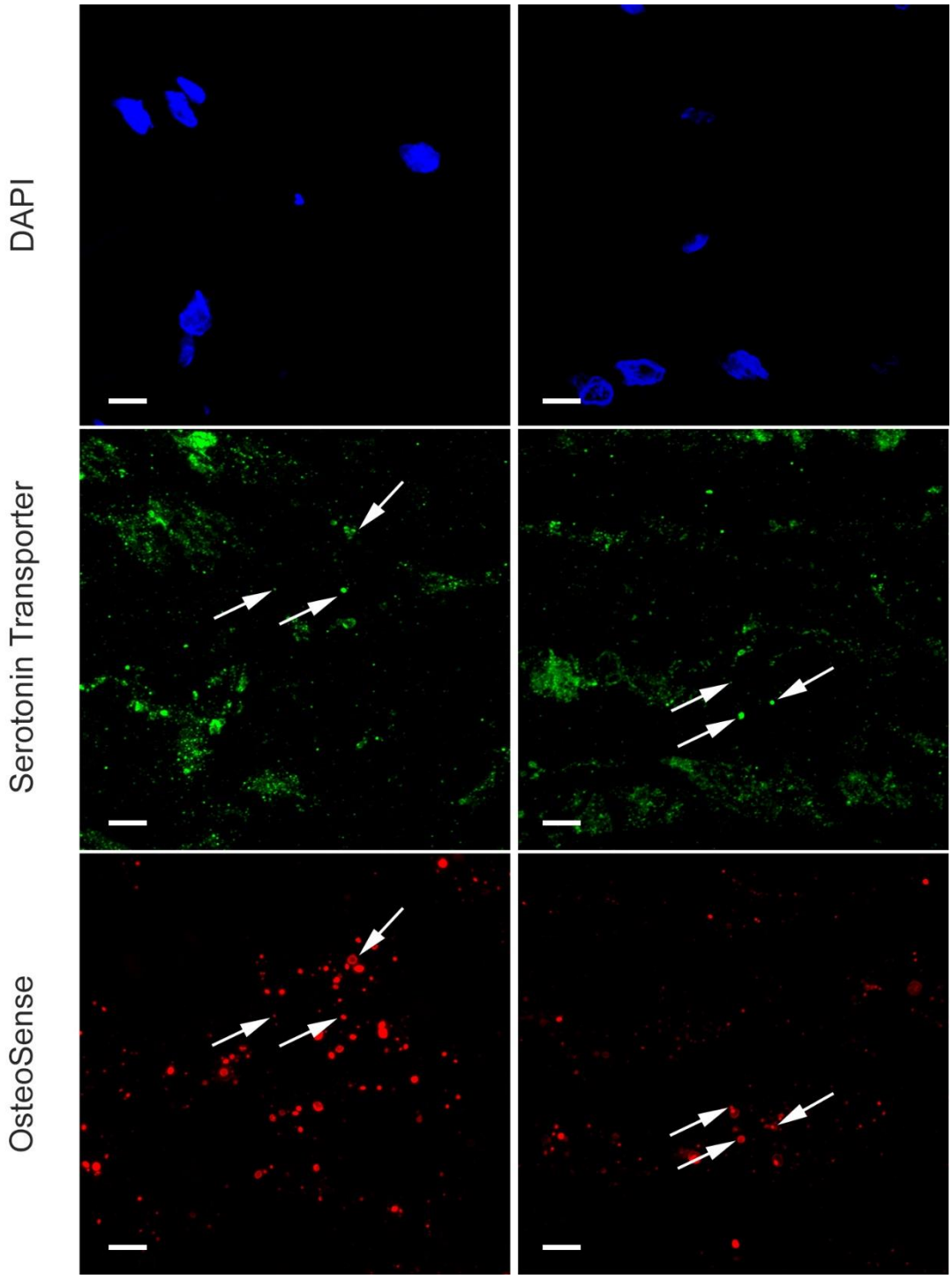

Figure 4.11: Fluorescence images of aortic tissue showing individual channels: DAPI (blue), serotonin transporter (green), and OsteoSense (red). *Scale bars = 5 µm.*

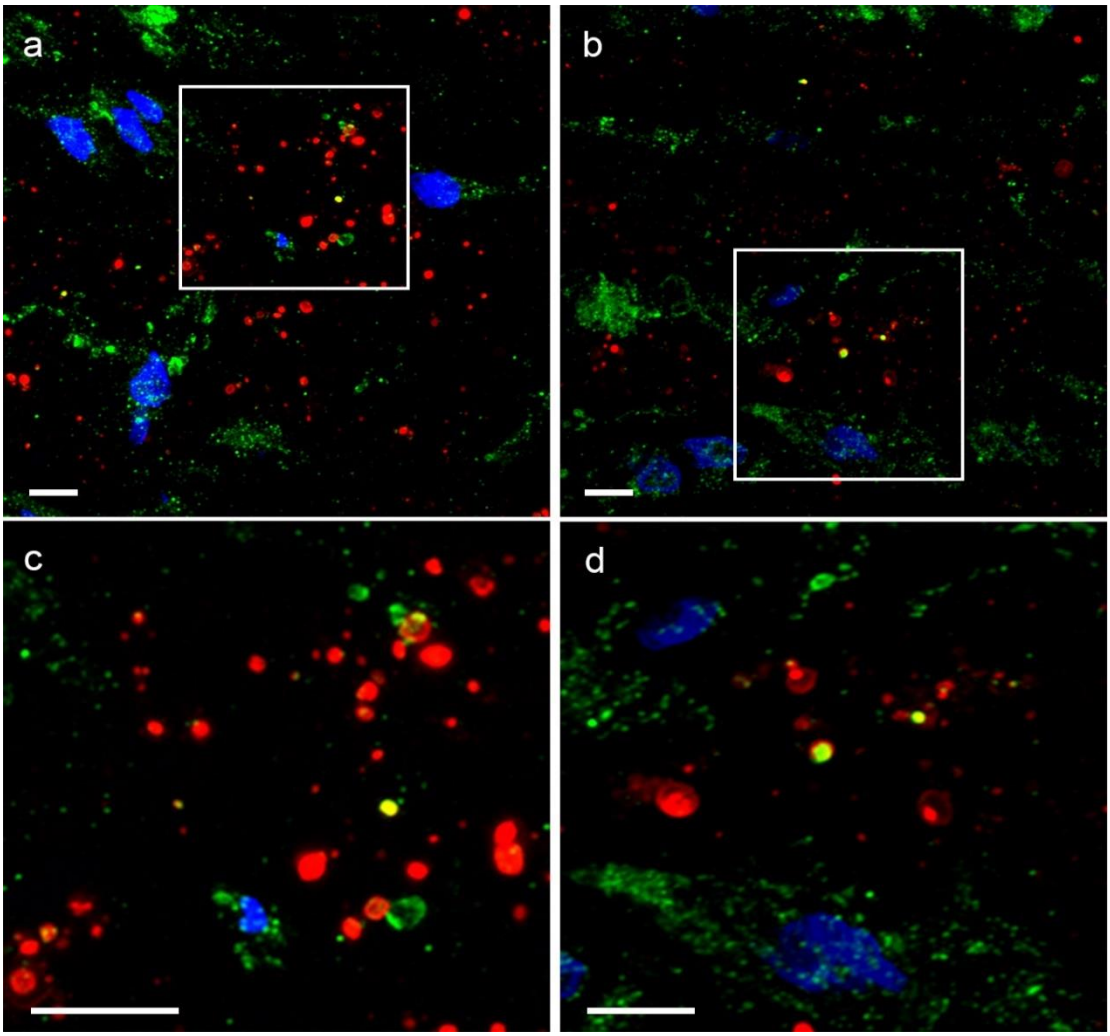

Figure 4.12: Fluorescence images of aortic tissue showing DAPI (blue), serotonin transporter (green), and OsteoSense (red). (a) *and* ***(b)*** *Low magnification images and* ***(c)*** *and* ***(d)*** *high magnification images showing the regions indicated with white rectangles in* ***a*** *and* ***b*** *respectively****.*** *A resulting yellow colour indicated co-occurrence of the OsteoSense and serotonin transporter staining. Scale bars = 5 µm.*

To further investigate whether the staining was specific to the organic material encapsulated within the nanoparticles, the experiment was repeated following a short demineralisation with 0.5 M EDTA. The EDTA was applied for 30 minutes and was followed by the standard immunofluorescence procedure. It was then examined whether the degree of co-localisation between the OsteoSense staining and CD41 or serotonin transporter antibodies would change as a result of slight mineral dissolution, which would lead to more organic material being exposed. Three samples with and three without demineralization from three different patients were used. The results indicated a slight increase in the degree of co-localisation between the antibody staining and the OsteoSense signal (Figure 4.13).

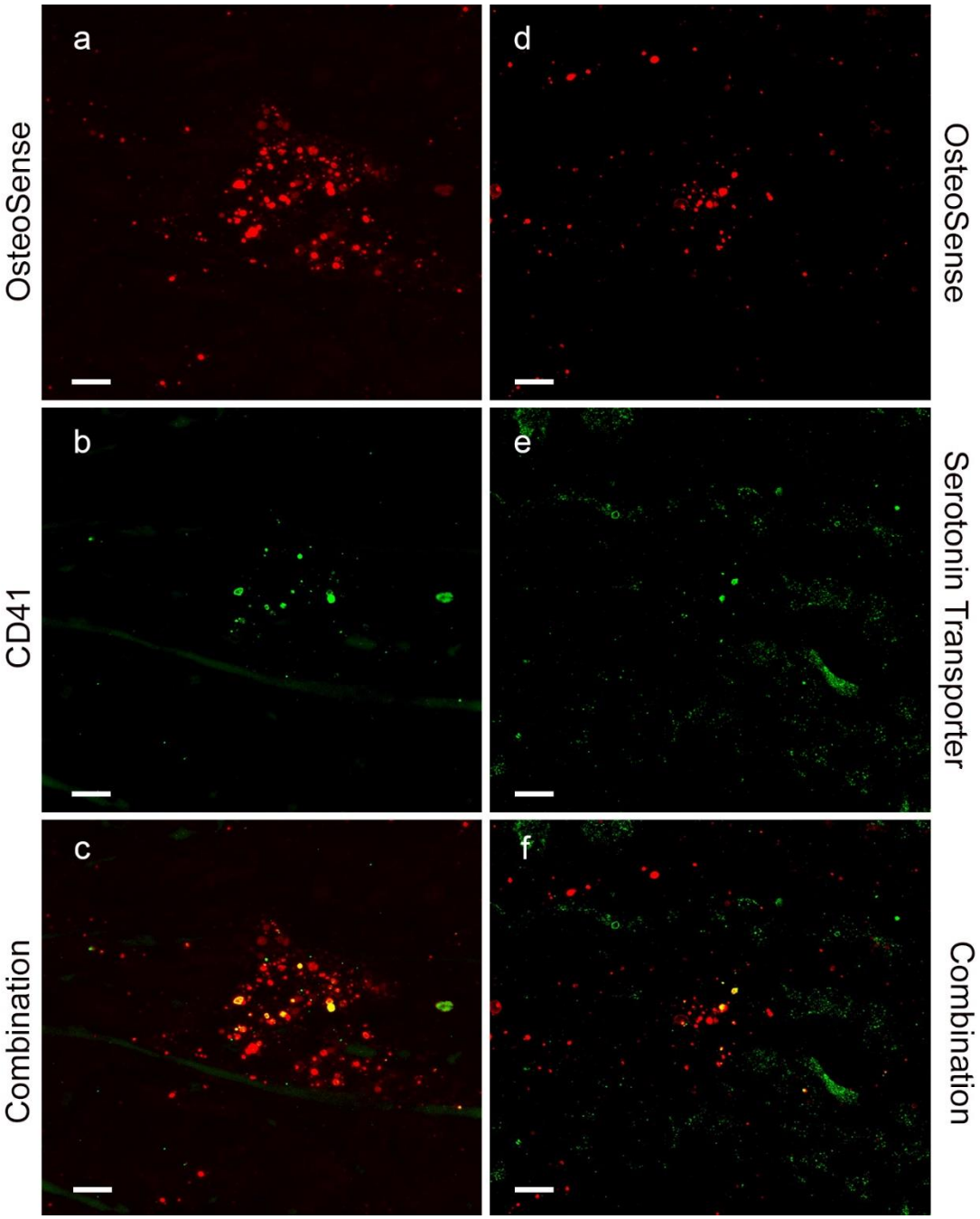

Figure 4.13: Co-localisation of CD41 and serotonin transporter staining with OsteoSense after EDTA treatment. (a) *Fluorescence image of sample following EDTA treatment stained with OsteoSense (red).* ***(b)*** *Fluorescence image of sample following EDTA treatment stained with CD41 (green).* ***(c)*** *Fluorescence image of sample following EDTA treatment where the overlapping of the two is indicated by yellow.* ***(d)*** *Fluorescence image of sample following EDTA treatment stained with OsteoSense (red).* ***(e)*** *Fluorescence image of sample following EDTA treatment stained with serotonin transporter (green).* ***(f)*** *Fluorescence image of sample following EDTA treatment where the overlapping of the two is indicated by yellow. Scale bars = 5 µm.*

Specifically for CD41, without EDTA treatment, 31 ± 15 % of the OsteoSense staining was overlapping with the CD41 staining. On the other hand, following the EDTA treatment, it was found that 41 ± 14 % % of the OsteoSense was overlapping with the CD41 staining however this increase was not found to be significantly different (Figure 4.14 (a)). The co-localisaiton of the serotonin transporter staining and the calcification also had a substantial increase in the EDTA treated samples (Figure 4.14 (b)). Without the EDTA treatment, only 8 ± 11% of the OsteoSense was co-localizing with serotonin transporter staining, while after the EDTA treatment, 37 ± 23% of the OsteoSense staining was overlapping. This difference was found to be statistically significant with a p-value smaller than 0.0001, indicating that the increase in the co-occurrence was a result of the demineralisation.

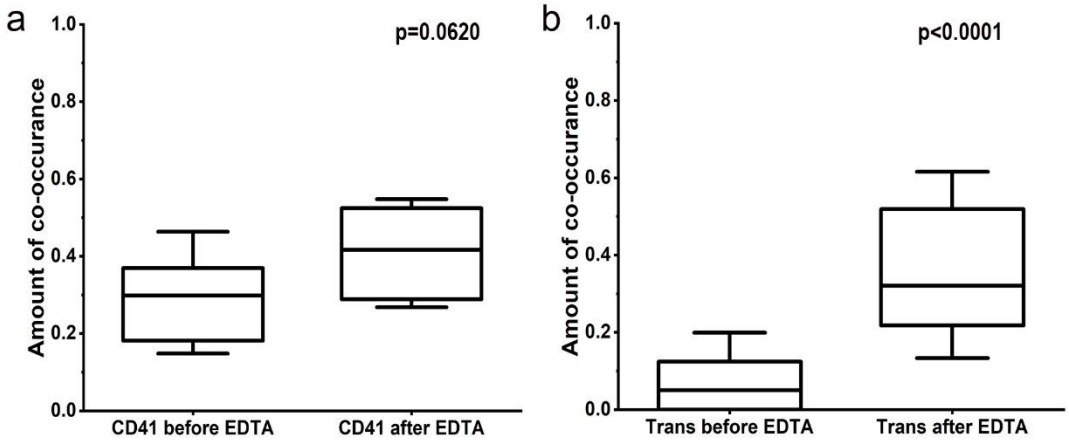

Figure 4.14: Co-localisation of CD41 and serotonin transporter staining with OsteoSense after EDTA treatment. (a) *Statistical analysis of the level of overlapping between the OsteoSense and CD41 with and without EDTA treatment (n = 15). p = 0.0620.* ***(b)*** *Statistical analysis of the level of overlapping between the OsteoSense and serotonin transporter with and without EDTA treatment (n =15). p < 0.0001.*

Moreover, staining using collagen and alpha smooth muscle actin to evaluate the relationship of collagen (Figure 4.15) and vascular smooth muscle cells (Figure 4.15) with the whitlockite nanoparticles was carried out. The use of these markers also acted as a control, to ensure the antibodies were not attaching to the mineral through an unspecific process but rather to the organic material encapsulated in it or surrounding it. A meagre amount of co-occurrence between the collagen (Figure 4.16 (a,c)) and the whitlockite nanoparticles was observed even though the vast presence of collagen fibres had been reported previously in cardiovascular calcification (132). In contrast to those results, most of the nanoparticles were found in spaces where no collagen staining was observed, suggesting a non-osteogenic process could be responsible for their formation; as the bone mineral is strongly associated with the presence of collagen

fibres (380, 381). This observation could also suggest that the particles originate from possibly platelet vesicles getting trapped in these gaps prior to mineralisation. The co-occurrence of alpha smooth muscle actin and OsteoSense (Figure 4.16 (b, d)) was also rarely observed. Similarly to collagen, this indicated that the whitlockite nanoparticles do not originate from vascular smooth cell extracellular vesicles (382) or at least not from their physiological phenotype (120).

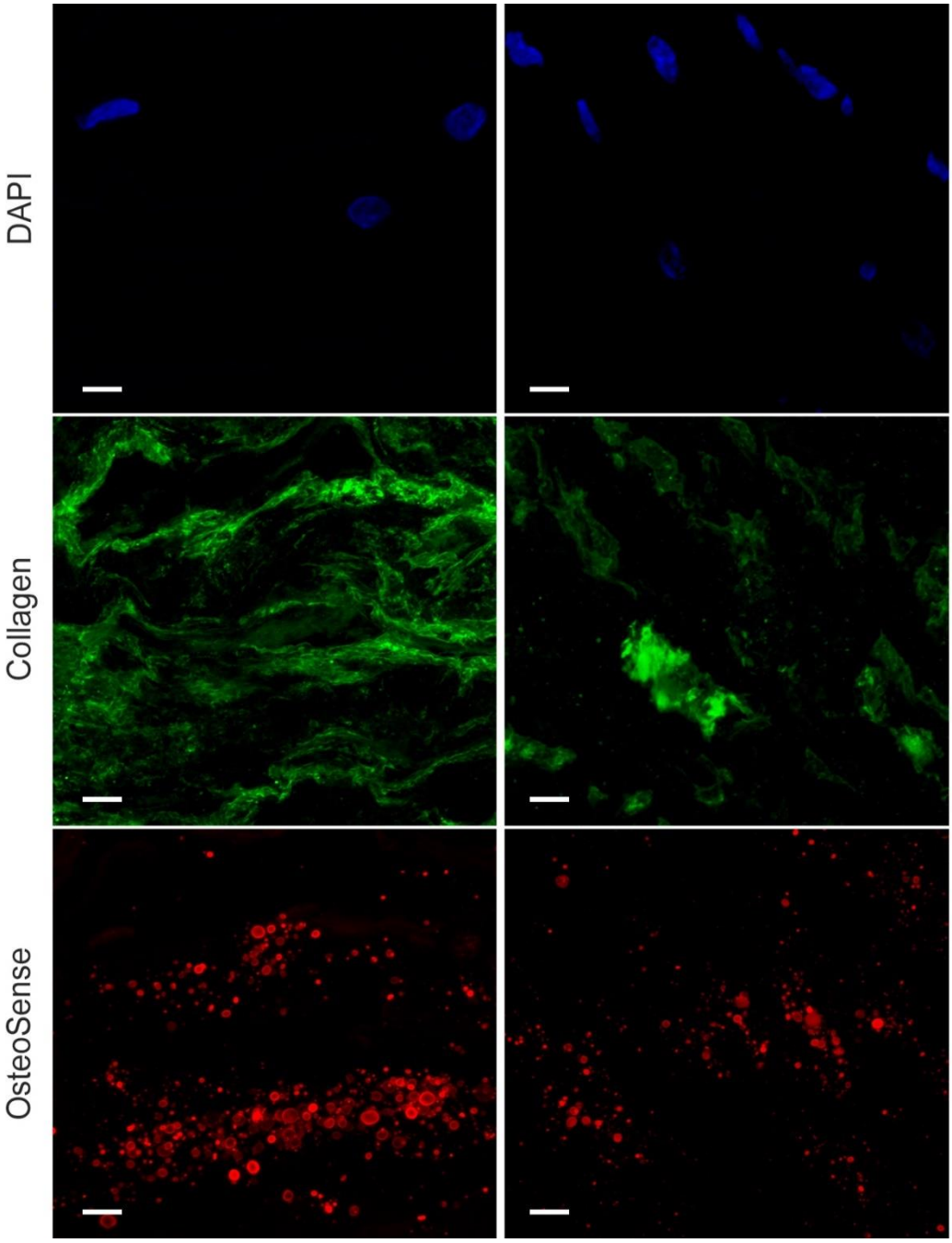

Figure 4.15: Fluorescence images of aortic tissue showing individual channels: DAPI (blue), collagen/alpha smooth muscle actin (green), and OsteoSense (red). *Scale bars = 5 µm.*

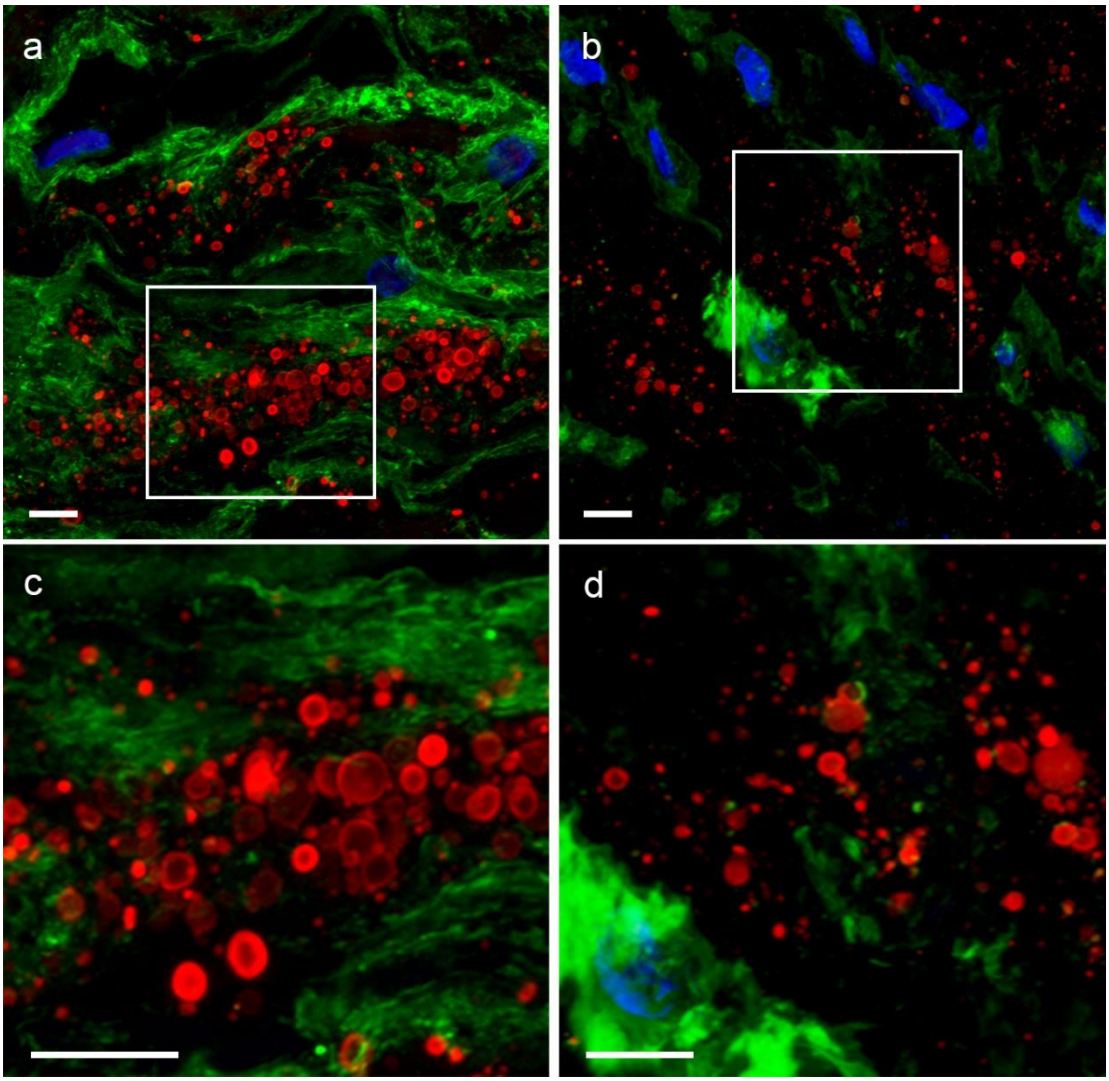

Figure 4.16: Fluorescence images of aortic tissue showing DAPI (blue), collagen or alpha smooth muscle actin (green), and OsteoSense (red). (a) *Low magnification image of DAPI, collagen, and OsteoSense staining and* ***(b)*** *Low magnification image of DAPI, alpha smooth muscle actin, and OsteoSense****. (c)*** *and* ***(d)*** *high magnification images showing the regions indicated with white rectangles in* ***a*** *and* ***b*** *respectively****.*** *A resulting yellow colour indicated co-occurrence of the OsteoSense and collagen/ alpha smooth muscle actin staining. Scale bars = 5 µm.*

4.3.2.3 Role of platelet dense granules

Based on the results, it was concluded that platelets indeed are directly correlated to the whitlockite nanoparticles. However, as the whitlockite nanoparticles express CD41 and serotonin transporter, markers found in several platelet vesicles and products, it was not possible to identify which of these are responsible for their formation. Subsequently, more work needs to be done to identify specific platelet products that could play a role in the process or be the precursors of nanoparticles. Through the evaluation of platelets, we although propose that platelet dense granules could be the origin of the whitlockite nanoparticles.

Dense granules were named dense due to their opaque appearance on TEM images (383) (Figure 4.17 (a)) as a result of their contents (384). In detail they contain; serotonin, histamine, adenosine diphosphate (ADP), adenosine triphosphate (ATP) (353), ionic calcium, ionic magnesium, and potassium, inorganic polyphosphate (384, 385). Therefore, from a chemical perspective, due to their high contents of calcium, magnesium, and phosphates (Figure 4.17 (b)), they may act as mineral nucleation sides. Moreover, other than their elemental similarities, dense granules as vesicles also have a similar shape (spherical) (Figure 4.17) to the whitlockite nanoparticles, which could also suggest that they are their precursors. Additionally, an analysis of 600 dense granules and 1300 whitlockite nanoparticles indicated similarities in the diameter range of the two entities. Dense granules were found to have a shorter size range ranging from 38 nm to 436 nm (average value of 163 nm, standard deviation ± 62.9 nm) while the whitlockite nanoparticles are ranging from 41 nm to 2415 nm (average value of 459 nm, standard deviation ± 314.6 nm) (Figure 4.18). The whitlockite nanoparticles were however found to have a longer tail than the size distribution of dense granules which could be a result of crystal growth over time (386).

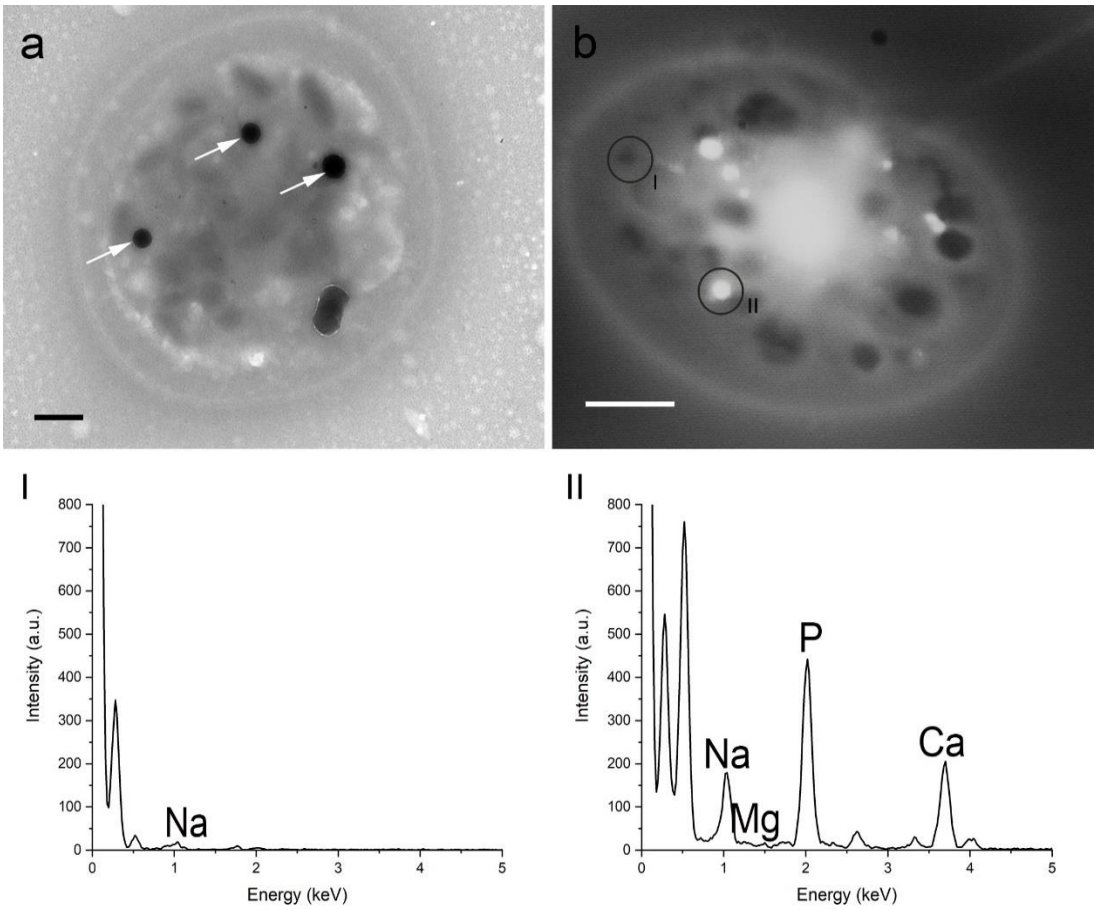

Figure 4.17: Electron microscopy analysis of dense granules in platelets. (a) *TEM micrograph of a platelet with dense granules appearing as black (white arrows). Scale bar = 500 nm.* ***(b)*** *Scanning transmission electron dark-field micrograph of platelets where less dense material is indicated as darker and dense features (dense granules) as white along with* ***(I)*** *an EDS spectrum of a darker area far away from the dense granules and* ***(II)*** *an EDS spectrum of a dense granule indicating calcium, phosphorus and a small peak of magnesium. Scale bar = 1 µm.*

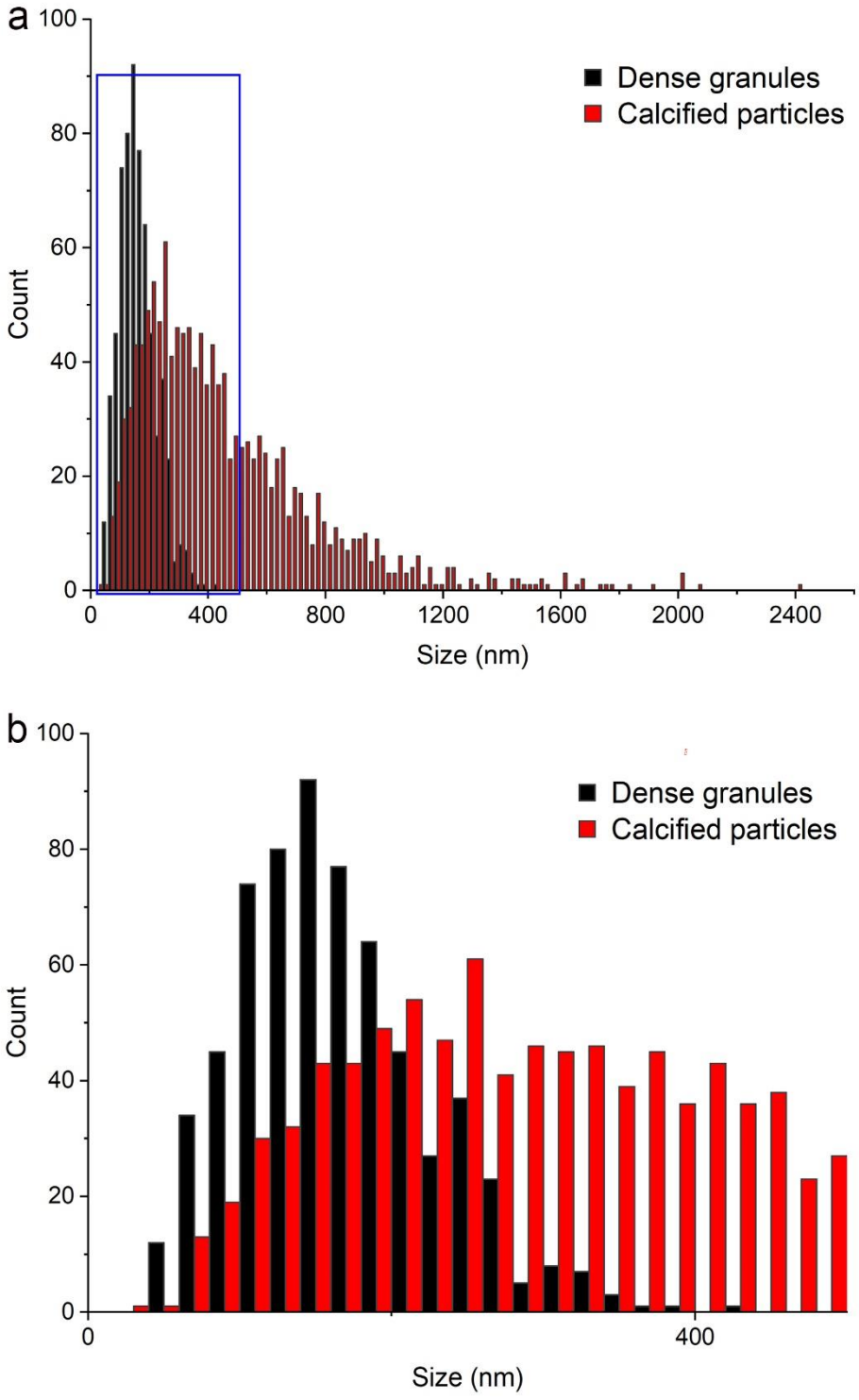

Figure 4.18: Size distribution graphs for the platelet dense granules and the whitlockite nanoparticles. (a) *Full range size distribution of the dense granules indicated with black and the whitlockite particles indicated with red.* ***(b)*** *Higher magnification of the part indicated with a blue rectangle in a showing the size distribution of the dense granules in black and the whitlockite particles in red. The smaller dense granule and particle had a diameter of 41 nm and 38 nm respectively.*

Taking into account the results confirming the presence of CD41 and serotonin transporter molecules in the whitlockite nanoparticles and comparing that with proteomics analysis of dense granules found in the literature, it was found that they widely express CD41 (356). However, the serotonin transporter molecule tested in this work is not directly present on dense granules in resting platelets but rather on the surface of the platelet cytoskeleton (373). Interestingly though the molecule gets internalized during platelet activation (373) thus, it could be found in a range of platelet compartments. Therefore, the association of the molecule to the whitlockite nanoparticles could be due to the presence of platelet cytoskeleton fragments and proteins, or due to molecules getting captured during granule release and mineralization. For example, the CD41 receptor and other proteins observed in dense granules have been found to interact directly with the serotonin transporter molecule during platelet activation (376).

Further work needs to be carried out to support such claims, involving both the testing of other markers such as the vesicular monoamine transporter 2 and histamine, which are also found in the dense granules. More importantly, though the ability of dense granules to mineralize needs to be investigated. For such purposes, it was attempted to isolate dense granules. However, the results indicated that complete isolation was not achieved in any of the experiments carried out. TEM imaging of all fractions obtained, indicated structures resembling dense granules (Figure 4.19 (a)), although, other platelet fragments and components were also present (Figure 4.19 (b)). In addition, TEM-EDS analysis of the same fractions revealed that even though phosphorus was present in the structures resembling dense granules, no calcium was detected. An observation that indicated possible structural alterations during sample preparation.

To evaluate the presence of proteins, SDS PAGE of the dense granule fraction was also carried out (Figure 4.19 (c)). The resulting bands were compared to SDS PAGE results already reported in the literature (387, 388). A protein band at around ~225 kDa corresponding to a fragment of talin, transgelin, or to myosin (all of which are cytoskeletal proteins), observed in both platelets and dense granules (356, 389-392) was observed. The ~200 kDa was also thought to be corresponding to a myosin subunit (393). Furthermore, the protein band at ~114 kDa was possibly corresponding to the heavy chain of the membrane protein integrin glycoprotein IIb (356, 394), the ~87 kDa band to p-selectin (a platelet activation marker) (356, 361), and a band close to ~62 kDa to glycoprotein VI (also a membrane protein) (395) or the serotonin transporter molecule (~67 kDa) (396). The ~62 kDa could also, however, be corresponding to serum albumin (the most abundant protein in the blood) that has an expected molecular weight of ~66 kDa (356, 397). Finally, the band observed at ~45 kDa was thought to be corresponding to the platelet vasodilator stimulate phosphoprotein (398)

due to its high expression in platelets. Despite, proteins such as the lysosome-associated membrane glycoproteins (LAMP1 and LAMP 2 with expected molecular weights 120 kDa and 40 kDa respectively) and CD63 (molecular weight expected at 25 kDa) which have been widely used for the identification of platelet granules were not observed (356, 361, 377, 399). A faint protein band at ~52 kDa was however detected which might be corresponding to CD63 (400).

Taken together, it was inconclusive whether these fractions corresponded to dense granules as most of the protein bands observed are also present in other parts of platelets (356, 361). Therefore, the observed bands could also be a result of platelet cytoskeletal and membrane fragments observed in the TEM images. As a result, it was concluded that these fractions could not be used for reliable comparison analysis and that more experimental work is needed to examine the relation between platelet dense granules and the whitlockite nanoparticles.

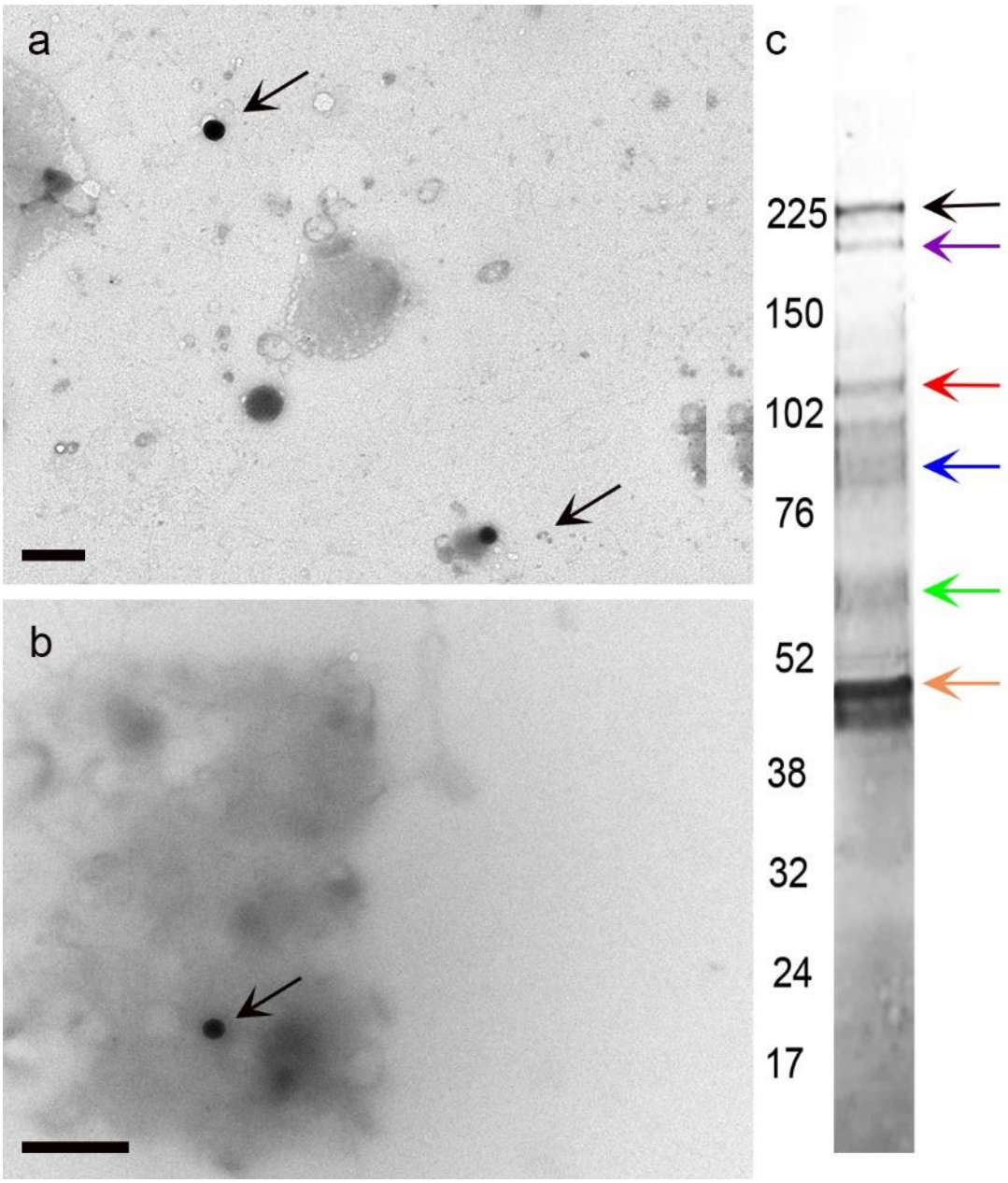

Figure 4.19: TEM micrographs of platelet dense granule fraction and corresponding results of SDS PAGE. (a) *TEM micrograph of isolated dense granules (arrows) where other organic material can also be observed.* ***(b)*** *TEM micrograph of a dense granule (arrow) attached to part of a platelet. Scale bars = 5 µm.* ***(c)*** *Silver stained SDS PAGE gel showing the main protein bands at 225 kDa (black arrow), 200 kDa (purple arrow), 114 kDa (red arrow), 87 kDa (blue arrow), 66 kDa (green arrow), 45 kDa (orange arrow), observed in the dense granule fraction.*

4.4 Conclusions and future work

The results of this work indicate a new possible mechanism of formation for the whitlockite nanoparticles observed in cardiovascular calcification, directly involving platelets, while their shape and size suggest a mechanism involving possibly a platelet vesicle. Based on the chemical composition of the particles, it is also proposed that platelet dense granules are acting as mineral nucleation sides for their formation due to the high amounts of phosphate, calcium, and magnesium they contain. Furthermore, as no mineralized particles were found in the blood of diseased or healthy volunteers, it was concluded unlikely that the mineralisation process initiates in the bloodstream but rather, that it is taking place within the vascular wall following platelet activation and aggregation due to stimulus.

More research needs to be done; however, for the role of platelet dense granules to be established. As they do not present any specific markers, further *in vitro* work needs to be done to understand whether they can be released and stay intact to penetrate through the vascular endothelial and other cells prior they mineralize. A number of microvesicles and microparticles are released upon platelet activation, many of which have been reported to express platelet granule's markers (354), and were found to circulate in the blood; however, no study has to date showed the presence of free dense granules neither in the bloodstream nor within vascular cells.

Additional work also needs to be done to understand the complete proteome analysis of the whitlockite nanoparticles. This can be obtained through a full proteomics analysis of the nanoparticles and the tissue using mass spectroscopy through in-gel digestion. Such profiling opens a new pathway of a direct study of cardiovascular and other minerals as a full proteomics profiling of the isolated nanoparticles (and also the other minerals observed) will also allow the direct investigation of the presence or absence of markers such as: the matrix metalloproteinase, the extracellular matrix metalloproteinase inducer (401-403), bone (336) (bone morphogenic protein, matrix gla protein, and osteonectin, alkaline phosphatase protein, runt-related transcription factor 2 and osteopontin (132, 336, 357)) and macrophage markers (120, 131, 404), all of which have been associated to the presence of cardiovascular calcification. Despite, even though proteomics analysis will allow the examination of the presence of other proteins, immunofluorescence staining using the identified markers should also be employed to examine which markers are directly related to the nanoparticles.

Other than that, probably most importantly, the mineralizing ability of platelets and dense granules should also be evaluated *in vitro*. An ongoing study is carried out to evaluate whether the formation of whitlockite nanoparticles can be observed in an artificial environment mimicking the arterial wall. A collagen hydrogel containing

platelets, isolated dense granules, and platelet-poor plasma (as a control) was immersed in simulated body fluid to examine whether the formation of minerals is possible. As expected, no whitlockite particles were observed in the platelet-poor plasma samples, but some whitlockite nanoparticles were found in the platelet samples. No such particles were observed in the dense granule samples; however, this was concluded to be due to the loss of their calcium contents during isolation mentioned earlier. This preliminary result suggested further that platelets can take part in a mineralization process, although again a direct correlation to platelet dense granules could not be made. Moreover, the physicochemical characterisation of these 'synthetic' particles is needed to confirm that they share the same internal structure and crystallinity with the whitlockite nanoparticles observed *in vivo.* Additionally, protein isolation from these nanoparticles could also allow the comparison between their protein contents to those found *in vivo.* Using the same model, it is also possible to investigate the role of dense granules through the use of staining methods. For example, dense granules can be stained using DAPI (384) or mepacrine (405) within the hydrogel, while the presence of the mineral particles can be confirmed through OsteoSense staining. Subsequently, a decrease in the dense granule staining accompanied by an increase in the OsteoSense staining would hint that dense granule can indeed mineralize.

Further down the line, *in vitro* cell cultures can also be employed to understand the effect of these particles on vascular and valvular cells, their role in the development of other types of calcification and the associated diseases. Comprehending the mineralization mechanisms and the impact of the minerals to the surrounding cells could also lead to the development of new treatment methods to prevent the progression of many calcific cardiovascular diseases. Blood thinners such as aspirin have been for many years, known as a prevention method for atherosclerosis (406), which reduce the activation and aggregation of platelets and subsequently can lead to excess bleeding and death. This work shows the direct relationship of platelets with cardiovascular calcification which explains the benefits of aspirin; therefore, understanding in further detail the mechanism of formation of the whitlockite nanoparticles will also allow the development of more suitable drugs.

Chapter 5: Breast mineralisation in breast cancer

5.1 Introduction

The association of minerals to cancer is so strong (407) that their presence in breast tissue is one of the fundamental features for the early diagnosis of breast cancer (176, 408-410). Breast screenings are widely used to examine for the presence of minerals or as more generally called, calcifications, which are in many cases, the only detectable sign of a developing tumour (411). Additionally, calcifications are not only used as an indication of disease (412) but also to guide breast biopsies, used for the confirmation of the presence of cancer (176, 413).

It has been found that breast calcifications can be present in all types of breast tumours, that been benign or malignant (408, 414-418) and are commonly presented clinically in two major calcification categories: macrocalcifications and microcalcifications (411, 419). Macrocalcifications are large minerals associated with fat necrosis or highly developed benign diseases such as fibroadenoma (420). On the other hand, microcalcifications are associated with both benign and malignant tumours (25, 411, 421, 422). As previously mentioned, despite the evident importance of breast calcifications, few are the works in the literature that provide some characterization of them (24, 184, 423, 424), with their detailed physicochemical characteristics and how these can be related to different microenvironments, types, and grades of tumours still being unclear. More importantly, it is unknown what these characteristics can tell us about biological mechanisms occurring in breast tumours.

In this work, two major questions are to be addressed; ***what are the exact physicochemical properties of the minerals observed in breast tissue*** and ***is there an association of any mineral property to breast malignancies.*** For these to be addressed, electron microscopy techniques were employed to identify the properties of breast tissue minerals at the nanoscale. Tissues of healthy donors and biopsies of benign and malignant tumours were analysed to distinguish any correlations between different minerals and the clinical information of the samples obtained. Other than examining ***the relation of specific mineral nano characteristics to breast malignancies in general, these will also be examined against malignant tumour type and grade.***

5.2 Materials and Methods

5.2.1 Tissue

Eighty-one samples were analysed (Table 5.1) in total. The samples were obtained from the Department of Surgery and Cancer at the Imperial Centre for Translational and Experimental Medicine (UK), Breast Cancer Now Tissue Bank (UK) and the Cantonal Hospital of St. Gallen (Switzerland). For sample collection, informed signed consent was obtained from the patient or next of kin, and the samples were processed, analysed and disposed of according to the ethical approval obtained.

Table 5.1: Diagnostic categorisation of samples.

Type of tissue	**Number of cases**
Healthy tissue	11
Fibroadenoma	14
Benign Phyllodes tumour	1
Fibrotic change and cysts	1
Fibroepithelial lesion	1
Benign complex sclerosing papillary lesion	1
Sclerosing adenosis	1
Hamartoma	1
Uncapsulated mass with slightly disorganised glands and pseudo angiomatous stromal hyperplasia favouring Hamartoma	1
Paget's disease	1
Borderline Phyllodes	1
Ductal Carcinoma in Situ (DCSI)	2
Invasive Ductal Carcinoma (IDC)	16
Invasive Cribriform Carcinoma (ICC)	7
Invasive Lobular Carcinoma (ILC)	8
Invasive carcinoma of unknown type	14

5.2.2 Histology

Histopathological slides of breast cancer biopsies were produced by the tissue biobanks using standard preparation procedures. The tissue was formalin-fixed and paraffin-embedded, and then cut into sections of 5 μm in thickness, using a microtome and mounted onto glass slides. Haematoxylin and Eosin (H&E) staining was carried

out if consecutive slides were available, which were scanned using a Leica SCN400 scanner and a VS120 Olympus microscope.

5.2.3 Scanning electron microscopy

For SEM analysis, the samples were prepared as detailed in c*hapter 3, section 3.3.4.2*. Samples were coated with silver conductive paint and with carbon, using a Quorum K975X coater before imaging. A Hitachi S-3499N, a Carl Zeiss Crossbeam, and a LEO were for SEM imaging, and Oxford Instruments energy-dispersive X-ray detectors integrated on the machines were used for elemental analysis. Voltage, current, aperture and working distance were adjusted for individual samples and microscope. All SEM analysis was carried out double-blinded to avoid bias.

5.2.4 Focused Ion Beam- Transmission electron microscopy

A FEI Helios NanoLab 600 DualBeam Focused Ion Beam System and Zeiss Auriga Cross Beam were used as described in c*hapter 3 section 3.4.3.2* for milling of the samples, which was carried out with the help of Dr Sergio Bertazzo. Focused ion Beam prepared sections were then analysed using a Joel 2100Plus at a voltage of 200kV and 120kV.

All TEM electron diffraction patterns were obtained with the help of Dr Ecaterina Ware (Imperial College London). Indexing was carried out as detailed in *chapter 4, section 4.2.5.*

5.2.5 Raman spectroscopy

The author of this work did not carry out the Raman spectroscopy measurements. All measurements were done in collaboration with the group of Professor Inge K. Hermann as a confirmation for the electron microscopy results.

Raman spectral imaging was performed on a WITec alpha300R Confocal Raman Microscope (WITec, Ulm, Germany) using de-paraffinized histology sections previously SEM imaged. A diode laser, 532nm, 75mW, was used for excitation. The laser beam was focused through a 50x objective (NA 0.8, Zeiss EC "Epiplan-Neofuar" DIC, Zeiss, Oberkochen, Germany). Raman signals were dispersed by grating (600 g mm−1 for the mapping, and the single spectrum of the compact calcification (10 mW, 5s)), 1800 g mm−1 for the spectra of microparticles (3 mW, 90 s) spectrograph (UHTS 300 for VIS, WITec, Ulm, Germany) and the spectra were acquired with a thermoelectrically cooled CCD detector. Control FOUR software (WITec) was used for measurement and Project FOUR Plus (WITec) for spectral data processing.

5.2.6 Image analysis

Image J was used for all image analysis done. For all analysis, images of eligible samples were used which were taken at the same magnification and same microscope settings. All physicochemical characterisation measurements (occurrence, size, spatial density) were done manually. Information on the dimensions and density of structures was obtained manually using FIJI Image J software. Image scale bars were used as a reference.

5.2.7 Statistical analysis

All statistical analysis was done using OriginLab 2019 and GraphPad Prism 8.3.1 software. A One-way Brown-Forsythe and Welch ANOVA with Dunnett's T3 multiple comparisons post hoc test (425) was used ($p<0.05$). The test allows comparison between more than two independent groups where all individual means are compared with each other and assumes a different standard deviation for each group of data points. All box blots represent the upper and lower quartiles; the whiskers indicate standard deviation, and the middle line the median value. All data is represented as the average value ± standard deviation.

5.3 Results and discussion

5.3.1 Physicochemical characterisation

In order to identify the minerals present in breast tissue, all samples were first SEM imaged. From the micrographs, it was clear that the calcification was present in two forms: large calcifications (Figure 5.1 (a, b, c)) with no specific morphology and calcified particles (Figure 5.1 (d, e, f)). The large compact calcification had dimensions between 10 and 300 μm and was observed in all types of tissue; healthy, benign and malignant, while the calcific particles were significantly smaller (down to hundreds of nanometres) and only observed in malignant cases.

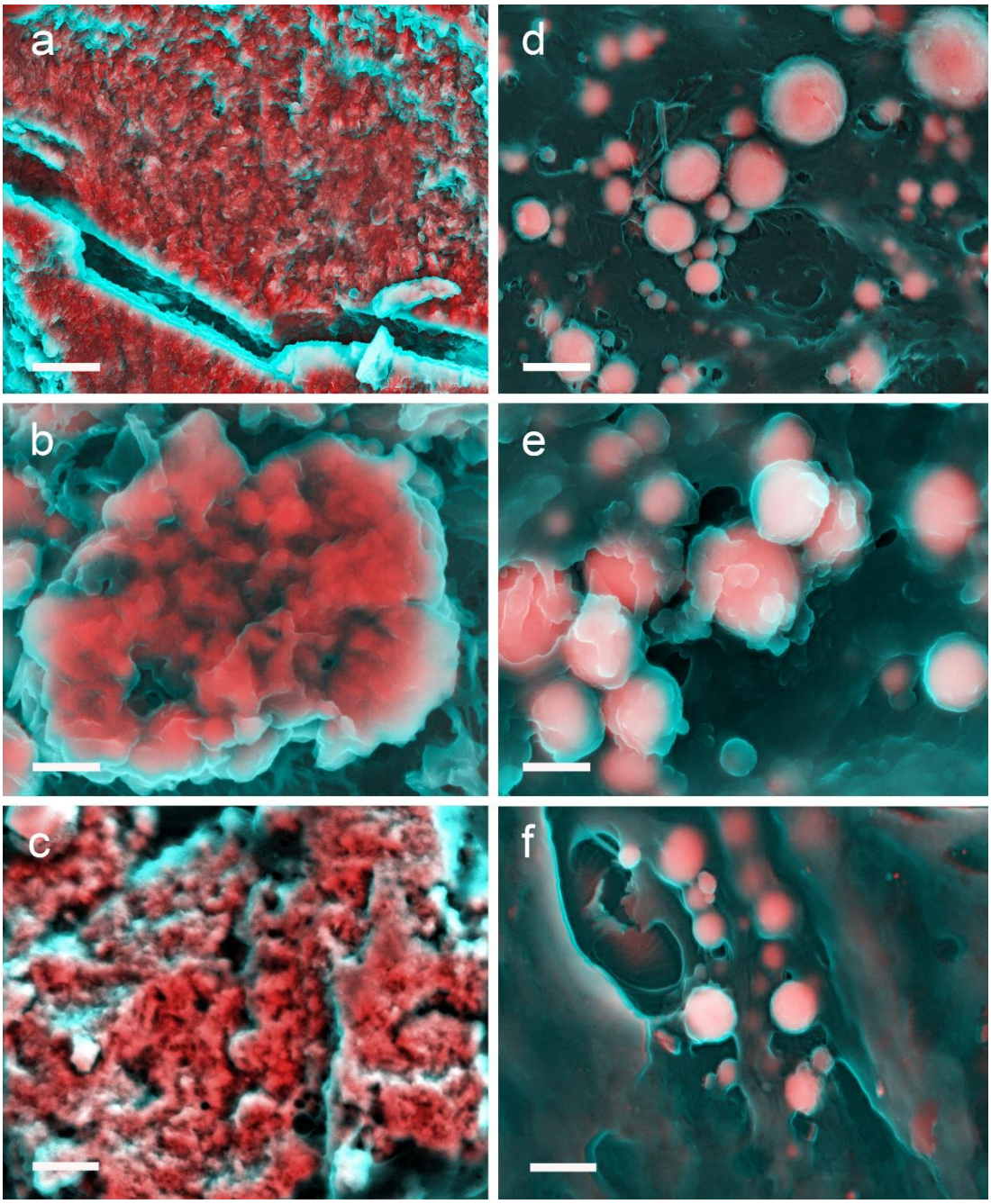

***Figure 5.1: DDC-SEM of calcification observed in breast tissue**. Red and pink indicate inorganic and turquoise (blue/green) indicates organic material. (**a)** DDC-SEM micrograph of a large mineral present in an invasive lobular carcinoma case. Scale bar = 2 µm. **(b)** DDC-SEM micrograph of a large mineral present in a benign sclerosing papillary case. Scale bar = 3 µm. **(c)** DDC-SEM micrograph of a large mineral present in a healthy case. Scale bar = 4 µm. **(d)** DDC-SEM micrograph of nanoparticles in an invasive cribriform carcinoma case. Scale bar = 2 µm. **(e)** DDC-SEM micrograph of nanoparticles in an invasive lobular carcinoma case. Scale bar = 300 nm. **(f)** DDC-SEM micrograph of nanoparticles in an invasive ductal carcinoma case. Scale bar = 1 µm.*

EDS analysis done on the same samples during imaging indicated that all large calcifications were formed by calcium and phosphorus in all types of tissues (Figure 5.2), while the calcified nanoparticles were containing magnesium in addition to calcium and phosphorus (Figure 5.3).

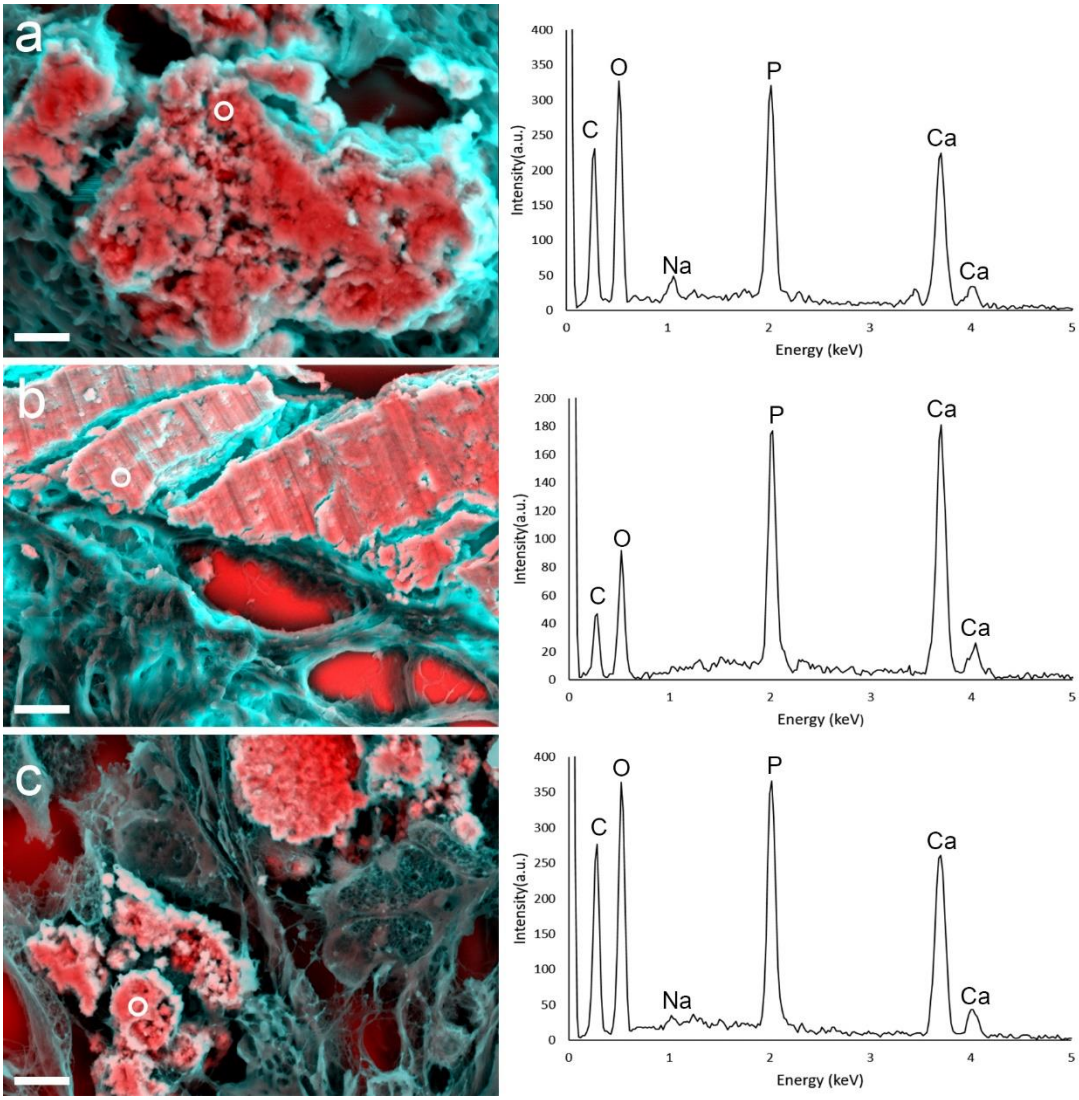

Figure 5.2: DDC-SEM micrographs of large calcifications found in breast tissue and corresponding EDS chemical analysis spectra on the right showing a chemical composition of calcium phosphate. *Red and pink indicate inorganic and turquoise (blue/green) indicates organic material.* ***(a)*** *DDC-SEM micrograph of a large mineral present in an invasive lobular carcinoma case and EDS spectrum of the region marked by a circle. Scale bar = 2 µm.* ***(b)*** *DDC- SEM micrograph of a large mineral present in an invasive ductal carcinoma and EDS spectrum of the region marked by a circle. Scale bar = 10 µm.* ***(c)*** *DDC-SEM micrograph of a large mineral present in an invasive cribriform carcinoma and EDS spectrum of the region marked by a circle. Scale bar = 2 µm.*

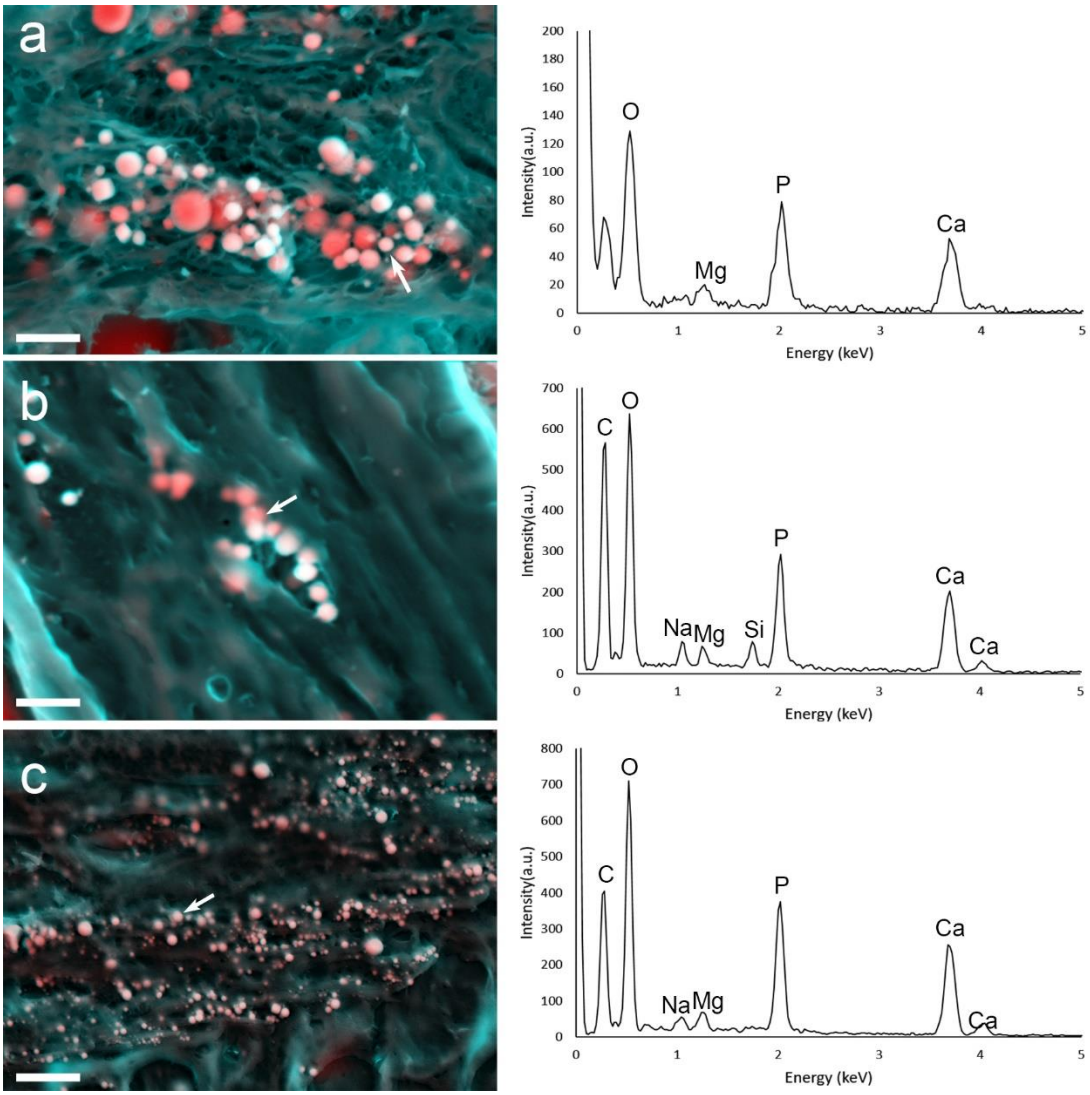

Figure 5.3: DDC-SEM micrographs of calcified particles found in breast tissue and corresponding EDS chemical analysis spectra on the right showing a chemical composition of a magnesium containing calcium phosphate. *Red and pink indicate inorganic and turquoise (blue/green) indicates organic material.* ***(a)*** *DDC-SEM micrograph of nanoparticles present in an invasive lobular carcinoma and EDS spectrum of particle marked by an arrow. Scale bar = 1 µm.* ***(b)*** *DDC-SEM micrograph of nanoparticles present in an invasive ductal carcinoma case and EDS spectrum of particle marked by an arrow. Scale bar = 1 µm.* ***(c)*** *DDC-SEM micrograph of nanoparticles present in an invasive cribriform carcinoma EDS spectrum of particle marked by an arrow. Scale bar = 4 µm.*

Following, EDS mapping and SAED analysis of calcifications sectioned by FIB were carried out for the elemental composition of the minerals to be confirmed and for information on the crystallinity of the minerals to be obtained. For the large calcification, EDS mapping confirmed a uniform distribution of calcium and phosphorus and

the absence of magnesium from the mineral. TEM micrographs of FIB prepared sections of the same type of calcification revealed an unorganised internal structure (Figure 5.4), while the SAED patterns obtained from the same samples indicated a polycrystalline structure (Figure 5.5). Indexing of the diffraction patterns suggested a chemical phase corresponding to hydroxyapatite (426) (Figure 5.6).

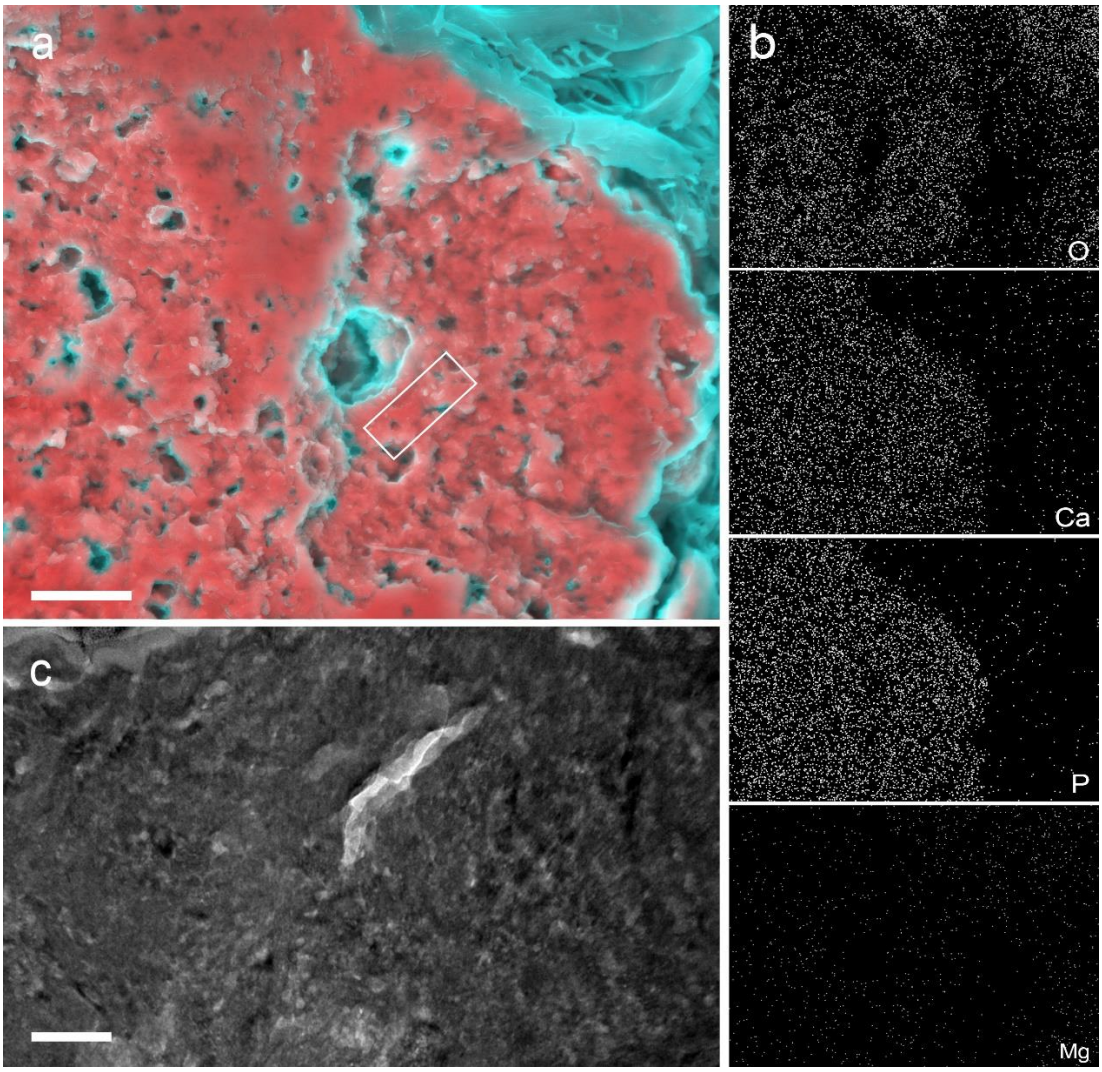

Figure 5.4: EDS mapping and TEM micrograph of large calcification observed in a benign phyllodes tumour case. (a) *DDC-SEM micrograph of large calcification where red and pink indicate inorganic material and turquoise (blue/green) indicates organic material. Scale bar = 2 µm.* ***(b)*** *EDS mapping of the same mineral confirms a uniform presence of calcium, oxygen and phosphorus and the absence of magnesium.* ***(c)*** *TEM micrograph of the region marked by a triangle in* ***a*** *indicating an unorganised internal structure. The SAED of the region suggests polycrystalline hydroxyapatite. Scale bar = 100 nm.*

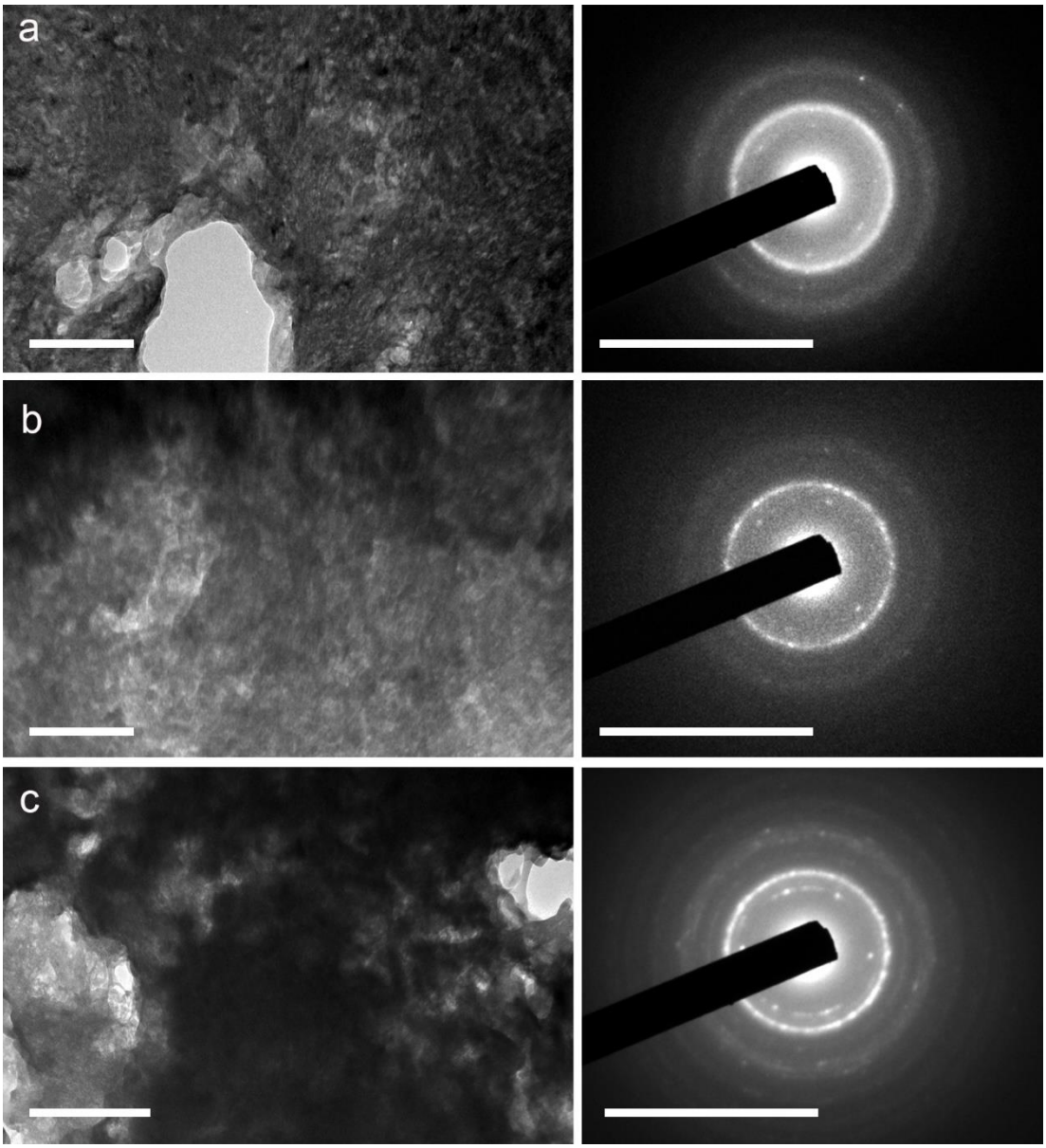

Figure 5.5: TEM micrographs of large calcification and representative SAED patterns on the right. (a), (b), (c) *TEM micrographs of large calcification. Scale bars = 200 nm, 100 nm and 500 nm. SAED patterns of the regions shown show a polycrystalline structure. Scale bars = 10 nm^{-1}.*

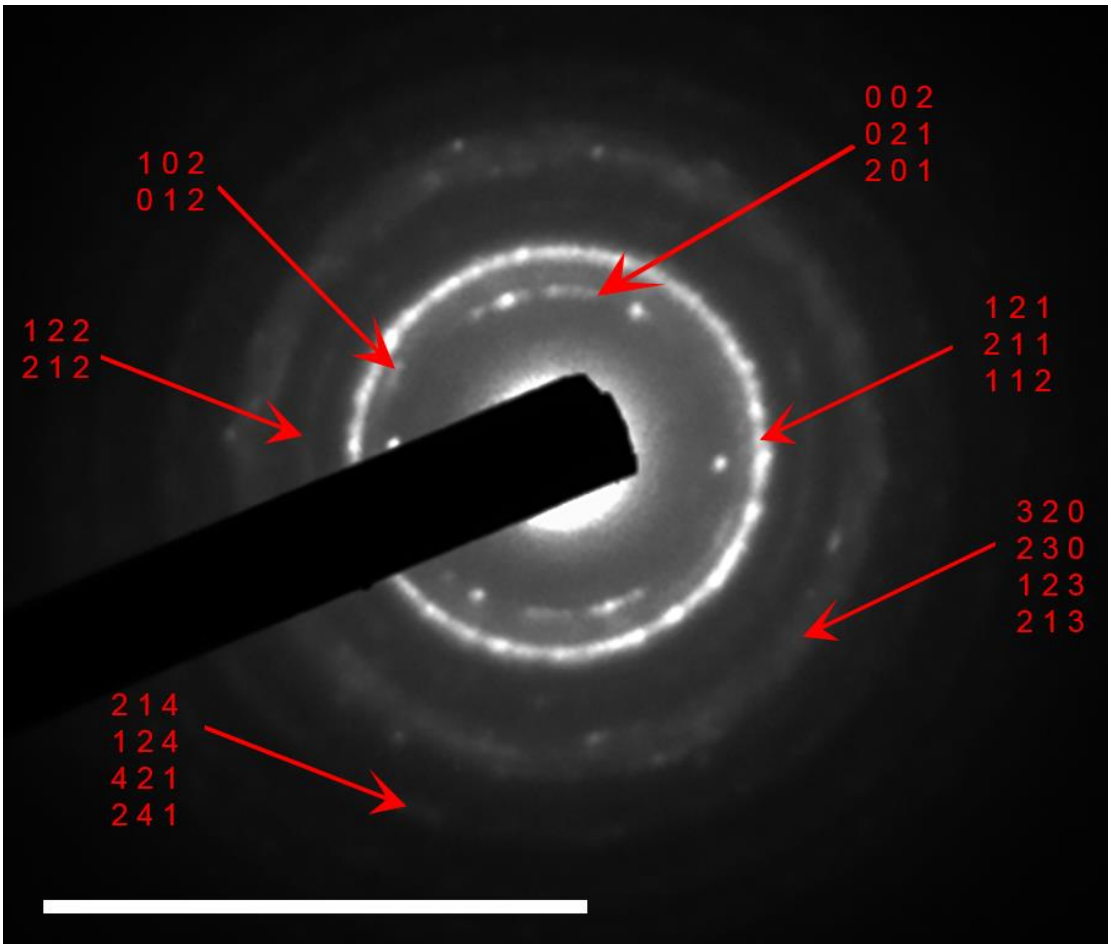

Figure 5.6: Electron diffraction pattern obtained from a large mineral showing the corresponding hydroxyapatite planes for each observed ring. *Scale bar = 10 nm[1].*

For the calcified nanoparticles, on the other hand, EDS mapping confirmed the presence of calcium, phosphorus, and magnesium (Figure 5.7). Interestingly, the TEM micrographs obtained showed that the internal structure of the nanoparticles was heterogeneous with some showing less dense cores (Figure 5.8 (a, b, c)), while others appeared to have a homogeneous density (Figure 5.8 (d, e, f)), with some presenting crystals organized radially and mineralised concentric rings (Figure 5.8 (e, f)).

The SAED patterns of the same nanoparticles, which presented spots rather than rings, showed that they have diffraction properties of single crystals rather than polycrystalline materials (Figure 5.8 (g, h, i)). Moreover, indexing of the diffraction patterns suggested a chemical phase of magnesium whitlockite (333) (Figure 5.9 (a, b)). The chemical identity of both minerals was also confirmed through Raman spectroscopy measurements, with characteristic peaks at 970 cm^{-1} and 960 cm^{-1} observed for magnesium whitlockite and hydroxyapatite respectively (427-429) (Figure 5.9 (c, d)).

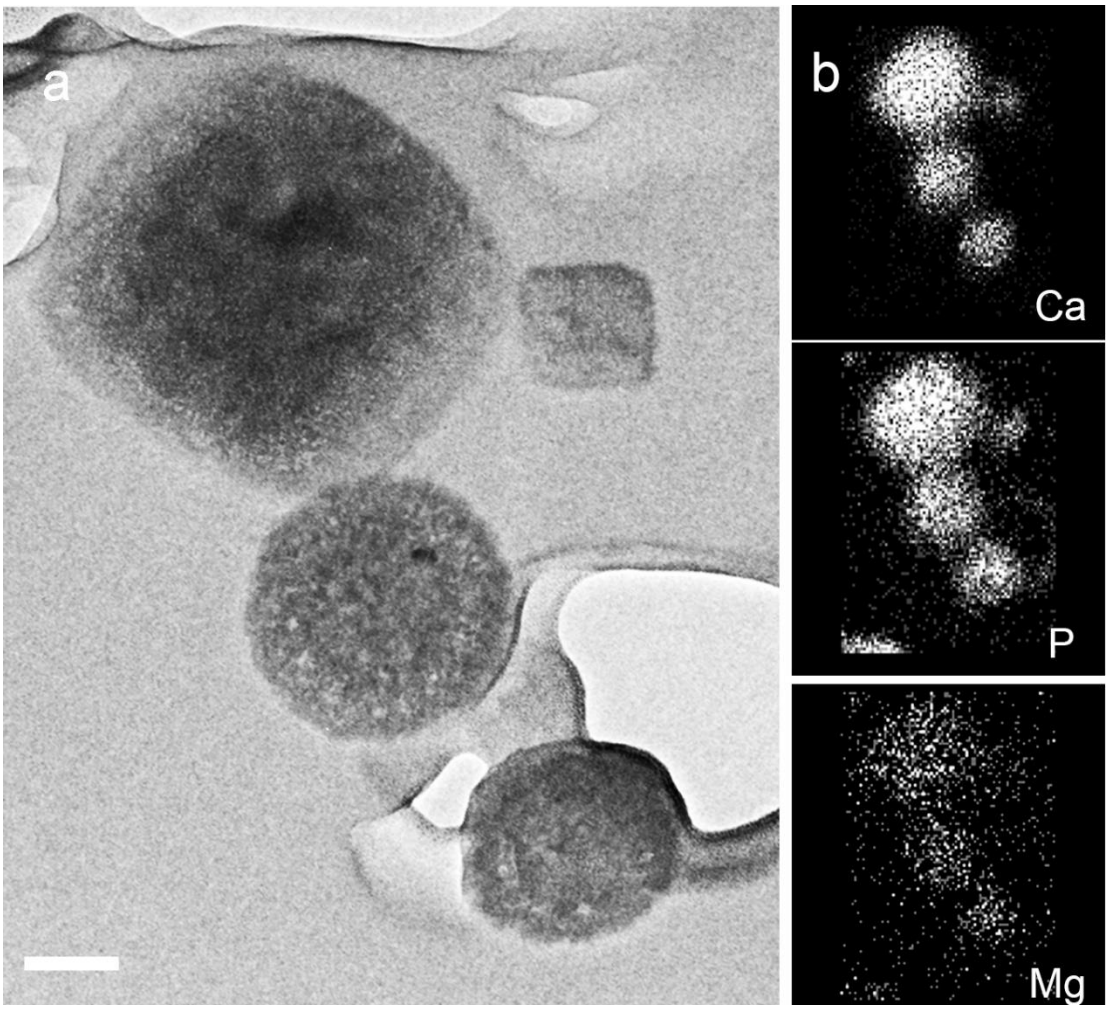

Figure 5.7: TEM micrograph of a FIB prepared section of calcified nanoparticles and corresponding EDS map. (a) *TEM micrograph of nanoparticles observed in an invasive lobular carcinoma case. Scale bar = 100 nm.* ***(b)*** *Elemental mapping of the same nanoparticles showing calcium (Ca), phosphorus (P) and magnesium (Mg).*

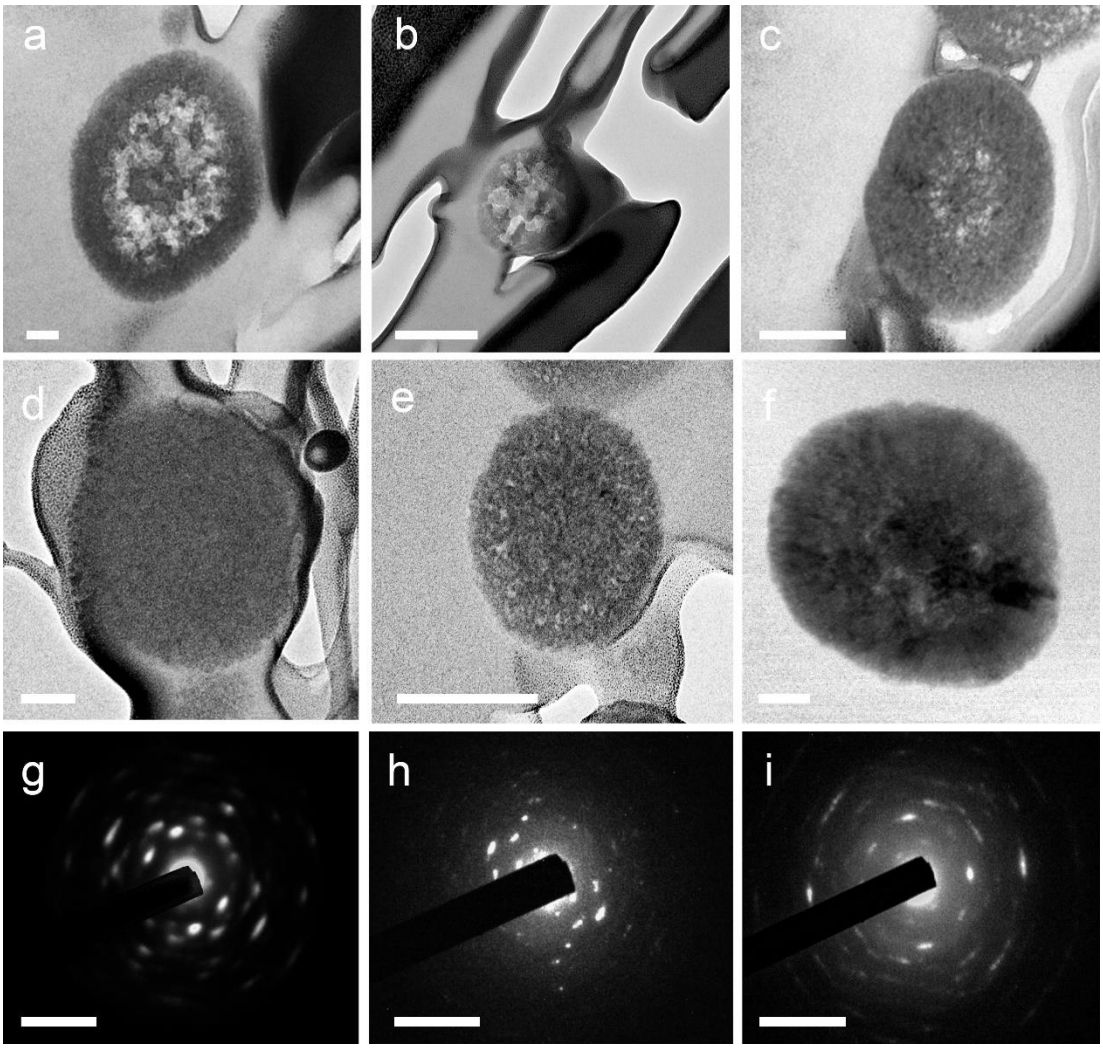

Figure 5.8: TEM micrograph of FIB prepared sections of calcified nanoparticles and representative SAED patterns obtained. (a) *TEM micrograph of a nanoparticle with a less dense interior surrounded by a dense mineralised ring observed in an invasive ductal carcinoma case. Scale bar = 50 nm.* ***(b)*** *TEM micrograph of a nanoparticle with a less dense appearance observed in an invasive ductal carcinoma case. Scale bar = 250 nm.* ***(c)*** *TEM micrograph of a nanoparticle showing some less dense material around its core observed in an invasive lobular carcinoma case. Scale bar = 100 nm.* ***(d)*** *TEM micrograph of a dense nanoparticle showing a uniform density observed in an invasive cribriform carcinoma case. Scale bar = 50 nm.* ***(e)*** *TEM micrograph of a dense nanoparticle showing radially organised crystals observed in an invasive lobular carcinoma case. Scale bar = 200 nm.* ***(f)*** *TEM micrograph of a dense nanoparticle showing radially organised crystals observed in an invasive lobular carcinoma case. Scale bar = 50 nm.* ***(g)*** *SAED pattern of the particles shown in* ***c.*** ***(h)*** *SAED pattern of the particles shown in* ***e.*** ***(i)*** *SAED pattern of the particles shown in* ***f.*** *Scale bars = 5 nm^{-1}.*

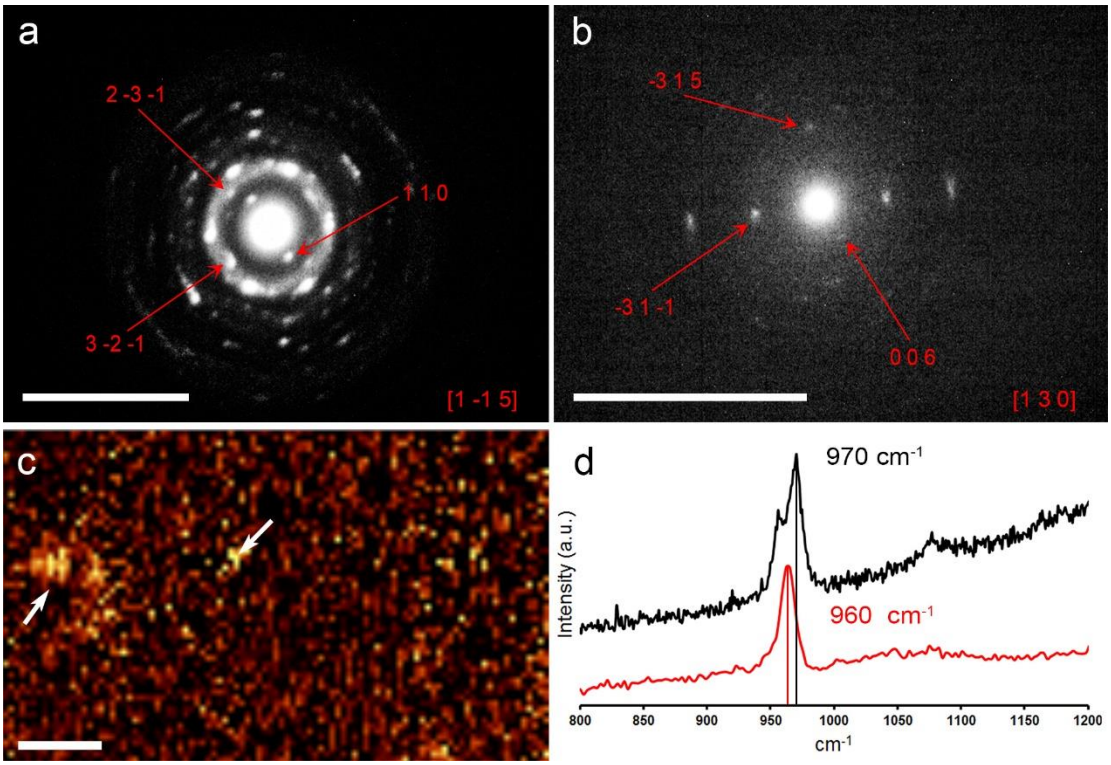

Figure 5.9: Electron diffraction pattern and raman spectroscopy mapping of the nanoparticles. (a) *Electron diffraction pattern obtained from a nanoparticles showing the vector points (1 1 0), (-3 1 5) and (-3 1 -1), corresponding to the zone axis [1 -1 5].* ***(b)*** *Electron diffraction pattern obtained from a nanoparticles showing the vector points (0 0 6), (2 -3 -1) and (3 -2 -1), corresponding to the zone axis [1 3 0]. Scale bars = 10 nm^{-1}.* ***(c)*** *Raman 970 +/-20 cm-1 peak map confirming the presence of small whitlockite particles (arrows) in the tissue. Scale bars = 3 µm.* ***(d)*** *Raman spectrum obtained from nanoparticles particles (black spectrum) and large calcification (red spectrum).*

The same magnesium whitlockite particles have, interestingly, been previously observed in cardiovascular and ocular tissues (13, 14), as well as in osteoporotic bone (430). Magnesium whitlockite has also been reported to some extent in bone, teeth, cartilage and synovial fluid, however, it is usually observed in a rhombohedral shape and lower crystallinity (335, 431-433), hinting a different mechanism of formation to the whitlockite nanoparticles found in the breast and other tissues under pathological conditions. Furthermore, the formation of whitlockite even in a synthetic setting has proven challenging (335, 431); thus, its exact formation mechanisms in the human body are yet to be uncovered. Subsequently, based on such distinct chemical composition, we propose that these nanoparticles are of the same origins as those observed in cardiovascular diseases, discussed in the previous chapter.

The presence of hydroxyapatite (25, 408, 419) and whitlockite (also referred to as magnesium substituted calcium phosphate) (184, 414, 419) minerals has been acknowledged previously in breast tissues; however, they have never been identified

as separated entities. Moreover, to the best of our knowledge, it is the first time that calcification in breast tissue is identified to have the clear morphology of spherical nanoparticles of an average diameter of 434 nm ± 228 nm. The particles were found to be present in different sizes with the smallest particle having a diameter of 46 nm and the largest one a diameter of 2.15 µm (Figure 5.10).

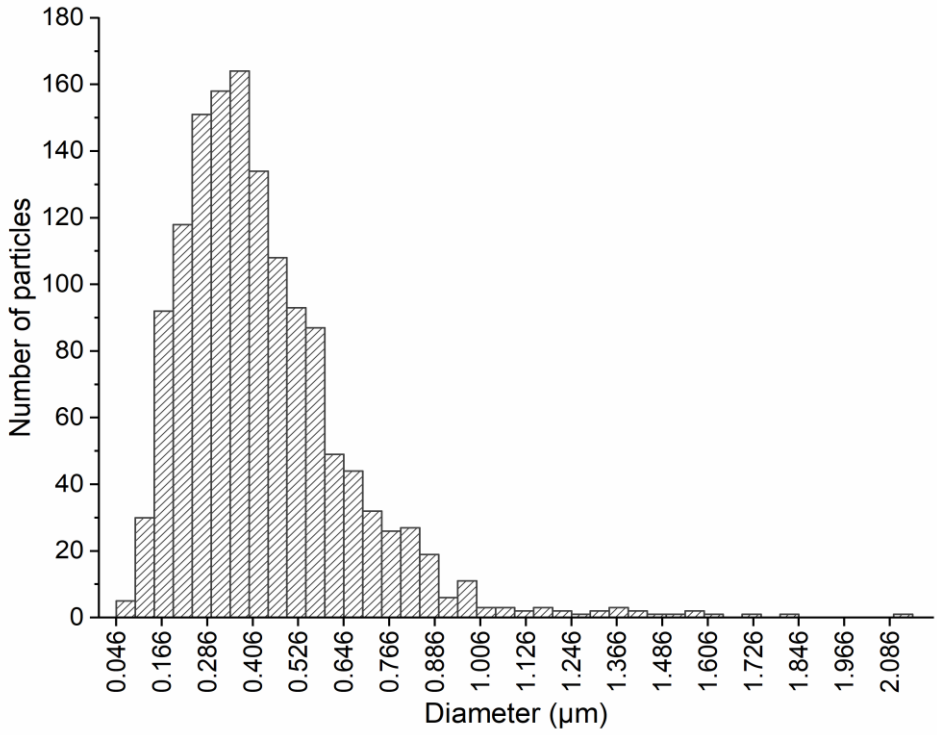

Figure 5.10: Size distribution of 1400 nanoparticles. The smallest particle had a diameter of 46 nm and the largest a diameter of 2.15 µm with the average size being 434 nm and a standard deviation of ± 228 nm.

Based on the size distribution and shape, it was concluded that the whitlockite nanoparticles are formed through a mineralisation process involving a vesicle, which possibly mineralises over time. The particle size range of the whitlockite nanoparticles observed also fit the same range as the particles observed in calcific cardiovascular diseases; further supporting a common origin. Additionally, as the nanoparticles retained their shape and size and were not observed to grow into larger structures with no defined shape nor were observed as parts of the large apatite minerals, it was also concluded that they follow a different mechanism of formation to the large apatite mineral. The independent presence of the large apatite mineral in healthy and benign cases also suggested that its formation does not trigger the deposition of the whitlockite nanoparticles. However, the increased occurrence of the large mineral in samples

presenting the nanoparticles might hint an effect on the tissue microenvironment triggering other mineralisation processes.

5.3.2 Diagnostic significance

With the identification of the morphology, composition and crystallinity of the minerals present in breast tissue, it was evaluated whether any correlations can be found between the two types of minerals and breast tumours. Interestingly, the whitlockite nanoparticles were only observed in cases with a diagnosis of invasive breast malignancies. No nanoparticles were observed in healthy cases, benign tumours nor non-invasive malignant tumours. In contrast, as previously mentioned, large calcifications were observed in all types of tissue (Figure 5.11).

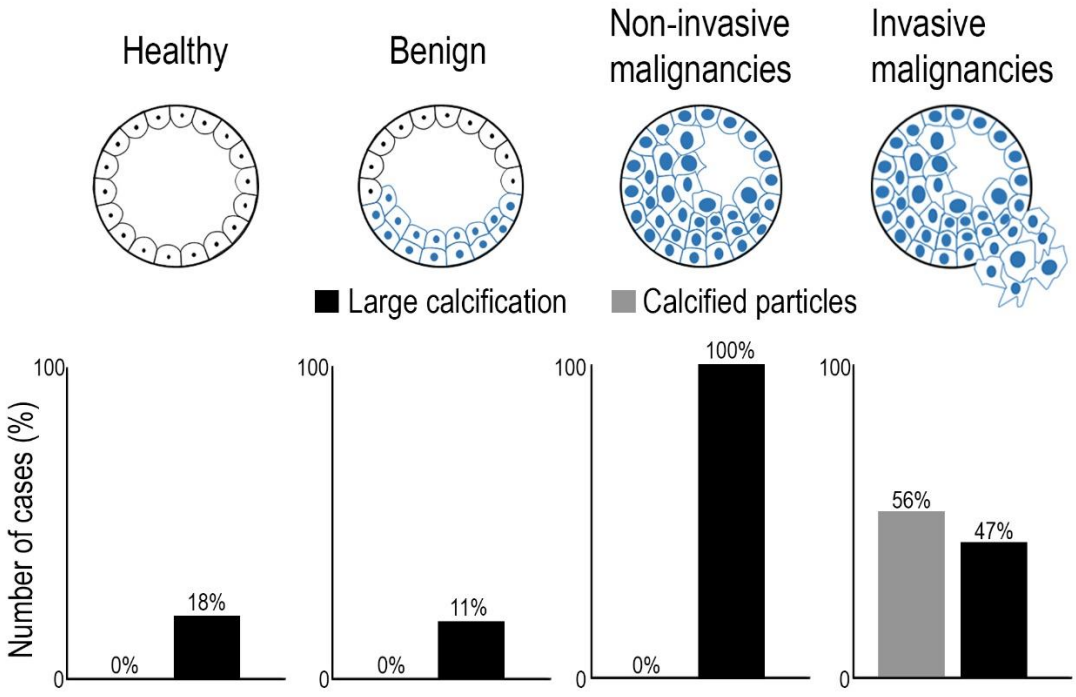

Figure 5.11: Histograms indicating the percentage of cases in 11 healthy, 23 benign, 2 non-invasive, and 45 invasive malignancies in which large calcifications and calcified nanoparticles were observed.

The location of the two minerals in the tissue was also evaluated through the imaging of haematoxylin and eosin (H&E) stained histological slides, consecutive to those used for the electron microscopy analysis. It was observed that large apatite calcifications were present in the ducts and the stroma of the tissue (Figure 5.12 (a, b)), while the calcified nanoparticles were only observed in vascular tissue (Figure 5.12 (c, d)).

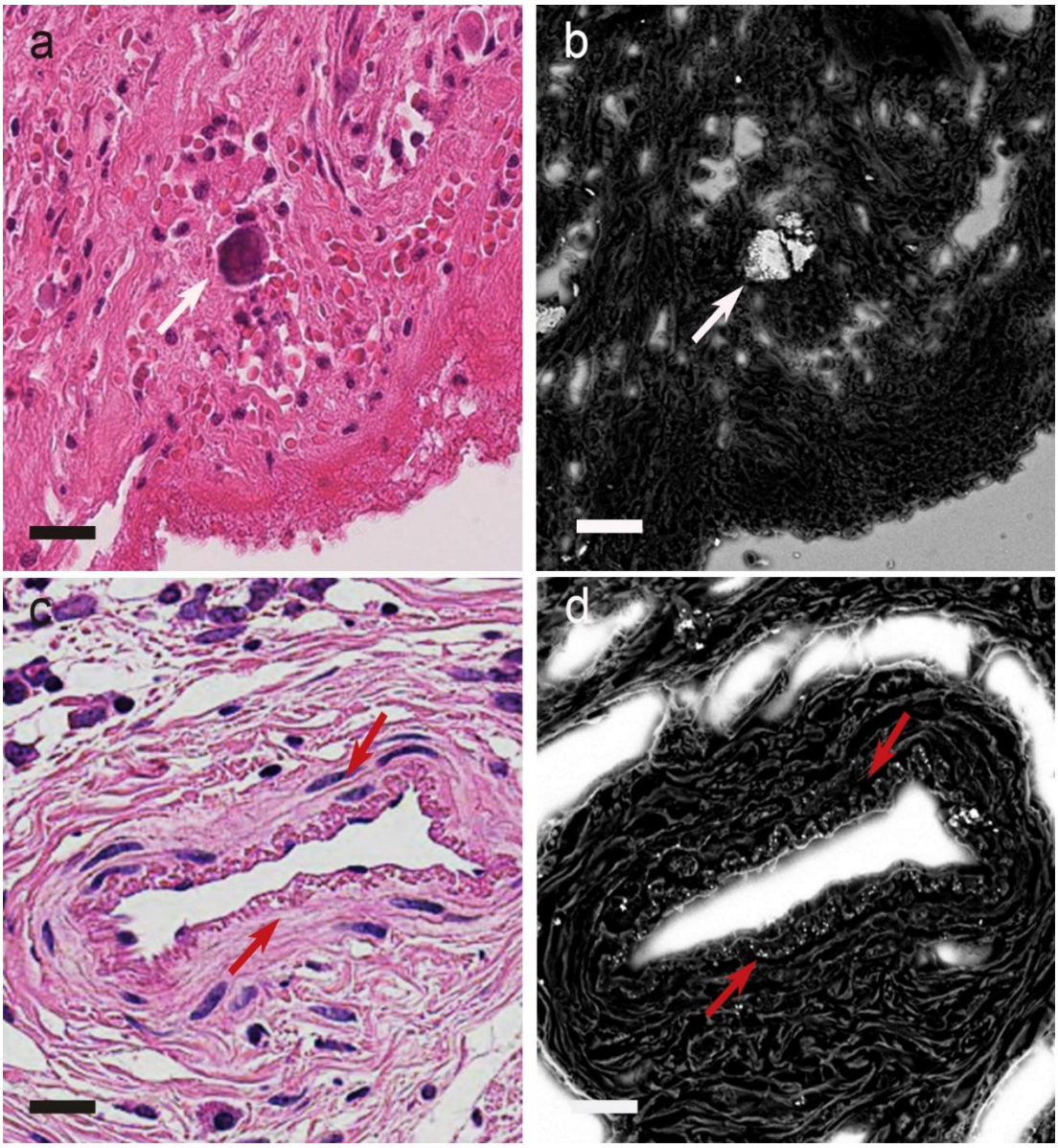

Figure 5.12: H&E and electron micrographs of breast tissues showing the microanatomical regions where mineralized structures were observed. (a) *Optical micrograph of a tissue slide from an invasive ductal carcinoma case, stained with H&E indicating large mineral (arrow). Scale bar = 15 µm.* ***(b)*** *Backscattering electron micrograph showing the same calcification (arrow). Scale bar = 15 µm.* ***(c)*** *Optical micrograph of a slide of breast tissue with invasive cribriform carcinoma, stained with H&E showing a vessel (arrows). Scale bar = 10 µm.* ***(d)*** *Backscattering electron micrograph of the same region shown in c, indicating the presence of whitlockite nanoparticles (arrows). Scale bar = 10 µm.*

Additionally, a more specific analysis on the invasive malignant samples showed that the sections, which did not present calcified particles, did not have any distinct vasculature either. Furthermore, no particles were found in healthy, benign and non-invasive cases despite the presence of vasculature in some of the sections. The occurrence of the calcified particles in vasculature tissue was therefore found to be a good indicator of invasive malignancies (Figure 5.13).

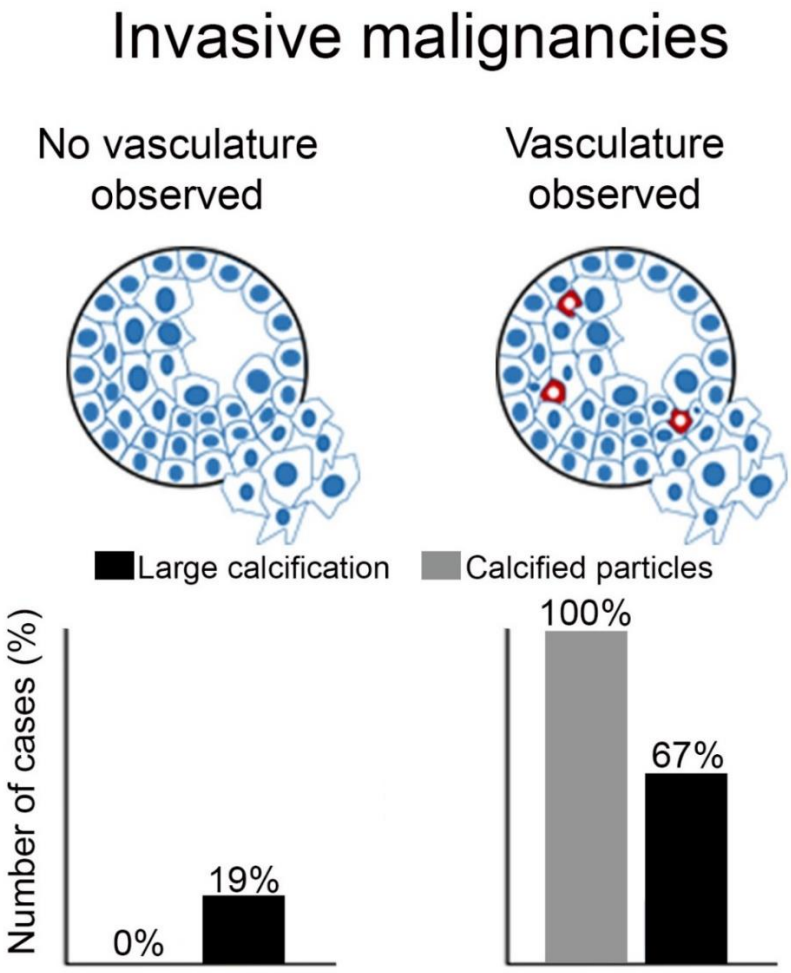

Figure 5.13: Histograms indicating the percentage of invasive malignant cases in which calcified nanoparticles and large calcification were observed based on the absence or presence of distinct vasculature in the tissue slides. In total, 45 invasive malignant cases were used; 25 of which presented distinct vasculature.

Using the samples that presented nanoparticles in well distinct vessels, the association of their aggregation and size with the grade or type of malignancy was investigated. Based on measurements on 270 particles from each type of invasive malignancy, no significant difference was found between the size of the particles observed in invasive lobular carcinoma (444 ± 297 nm), invasive cribriform carcinoma (473 ± 276 nm) and invasive ductal carcinoma (439 ± 165 nm) (Figure 5.14). A result

which indicated a mineralisation process shared among the different types of malignancies and indicated that the presence of particles and their growth did not depend on the anatomical location of the tumour.

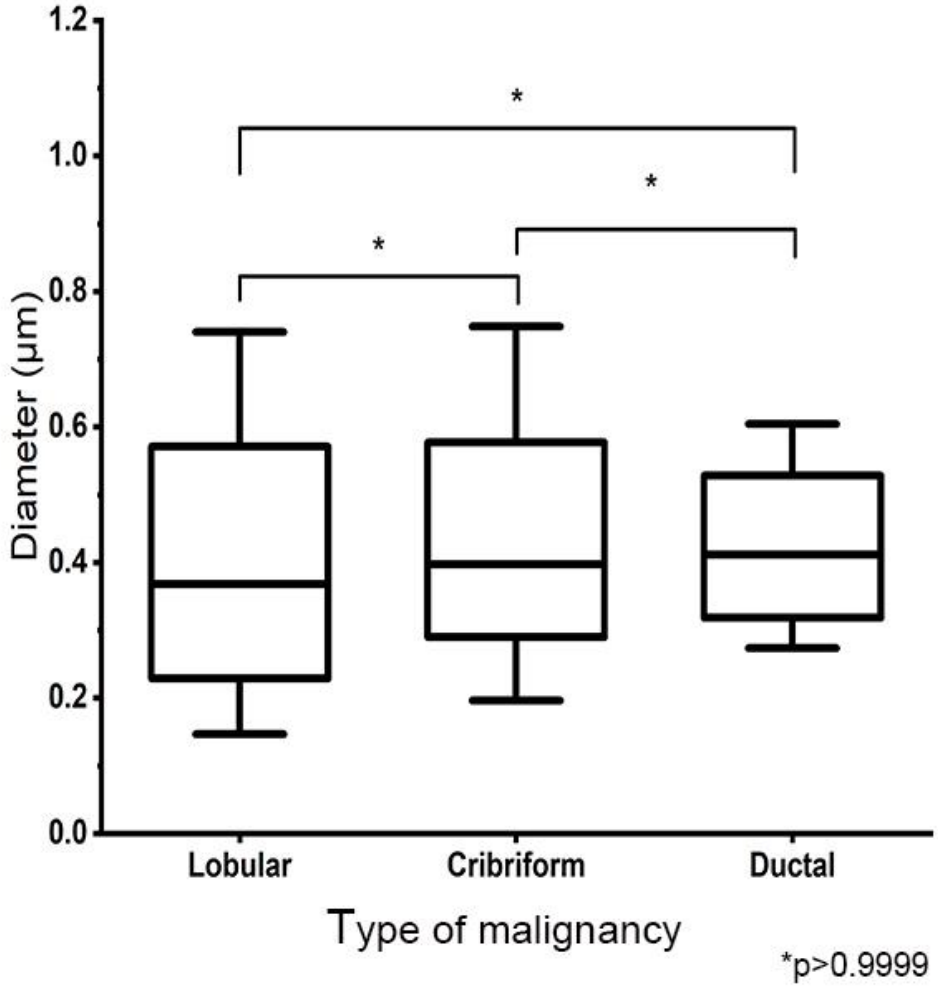

Figure 5.14: Box blot indicating the relationship between the size of the calcified nanoparticles and three types of breast carcinomas; invasive lobular carcinoma, invasive cribriform carcinoma and invasive ductal carcinoma. *One-way Brown-Forsythe and Welch ANOVA with Dunnett's T3 multiple comparisons post hoc test gave a p-value higher than 0.9999, indicating no statistical significance between the particle size and the type of breast carcinoma. For the analysis, a total of six invasive lobular, five invasive cribriform and seven invasive ductal carcinoma cases were used.*

The statistical analysis between the nanoparticle size and the grade of malignancies, however, indicated a statistically significant difference between the size of the particles observed in grade 1 (614 ± 369 nm) and grade 3 (407 ± 170 nm) malignancies. However, there was no statistical significance between the size of particles observed in grade 1 and grade 2 (456 ± 273 nm) nor between grade 2 and grade 3

(Figure 5.15). Therefore, it was unclear whether the average size of the nanoparticles could be confidently related to tumour grade. A limitation to these measurements was the small number of particles observed in grade 1 tumours (< 40) in comparison to measurements on 600 particles for grade 2 and 3.

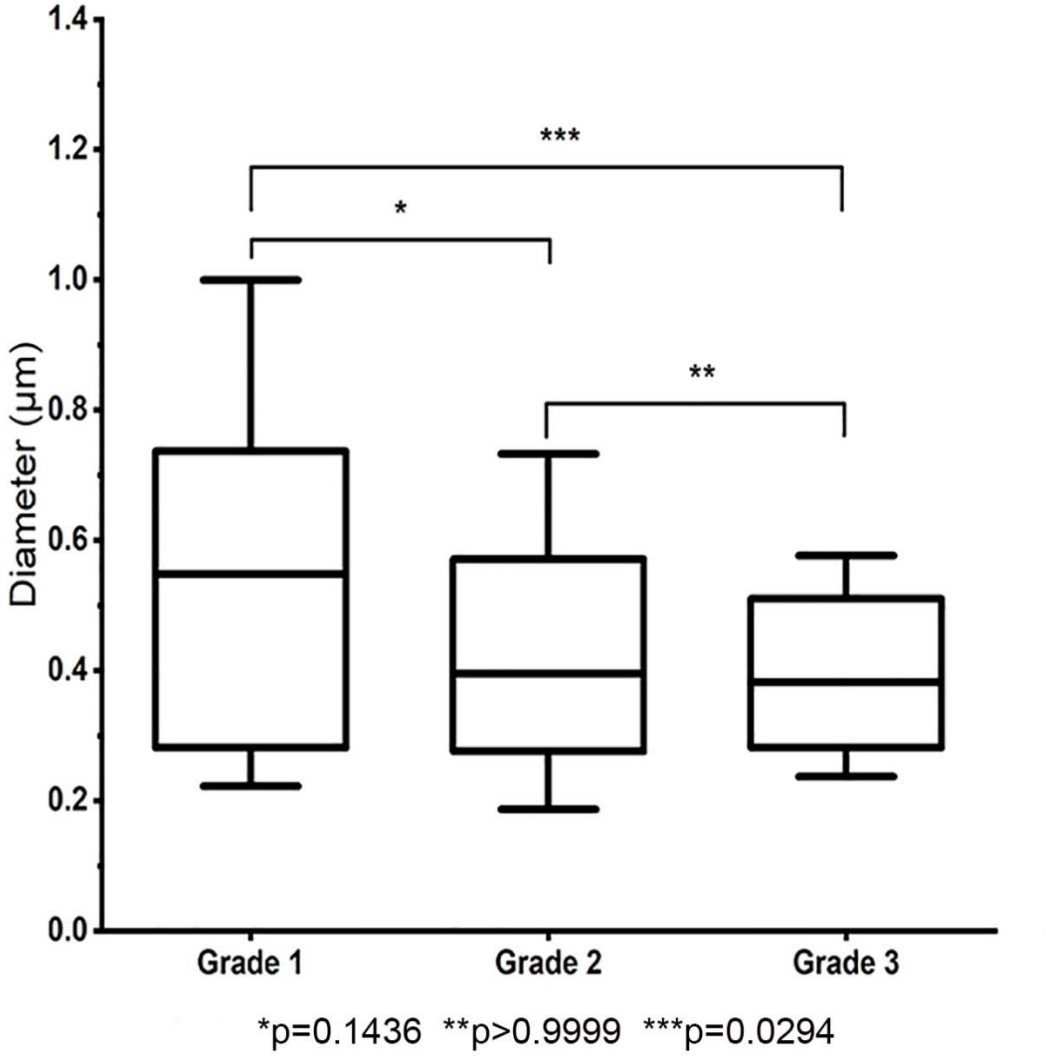

Figure 5.15: Box blot indicating the relationship between the size of the calcified nanoparticles and grades of carcinoma; grade 1, 2 and 3. *One-way Brown-Forsythe and Welch ANOVA with Dunnett's T3 multiple comparisons post hoc test gave a p-value of 0.1436 between grade 1 and grade 2 showing no statistical significance. A p-value larger than 0.9999, indicating no statistical significance was also obtained between grade 2 and grade 3. Statistical significance was only observed between grade 1 and grade 3 with a p-value of 0.0294. For the analysis samples from a total of two grade 1, seven grade 2 and three grade 3 cases were used.*

Subsequently, the relationship between the average spatial density of the particles and the grade of malignancies was also evaluated. This data was obtained from

particles observed in grade 1 tumours (< 40) and more than 600 particles for grades 2 and 3. Despite, based on the available data, a significant difference was only observed between the spatial density of the particles in grade 1 (7.00 ± 9.46 particles/200µm^2) and grade 2 (82.3 ± 45.8 particles/200µm^2). No statistical significance was observed between grade 2 and grade 3 nor between grade 1 and grade 3 (190 ± 84.9 particles/200µm^2) (Figure 5.16). This outcome could suggest that the mineralization processes causing the presence of the whitlockite nanoparticles onset as early as the tumour itself, thus the presence of the particles in small amounts could be used as an indication of early invasive malignancies.

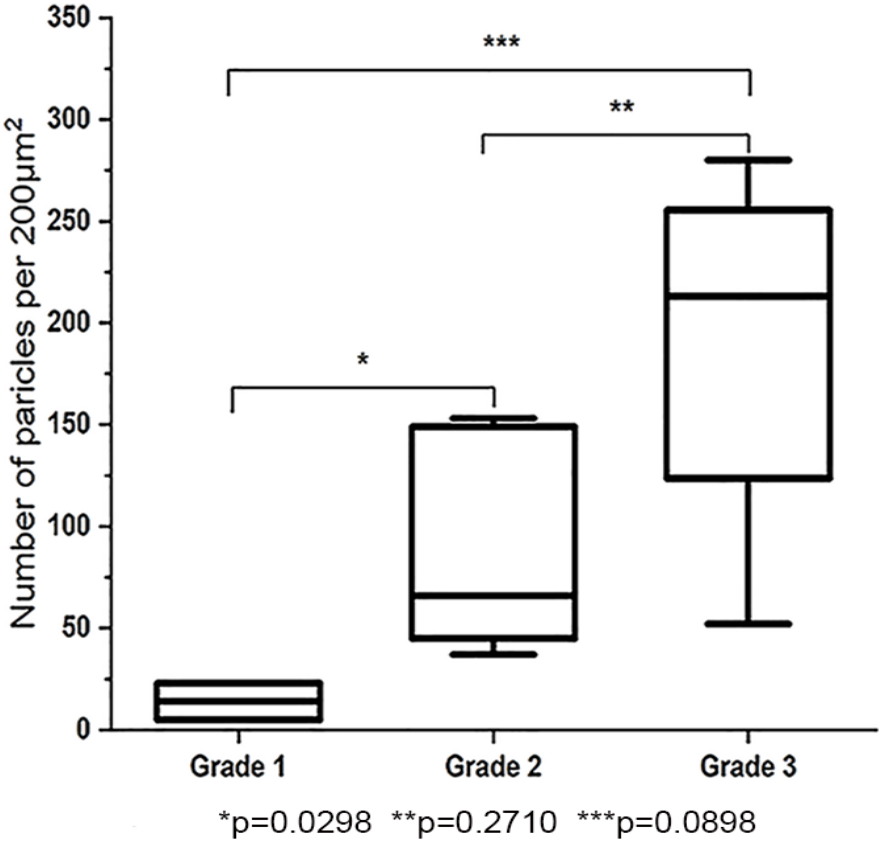

Figure 5.16: Box blot indicating the relationship between the average spatial density of the calcified nanoparticles and grades of carcinoma; grade 1, 2 and 3. *One-way Brown-Forsythe and Welch ANOVA with Dunnett's T3 multiple comparisons post hoc test gave a p-value of 0.0298 between grade 1 and grade 2 showing a statistical significance. A p-value of 0.2710 indicating no statistical significance was obtained between grade 2 and grade 3. No statistical significance was also observed between grade 1 and grade 3 with a p-value of 0.0898. For the analysis, samples from two grade 1, seven grade 2 and three grade 3 cases were used.*

Hence, the exact location of the particles in the vascular wall was also evaluated to identify possible cellular origins. As very few particles were observed in grade 1 invasive malignancies, the resulting distribution mostly reflected the particles observed in grades 2 and 3. The majority of these nanoparticles were found close to the lumen accumulating considerably in the internal elastic lamina and tunica media (103) with 99.8% of all nanoparticles observed within the vascular wall (Figure 5.17). A similar observation to the localisation of the nanoparticles in aortic tissue, even though due to size differences of the vascular wall, the particles appeared more spread out in the aortic wall. In addition, most particles were observed within a physical distance of 60 µm from the lumen, suggesting that the affected vessels were possibly medium-sized, mostly arteries, and in some cases arterioles due to their wall thickness (434).

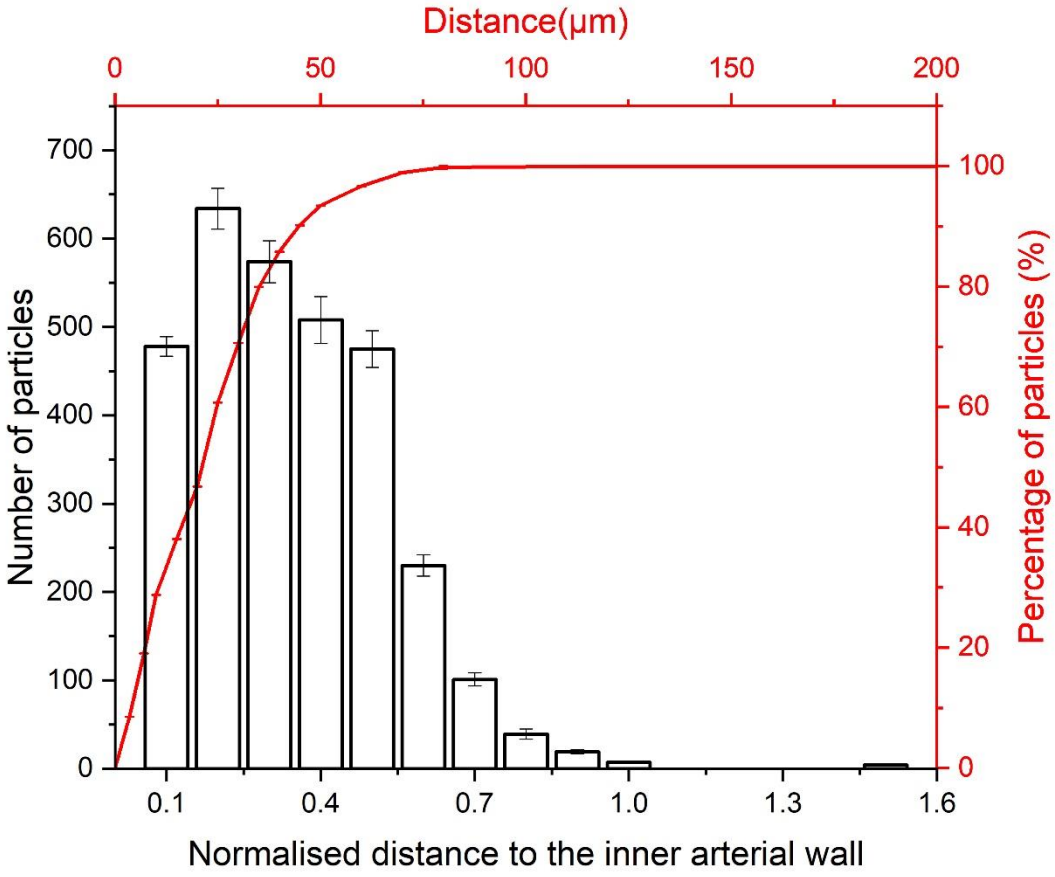

Figure 5.17: Graphical representation of the distribution of the calcified nanoparticles in the vascular wall (normalised distance) with values over one indicating tissue outside the vascular wall (black graph) and the corresponding non-normalised distribution of nanoparticles within 200 µm from the internal vascular wall (red graph).

The distribution of the nanoparticles across the vascular wall further suggested that the whitlockite particles originating from mineralizing features of a specific size provided continuously to the vasculature of invasive malignant tumours through the bloodstream. In addition, the increased amounts of particles in grades 2 and 3 indicated a continued accumulation that comes in agreement with the fact that the particles retained their shape rather than grow to form larger unstructured minerals, an observation also supporting a unique mineralisation process being responsible for the formation of these particles. Moreover, the initial assumption that the nanoparticles originating from a vesicle driven mineralisation process was further supported by the fact that the average radius of the nanoparticles remained relatively constant in all grades of malignancy thus their growth into larger minerals is unlikely to be time-dependent.

5.4 Conclusions and future work

The presence of whitlockite nanoparticles in invasive malignant tumours was reported for the first time in this work. Their presence to some extent is a useful marker for invasive malignancy despite the grade or type of disease, suggesting that the nanoparticles can be observed in the vasculature of all invasive malignancies or at least invasive tumours presenting specific properties. Based on this, these nanoparticles have high diagnostic potential as markers of invasive malignancies; however, testing at a larger scale should be carried out to confirm this potential. Further work should be carried out to understand whether clinical information other than type and grade, for example on the tumour profile can also be correlated to the presence, size or accumulation of the nanoparticles observed and subsequently whether their formation is tumour microenvironment specific or not.

Also, their presence on the vasculature could be an indication of the enhanced permeability and retention (EPR) effect observed in tumour vasculature, the presence of which has been strongly debated (435). The effect is argued to be present in all tumours to some extent; as a result of loose junctions between the vascular endothelial cells due to poor vascular architecture, allowing for blood components to pass through (436). Emerging nanoparticle therapy concepts have been based on the theory; showing that it is possible to deliver nanoparticles to the tumour through the bloodstream (436). It was however recently been suggested that the assumption of loose cellular junctions might not be the only cause of this effect, as TEM analysis showed that there are no significantly larger or more gaps between endothelial cells (340) proposing that the transportation of blood components to the tumour happens through the endothelial cells in a way similar to transcytosis (340, 437). Therefore, the presence of the whitlockite nanoparticles in the vascular wall could also be a result of a process happening

similarly; with their precursors originating in blood and through a transendothelial transport pathway aided by poor vascular architecture, to be accumulated in the vascular wall.

As previously mentioned, the same whitlockite nanoparticles have also been observed in cardiovascular tissues and have been related to calcific cardiovascular diseases (13). Platelet markers have been identified in these nanoparticles indicating an origin different from the possible mechanisms already reported in the literature, while from a physicochemical perspective platelet dense granules could be acting as the nucleation sides for the formation of the nanoparticles. Similarly to cardiovascular diseases, platelets and platelet products have also been found to have a role in the metastasis of breast and other cancer types (438-440). For example, an increase in platelet activation and the release of platelet vesicles have been observed in many cancer types (439), while platelet and platelet vesicles have been found to play a role in the adaptation of an invasive phenotype of breast cancer cells (438, 441). Furthermore, a study has shown that the release of platelet dense granules in the tumour microenvironment, enhances cancer cell migration and metastasis (440), results confirmed by another study where inhabitation of platelet granule secretion was found to prevent tumour cell metastasis (442). Subsequently, it is possible that even though the original stimulus causing their occurrence might vary, the formation of these nanoparticles follows the same mechanisms of formation as the whitlockite nanoparticles associated with calcific cardiovascular diseases.

Besides, the origins of the particles, other questions have also arisen, one of the most important being the role played by them in tumour development and metastasis. Calcium phosphate minerals in soft tissues can have a significant impact on the recruitment and transdifferentiation of local or circulating cells (443-445) through mechanobiological signalling, as stiffer matrices have been shown to have remarkable effects on cells (446). Subsequently, it might be possible that the presence of a mineral in the breast tissue will drastically alter the mechanical properties of the tumour tissue microenvironment, and have a dramatic effect on its cells. Additionally, it has been found that an increased amount of hydroxyapatite induces apoptosis in human breast cancer cells (447). It has been previously also proven that breast cancer cells behave differently when hydroxyapatite of different carbonate contents is used (416). The size of hydroxyapatite crystals was also found to increase cell adhesion while an increase in mineral crystallinity was observed to have the opposite effect (448). Higher crystalline hydroxyapatite was, however, also observed to reinforce the secretion of osteolytic proteins from breast cancer cells (448, 449), an effect which has been correlated to bone metastasis (449). These and many other studies found in the literature show the apparent effect of hydroxyapatite and specific mineral properties on cancer cells and

hint their role in cancer progression, similar work has not however been carried out using magnesium whitlockite nor the whitlockite particles observed in this work. Thus moving forward, the effects of such mineral composition, size and shape on breast cancer cells should also be investigated through *in vitro* studies. Another important aspect about calcium phosphate nanoparticles is their ability to carry DNA fragments and transfect cells (450, 451). This property could also apply to whitlockite nanoparticles, therefore should be studied in relation to the effect of their interactions with healthy cells and whether they play any role in breast cancer proliferation. Isolated whitlockite nanoparticles from cancer biopsies could be used to study *in vitro* their effect on healthy breast cells and whether they can induce tumourigenic phenotypes.

To conclude, the fact that the whitlockite nanoparticles have only been observed in invasive breast malignancies gives rise to a number of questions on their real contribution to tumour progression and whether their presence marks tumour invasiveness or affects it. Moreover, their diagnostic potential should also be considered for future studies, as it could be a valuable tool to aid the precise and early diagnosis of breast cancer.

Chapter 6: Brain Mineralisation in Alzheimer's disease

6.1 Introduction

Alzheimer's disease (AD) has been the focus of a large number of scientific works worldwide. However, due to the complexity of the pathology, its pathophysiological mechanisms are yet not completely understood. Additionally, the symptoms of the disease are rarely diagnosed at early stages; thus in recent years several biomarkers have been identified that could aid that, including amyloid positron emission tomography imaging and analysis of the levels of tau protein in the cerebrospinal fluid (452). A recent pilot study has also indicated that a specific type of calcification in the retina can act as a biomarker for AD (453). Additionally, intracranial vascular calcification has been observed in AD patients, although it has not been treated as a marker nor a consequence of the disease. Moreover, very little information exists in the literature on the physicochemical properties of these minerals as most studies are carried out in a clinical setting; thus, the minerals are only observed in the macroscale.

Therefore, the main aims of this work are ***to provide information on the physicochemical properties of brain minerals*** and to understand ***whether any type of brain mineralisation can be associated with AD pathology***. This was done through an in-depth characterisation of minerals in the brains of Alzheimer's disease patients (> 55 years old), elderly (> 55 years old), and young donors (< 40 years old) using electron microscopy. The three groups were chosen such that the elderly group acted as a control to evaluate the association of minerals to clinical AD diagnosis and the young group to evaluate the relationship of the minerals to ageing. For each case, three brain regions were examined. The hippocampal region and part of temporal lobe were chosen, as both regions have been associated with AD changes. Tissue from the basal ganglia was also examined, even though it is not directly related to AD; as brain minerals have been reported widely in this region. Based on the results of the initial mineral characterisation and their clinical significance, ***the relationship of phosphorylated tau (pTau), a hallmark of AD pathology to the mineralised regions was investigated.*** This was evaluated using immunofluorescence staining.

6.2 Materials and methods

6.2.1 Tissue

Brain tissue from 22 Alzheimer's disease cases (> 55 years old) (Table 6.1), 22 elderly donors (> 55 years old) (Table 6.2) and 15 young (< 40 years old) (Table 6.3) donors were obtained from the Queen Square Brain Bank (UCL) and the Brain Tissue Bank of the University of Edinburgh. Tissue from the basal ganglia at the level of the anterior commissure, hippocampal area at the level of the lateral geniculated body and temporal neocortex (Brodmann areas 21 and 22) were obtained. All brain samples were obtained as formalin-fixed and paraffin-embedded histological slides of a thickness of 5 µm. At least two consecutive slides were obtained for each case, where possible.

Table 6.1: Clinical information of the AD cases analysed in this work.

Case	Sex	Patient Age
1	M	64
2	F	56
3	F	62
4	M	75
5	F	79
6	M	80
7	M	77
8	F	88
9	M	57
10	M	76
11	F	67
12	F	71
13	F	79
14	M	69
15	F	76
16	F	61
17	F	76
18	M	62
19	F	66
20	M	72
21	M	68
22	M	88

Table 6.2: Clinical information of the elderly cases with no AD diagnosis analysed in this work.

Case	Sex	Patient Age
1	F	82
2	F	56
3	F	87
4	F	88
5	F	78
6	M	95
7	M	85
8	F	80
9	M	83
10	F	79
11	F	86
12	M	87
13	F	82
14	M	87
15	F	89
16	F	78
17	F	68
18	F	87
19	F	80
20	M	88
21	F	93
22	F	92

Table 6.3: Clinical information of the young, healthy cases analysed in this work.

Case	Sex	Patient Age
1	M	17
2	M	25
3	F	20
4	F	40
5	M	40
6	M	39
7	M	34
8	M	26
9	M	19
10	M	25
11	M	25
12	M	21
13	M	22
14	M	16
15	M	28

6.2.2 Scanning electron microscopy

For SEM analysis, the samples were prepared as detailed in *chapter 3, section 3.3.4.2.* A Hitachi S-3499N, a Carl Zeiss Crossbeam and a Zeiss LEO 1530 were used for SEM imaging. Voltage, current, aperture and working distance were adjusted for individual samples and microscope. Oxford Instruments energy-dispersive X-ray detectors integrated on the machines were used for elemental analysis.

6.2.3 Focused Ion Beam- Transmission electron microscopy

A FEI Helios NanoLab 600 DualBeam Focused Ion Beam System and Zeiss Auriga Cross Beam were used as described in *chapter 3 section 3.4.3.2* for milling of the samples. Dr Sergio Bertazzo carried out the FIB milling of all brain samples. FIB prepared sections were then analysed using a Joel 2100Plus TEM at a voltage of 200kV.

6.2.4 Von Kossa staining

Deparaffinisation of the samples took place by immersing the samples in two changes of 100% xylene solution for 10 minutes each and rehydration of the samples took place through a series of decreasing ethanol concentrations; 100% (x3), 70% (x2), 50% (x2) for 3 minutes each. The samples were then immersed in deionised

water for 10 minutes and incubated with 5% silver nitrate (abcam® ab150687) for 45 minutes. Throughout this time, the samples were exposed to a 60 or 100 Watt incandescent light. The bulb was placed at a distance of around 5 cm away from the samples. Following, the samples were rinsed with deionized water and were incubated with 5% sodium thiosulphate for 3 minutes (abcam® ab150687). The samples were rinsed using running tap water for 2 minutes and were then washed twice with deionised water for 1 minute. Nuclear fast red stain was then used for 5 minutes to counterstain the tissue (Sigma-Aldrich N8002). Samples were rinsed again for two minutes with tap water and washed twice with deionised water for 1 minute. Dehydration followed using absolute ethanol for one minute before washing in xylene for one minute. A coverslip was placed over the tissue using DPX mounting medium (Sigma-Aldrich 06522) along the lengths of the sample; ensuring there are no bubbles. Imaging of the von Kossa stained samples was done using a Leica DM5500 Fluorescence Upright Microscope. Von Kossa staining was only employed for basal ganglia sections due to sample availability.

6.2.5 Immunofluorescence staining

The staining procedure was done, as described in c*hapter 3, section 3.6.5.* Following deparaffinisation and rehydration of the samples, the tissue was then blocked for 1 hour using 1:20 goat serum diluted in TBT. Samples were washed twice with TBT for 3-minute intervals and incubated with an AT8 pTau mouse anti-human IgG1 (Thermofisher MN1020) monoclonal primary antibody for one hour at a concentration of 1:100 by diluting in TBT. Following, that the samples were washed three times with TBT for 5 minute- intervals, and incubated with polyclonal secondary antibodies (Thermofisher A-21121 or abcam® ab97239) diluted in TBT to a concentration of 1:200 for 1 hour. The samples were rewashed three times with TBT for 5-minute intervals and incubated with OsteoSense 680EX (PerkinElmer NEV10020EX) at a concentration of 1:10 (diluted in PBS) for 20 minutes. Two 10-minute long PBS washes were carried out, and the tissue was incubated using a DAPI stain (Hoechst) at a concentration of 1:1000 (diluted in PBS) for 15 minutes. Finally, the samples were washed twice using TBS for 3 minute-intervals and were mounted with a coverslip using Fluoroshield mounting medium (abcam® ab104135) and was sealed using nail polish at the edges of the coverslip. All samples were imaged using an Olympus FV1000, a Leica SP5 and a Zeiss LSM 980 Airyscan confocal microscope. All antibodies were tested for specificity using a secondary antibody, and negative controls where appropriate.

6.2.6 Image analysis

FIJI Image J software was used for all image analysis done. For analysis, ten images per sample were used, which were taken at the same magnification.

For physicochemical characterisation measurements (occurrence and size), the SEM images used taken at similar magnifications. Images from all samples presenting minerals were used, and all measurements were done manually. Information on the dimensions of structures was obtained manually using the FIJI Image J software.

For the quantitative data on the co-occurrence of stains, all fluorescence imaging was done using a Zeiss LSM 980 Airyscan confocal microscope for consistency. In total, ten samples were used, and all images were taken using an x63 lens. Suitable co-occurrence methods found in the literature were then employed (330, 331). Individual images for each fluorescence signal were extracted from the original files using Image J. Any background signal or cross-talk between channels was initially eliminated as much as possible during the imaging process. At the same time, during analysis, a threshold value was also applied to all images to eliminate wrongful co-localisation of background pixels. Coloc 2 function of FIJI Image J software was used to obtain the amount of individual stains co-occurring with each other; which was obtained as the Mandres' overlap coefficient (330, 331).

6.2.7 Statistical analysis

All statistical analysis was done using OriginLab 2019 and GraphPad Prism 8.3.1 software. For the co-occurrence analysis, a Mann-Witney two-tailed unpaired U test (332) was used ($p<0.05$). The test is non-parametric thus; it does not assume that the data points follow a normal distribution, which was found not to be the case for the data points obtained. Box blots were created to represent the data, where the box represents the upper and lower quartiles; the whiskers indicate the standard deviation and the middle line, the median value. All co-occurrence data in the text is represented as average ± standard deviation.

6.3 Results and discussion

6.3.1 Physicochemical characterisation

As most soft tissue mineralisation is formed by calcium and phosphorus, von Kossa staining of basal ganglia sections from Alzheimer's disease, elderly donor and young cases was initially employed. This was done to evaluate the presence of such minerals in the tissue. The staining indicated the presence of vascular (Figure 6.1 (a, b)) mineralisation, as well as the presence of mineralised spheres and fibres (Figure 6.1 (c, d, e)) in the tissue. Vascular calcification was not correlated to a specific anatomical or biological feature, however; the mineralised spheres and fibres were found to be concentrated near the edge of the tissue in a particular band pattern (Figure 6.1 (c)).

Von Kossa staining was however found not to be fully representative of the structures and amounts of minerals observed, thus should be used in line with other methods. Therefore, to confirm that the minerals are made of calcium phosphate and to observe them in their natural stage at higher magnification and resolution, SEM analysis was then employed.

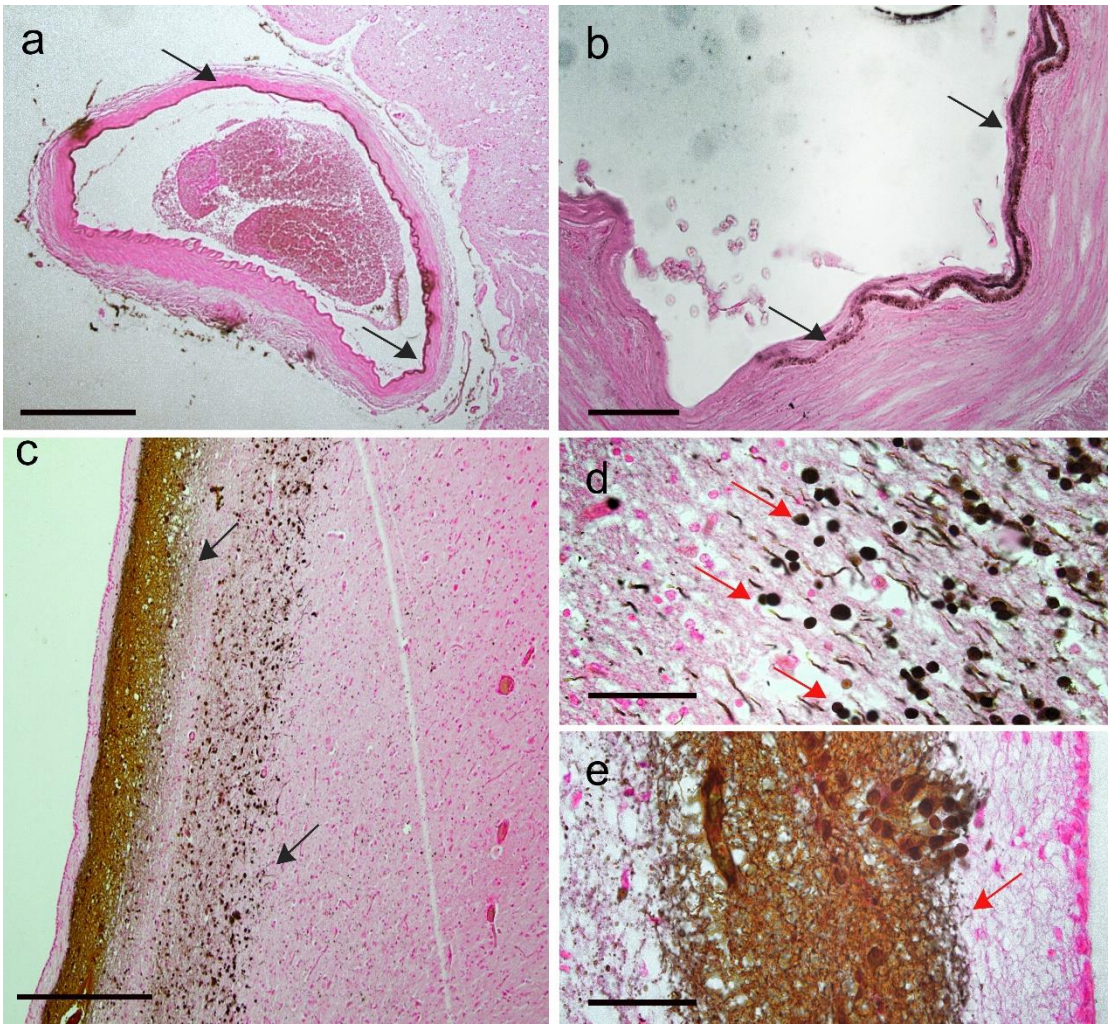

Figure 6.1: Tissue calcification as observed using von Kossa staining in the basal ganglia of elderly donors and AD patients. (a) *Low magnification optical micrograph of vascular calcification (black arrows) in the basal ganglia of an AD patient. Scale bar = 500 µm.* ***(b)*** *High magnification optical micrograph of vascular calcification (black arrows) in the basal ganglia of an AD patient. Scale bar = 50 µm.* ***(c)*** *Low magnification optical micrograph of areas where calcified spheres and fibres are observed forming bands near the edge of the tissue (black arrows) in the basal ganglia of an elderly donor. Scale bar = 500 µm.* ***(d)*** *High magnification optical micrograph of an area showing the calcified spheres (red arrows) in the basal ganglia of an elderly donor. Scale bar = 50 µm.* ***(e)*** *High magnification optical micrograph of an area showing the calcified fibres (red arrows) in the basal ganglia of an elderly donor. Scale bar = 50 µm.*

The presence of the same types of calcification was confirmed in all three anatomical regions, while no other type of mineral was repeatedly observed in the investigated sections. In vascular calcification, both small particles and big chunks of calcification were observed (12). EDS analysis indicated that the calcified particles were formed by calcium, phosphorus and magnesium in contrast to the large calcification that was formed by calcium and phosphorus only (Figure 6.2). These findings are in agreement with previous findings on the elemental composition of vascular calcification (13). In the brain, elemental analysis of vascular calcification has been rarely carried out, however, the presence of minerals in the vasculature has been reported, investigated mainly through von Kossa staining and computed tomography (CT) imaging (454-457). Intracranial vascular calcification has been observed in relation to a number of diseases; in the basal ganglia (455), hippocampus (454, 457) and thalamus (456).

In AD patients, the presence of vascular calcification in the hippocampus has been studied before, with the related study reporting that 59% of the AD cases presented hippocampal vascular calcification, in comparison to 40% of the control group (223). Our results have shown a prevalence of intracranial vascular calcification (including basal ganglia, hippocampal and temporal lobe sections) in only 41% of the AD cases and 36% of the elderly control group cases. No vascular calcification was observed in the young control group.

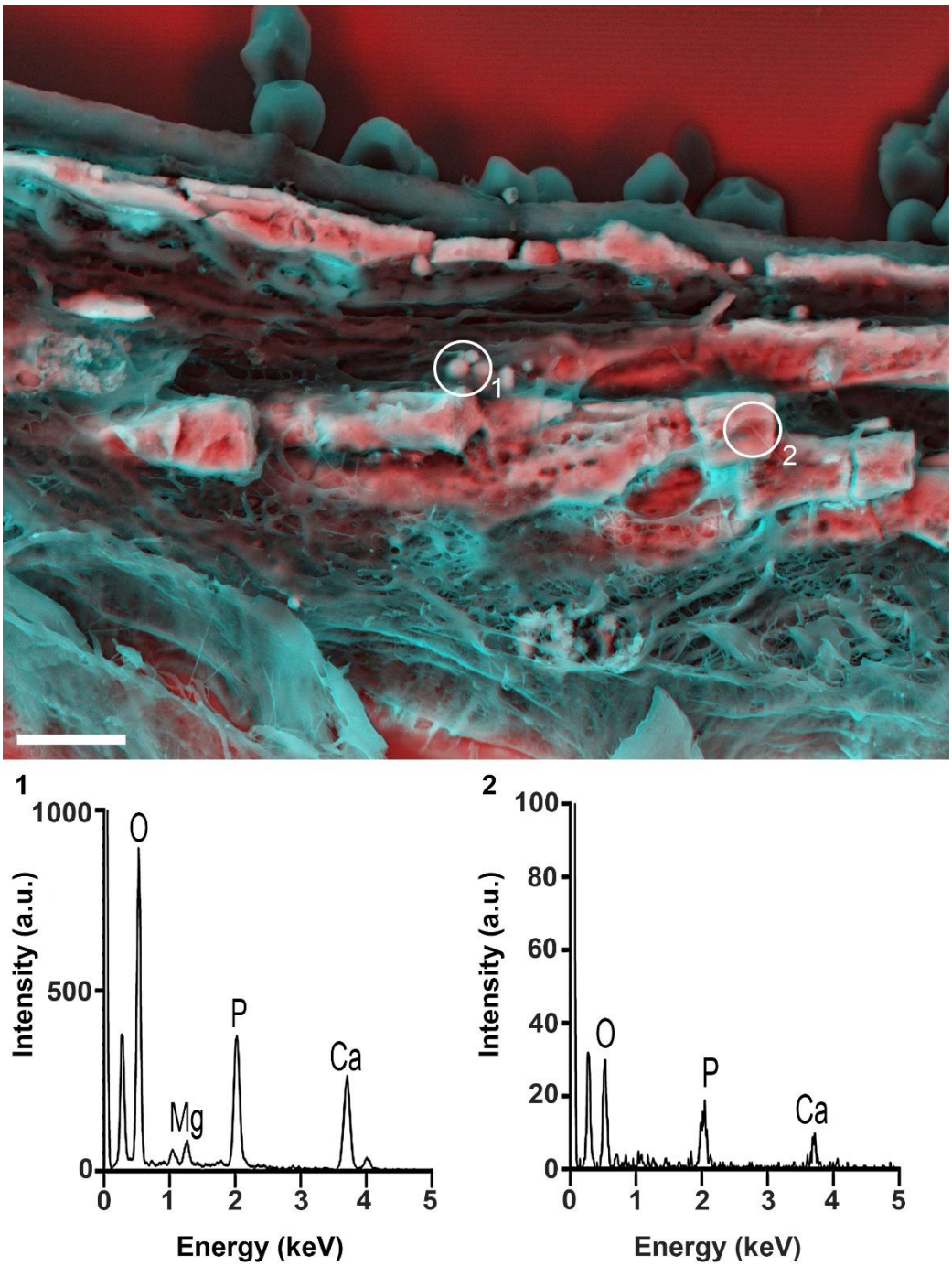

Figure 6.2: DDC-SEM image of vascular calcification observed in the basal ganglia of an AD patient where pink-red indicate calcification and turquoise indicates tissue. *The red, dark background of the image corresponds to the glass below the tissue. EDS spectra indicated that region **1** corresponding to a calcified particle contains magnesium, calcium and phosphorus while region **2**, corresponds to a part of a large calcification, contains calcium and phosphorus only. Scale bar = 4 µm.*

For the calcified spheres, SEM imaging indicated a wide size range with the average diameter being 8.08 µm, with a standard deviation of ± 2.76 µm. All calcified spheres despite size were formed by calcium and phosphorus (Figure 6.3). Calcium

and phosphorus were also observed in the calcified fibres, which had an average diameter (width) of 1.40 µm with a standard deviation of ± 0.77 µm (Figure 6.4). The length of the calcified fibres was widely varying; therefore, it was not measured.

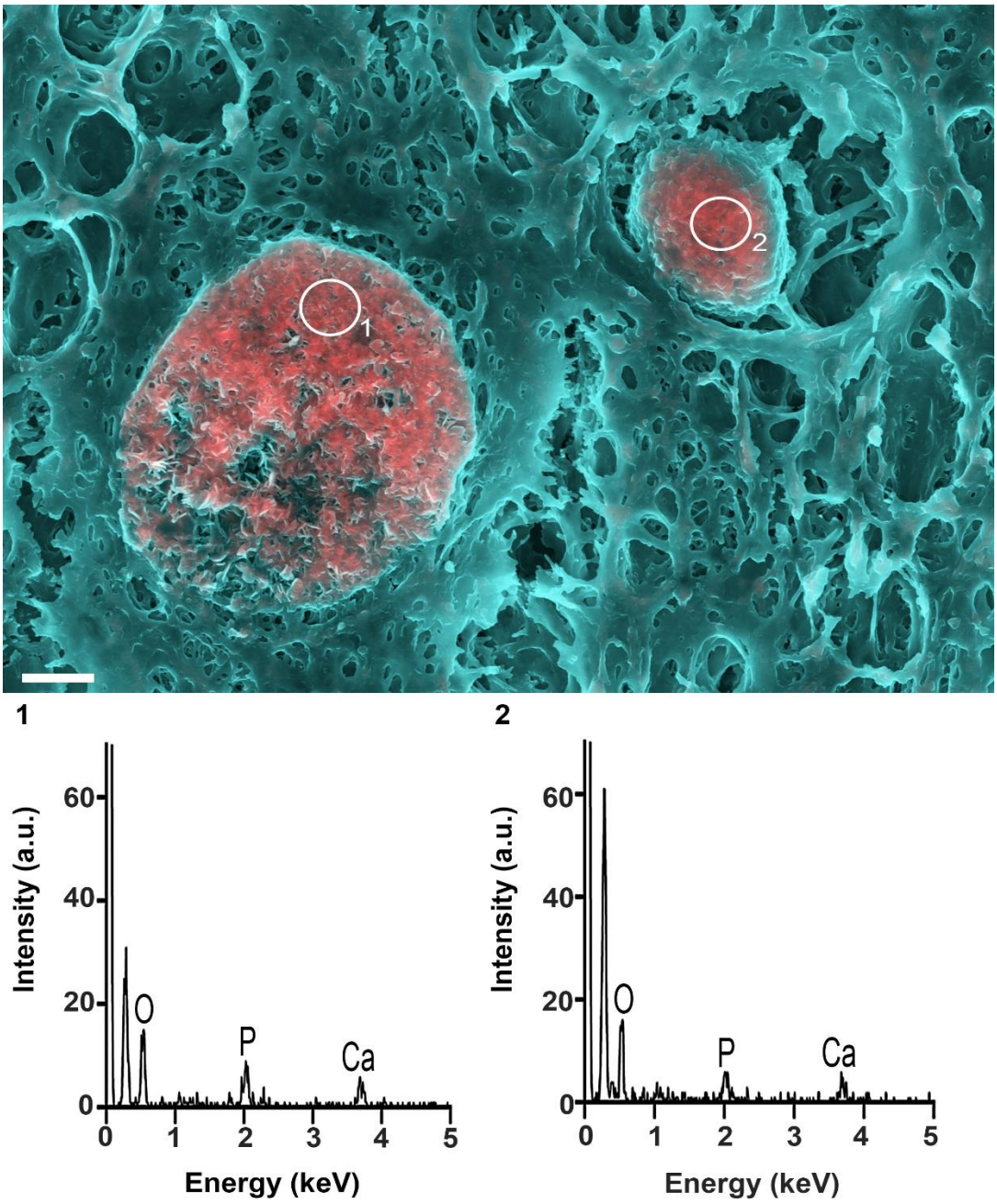

Figure 6.3: DDC-SEM image of calcified spheres observed in the basal ganglia of an elderly donor where pink-red indicate calcification and turquoise indicates tissue. *EDS analysis indicated that all calcified spheres despite their size were formed by calcium and phosphorus only. Scale bar = 2 µm.*

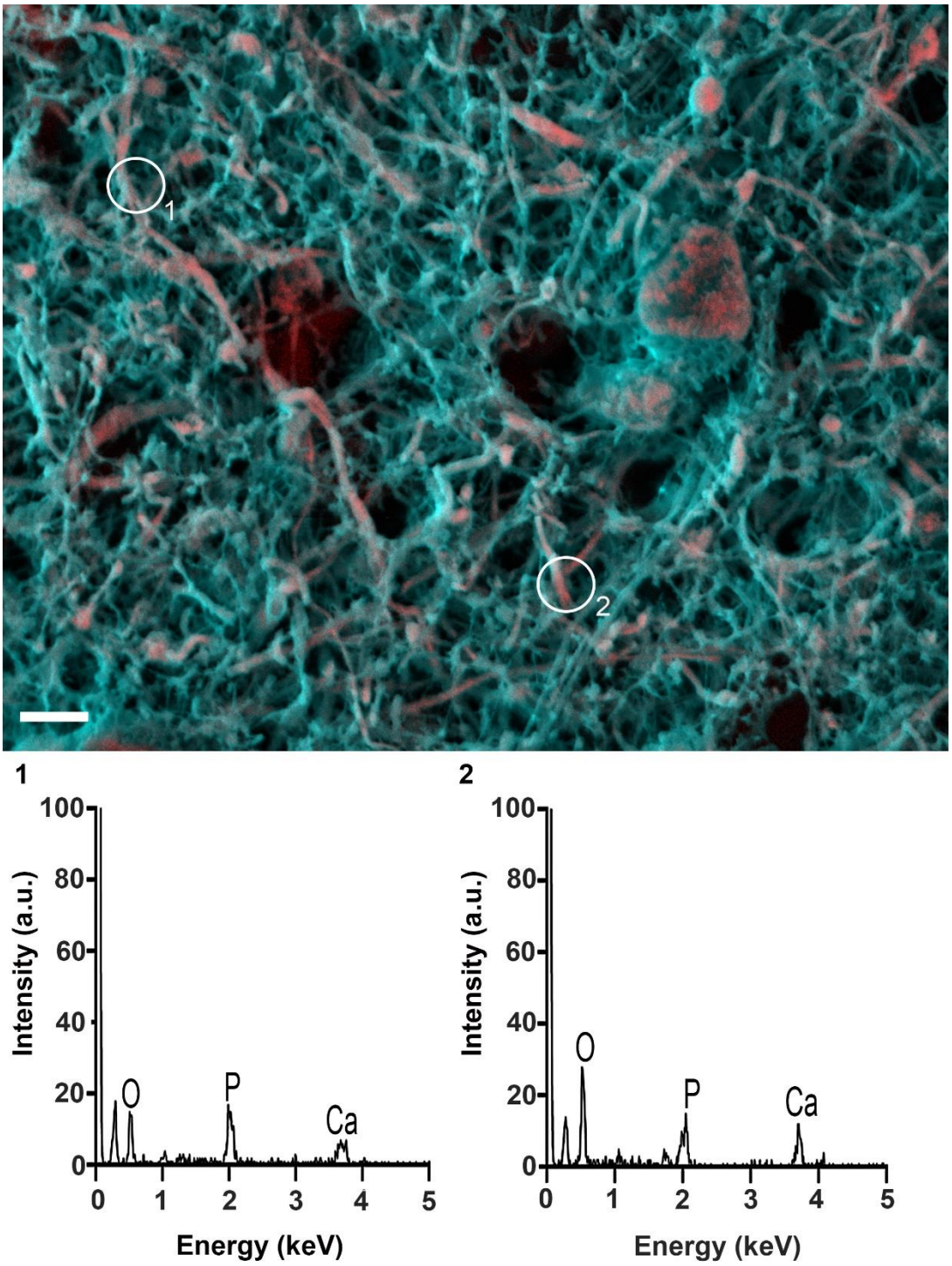

Figure 6.4: DDC-SEM image of calcified fibres observed in the basal ganglia of an AD patient where pink-red indicate calcification and turquoise indicates tissue. *EDS analysis indicated that all calcified fibres were formed by calcium and phosphorus only. Scale bar = 10 µm.*

Calcified spheres and fibres were observed in any of the three brain parts investigated, in 72% of the AD cases and 77% of the elderly cases (Figure 6.5 (a)). In individual brain regions, however, more cases presenting calcification were found in the AD group (Figure 6.5 (a)). It was observed that even though in the elderly group calcification was found in more cases, in 53% of these cases calcification was found in only one brain region, in 47% in two anatomical regions and only in 6% of the cases in all three anatomical regions studied (Figure 6.5 (b)). On the other hand, in the AD cases, calcification was found in only one region in 50% of the cases, 12.5% of the cases had calcification in two anatomical regions, and 37.5% in three anatomical regions (Figure 6.5 (b)). Interestingly the temporal lobe appeared to be more prompt to mineralisation as more cases presented minerals in this region in both groups. No such mineralisation was observed in the young donor group.

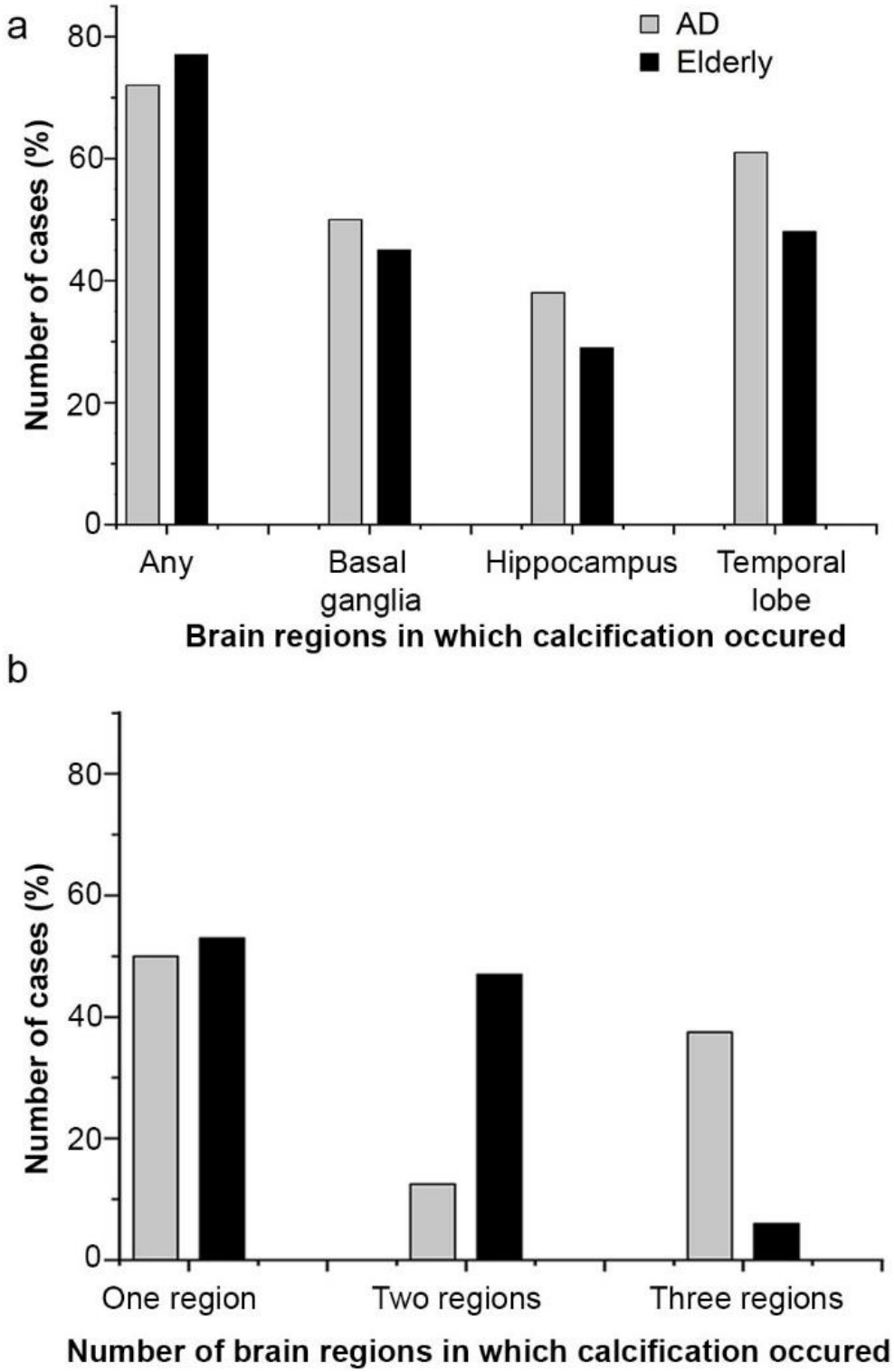

Figure 6.5: Percentage of total cases showing calcification. (a) *Total number of cases in which calcification was observed and number of cases in which calcification was observed in the basal ganglia, hippocampal region and temporal lobe sections.* ***(b)*** *Number of cases in which calcification was observed in one, two or three anatomical locations. Grey bars represent the AD group and black bars the elderly control group, for both graphs.*

Based on these results, the occurrence of the minerals did not suggest any clear relationship between an AD pathophysiology; therefore, our attention was drawn to the particular pattern of calcification remaining consistent despite anatomical location. The same pattern of calcification was observed in the outer layers of the tissue in all three brain regions, basal ganglia (Figure 6.6 (a, b, c)), temporal lobe (Figure 6.6 (d, e, f)), and hippocampal region (Figure 6.6 (g, h, i)), even though the number of minerals and the occurrence of spheres and fibres in the calcified bands was observed to be varying between samples.

For the basal ganglia sections, in AD patients, calcified spheres were observed in 45% of the cases, while only 27% presented calcified fibres (Figure 6.6 (c)). In the elderly control group, 36% presented calcified spheres and 32% calcified fibres (Figure 6.6 (c)). Calcified spheres were observed in the hippocampal region of 38% and 29% of the AD and elderly cases respectively (Figure 6.6 (f)), while 33% of the AD and 19% of the elderly cases presented calcified fibres (Figure 6.6 (f)). Finally, in the temporal lobe, 61% of AD cases presented calcified spheres and 33% fibres (Figure 6.6 (i)), in comparison to 42% and 38% of the elderly cases which presented calcified spheres and fibres respectively (Figure 6.6 (i)). It was therefore concluded that calcified spheres are slightly more prevalent in the AD group. On the other hand, the calcified fibres did not show a clear association with any group.

To the best of our knowledge, neither types of calcification (calcified spheres and fibres) nor calcification pattern have been observed in human brains before. Therefore, the exact anatomic location of the calcification band was also investigated. This was done through the examination of nuclear fast red counterstained or haematoxylin and eosin samples, which allowed the visualisation of anatomical structures to aid the identification of the exact anatomical location. Based on the examination of these slides and anatomical information provided by the tissue biobanks (from which the tissues were obtained), it was concluded that the calcification band in the basal ganglia was always observed in the outer layers of the caudate nucleus. In the hippocampal area, the calcification was only observed in the outer layers of the parahippocampal gyrus and the temporal lobe in the outer cortex layers of Brodmann areas 21 and 22 (middle and superior temporal gyrus respectively).

Investigating the relation of these areas to AD and cognitive impairment, it was found that the caudate nucleus contains neural clusters that are connected to cortical areas involved in cognitive and emotional processing. Lesions in the nucleus have been found to cause impairments in multiple cognitive and behavioural domains, while changes in its shape have been observed in Alzheimer's patients (219, 220). The parahippocampal gyrus is the outer cortex region of the brain that is located below the hippocampus, and it is a part of the temporal lobe. It is primarily formed by grey matter,

and it is responsible for visual perception. Similarly, the middle and superior temporal gyri are also primarily formed by grey matter; however, the regions are believed to be responsible for auditory and virtual naming as well as visual perception (198). As parts of the temporal lobe, all of the three gyri are affected in AD and other neurodegenerative dementias (203). Additionally, in regards to changes related to AD pathology, both amyloid plaques and neurofibrillary tangles have been observed in increased amounts in these gyri, marking the temporal lobe, as a whole, one of the most affected areas of the brain (219, 458).

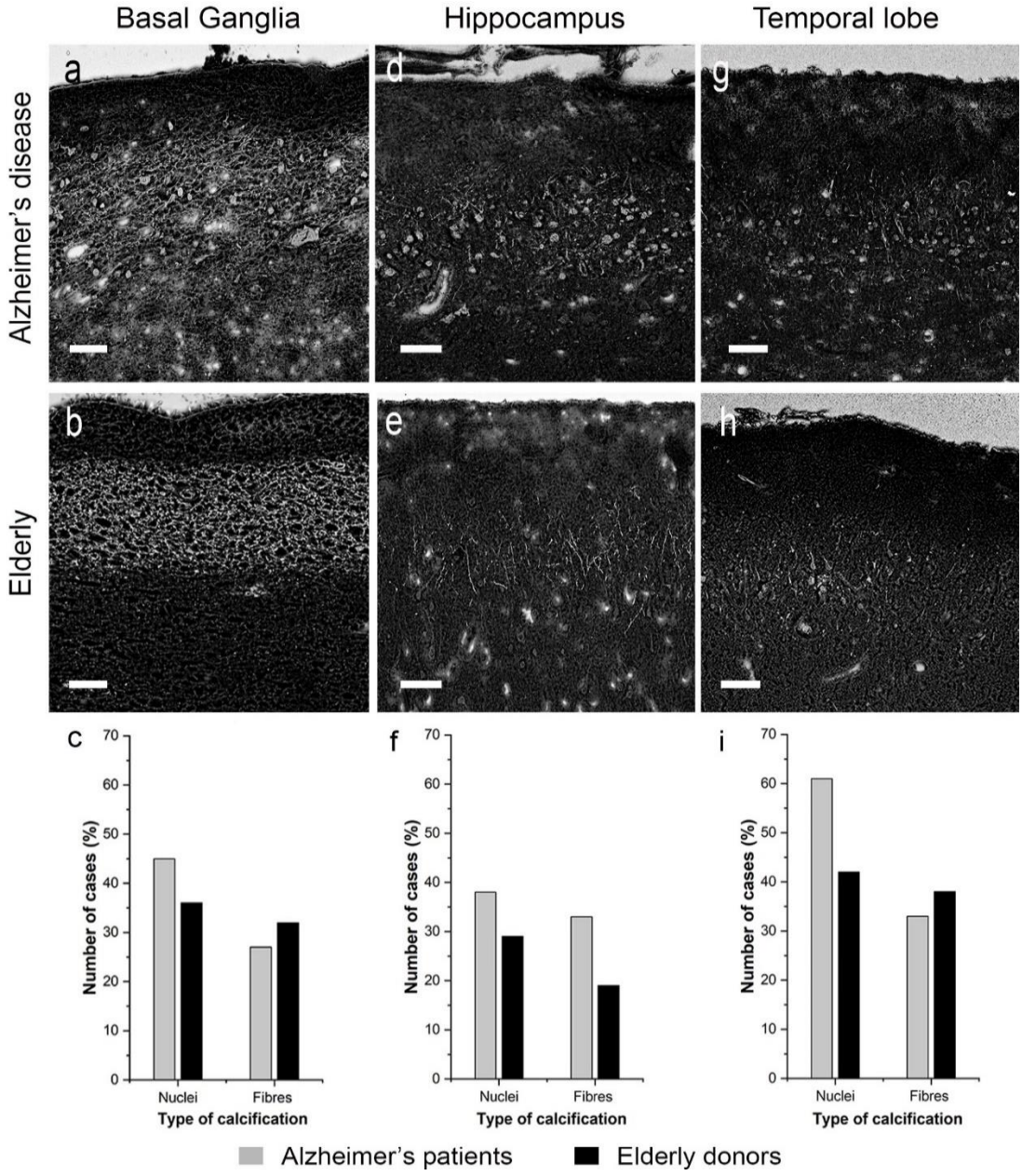

Figure 6.6: BSE images showing the calcification pattern observed along with the prevalence of calcified sphere and fibres in the calcified band in the basal ganglia, hippocampal and temporal lobe tissues. (a) *Calcification pattern observed in the basal ganglia of an AD patient and* ***(b)*** *in the basal ganglia of an elderly donor.* ***(c)*** *Number of cases in which calcified spheres and fibres were observed in the basal ganglia.* ***(d)*** *Calcification pattern observed in the parahippocampal gyrus of an AD patient and* ***(e)*** *the parahippocampal gyrus of an elderly donor.* ***(f)*** *Number of cases in which calcified spheres and fibres were observed in the parahippocampal gyrus.* ***(g)*** *Calcification pattern observed in the in the middle and superior temporal gyrus of an AD patient and* ***(h)*** *in the middle and superior temporal gyrus of an elderly donor.* ***(i)*** *Number of cases in which calcified spheres and fibres were observed in the in the middle and superior temporal gyrus. Scale bars = 150 µm.*

Taking into account the anatomical location of the calcification; in the outer cellular layers of the neocortex (predominantly spread in the molecular, external granular and pyramidal layers) and the caudate nucleus both of which contain neuronal bodies, it was hypothesised that the calcified spheres might correspond to calcified nuclei, and at least some of them correspond to neural cells. The dimensions of the calcified spheres were analysed as observed on SEM images. These dimensions were then compared to the dimensions obtained by fluorescent images of the same micro-anatomical locations with nuclear staining (DAPI). Samples from four cases were stained, in which no calcification was observed. The aim was to compare whether stained nuclei in the same anatomical regions have the same dimensions as the minerals to gain a first indication on their origin. The results of the diameter measurements on 350 calcified spheres and 350 DAPI stained nuclei indicate that indeed the two structures had a similar diameter range. Calcified spheres as previously mentioned had an average diameter of 8.08 µm with a standard deviation of ± 2.76 µm, while the DAPI stained nuclei were found to have an average diameter of 7.516 µm with a standard deviation of ± 1.82 µm (Figure 6.7).

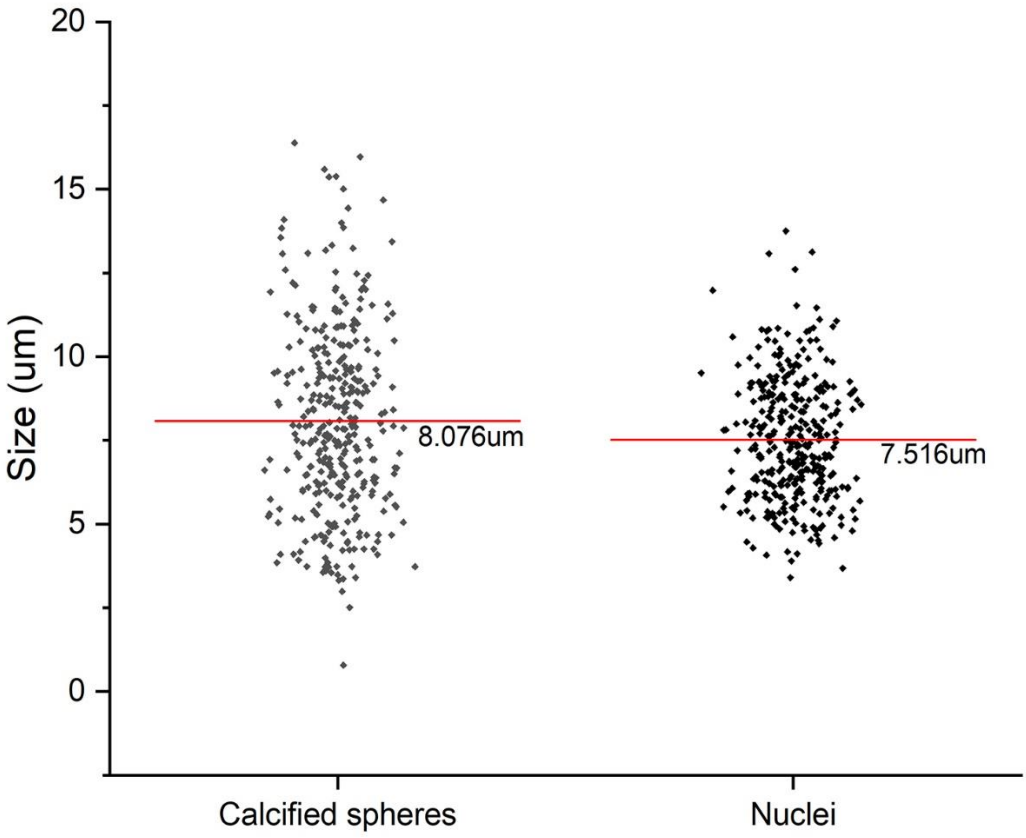

Figure 6.7: Scatter plot showing the size distribution of 350 calcified spheres and 350 DAPI stained nuclei in the same anatomical region.

This finding suggested that the mineral observed could indeed correspond to calcified cell nuclei, thus from this point on, we will refer to calcified spheres as calcified nuclei. Additionally, based on the broad range of dimensional values observed in both the SEM and fluorescence images, it was suggested that possibly the calcification does not affect only one cell type but rather both glial or neuronal cells, as these present nuclei of slightly different sizes. However, as the measurements were done on histological slides, a large number of nuclei were observed as cross-sections, not whole; therefore, the dimensional differences might also correspond to different cross-sectional regions. Furthermore, based on both distributions, it was not possible to identify two individual groups of diameter ranges, which would correspond to bigger and smaller nuclei.

To evaluate the presence of organic material in the calcified nuclei, which would further support the hypothesis of cell nuclei mineralising, the minerals were cut and imaged using a FIB-SEM. TEM analysis was also carried out to gain more information on the mineral structure. The results showed that the FIB cut nuclei encapsulated organic material (Figure 6.8 (a)) while the TEM imaged FIB prepared sections showed a needle-like structure (Figure 6.8 (b, c)) which comes in agreement with the high-resolution SEM images obtained (Figure 6.8 (d)). Interestingly, the selected area electron diffraction (SAED) indicated an amorphous material (Figure 6.8 (c)), suggesting a simple physicochemical precipitation rather than a cell-mediated process (459).

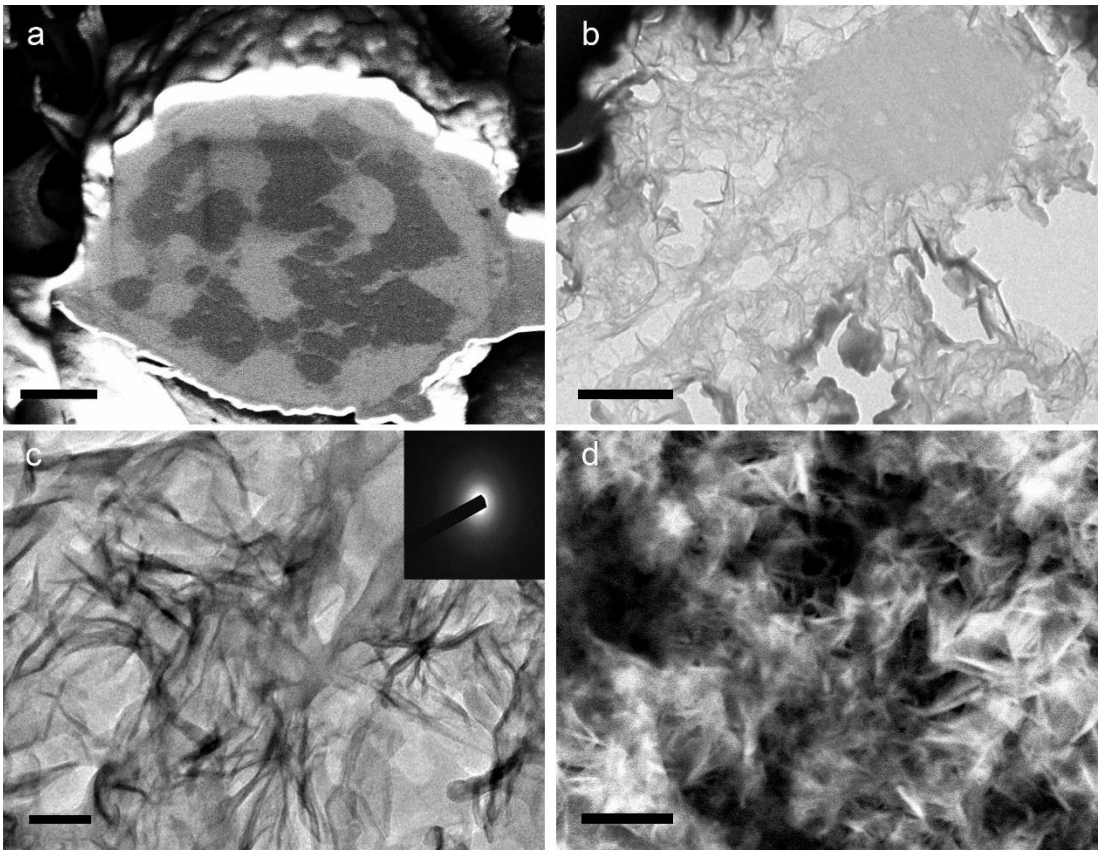

Figure 6.8: Internal structure of the calcified nuclei. (a) *SEM micrograph of FIB cut sample indicated that the mineral contains organic material inside. Scale bar = 400 nm.* ***(b)*** *TEM micrograph of FIB cut prepared section of the same material shows an unorganised internal structure of mineral surrounding areas of organic material. Scale bar = 500 nm.* ***(c)*** *Higher magnification TEM micrograph of the mineral shows a needle-like structure, while the SAED pattern (inset) shows an amorphous material. Scale bar 100 nm.* ***(d)*** *High magnification SEM image of a cross-section of a calcified nucleus also shows a needle-like structure. Scale bar = 1 µm.*

Interestingly, during the SEM and FIB analysis, it was also observed that some of the calcified nuclei and fibres were attached, resembling neuronal bodies (Figure 6.9). Such structures were only observed in AD. Despite their low prevalence in the SEM analysed samples, the presence of these structures indicated that the calcified fibres could be calcified neuronal axons.

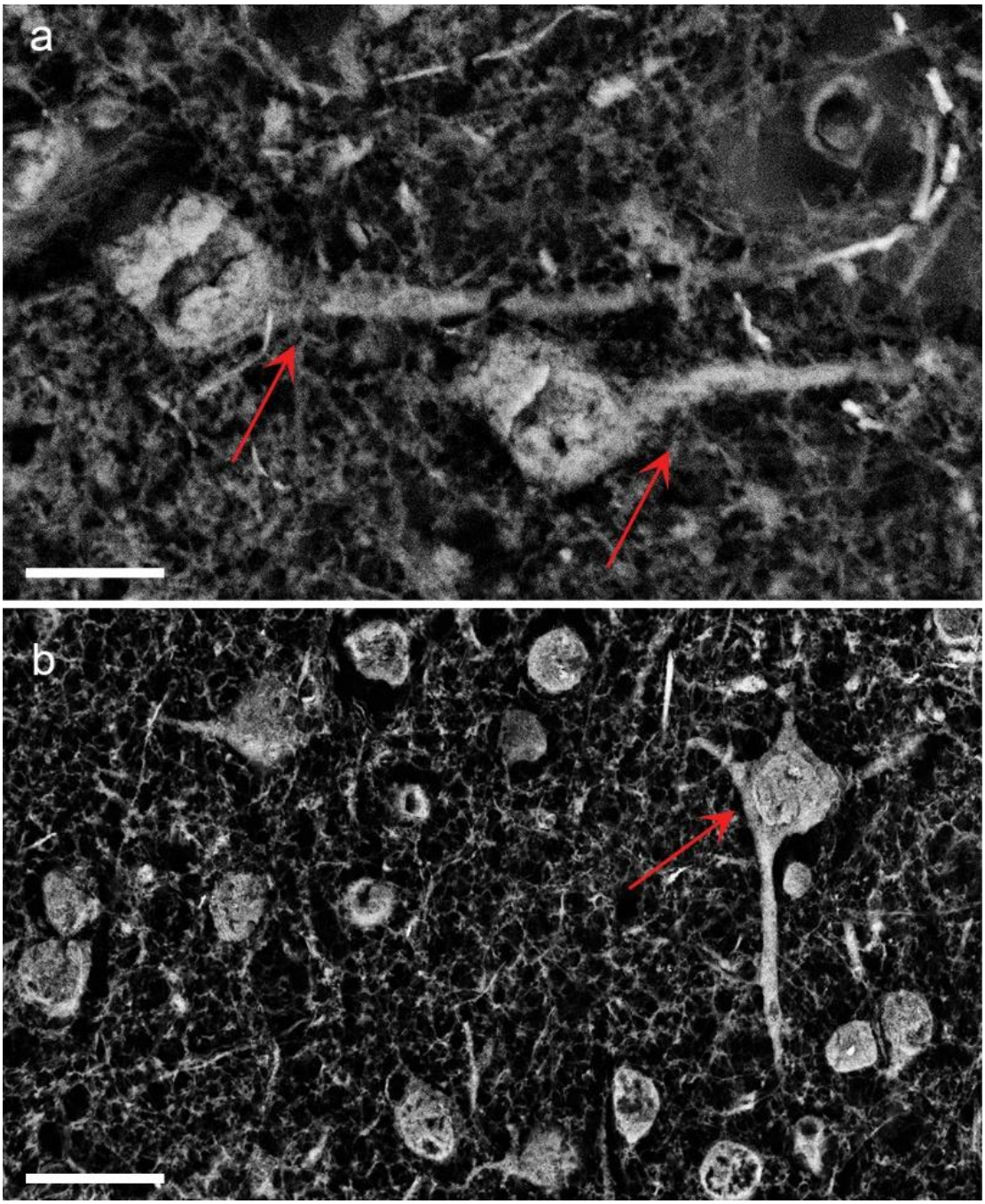

Figure 6.9: BSE micrographs of calcified structures observed in AD brains resembling neuronal bodies, where the inorganic material is shown as light grey/white and the organic material as black/dark grey. (a) *BSE micrograph showing two calcified structures resembling neurons (arrows). Scale bar = 10 µm.* ***(b)*** *BSE micrograph showing a calcified structure resembling a neuronal cell with the cell body and nucleus being distinguished (arrow). Scale bar = 15 µm.*

Based on the electron microscopy analysis it was therefore hypothesised that the mineralisation processes leading to the calcified nuclei and the calcified fibres are related to cellular degeneration and possibly cell death either as a consequence or a

cause, rather than an osteogenic or another cell-mediated process. Neuronal nuclear calcification has, to the best of our knowledge, never been observed in humans before; however, the nuclei of dead cells have been reported to undergo deposition of calcium and phosphorus (460, 461). Intracellular mineralisation in astrocytes has also been previously reported in chick brains but not in humans (462). The same study also reports the possibility that some of the mineralised cells are neurons; however, this was not proven (462). Additionally, a study in areas of neural degeneration due to ischemic episodes has reported calcification in the mitochondria of dendrites and neural somas, but no nuclear calcification was reported (463).

As the calcification was not observed in young brains, it was also concluded that the mineralisation process might be partially a result of ageing. The fact that calcified nuclei were more prevalent in the AD cases indicated, however, a possible correlation with AD pathology. This was also suggested by the calcification pattern observed, a similar pattern reported in Braak staging for AD, observed in areas stained for neurofibrillary tangles (464). Therefore, the similarity in the pattern might also suggest that some of the calcified nuclei and cell bodies observed belong to neuronal and glial cells affected by tau related pathological changes.

6.3.2 Role of pTau in brain mineralisation

The presence of neurofibrillary tangles has been suggested to lead to functional and morphological abnormalities and cell death (219, 464-471). On the other hand, some studies suggest that the neurofibrillary tangles as an individual entity are not harmful to the neurons but a toxic soluble form of pTau protein, is instead responsible for the damage as it has correlated to elevated calcium levels in neurons, loss of dendrite shape and cell death (465, 468, 472-478). Either way, based on the electron microscopy results, it was hypothesised that it is possible that a form of pTau protein is also responsible or at least has a role in the mineralisation processes lead. Arguably, pTau protein might not explain the presence of minerals in elderly brains as it is considered an AD hallmark. Studied have, however, shown that neurofibrillary tangles are also present in many individuals with no AD diagnosis.

Analysis of the clinical data for the set of samples analysed in this work for both the AD and elderly cases indicated that AD-associated changes were also observed in the elderly group patients, even though no AD diagnosis was made. Concerning the calcification, the analysis also indicated that most cases in which calcification was present had brain changes associated with Braak staging. All AD patients had a Braak stage four or five while most of the elderly patients had changes corresponding to Braak stages one, two or three. The observation could, therefore, suggest that the

presence of calcification in the brains of elderly donors is a result of low levels of AD pathology changes. Despite, some AD cases pathologically classified with Braak stages four and five did not present calcification in the regions investigated; as a result no specific correlation between Braak staging and the presence or amount of calcification in the specific brain regions could be made.

To test the arising hypotheses, the next step of the work was to verify that the calcified 'nuclei' are indeed cell nuclei and to examine the correlation of pTau protein to the calcification pattern observed. Immunofluorescence staining for the visualization of cellular DNA present in the nuclei (DAPI), pTau protein and calcification (OsteoSense 680EX) in the hippocampal region and the temporal lobe was therefore carried out. In agreement with the SEM results, in the fluorescence imaging, it was possible to observe a similar pattern of calcification in AD patients and elderly donors (Figure 6.10 (a, b)). No OsteoSense staining was observed in any of the tissues obtained by young donors (Figure 6.10 (c)).

Analysis of the fluorescence staining using 30 sampling points (n = 30) obtained from five patients from each group, indicated that in AD patients, calcification covered 38 ± 24% of the tissue in calcified regions (Figure 6.10 (d)). On the other hand, for the elderly organ donors, the calcification covered only 4 ± 9% of the calcified tissue region (Figure 6.10 (d)). This shows that even though elderly patients develop the same type of calcification in their brain, the amount of calcification found is considerably lower than in AD patients. The statistical analysis also indicated a p-value smaller than 0.0001, showing a statistically significant difference between the two groups, suggesting that the amount of calcification can be correlated to AD pathology. Subsequently, the cases with increased amounts of calcification were corresponding to Braak staging four and five, while low amounts of calcification were observed in donors with pathological changes corresponding to Braak stages one, two and three. No direct correlation, could although be made between specific amounts of calcification and the individual five levels of Braak staging independently of the regions investigated.

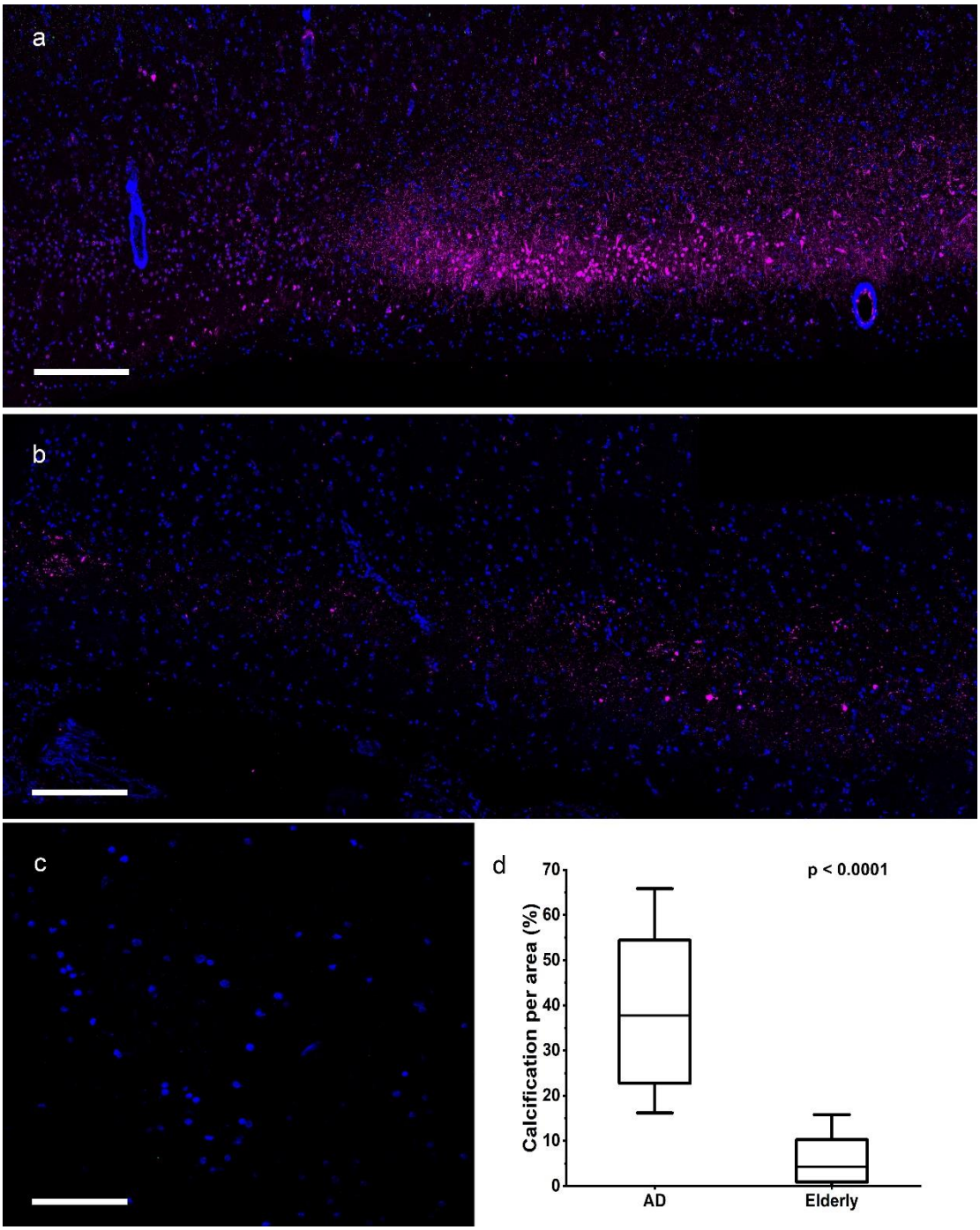

Figure 6.10: Immunofluorescence staining of brain tissue using OsteoSense 680 (magenta) and DAPI (blue). (a) *Calcification pattern observed in the temporal lobe of an AD case.* ***(b)*** *Calcification pattern observed in the hippocampus of an elderly donor. Scale bars = 300 µm.* ***(c)*** *No OsteoSense staining was observed in the samples obtained from young donors. Scale bar = 70 µm.* ***(d)*** *The spatial density of the staining between AD cases and elderly donor cases indicates a spatial density of calcification much higher in AD patients than in the elderly donors (n = 30). Statistical analysis indicated a p-value smaller than 0.0001, indicating a statistically significant difference between the two groups.*

At a closer inspection, it was possible to identify that OsteoSense staining was overlapping with nuclear staining, confirming the assumption of the presence of nuclear calcification. Co-occurrence analysis indicated that in AD patients, 78 ± 21% of the nuclear staining overlapped with the calcification staining (Figure 6.11 (a, c)). On the other hand, nuclear calcification was not as prominent in elderly donors, with only 6 ± 28% of the nuclear staining overlapping with calcification (Figure 6.11 (b, c)). In addition, it was possible to notice that the OsteoSense staining overlapped with DAPI staining in 48 ± 18% and 15 ± 23% of the AD and elderly cases respectively (Figure 6.11 (d)). This result supported the SEM results, which showed a considerable amount of calcification in the form of fibres. Subsequently, out of the total amount of calcification observed in AD patients, 48% was in the form of nuclear calcification, and 52% was fibre or other forms of calcification, while in the elderly cases only 15% of the calcification was in the form nuclear calcification with the rest (85%) being other minerals, predominantly in the form of fibres.

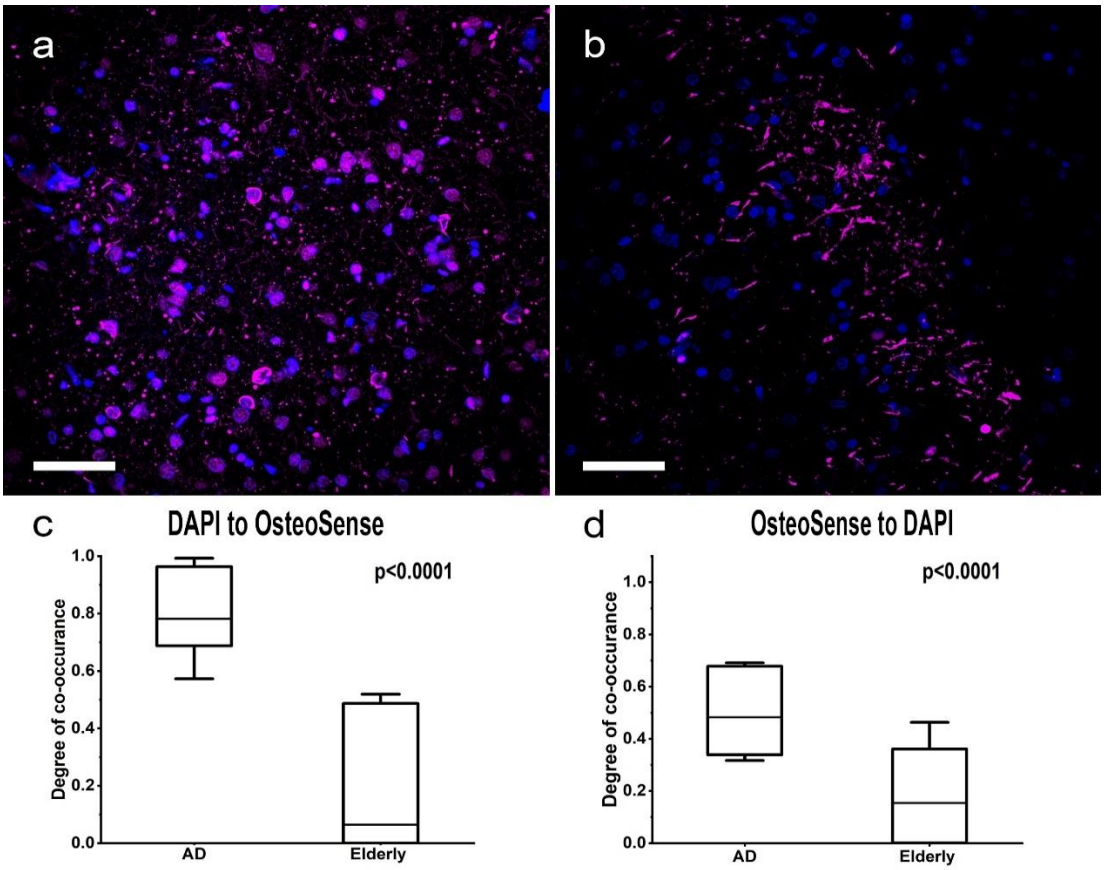

Figure 6.11: DAPI (blue) and OsteoSense 680 (magenta) co-occurrence in AD and elderly cases. (a) *Fluorescence image showing OsteoSense staining overlapping with DAPI staining in the temporal lobe of an AD case.* ***(b)*** *Fluorescence imaging showing a small amount of OsteoSense staining overlapping with DAPI staining in the hippocampal region of an elderly donor case. Scale bars = 40 µm.* ***(c)*** *Box blot showing the amount of DAPI co-occurrence with OsteoSense (n = 30), indicating a statistically significant difference (p < 0.0001).* ***(d)*** *Box blot indicating the amount of OsteoSense co-occurrence with DAPI (n = 30), indicating a statistically significant difference (p < 0.0001).*

The presence of pTau in the calcified regions was also observed, while it was possible to identify elevated amounts of pTau staining in the AD group as expected. Interestingly though pTau staining was not only observed around cell nuclei but was also co-localising with the DAPI staining (Figure 6.12 (a, b)). In AD cases 53 ± 17% of pTau staining was found in the nucleus (Figure 6.12 (c)), while in elderly donors, the amount of pTau associated to nuclei was 41 ± 26% (Figure 6.12 (c)), showing that there is a statistically significant correlation between nuclear pTau and AD pathology. Furthermore, in 53 ± 35% and 12 ± 13% of the observed nuclei, co-occurrence with pTau staining was observed (Figure 6.12 (d)), indicating a significant correlation with AD pathology again.

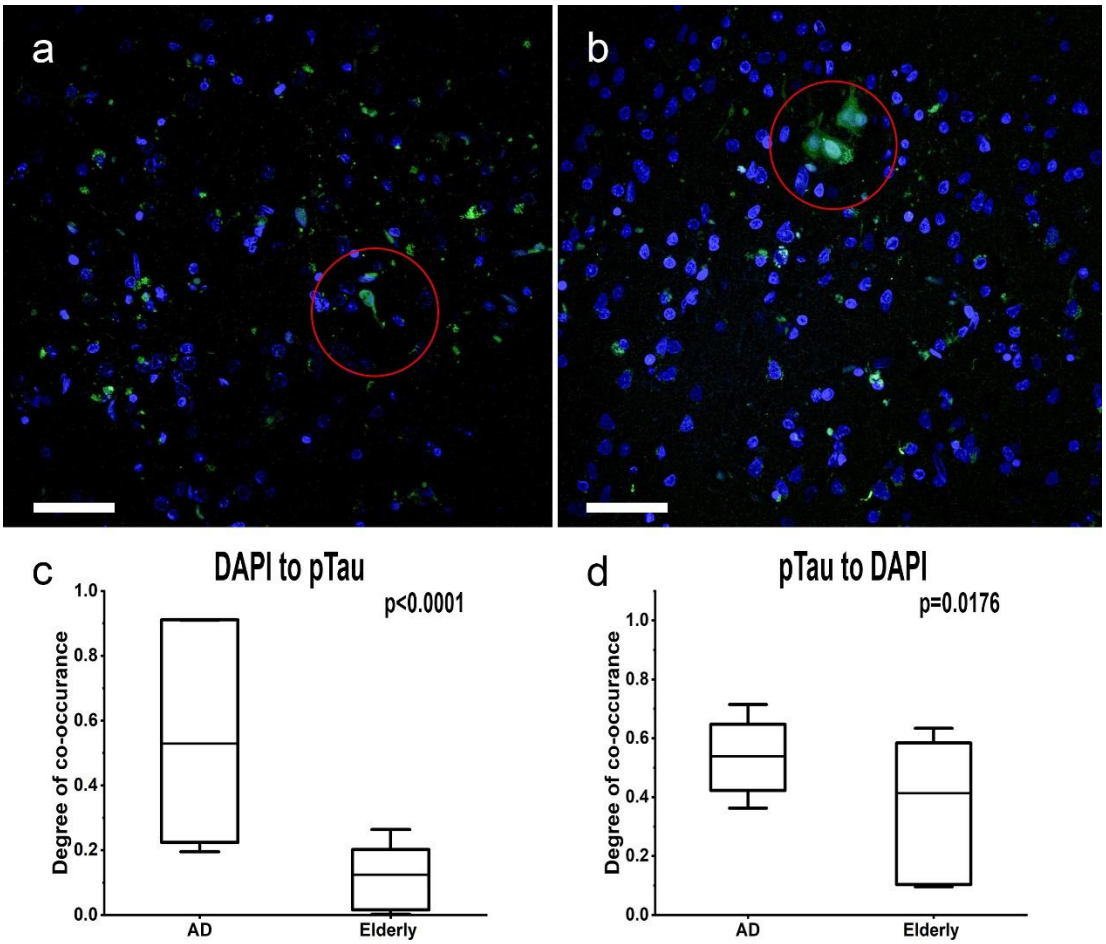

Figure 6.12: DAPI (blue) and pTau (green) co-occurrence in AD and elderly cases. (a) *Fluorescence image showing pTau staining overlapping with DAPI in the temporal lobe of an AD case.* ***(b)*** *Fluorescence imaging showing pTau staining overlapping with DAPI staining in the hippocampal region of an elderly donor case. Scale bars = 40 µm.* ***(c)*** *Box blot showing the amount of DAPI co-occurrence with pTau (n = 30), indicating no statistical significance between the two groups difference (p<0.0001).* ***(d)*** *Box blot showing the amount of pTau co-occurrence with DAPI (n = 30), indicating a statistically significant difference (p=0.0176).*

The association of Tau protein with cell nuclei in both AD patients and elderly individuals has been previously reported (479), while nuclear tau has also been observed in other cell types such as fibroblasts (480). Its presence in the nucleus is suggested to be due to its ability to attach to DNA, acting protectively against age-related changes (481, 482). Even though it was initially believed that phosphorylated tau does not occur in the nucleus, studies have indicated that this is not true (482). A study has also suggested that tau phosphorylation might take place in other parts of the cell, with the resulting phosphorylated protein penetrating through to the nucleus (483).

Our observation of pTau in the nuclei comes in agreement with other studies; however, it is not the intention of this work to examine whether phosphorylation of tau happens within or outside the nucleus. What can be concluded is that an increased amount of nuclear pTau has been observed in the AD group, in which the amount of nuclear calcification is also substantially more than that observed in the elderly group. Therefore, it was concluded that the presence of nuclear pTau might play a role in the mineralisation process.

To investigate that, the relationship between pTau staining and calcification (Figure 6.13 (a, b)) was also evaluated. It was found that the OsteoSense staining was overlapping with pTau staining in 51 ± 33% and 16 ± 23% in the AD and elderly cases respectively (Figure 6.13 (c)) showing a statistical significance between the two groups. Additionally, 83 ± 24% and 19 ± 35% of the pTau staining was overlapping with OsteoSense in the AD and elderly groups, respectively (Figure 6.13 (d)). The co-occurrence of the two stains was observed within the nuclei, the calcified cell bodies and fibres.

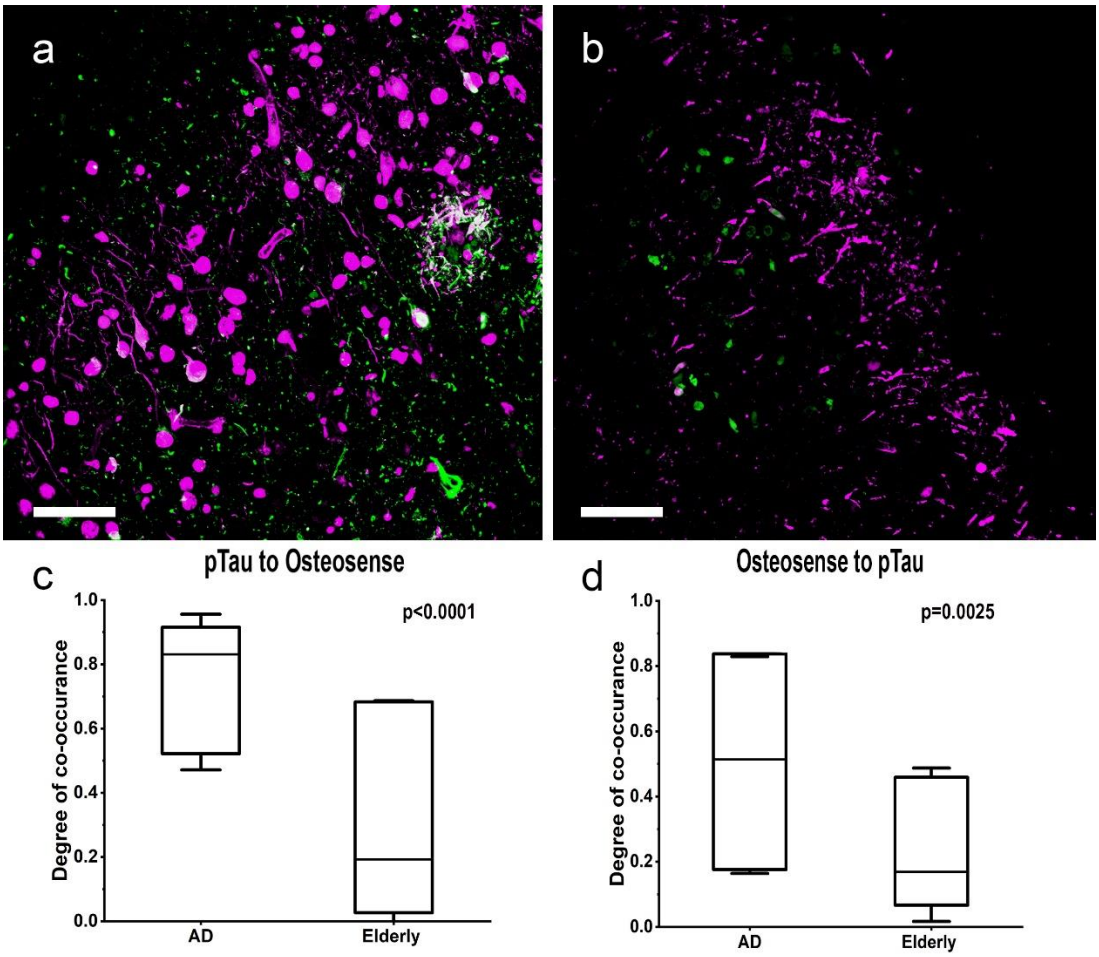

Figure 6.13: OsteoSense (magenta) and pTau (green) co-occurrence in AD and elderly cases. (a) *Fluorescence image showing pTau staining overlapping with OsteoSense staining in the temporal lobe of an AD case****. (b)*** *Fluorescence imaging showing little pTau staining overlapping with OsteoSense staining in an elderly donor case.* ***(c)*** *Box blot indicating the amount of pTau staining co-occurrence with OsteoSense (n = 30), indicating a statistical significance between the two groups difference (p < 0.0001). Scale bars = 15 µm.* ***(d)*** *Box blot showing the amount of OsteoSense co-occurrence with pTau (n = 30), indicating a statistical significance between the two groups (p = 0.0025).*

The results confirmed the original hypothesis; pTau protein was found to be associated with the mineralisation processes giving raise to calcified fibres, cell bodies, and nuclei. Even though no neuronal staining was done on the same samples, the fact that the calcified fibres were overlapping with pTau staining (Figure 6.14 (a)) confirms that these are neuronal axons and dendrites. In the AD cases, it was also possible to identify calcified, cellular somas as also indicated by SEM, some of which resembled neurons (Figure 6.13 (a), Figure 6.14 (b, c, d)). The identity of these cells was confirmed trough the imaging of brain tissues stained for microtubule-associated

protein 2 (MAP2), a marker used for the identification of dendrites, axons, and neuronal bodies (484) (Figure 6.15). Furthermore, the overlapping of some of the mineralised cell bodies with pTau staining (Figure 6.14. (a, c)), and the similarities between their shape and neurofibrillary tangles (Figure 6.14 (b, d)), suggested that some of the mineralised cells were neuronal bodies presenting neurofibrillary tangles, further supporting a correlation with AD pathology.

Additionally, based on the staining observed, some of the calcified neuronal bodies did not present any pTau protein staining (Figure 6.14 (d)), which was considered to be due to different degrees of cell mineralisation, instead of the absence of pTau protein. This could be due to the mineral leading to protein degradation or their encapsulation, not allowing the penetration of the antibodies. Other than the pTau staining, the intensity of the DAPI staining was also observed to vary between mineralised nuclei; with the DAPI intensity decreasing as the OsteoSense intensity was increasing. In some cases, it was also possible to observe mineralised nuclei with no DAPI staining.

Therefore, it was suggested that the results on the degree of co-occurrence of different labels obtained by the quantitative analysis might be slightly different from the actual values. Based on the results, it was concluded that the exact amount of co-occurrence between pTau, DAPI, and OsteoSense might be higher than the values obtained in the analysis carried out in this work. As this would be, however, the case in both the AD and elderly groups, the differences between the two groups would possibly remain constant. Additionally, this might explain the heterogeneity in the amount of co-occurrence that was observed within the two groups.

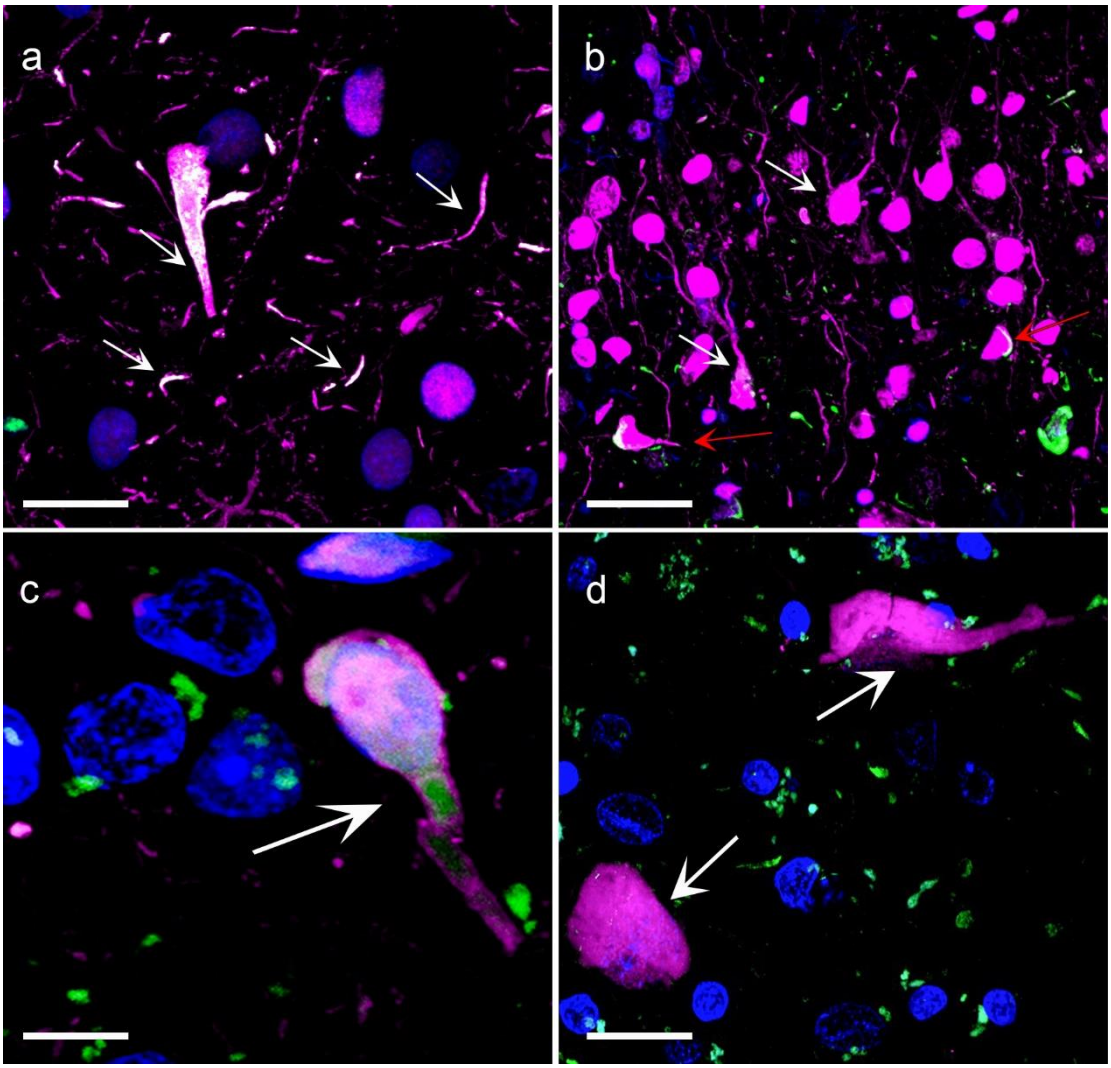

Figure 6.14: Fluorescent images obtained from AD brains stained with DAPI (blue), OsteoSense (magenta), and pTau (green) showing mineralised neurons. ***(a)*** *Image taken in the parahippocampal gyrus region showing calcified fibres overlapping with pTau staining (white arrows). Scale bar = 15 µm.* ***(b)*** *Image taken in the temporal cortex where some of the calcified structures resemble neurons (white arrows). Some calcified structures resemble neuronal cell bodies in which pTau staining can also be observed (red arrows). Scale bar = 40 µm.* ***(c)*** *Image taken in the parahippocampal gyrus region showing a structure resembling a neuron where pTau staining can also be observed (arrow). Scale bar = 10 µm.* ***(d)*** *Image taken in the parahippocampal gyrus region showing structures similar to neurofibrillary tangles with no pTau staining observed (arrows). Scale bar = 15 µm.*

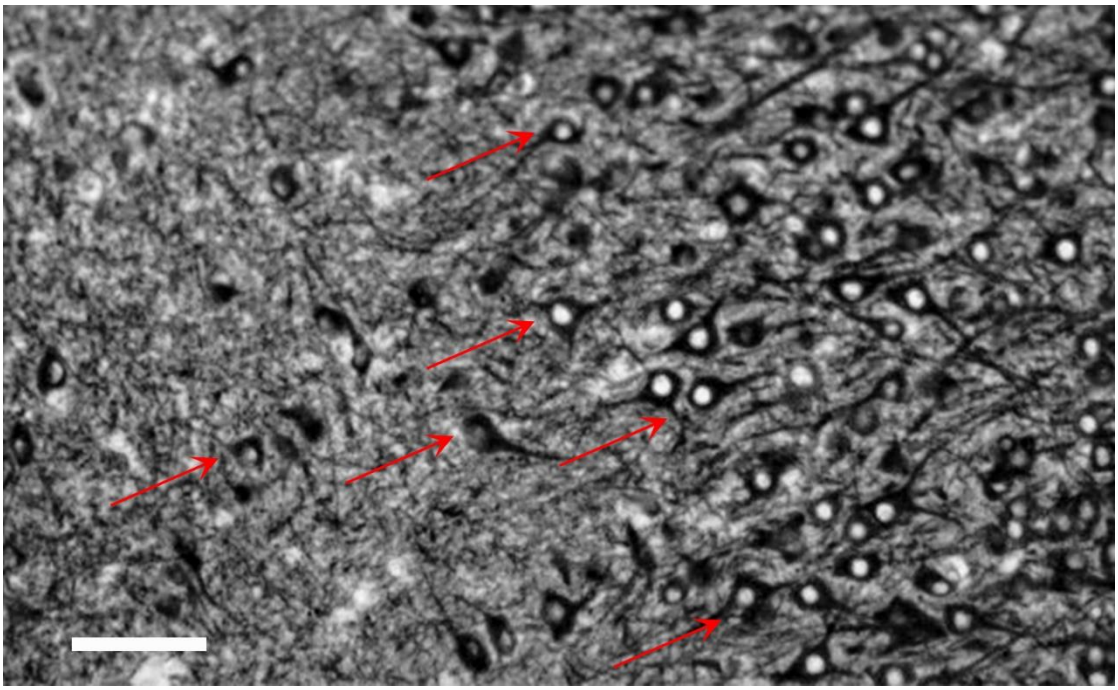

Figure 6.15: Optical microscopy image showing neuronal cells (arrows) stained by a MAP-2 antibody. *Scale bar = 60 µm.*

Other than neurons, structures resembling possibly glial cells such as astrocytes (201), activated microglia (202), or oligodendrocytes (197) were observed (Figure 6.16). No work was done to confirm the identity of these cells; however, the observation suggested that mineralisation processes are not cell-specific, but are rather affecting a whole region in which all cells are calcifying. More work needs to be done at a cellular level to understand the exact mechanisms of mineralisation and why these are contained within cell bodies and not penetrating through to the extracellular matrix. One possibility could be that the interneuron movement of tau protein and its different forms (473) might lead to the calcification being contained within the neural cell, with a mineralised neuron triggering mineralisation in the surrounding cells. For glial cells, the mineralisation process might have a similar 'domino' effect, with neurons becoming calcified causing the glia cells, they interact with, to also calcify. In addition, the presence of pTau and neurofibrillary tangles has also been associated to the degeneration of glial cells in the affected areas, which might also be responsible for the mineralisation process.

As previously mentioned the hypothesis of a cell death driven mineralisation process is also supported by the physicochemical properties of the mineral showing an amorphous material. Despite, based on the staining results, it is not possible to identify whether these cells are undergoing apoptotic or necrotic changes; the nuclei of apoptotic and necrotic cells at late stages disintegrate to form smaller bodies (485,

486), changes which could be distinguishable by the DAPI staining. However, the possibility that these cells are undergoing early apoptotic or necrotic changes cannot be eliminated.

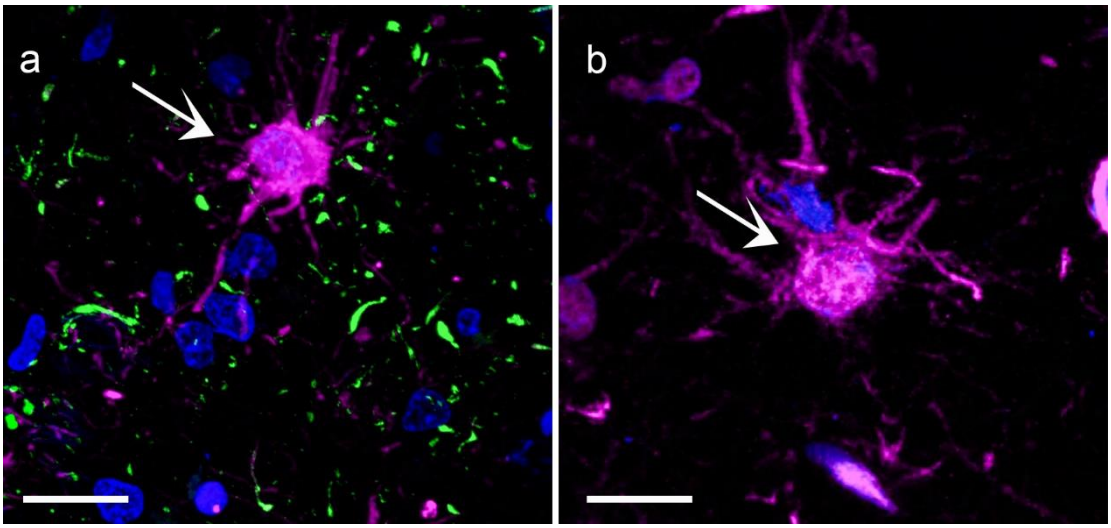

Figure 6.16: Fluorescent images obtained from AD brains stained with DAPI (blue), OsteoSense (magenta), and pTau (green) showing mineralised cells resembling glial cells. (a) *Image from the temporal lobe showing a structure similar to a glial cell (arrow). Scale bar = 20 µm.* ***(b)*** *Image from the hippocampal region showing a structure similar to a glial cell (arrow). Scale bar = 10 µm.*

Finally, based on the results of the IF staining, not all cells that presented nuclear pTau and neurofibrillary tangles were calcified. Also, it is worth to note that regions of high pTau protein concentrations in the AD brains were also observed, which did not present any calcification. For example, neurons in the hippocampus a structure involved in AD pathology from the early stages did not present any calcified neurons despite the high amount of pTau staining. This could indicate that specific regions are more susceptible to mineralisation than others due to factors other than the presence of pTau protein.

6.4 Conclusions and future work

Our results, confirmed the presence of calcium phosphate minerals in the brains of both AD patients and elderly donors, while no minerals were observed in the brains of young donors. The main types of calcification observed were vascular calcification, and calcified nuclei, cell bodies, and fibres. Calcification of neuronal and glial cell bodies was observed, which to the best of our knowledge was not reported before in humans. The number of calcified nuclei and fibres was found to be substantially more in the AD group and can be attributed to the elevated amounts of neurofibrillary

tangles, and nuclear or cellular pTau protein observed in the brains of AD patients both in our work and in the literature (217). As a large amount of calcification was correlated with pTau staining, it was concluded that the protein has a crucial role in the mineralisation process.

Even though this work has achieved its aims on characterising the minerals present in the brain and examining the correlation between brain calcification and a hallmark of AD pathology, more work needs to be done to understand the mineralisation mechanisms fully. Firstly, staining using apoptotic and necrotic markers should be carried out to identify whether the mineralised cells are undergoing cell death changes prior to the mineralisation process. This will indicate whether mineralisation processes are directly related to cell death. However, *in vitro* work is needed to understand whether cell death induces cellular mineralisation or the other way around. Furthermore, a better understanding of the cellular profile of the mineralised regions will also give accurate information on the type of cells calcifying. A proteomics profiling of these cells and cells in regions where no mineralisation was observed, will allow differences to be identified which might lead to specific cell types being more susceptible to degeneration, cell death, and calcification. Additionally, the effect of mineralised cells on the surrounding cells should also be investigated *in vitro,* which will add to our understanding of the progression of cellular mineralisation and whether this has any effect on AD progression.

To conclude, the results of these work show for the first time cellular and nuclear mineralisation of human brain cells. Further work needs to be done to understand in detail the mineralisation processes involved; however, the results of this work indicated a relationship between pTau protein and mineralisation in AD brains. Whether the accumulation of pTau protein leads to cell death and subsequently mineralisation or the other way around should be further investigated. Either way, our findings hint for the first time that cellular mineralisation has a role in AD development and cognitive impairment, as inevitably the presence of minerals would cellular connections and the surrounding cells.

Chapter 7: Conclusions

7.1 Summary of results

This work has provided new data on pathological minerals found in the cardiovascular, breast, and brain tissues.

To the best of our knowledge, this is the first time neuronal (nuclear and intracellular) mineralization has been observed in the brains of elderly donors and Alzheimer's disease patients. Additionally, it is the first time that the relationship between phosphorylated tau and cellular brain mineralization is reported, hinting on a complex mineralisation mechanism possibly affecting the progression of Alzheimer's pathology as the presence of minerals in tissues has a range of effects on the surrounding cells. As a result, fully comprehending the mineralisation processes taking place could add to our understanding of Alzheimer's disease and neurodegeneration in general.

Furthermore, this work reports for the first time the diagnostic potential of distinct whitlockite nanoparticles in malignant invasive breast tumours. Even though the presence of magnesium containing calcium phosphate has been reported in breast calcification before, the unique properties of the mineral had not been investigated in depth. Despite the clear association of these particles with invasive malignancies reported in this work, a study of a larger scale in a clinical setting should be carried out to validate the results. Moreover, the presence of the whitlockite nanoparticles also hints a uniqueness in the invasive tumour microenvironment leading to their formation. As a result, understanding the mineralisation mechanisms and the effect these nanoparticles have on cancer cells will provide vital information on cancer progression and metastasis.

Finally, the presence of the whitlockite nanoparticles in tumour vasculature hinted a new mechanism of mineral formation originating from the blood, possibly shared with calcific cardiovascular diseases where the same nanoparticles are also observed. The investigation on the possible origins of these nanoparticles observed in cardiovascular tissue led to the conclusion that platelets and possibly platelet dense granules are involved in their formation. These results unveiled a new pathway towards treatment and prevention methods for calcific cardiovascular diseases, as prevention of the formation of the whitlockite nanoparticles could also prevent the onset or the progression of the diseases.

7.2 Limitations and challenges

Most of the challenges encountered throughout this work were successfully addressed; however, unfortunately, not all limitations and challenges could be tackled.

For example, even though the physicochemical characterization of the minerals did not present any significant challenges, a higher number of samples in specific subgroups and more extensive available clinical information could have aided the identification of other correlations between the mineral properties and specific pathophysiological features widely used in the clinic. It was unclear from this work whether the amount of phosphorylated tau associated with calcification reflects the pathological Braak staging of Alzheimer's disease due to the lack of a sufficient amount of samples for each staging. Additionally, the absence of calcification in some AD brains could not be correlated to any of the available information; thus, it was unclear why this was the case. Subsequently, only the correlation of high amounts of calcification to phosphorylated tau and AD pathology, in general, could be made.

Similarly, it was not determined whether the whitlockite nanoparticles are related to tumour characteristics other than type and grade, such as staging, metastatic status, and genetic information as such information was not provided. Moreover, the restricted number of grade 1 invasive breast tumour samples (as breast cancer cases are usually not diagnosed that early on) would give more precise data on the presence of the particles early on in the disease, which will add to their diagnostic potential. A limited amount of samples was also the reason why no investigation of the origins of the whitlockite nanoparticles in breast tissue was carried out. As a result, as the same nanoparticles observed in breast malignancies were also found in cardiovascular diseases; their origins were studied indirectly through the study of such particles in aortic tissue.

Lastly, whilst in the study of the whitlockite nanoparticles in aortic tissue, no such limitations were encountered due to the extensive presence of particles in practically all individuals; other challenges were noted. For instance, the obtainment of enough fresh samples (less than 24 hours after extraction), suitable for a range of biochemical assays to be used, was proven to be difficult. This was mainly the case due to the extensive optimization needed for these methods to be applied to the study of pathological minerals, which had as a result for the majority of tissue to be used before the final experiments were contacted. As a result, methods using fixed tissues were proven more beneficial in parts of the study.

7.3 Scientific contribution

Despite the limitations, the results provide new insights on pathological mineralization mechanisms, different from osteogenic processes usually reported in the literature. The unique minerals observed in soft tissues suggest complex processes involved, some of which might indeed involve osteogenic cells and features. For example, as mentioned earlier in this work, some of the minerals observed (large apatite calcifications in breast tissues), could be a result of such processes. In contrast, the properties and location of the whitlockite nanoparticles suggested a different formation mechanism, thus should not be omitted. Furthermore, some pathological minerals have been thought to be a result of cell death, thus being irrelevant in the development of diseases. The study of the brain minerals in Alzheimer's disease has although suggested that even though cell death could be responsible for their presence or be a consequence of mineralisation, a complex process related to the development of the disease has led to the mineralization events that in return will promote the progression of the pathology.

This work also highlights the benefits of the direct study of pathological minerals as the methods used unveiled important information on their nature and origins. As discussed previously, protocols used for inorganic features (for example, cells and tissues) might be unsuitable for the study of minerals, which can make the research on pathological mineralization challenging. Subsequently, probably the most significant contribution of this work to the scientific community is the identification of suitable techniques for the in-depth study of biological minerals. A considerable amount of the research presented here has focused on evaluating the applicability of many methods and the optimization of traditional sample preparation protocols, methods and techniques used in other biological fields such that they can be employed directly to pathological minerals. These same optimized protocols and methods can also be used for the study of physiological minerals and mineralizing models, aiding the understanding of the mineralization mechanisms. Application of these same methods in the evaluation of proposed mineralizing models will additionally assist the development of more suitable models for pathological mineralisation as the minerals present can be easily compared to those found in native tissues.

7.4 Future work

The next steps following on from this thesis include a complete proteomics profiling of the minerals to enable an understanding of all the proteins and cells in-

volved in the mineralization processes. For example, even though it is clear that phosphorylated tau plays a role in brain mineralization and platelets are associated to the presence of the whitlockite nanoparticles, information on proteins, other than the ones investigated in this work, present in the minerals will shed light on the exact processes taking place. It is also essential to identify the processes through which the associated cells can produce these minerals, which can be done *in vitro* (through cell culture or using other artificial ways to recreate what is happening *in vivo*). In this step, it will be important to compare the produced minerals *in vitro* with the minerals found *in vivo* using the same material methods for characterization. Finally, the effects of these specific minerals on the tissue microenvironment and the surrounding cells need also to be investigated through possibly cell culture experiments. Such results will then be used to produce good mineralisation models that will aid the understanding of the exact effects the minerals have on the progression of specific diseases and to also identify possible biological targets for the prevention of their formation through cell culture, animal work, and eventually clinical studies.

Furthermore, this study has concentrated on the basic research of pathological minerals, not an in-depth association of the mineral nanoscale properties to particular clinical classifications. It is, therefore, also crucial for such associations to be made for better comprehension of the mineral occurrence in relation to diseases both in an academic setting and also in the clinic. As previously mentioned, the main limitation of this work was the restricted number of available samples and limited clinical information. Subsequently, the next steps should include a more targeted study to be able to correlate the minerals observed with other pathophysiological features widely used in the clinic.

Following, studies in close collaboration with clinicians could also include clinical imaging data of the patients, which can indicate whether the appearance of the minerals at the macroscale can be correlated to its appearance at the nanoscale. Such a study will probably be more relevant in breast cancer research due to the diagnostic potential of the whitlockite nanoparticles. For example, mammographic data and information on the location from where the biopsy was taken, would allow for the mineral properties identified in this study to be associated with their mammographic appearance if possible, which could also aid the diagnostic process in the clinic. Studies of a similar workflow can also be employed in the research of Alzheimer's disease and calcific cardiovascular diseases to aid early diagnosis. However, work using suitable mineralisation animal models is also needed in these cases as a biopsy can not be obtained for the study. Therefore the macroscopic appearance of the associated minerals in the animal models at the onset of the diseases could assist their detection at early, more manageable stages.

Appendix A: Pregnancy-induced placenta calcification

The results presented in this appendix were part of a collaborative project and have been published in the research paper: Anthis AHC, Tsolaki E*, et al., Nano-analytical characterization of endogenous minerals in healthy placental tissue: mineral distribution, composition and ultrastructure, Analyst 2019, 144 (23), 6850-6857, doi: https://doi.org/10.1039/C9AN01312A. * These authors contributed equally as first authors.*

A.1 Introduction

A.1.1 Placenta

In humans, the placenta is essentially the interface between the developing fetus and the mother (Figure A.1). It is divided into the maternal and fetal side (487) (Figure A.1). The fetal side also called the chorionic plate, is the surface where the umbilical cord is attached (200). The umbilical cord is formed by umbilical arteries and veins, transporting blood towards and away from the fetus (Figure A.1). These supply blood to the villous trees (488) which are located in the middle part of the placenta, the lacunae (Figure A.1) that are filled with maternal blood originating from blood vessels of the maternal side. The maternal side of the placenta is called the basal plate and is attached to the uterus (487). The villous trees are the main parts of the placenta and are divided into different villous types (488), which mainly control the exchange of nutrients and gas between the mother and the fetus (487).

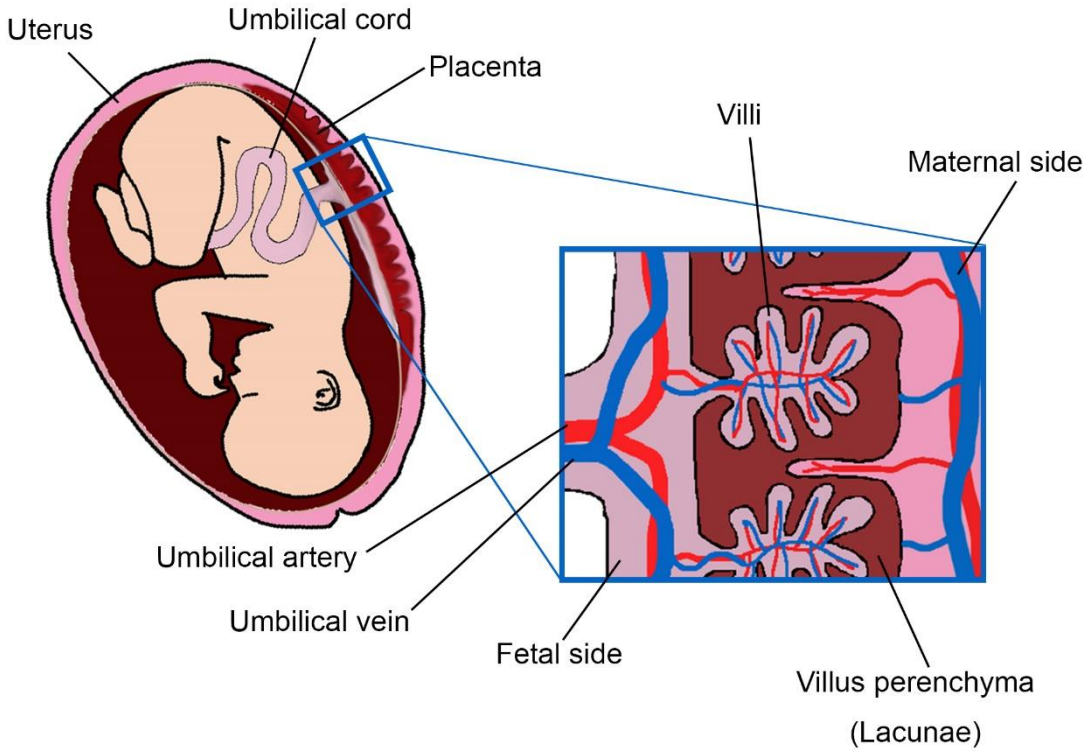

Figure A.1: Graphical illustration of the placenta.

A.1.2 Pregnancy-induced mineralisation

As with other types of calcification, placental calcification is also a well-known phenomenon observed routinely in the clinics. Up to forty per cent of women develop some degree of placental calcification during pregnancy (489). Of all pregnant women, 18% develop severe mineralisation (490), which increases the risk of early preterm labour (491). While it is associated with pregnancy-induced hypertension (PIH) (492) affecting the mother, and can also have unfavourable effects on the growth and maturation of the foetus and of the placenta itself.

Placental mineralisation is divided into different grades, classified according to the Grannum grading system (493). The presence of low amounts of minerals has been suggested to be a natural process and harmless through pregnancy, due to the ageing of the placenta and progressive with gestational age (490, 494), while extensive mineralisation has been shown to carry several risks (495). Studies on these minerals have been carried out in a clinical setting (491, 495, 496) leaving, however, a few open questions. The origins of these minerals remain unknown, but a higher incidence has been correlated to smoking (497), passive smoking (498), and bacterial infections (499). On the other hand, intake of alpha-tocopherol, beta carotene, and vitamin C were found to contribute to the reduction of minerals in placental villi, in some women (497).

As is the case for most other mineralizing pathologies, placental mineralisation is known to be formed from apatite (500, 501), but little work has been done on the characterization of these minerals. Electron microscopy has revealed that calcifications tend to spread over the whole of the placental surface, where different structures have been observed, including mineralized plaques and large concretions (494), all with a calcium-to-phosphorous ratio lower than what is typically found in bone (429, 501). It has therefore been suggested that placental mineralisation is caused by supersaturation of the physiological solutions surrounding the tissue such as blood, rather than either the physiological process of bone formation or the dystrophic processes caused by tissue necrosis (501).

A.1.3 Aims

Despite the strong correlation between placental calcification and fetal outcome, the minerals have been only rarely researched, as most studies providing information are done through histological analysis or medical imaging such as ultrasound. Therefore the primary aim of this work is to investigate the exact ***physicochemical properties of the minerals found in the placental tissue*** and to examine ***whether any type of mineral can be associated to the fetal and maternal side of the placenta.***

A.2 Materials and methods

A.2.1 Samples

The project was done in collaboration with Professor Inge K. Hermann (ETH Zurich and the Swiss Federal Laboratories for Material Science and Technology (EMPA) St Gallen, Switzerland) which holds ethical approval. Fourteen human placentas were obtained from uncomplicated term pregnancies after caesarean section from the Kantonsspital St Gallen (KSSG), from two different locations; the fetal and maternal part. Written informed consent was obtained prior to delivery. Animal placentas from different species were also obtained including; four cat, two dog, two horse, and two rabbit placentas.

A.2.2 Scanning electron microscopy

For SEM analysis, the samples were prepared as detailed in c*hapter 3, section 3.3.2*. A Hitachi S-3499N, a Carl Zeiss Crossbeam, and a LEO were used at an accelerating voltage of 10 kV for SEM imaging, and Oxford Instruments energy-dispersive X-ray detectors integrated on the machines were used for elemental analysis.

A.3 Results and discussion

Scanning electron microscopy of the human placentas showed the presence of large mineral structures (Figure A.2 (a)) distributed throughout the samples. Two distinct structures could be identified; calcified particles (Figure A.2 (b)) and needle-like (Figure A.2 (c)) structures.

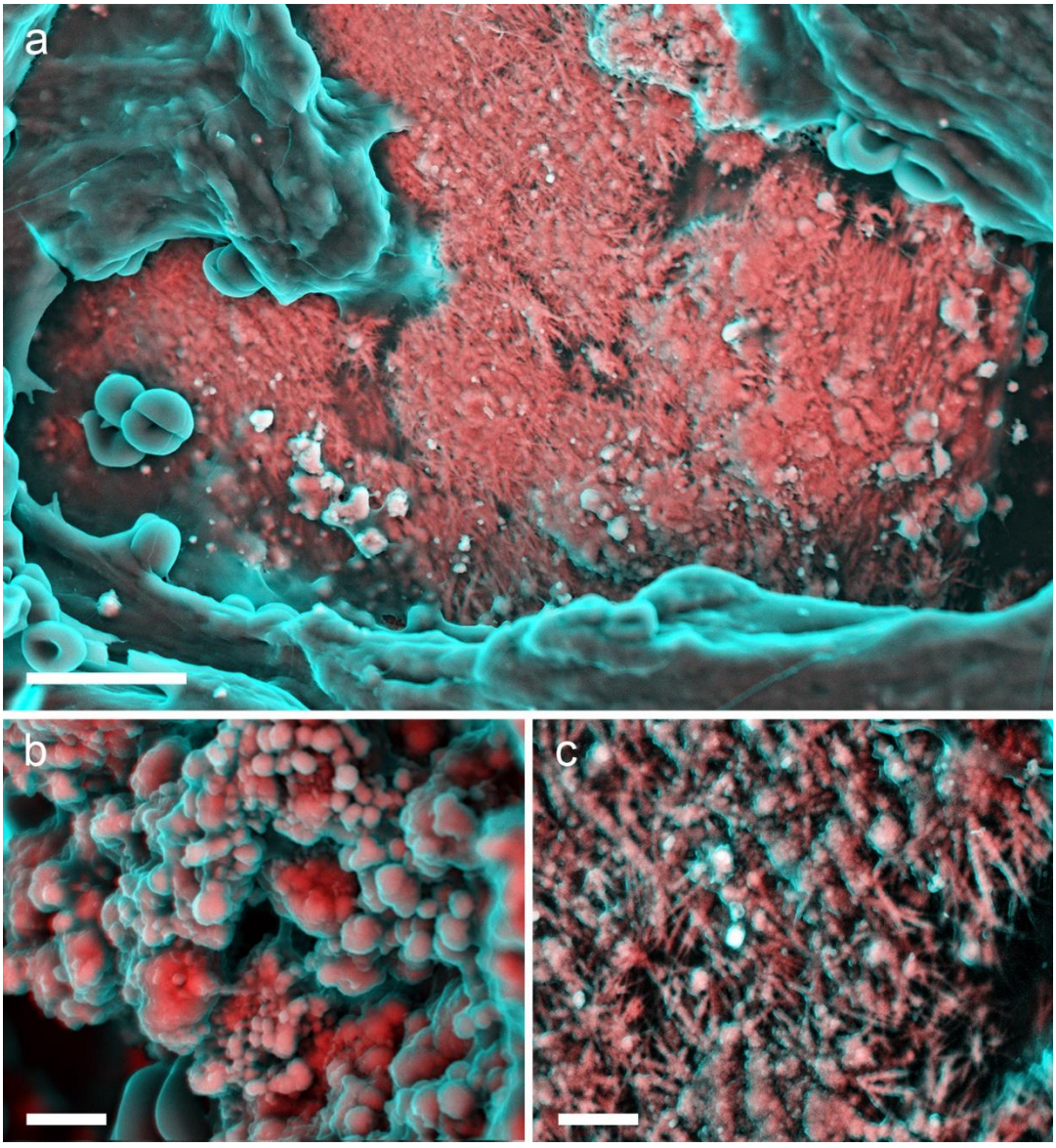

Figure A.2: Electron micrographs of minerals found in placental tissue, where inorganic material is indicated by red/pink and organic material by turquoise. (a) *DDC-SEM micrograph of a large mineral structure surrounded by organic material. Scale bar = 10 µm.* ***(b)*** *DDC-SEM micrograph of calcified particles and* ***(c)*** *needle-like mineral structures. Scale bars = 2 µm.*

Chemical composition analysis of the same samples indicated that the particle (Figure A.3 (a)) and needle-like (Figure A.3 (b)) structures contained calcium, phosphorus, and magnesium. On the other hand, minerals observed which did not have

such morphology, but instead presented a poorly defined shape (Figure A.4) were found not to contain magnesium (Figure A.4). The elemental composition of the minerals was also confirmed through Raman spectroscopy measurements (102).

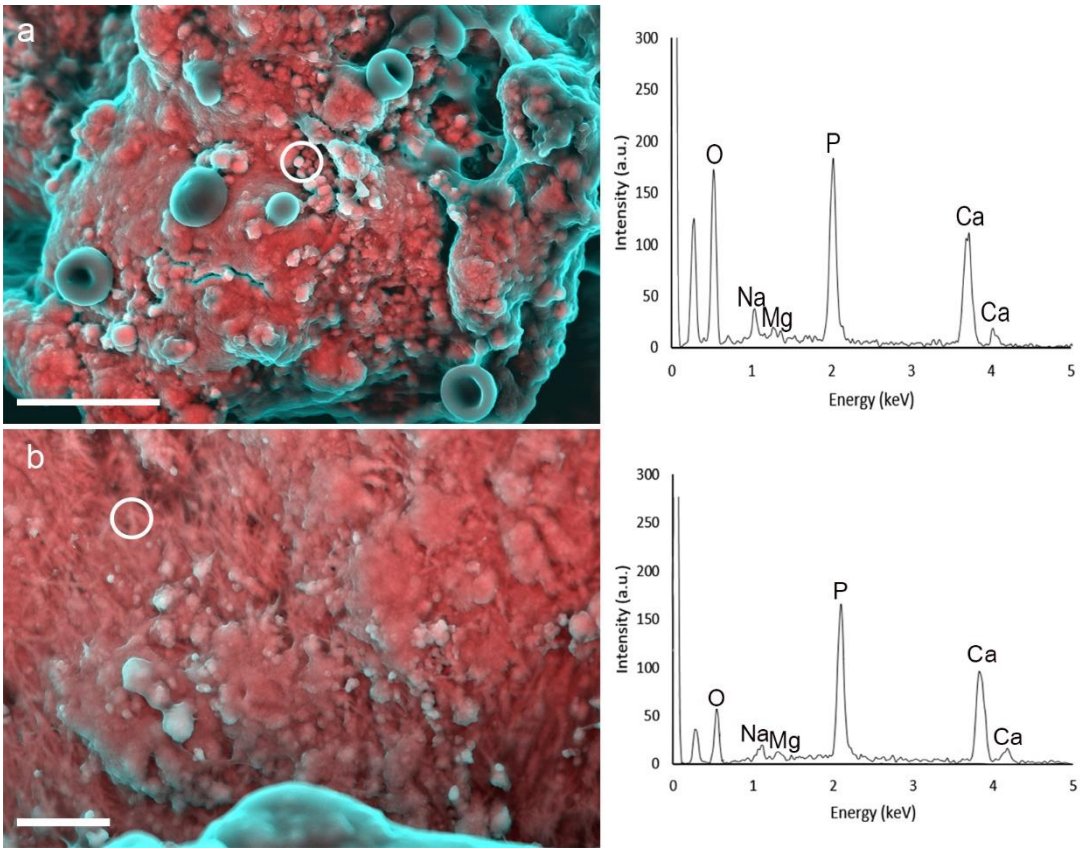

Figure A.3: Electron micrographs and corresponding EDS spectra of particle and needle-like mineral structures. (a) *DDC-SEM of mineral containing particle-like structures with EDS spectrum of the region marked by a white circle. Scale bar = 10 µm.* ***(b)*** *DDC-SEM of mineral containing needle-like structures with EDS spectrum of the region marked by a white circle. Scale bar = 5 µm.*

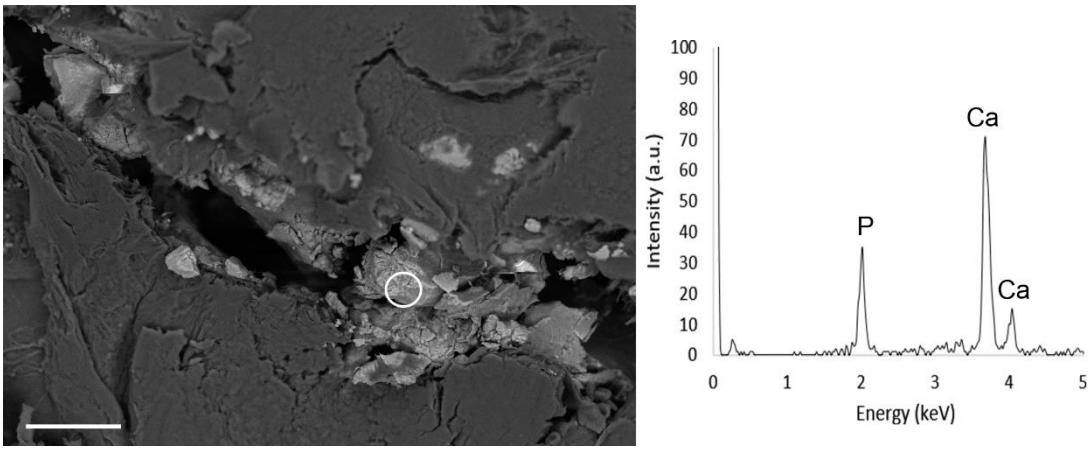

Figure A.4: Electron micrograph and corresponding EDS spectrum of mineral with no definitive shape. *Backscattered electron micrograph of mineral of no definitive shape with EDS spectrum of the region marked by a white circle. Scale bar = 25 µm.*

Similar calcified particles containing magnesium were reported in this work in breast, brain, and cardiovascular tissues, however, some of the particles observed in the placenta were much bigger than those observed in the other tissues. Based on these results, it was concluded that some of the particles might have the same origins as those in other tissues despite not being explicitly observed in the vasculature. The large amounts of blood the placenta contains for nutrition purposes might, however, be triggering the mineralisation processes.

On the other hand, the needle-like structures containing magnesium have not been observed previously in association with magnesium containing calcified particles, which hints different origins. Magnesium containing calcium phosphate minerals have been previously observed in dystrophic mineralisation of skin and muscles (502), a result of increased magnesium, calcium, and phosphorus concentrations. Moreover, for the large calcium phosphate minerals, X-ray diffraction patterns done as part of this work confirmed a structure of hexagonal hydroxyapatite (102). Hydroxyapatite has also previously been observed in other tissues. In the placenta, its presence has been reported to be due to tissue necrosis and thus follow metastatic processes (501), while in aortic valve tissue hexagonal hydroxyapatite was believed to be dystrophic (503).

Examining the total amount of minerals, that be magnesium or no magnesium-containing, it was observed to be slightly higher on the maternal side of the placenta than the fetal side. This observation was also confirmed by measurements of the isolated mineral contents of 15 placentas (102). It was found that the median value for the calcium content of the maternal side was 4.8 mg/g, while on the fetal side, it was 1.4 mg/g. However, the variations between individual samples and also between

measurements on different regions of the same sample were considerable, for a definitive significant correlation to be found.

Despite the amounts of minerals observed; some amount of mineral was observed in all human placentas. Therefore, to investigate the effect of gestation time to the presence of minerals, animal placentas were also analysed. Interestingly minerals were not present in the placentas of any of the animals also investigated. This could be due to shorter gestation times for cats, dogs, and rabbits. However, in horses, no calcification was observed regardless of having slightly longer gestation times than humans; therefore, it was concluded unlikely that gestation time is the only factor responsible for placenta mineralisation. Additionally, placental calcification was previously reported in the literature to be observed in mice (504), which have a gestation period of less than a month. The same study suggests that the presence of calcification is associated with poor phosphorus transport control rather than gestation time (504).

A.4 Conclusions

The different amounts and types of calcification identified in this study could hint a possible differentiation between minerals that can induce complications in pregnancies and minerals that are present in the placenta 'naturally'. In addition, the different types of minerals identified in this work hint to a complex process, possibly a result of more than one mineralization mechanism.

More work needs, however, to be done to understand which types of calcification might have an unfavourable effect, which will require more detailed clinical information on any pregnancy complications and the fetal outcome. Such information was not available in this study due to ethical constraints; therefore, the identification of potentially harmful minerals could not be made. The availability of more clinical information could aid the correlation between specific types of mineralization and their anatomical location to adverse health effects. Furthermore, a higher amount of samples is also needed to be able to access any statistically significant differences between mineral amounts and mineral location to clinical complications.

Bibliography

1. Brookmeyer R, Johnson E, Ziegler-Graham K, Arrighi HM. Forecasting the global burden of Alzheimer's disease. Alzheimer's & Dementia. 2007;3(3):186-91.
2. Momenimovahed Z, Salehiniya H. Epidemiological characteristics of and risk factors for breast cancer in the world. Breast Cancer (Dove Med Press). 2019;11:151-64.
3. Yazdanyar A, Newman AB. The burden of cardiovascular disease in the elderly: morbidity, mortality, and costs. Clinics in Geriatric Medicine. 2009;25(4):563-77.
4. Roth GA, Abate D, Abate KH, Abay SM, Abbafati C, Abbasi N, et al. Global, regional, and national age-sex-specific mortality for 282 causes of death in 195 countries and territories, 1980–2017: a systematic analysis for the Global Burden of Disease Study 2017. The Lancet. 2018;392(10159):1736-88.
5. Ginsburg O, Bray F, Coleman MP, Vanderpuye V, Eniu A, Kotha SR, et al. The global burden of women's cancers: a grand challenge in global health. The Lancet. 2017;389(10071):847-60.
6. Laslett LJ, Alagona P, Clark BA, Drozda JP, Saldivar F, Wilson SR, et al. The Worldwide Environment of Cardiovascular Disease: Prevalence, Diagnosis, Therapy, and Policy Issues: A Report From the American College of Cardiology. Journal of the American College of Cardiology. 2012;60(25, Supplement):S1-S49.
7. Xu J, Zhang Y, Qiu C, Cheng F. Global and regional economic costs of dementia: a systematic review. The Lancet. 2017;390.
8. Chen IH, Yang W, Meyers MA. Alligator osteoderms: Mechanical behavior and hierarchical structure. Materials Science and Engineering: C. 2014;35:441-8.
9. Morgan EF, Unnikrisnan GU, Hussein AI. Bone Mechanical Properties in Healthy and Diseased States. Annual Review of Biomedical Engineering. 2018;20(1):119-43.
10. Clarke B. Normal Bone Anatomy and Physiology. Clinical Journal of the American Society of Nephrology. 2008;3(Supplement 3):S131-S9.
11. Abou Neel EA, Aljabo A, Strange A, Ibrahim S, Coathup M, Young AM, et al. Demineralization-remineralization dynamics in teeth and bone. Int J Nanomedicine. 2016;11:4743-63.
12. Tsolaki E, Bertazzo S. Pathological Mineralization: The Potential of Mineralomics. Materials (Basel). 2019;12(19):3126.
13. Bertazzo S, Gentleman E, Cloyd KL, Chester AH, Yacoub MH, Stevens MM. Nano-analytical electron microscopy reveals fundamental insights into human cardiovascular tissue calcification. Nature Materials. 2013;12(6):576-83.
14. Tan ACS, Pilgrim MG, Fearn S, Bertazzo S, Tsolaki E, Morrell AP, et al. Calcified nodules in retinal drusen are associated with disease progression in age-related macular degeneration. Science translational medicine. 2018;10(466):eaat4544.
15. Durgawale P, Shariff A, Hendre A, Patil S, Sontakke A. Chemical analysis of stones and its significance in urolithiasis. Biomedical Research. 2010;21(3).
16. Radi MJ. Calcium oxalate crystals in breast biopsies. An overlooked form of microcalcification associated with benign breast disease. Archives of pathology & laboratory medicine. 1989;113(12):1367-9.
17. Aggarwal KP, Narula S, Kakkar M, Tandon C. Nephrolithiasis: molecular mechanism of renal stone formation and the critical role played by modulators. BioMed research international. 2013;2013.
18. Cox RF, Hernandez-Santana A, Ramdass S, McMahon G, Harmey JH, Morgan MP. Microcalcifications in breast cancer: novel insights into the molecular mechanism and functional consequence of mammary mineralisation. British journal of cancer. 2012;106(3):525.

19. Morgan MP, Cooke MM, Christopherson PA, Westfall PR, McCarthy GM. Calcium hydroxyapatite promotes mitogenesis and matrix metalloproteinase expression in human breast cancer cell lines. Molecular Carcinogenesis: Published in cooperation with the University of Texas MD Anderson Cancer Center. 2001;32(3):111-7.
20. Hutcheson JD, Goettsch C, Bertazzo S, Maldonado N, Ruiz JL, Goh W, et al. Genesis and growth of extracellular-vesicle-derived microcalcification in atherosclerotic plaques. Nature Materials. 2016;15:335.
21. Kapustin AN, Chatrou ML, Drozdov I, Zheng Y, Davidson SM, Soong D, et al. Vascular smooth muscle cell calcification is mediated by regulated exosome secretion. Circulation research. 2015;116(8):1312-23.
22. Kunitake JA, Choi S, Nguyen KX, Lee MM, He F, Sudilovsky D, et al. Correlative imaging reveals physiochemical heterogeneity of microcalcifications in human breast carcinomas. Journal of structural biology. 2018;202(1):25-34.
23. Baker R, Rogers K, Shepherd N, Stone N. New relationships between breast microcalcifications and cancer. British journal of cancer. 2010;103(7):1034.
24. Scott R, Kendall C, Stone N, Rogers K. Elemental vs. phase composition of breast calcifications. Scientific reports. 2017;7(1):136.
25. Frappart L, Boudeulle M, Boumendil J, Lin HC, Martinon I, Palayer C, et al. Structure and composition of microcalcifications in benign and malignant lesions of the breast: Study by light microscopy, transmission and scanning electron microscopy, microprobe analysis, and X-ray diffraction. Human Pathology. 1984;15(9):880-9.
26. Sutor DJ, Wooley SE. The crystalline composition of prostatic calculi. British journal of urology. 1974;46(5):533-5.
27. Dessombz A, Meria P, Bazin D, Daudon M. Prostatic stones: evidence of a specific chemistry related to infection and presence of bacterial imprints. PLOS one. 2012;7(12):e51691.
28. Suh JH, Gardner JM, Kee KH, Shen S, Ayala AG, Ro JY. Calcifications in prostate and ejaculatory system: a study on 298 consecutive whole mount sections of prostate from radical prostatectomy or cystoprostatectomy specimens. Annals of diagnostic pathology. 2008;12(3):165-70.
29. Smolski M, Turo R, Whiteside S, Bromage S, Collins GN. Prevalence of prostatic calcification subtypes and association with prostate cancer. Urology. 2015;85(1):178-81.
30. Cozzolino M, Mazzaferro S, Pugliese F, Brancaccio D. Vascular calcification and uremia: what do we know? American journal of nephrology. 2008;28(2):339-46.
31. Azpiazu D, Gonzalo S, Gonzalez-Parra E, Egido J, Villa-Bellosta R. Role of pyrophosphate in vascular calcification in chronic kidney disease. Nefrologia. 2018;38(3):250-7.
32. Hsu TH-S, Lin S-Y, Lin C-C, Cheng W-T. Preliminary feasibility study of FTIR microscopic mapping system for the rapid detection of the composited components of prostatic calculi. Urological research. 2011;39(3):165-70.
33. Hyun JS. Clinical significance of prostatic calculi: a review. The world journal of men's health. 2018;36(1):15-21.
34. Javadi S, Menias CO, Korivi BR, Shaaban AM, Patnana M, Alhalabi K, et al. Pancreatic calcifications and calcified pancreatic masses: pattern recognition approach on CT. American Journal of Roentgenology. 2017;209(1):77-87.
35. Cros J, Bazin D, Kellum A, Rebours V, Daudon M. Investigation at the micrometer scale of pancreatic calcifications in chronic pancreatitis by µFTIR spectroscopy and field emission scanning electron microscopy. Comptes Rendus Chimie. 2016;19(11-12):1642-55.
36. Ferenczy A, Talens M, Zoghby M, Hussain SS. Ultrastructural studies on the morphogenesis of psammoma bodies in ovarian serous neoplasia. Cancer. 1977;39(6):2451-9.

37. Maki M, Hirota S, Kaneko Y, Morohoshi T. Expression of osteopontin messenger RNA by macrophages in ovarian serous papillary cystadenocarcinoma: a possible association with calcification of psammoma bodies. Pathology international. 2000;50(7):531-5.
38. Mathonnet M, Dessombz A, Bazin D, Weil R, Frédéric T, Pusztaszeri M, et al. Chemical diversity of calcifications in thyroid and hypothetical link to disease. Comptes Rendus Chimie. 2016;19(11-12):1672-8.
39. Oh EM, Chung YS, Song WJ, Lee YD. The pattern and significance of the calcifications of papillary thyroid microcarcinoma presented in preoperative neck ultrasonography. Annals of surgical treatment and research. 2014;86(3):115-21.
40. Saleem S, Aslam HM, Anwar M, Anwar S, Saleem M, Saleem A, et al. Fahr's syndrome: literature review of current evidence. Orphanet Journal of Rare Diseases. 2013;8(1):156.
41. Jaworski K, Styczyńska M, Mandecka M, Walecki J, Kosior DA. Fahr syndrome–an important piece of a puzzle in the differential diagnosis of many diseases. Polish journal of radiology. 2017;82:490.
42. Blanco P, Viallard JF, Ellie E, Faure I, Mercie P, Pellegrin JL, et al. Extensive brain calcifications in systemic sclerosis: two cases. Journal of Neurology, Neurosurgery & Psychiatry. 1999;67(5):697-8.
43. Valenzuela A, Chung L. Management of calcinosis associated with systemic sclerosis. Current Treatment Options in Rheumatology. 2016;2(1):85-96.
44. McCarty Jr DJ, Gatter RA. Recurrent acute inflammation associated with focal apatite crystal deposition. Arthritis & Rheumatism: Official Journal of the American College of Rheumatology. 1966;9(6):804-19.
45. Oliva F, Via AG, Maffulli N. Physiopathology of intratendinous calcific deposition. BMC Medicine. 2012;10(1):95.
46. Chiou H-J, Hung S-C, Lin S-Y, Wei Y-S, Li M-J. Correlations among mineral components, progressive calcification process and clinical symptoms of calcific tendonitis. Rheumatology. 2009;49(3):548-55.
47. Gohr CM, Fahey M, Rosenthal AK. Calcific Tendonitis : A Model. Connective Tissue Research. 2007;48(6):286-91.
48. Halverson PB. Crystal deposition disease of the shoulder (including calcific tendonitis and milwaukee shoulder syndrome). Current Rheumatology Reports. 2003;5(3):244-7.
49. Reynolds TM. ACP Best Practice No 181: Chemical pathology clinical investigation and management of nephrolithiasis. Journal of Clinical Pathology. 2005;58(2):134-40.
50. Cloutier J, Villa L, Traxer O, Daudon M. Kidney stone analysis: "Give me your stone, I will tell you who you are!". World Journal of Urology. 2015;33(2):157-69.
51. Bihl G, Meyers A. Recurrent renal stone disease—advances in pathogenesis and clinical management. The Lancet. 2001;358(9282):651-6.
52. Kamoun A, Daudon M, Abdelmoula J, Hamzaoui M, Chaouachi B, Houissa T, et al. Urolithiasis in Tunisian children: a study of 120 cases based on stone composition. Pediatric Nephrology. 1999;13(9):920-5.
53. Childs MA, Mynderse LA, Rangel LJ, Wilson TM, Lingeman JE, Krambeck AE. Pathogenesis of bladder calculi in the presence of urinary stasis. The Journal of Urology. 2013;189(4):1347-51.
54. Dyer RB, Chen MY, Zagoria RJ. Abnormal calcifications in the urinary tract. Radiographics. 1998;18(6):1405-24.
55. Mendes EM, Meireles-Brandao L, Meira C, Morais N, Ribeiro C, Guerra D. Primary hypoparathyroidism presenting as basal ganglia calcification secondary to extreme hypocalcemia. Clinical Practice. 2018;8(1):1007.
56. Bilezikian JP, Khan A, Potts Jr JT, Brandi ML, Clarke BL, Shoback D, et al. Hypoparathyroidism in the adult: Epidemiology, diagnosis, pathophysiology, target-organ involvement, treatment, and challenges for future research. Journal of Bone and Mineral Research. 2011;26(10):2317-37.

57. Higgins CL, Marvel SA, Morrisett JD. Quantification of calcification in atherosclerotic lesions. Arteriosclerosis, Thrombosis, and Vascular Biology. 2005;25(8):1567-76.
58. Barrett HE, Mulvihill JJ, Cunnane EM, Walsh MT. Characterising human atherosclerotic carotid plaque tissue composition and morphology using combined spectroscopic and imaging modalities. BioMedical Engineering OnLine. 2015;14(1):S5.
59. Meadowcroft MD, Connor JR, Smith MB, Yang QX. MRI and histological analysis of beta-amyloid plaques in both human Alzheimer's disease and APP/PS1 transgenic mice. Journal of Magnetic Resonance Imaging. 2009;29(5):997-1007.
60. Förstl H, Burns A, Cairns N, Luthert P, Levy R. Basal Ganglia Mineralization in Alzheimer’s Disease: A Comparative Study of Clinical, Neuroradiological and Neuropathological Findings. Behavioural Neurology. 1992;5(1).
61. Chan ED, Morales DV, Welsh CH, McDermott MT, Schwarz MI. Calcium deposition with or without bone formation in the lung. Am J Respir Crit Care Med. 2002;165(12):1654-69.
62. Virtanen I, Lehtonen E, Wartiovaara J. Structure of psammoma bodies of a meningioma in scanning electron microscopy. Cancer. 1976;38(2):824-9.
63. Kraaij S, Brand HS, van der Meij EH, de Visscher JG. Biochemical composition of salivary stones in relation to stone- and patient-related factors. Medicina oral, patologia oral y cirugia bucal. 2018;23(5):e540-e4.
64. Berès F, Lignon G, Rouzière S, Mauprivez C, Simon S, Berdal A, et al. Physicochemical analysis of human pulpal mineralization secondary to FAM20A mutations. Connective Tissue Research. 2018;59(sup1):46-51.
65. Goldsmith CS, Miller SE. Modern Uses of Electron Microscopy for Detection of Viruses. Clinical Microbiology Reviews. 2009;22(4):552-63.
66. Wang L, Eng ET, Law K, Gordon RE, Rice WJ, Chen BK. Visualization of HIV T Cell Virological Synapses and Virus-Containing Compartments by Three-Dimensional Correlative Light and Electron Microscopy. Journal of Virology. 2017;91(2):e01605-16.
67. Roingeard P. Viral detection by electron microscopy: past, present and future. Biology of the Cell. 2008;100(8):491-501.
68. Rostron P, Gaber S, Gaber D. Raman spectroscopy, review. Laser. 2016;21:24.
69. Urabe H, Tominaga Y, Kubota K. Experimental evidence of collective vibrations in DNA double helix (Raman spectroscopy). The Journal of Chemical Physics. 1983;78(10):5937-9.
70. Watson JD, Crick FH. Molecular structure of nucleic acids. Nature. 1953;171(4356):737-8.
71. Franklin RE, Gosling RG. Molecular configuration in sodium thymonucleate. Nature. 1953;171(4356):740.
72. Shah FA, Ruscsák K, Palmquist A. 50 years of scanning electron microscopy of bone—a comprehensive overview of the important discoveries made and insights gained into bone material properties in health, disease, and taphonomy. Bone research. 2019;7(1):15.
73. Louvet L, Bazin D, Büchel J, Steppan S, Passlick-Deetjen J, Massy ZA. Characterisation of calcium phosphate crystals on calcified human aortic vascular smooth muscle cells and potential role of magnesium. PLOS one. 2015;10(1):e0115342.
74. Bazin D, Daudon M, Combes C, Rey C. Characterization and some physicochemical aspects of pathological microcalcifications. Chemical Reviews. 2012;112(10):5092-120.
75. Bigi A, Cojazzi G, Panzavolta S, Ripamonti A, Roveri N, Romanello M, et al. Chemical and structural characterization of the mineral phase from cortical and trabecular bone. Journal of inorganic biochemistry. 1997;68(1):45-51.
76. Boskey AL, Mendelsohn R. Infrared spectroscopic characterization of mineralized tissues. Vibrational Spectroscopy. 2005;38(1-2):107-14.
77. Boskey AL. Assessment of bone mineral and matrix using backscatter electron imaging and FTIR imaging. Current osteoporosis reports. 2006;4(2):71-5.
78. Lim JJ. Thermogravimetric analysis of human femur bone. Journal of biological physics. 1975;3(3):111-29.

79. Imbert L, Gourion-Arsiquaud S, Villarreal-Ramirez E, Spevak L, Taleb H, van der Meulen MC, et al. Dynamic structure and composition of bone investigated by nanoscale infrared spectroscopy. PLOS one. 2018;13(9):e0202833.
80. Gadaleta S, Paschalis E, Betts F, Mendelsohn R, Boskey A. Fourier transform infrared spectroscopy of the solution-mediated conversion of amorphous calcium phosphate to hydroxyapatite: new correlations between X-ray diffraction and infrared data. Calcified tissue international. 1996;58(1):9-16.
81. Lotsari A, Rajasekharan AK, Halvarsson M, Andersson M. Transformation of amorphous calcium phosphate to bone-like apatite. Nature communications. 2018;9(1):4170.
82. Ibsen CJ, Chernyshov D, Birkedal H. Apatite formation from amorphous calcium phosphate and mixed amorphous calcium phosphate/amorphous calcium carbonate. Chemistry–A European Journal. 2016;22(35):12347-57.
83. Eanes ED. Amorphous Calcium Phosphate: Thermodynamic and Kinetic Considerations. In: Amjad Z, editor. Calcium Phosphates in Biological and Industrial Systems. Boston, MA: Springer US; 1998. p. 21-39.
84. Blair HC, Larrouture QC, Li Y, Lin H, Beer-Stoltz D, Liu L, et al. Osteoblast differentiation and bone matrix formation in vivo and in vitro. Tissue Engineering Part B: Reviews. 2017;23(3):268-80.
85. Florencio-Silva R, Sasso GRdS, Sasso-Cerri E, Simões MJ, Cerri PS. Biology of bone tissue: structure, function, and factors that influence bone cells. BioMed research international. 2015;2015.
86. Gorski JP. Biomineralization of bone: a fresh view of the roles of non-collagenous proteins. Frontiers in bioscience (Landmark edition). 2011;16:2598.
87. Boskey AL. Noncollagenous matrix proteins and their role in mineralization. Bone and mineral. 1989;6(2):111-23.
88. Nudelman F, Pieterse K, George A, Bomans PHH, Friedrich H, Brylka LJ, et al. The role of collagen in bone apatite formation in the presence of hydroxyapatite nucleation inhibitors. Nature Materials. 2010;9(12):1004-9.
89. Boonrungsiman S, Gentleman E, Carzaniga R, Evans ND, McComb DW, Porter AE, et al. The role of intracellular calcium phosphate in osteoblast-mediated bone apatite formation. Proceedings of the National Academy of Sciences. 2012;109(35):14170-5.
90. Yu J-K, Pan H, Huang S-M, Huang N-L, Yao C-C, Hsiao K-M, et al. Calcium content of different compositions of gallstones and pathogenesis of calcium carbonate gallstones. Asian journal of surgery. 2013;36(1):26-35.
91. Sethmann I, Wendt-Nordahl G, Knoll T, Enzmann F, Simon L, Kleebe H-J. Microstructures of Randall's plaques and their interfaces with calcium oxalate monohydrate kidney stones reflect underlying mineral precipitation mechanisms. Urolithiasis. 2017;45(3):235-48.
92. Kudo M, Kameda J, Saruwatari K, Ozaki N, Okano K, Nagasawa H, et al. Microtexture of larval shell of oyster, Crassostrea nippona: a FIB-TEM study. Journal of Structural Biology. 2010;169(1):1-5.
93. Su X, Kamat S, Heuer AH. The structure of sea urchin spines, large biogenic single crystals of calcite. Journal of Materials Science. 2000;35(22):5545-51.
94. Liu C, Li S, Kong J, Liu Y, Wang T, Xie L, et al. In-depth proteomic analysis of shell matrix proteins of Pinctada fucata. Scientific reports. 2015;5:17269.
95. McNally EA, Schwarcz HP, Botton GA, Arsenault AL. A model for the ultrastructure of bone based on electron microscopy of ion-milled sections. PLOS one. 2012;7(1):e29258.
96. Xue J, Zavgorodniy AV, Kennedy BJ, Swain MV, Li W. X-ray microdiffraction, TEM characterization and texture analysis of human dentin and enamel. Journal of Microscopy

2013;251(2):144-53.
97. Boskey AL. Bone composition: relationship to bone fragility and antiosteoporotic drug effects. BoneKEy reports. 2013;2.

98. Omelon S, Ariganello M, Bonucci E, Grynpas M, Nanci A. A review of phosphate mineral nucleation in biology and geobiology. Calcified tissue international. 2013;93(4):382-96.
99. Sroga GE, Vashishth D. Effects of bone matrix proteins on fracture and fragility in osteoporosis. Current osteoporosis reports. 2012;10(2):141-50.
100. Introduction to Fluorescence. In: Lakowicz JR, editor. Principles of Fluorescence Spectroscopy. Boston, MA: Springer US; 2006. p. 1-26.
101. Farlay D, Panczer G, Rey C, Delmas PD, Boivin G. Mineral maturity and crystallinity index are distinct characteristics of bone mineral. Journal of bone and mineral metabolism. 2010;28(4):433-45.
102. Anthis AHC, Tsolaki E, Didierlaurent L, Staubli S, Zboray R, Neels A, et al. Nano-analytical characterization of endogenous minerals in healthy placental tissue: mineral distribution, composition and ultrastructure. Analyst. 2019;144(23):6850-7.
103. Hossler FE. Cardiovascular System. Ultrastructure Atlas of Human Tissues. Hoboken, NJ, USA: John Wiley & Son; 2014.
104. Kenny T. Cardiovascular Anatomy of the Healthy Heart. The Nuts and Bolts of Cardiac Resynchronization Therapy. Malden, Massachusetts, USA: Blackwell Publishing; 2007. p. 6-10.
105. Lu S-J, Kimbrel EA, Feng Q, Li F, Lanza R. Chapter 48 - Blood Components from Pluripotent Stem Cells. In: Lanza R, Langer R, Vacanti J, editors. Principles of Tissue Engineering (Fourth Edition). Boston: Academic Press; 2014. p. 1041-57.
106. Bain BJ. A beginners guide to blood cells Third edition. ed. Chichester, England Wiley-Blackwell; 2017.
107. Gresele P, Fuster V, Lopez JA, Page CP, Vermylen J. Platelets in Hematologic and Cardiovascular Disorders : A Clinical Handbook Cambridge: Cambridge University Press; 2007.
108. Benjamin EJ, Blaha MJ, Chiuve SE, Cushman M, Das SR, Deo R, et al. Heart disease and stroke statistics-2017 update: a report from the American Heart Association. Circulation. 2017;135(10):e146-e603.
109. Reamy BV, Williams PM, Kuckel DP. Prevention of Cardiovascular Disease. Primary Care: Clinics in Office Practice. 2018;45(1):25-44.
110. Tölle M, Reshetnik A, Schuchardt M, Höhne M, van der Giet M. Arteriosclerosis and vascular calcification: causes, clinical assessment and therapy. European journal of clinical investigation. 2015;45(9):976-85.
111. Peeters FE, Meex SJ, Dweck MR, Aikawa E, Crijns HJ, Schurgers LJ, et al. Calcific aortic valve stenosis: hard disease in the heart: a biomolecular approach towards diagnosis and treatment. European heart journal. 2017;39(28):2618-24.
112. Malakar AK, Choudhury D, Halder B, Paul P, Uddin A, Chakraborty S. A review on coronary artery disease, its risk factors, and therapeutics. Journal of Cellular Physiology. 2019;234(10):16812-23.
113. Leong DP, Joseph PG, McKee M, Anand SS, Teo KK, Schwalm JD, et al. Reducing the Global Burden of Cardiovascular Disease, Part 2: Prevention and Treatment of Cardiovascular Disease. Circulation Research. 2017;121(6):695-710.
114. Chistiakov DA, Melnichenko AA, Grechko AV, Myasoedova VA, Orekhov AN. Potential of anti-inflammatory agents for treatment of atherosclerosis. Experimental and Molecular Pathology. 2018;104(2):114-24.
115. Welsh RC, Peterson ED, De Caterina R, Bode C, Gersh B, Eikelboom JW. Applying contemporary antithrombotic therapy in the secondary prevention of chronic atherosclerotic cardiovascular disease. American Heart Journal. 2019;218:100-9.
116. Shah PK. Inflammation, infection and atherosclerosis. Trends in Cardiovascular Medicine. 2019;29(8):468-72.
117. Williams KJ, Tabas I. The response-to-retention hypothesis of early atherogenesis. Arteriosclerosis, thrombosis, and vascular biology. 1995;15(5):551-61.
118. Glass CK, Witztum JL. Atherosclerosis. Cell. 2001;104(4):503-16.

119. Doherty TM, Asotra K, Fitzpatrick LA, Qiao J-H, Wilkin DJ, Detrano RC, et al. Calcification in atherosclerosis: bone biology and chronic inflammation at the arterial crossroads. Proceedings of the National Academy of Sciences of the United States of America. 2003;100(20):11201-6.
120. Durham AL, Speer MY, Scatena M, Giachelli CM, Shanahan CM. Role of smooth muscle cells in vascular calcification: implications in atherosclerosis and arterial stiffness. Cardiovascular research. 2018;114(4):590-600.
121. Naghavi M, Maron DJ, Kloner RA, Berman DS, Budoff M, Superko HR, et al. Coronary artery calcium testing: A call for universal coverage. Preventive Medicine Reports. 2019;15:100879.
122. Pawade T, Sheth T, Guzzetti E, Dweck MR, Clavel M-A. Why and How to Measure Aortic Valve Calcification in Patients With Aortic Stenosis. JACC: Cardiovascular Imaging. 2019;12(9):1835-48.
123. Liu W, Zhang Y, Yu CM, Ji QW, Cai M, Zhao YX, et al. Current understanding of coronary artery calcification. Journal of geriatric cardiology : JGC. 2015;12(6):668-75.
124. Wang Z, Jiang A, Wei F, Chen H. Cardiac valve calcification and risk of cardiovascular or all-cause mortality in dialysis patients: a meta-analysis. BMC cardiovascular disorders. 2018;18(1):12.
125. Xie C, Ouyang L, Chen J, Zhang H, Luo P, Wang J, et al. The Emerging Role of Mesenchymal Stem Cells in Vascular Calcification. Stem cells international. 2019;2019.
126. Zazzeroni L, Faggioli G, Pasquinelli G. Mechanisms of arterial calcification: the role of matrix vesicles. European Journal of Vascular and Endovascular Surgery. 2018;55(3):425-32.
127. Demer LL, Tintut Y. Inflammatory, metabolic, and genetic mechanisms of vascular calcification. Arteriosclerosis, thrombosis, and vascular biology. 2014;34(4):715-23.
128. Ho CY, Shanahan CM. Medial arterial calcification: an overlooked player in peripheral arterial disease. Arteriosclerosis, thrombosis, and vascular biology. 2016;36(8):1475-82.
129. Tintut Y, Hsu JJ, Demer LL. Lipoproteins in cardiovascular calcification: Potential targets and challenges. Frontiers in cardiovascular medicine. 2018;5:172.
130. Hsu JJ, Lim J, Tintut Y, Demer LL. Cell-matrix mechanics and pattern formation in inflammatory cardiovascular calcification. Heart. 2016;102(21):1710-5.
131. Rogers MA, Aikawa M, Aikawa E. Macrophage Heterogeneity Complicates Reversal of Calcification in Cardiovascular Tissues. Circulation Research. 2017;121(1):5-7.
132. Demer LL, Tintut Y. Vascular calcification: pathobiology of a multifaceted disease. Circulation. 2008;117(22):2938-48.
133. Schmid K, McSharry WO, Pameijer CH, Binette JP. Chemical and physicochemical studies on the mineral deposits of the human atherosclerotic aorta. Atherosclerosis. 1980;37(2):199-210.
134. Tomazic BB, Brown WE, Queral LA, Sadovnik M. Physicochemical characterization of cardiovascular calcified deposits: I. Isolation, purification and instrumental analysis. Atherosclerosis. 1988;69(1):5-19.
135. Bigi A, Foresti E, Incerti A, Ripamonti A, Roveri N. Structural and chemical characterization of the inorganic deposits in calcified human aortic wall. Inorganica Chimica Acta. 1981;55:81-5.
136. Rogers M, Goettsch C, Aikawa E. Medial and intimal calcification in chronic kidney disease: stressing the contributions. J Am Heart Assoc. 2013;2(5):e000481.
137. Ho CY, Shanahan CM. Medial Arterial Calcification: An Overlooked Player in Peripheral Arterial Disease. Arterioscler Thromb Vasc Biol. 2016;36(8):1475-82.
138. Cottignoli V, Cavarretta E, Salvador L, Valfré C, Maras A. Morphological and Chemical Study of Pathological Deposits in Human Aortic and Mitral Valve Stenosis: A Biomineralogical Contribution. Pathology Research International. 2015;2015:14.
139. Weska RF, Aimoli CG, Nogueira GM, Leirner AA, Maizato MJ, Higa OZ, et al. Natural and prosthetic heart valve calcification: morphology and chemical composition characterization. Artif Organs. 2010;34(4):311-8.

140. Bertazzo S, Steele JAM, Chester AH, Yacoub MH, Stevens MM. Cardiovascular calcification violet pearl. The Lancet. 2014;384(9950):1294.
141. Agarwal S. Nanoscale characterisation of cardiovascular tissue calcification: Imperial College London; 2017
142. Legros R, Balmain N, Bonel G. Age-related changes in mineral of rat and bovine cortical bone. Calcified Tissue International. 1987;41(3):137-44.
143. Termine JD. Mineral chemistry and skeletal biology. Clin Orthop Rel Res. 1972;85:207-39.
144. Dorozhkin SV. Calcium orthophosphates. Journal of Materials Science. 2007;42(4):1061-95.
145. Tomazic BB. Physicochemical principles of cardiovascular calcification. Zeitschrift für Kardiologie. 2001;90(3):68-80.
146. Blaser MC, Aikawa E. Roles and Regulation of Extracellular Vesicles in Cardiovascular Mineral Metabolism. Frontiers in Cardiovascular Medicine. 2018;5(187).
147. Viegas CSB, Santos L, Macedo AL, Matos AA, Silva AP, Neves PL, et al. Chronic Kidney Disease Circulating Calciprotein Particles and Extracellular Vesicles Promote Vascular Calcification: A Role for GRP (Gla-Rich Protein). Arteriosclerosis, Thrombosis, and Vascular Biology. 2018;38(3):575-87.
148. Shroff RC, McNair R, Skepper JN, Figg N, Schurgers LJ, Deanfield J, et al. Chronic mineral dysregulation promotes vascular smooth muscle cell adaptation and extracellular matrix calcification. J Am Soc Nephrol. 2010;21(1):103-12.
149. New SEP, Goettsch C, Aikawa M, Marchini JF, Shibasaki M, Yabusaki K, et al. Macrophage-derived matrix vesicles: an alternative novel mechanism for microcalcification in atherosclerotic plaques. Circulation research. 2013;113(1):72-7.
150. Rutkovskiy A, Malashicheva A, Sullivan G, Bogdanova M, Kostareva A, Stensløkken KO, et al. Valve Interstitial Cells: The Key to Understanding the Pathophysiology of Heart Valve Calcification. J Am Heart Assoc. 2017;6(9).
151. Benton JA, Kern HB, Anseth KS. Substrate properties influence calcification in valvular interstitial cell culture. The Journal of heart valve disease. 2008;17(6):689-99.
152. Bertacco E, Millioni R, Arrigoni G, Faggin E, Iop L, Puato M, et al. Proteomic Analysis of Clonal Interstitial Aortic Valve Cells Acquiring a Pro-calcific Profile. Journal of Proteome Research. 2010;9(11):5913-21.
153. Chen J-H, Yip CYY, Sone ED, Simmons CA. Identification and Characterization of Aortic Valve Mesenchymal Progenitor Cells with Robust Osteogenic Calcification Potential. Am J Pathol. 2009;174(3):1109-19.
154. Tsang HG, Rashdan NA, Whitelaw CB, Corcoran BM, Summers KM, MacRae VE. Large animal models of cardiovascular disease. Cell Biochem Funct. 2016;34(3):113-32.
155. Arroyo LG, Hayes MA, Delay J, Rao C, Duncan B, Viel L. Arterial calcification in race horses. Vet Pathol. 2008;45(5):617-25.
156. Bistoni G, Farhadi J. Anatomy and physiology of the breast. Plastic and reconstructive surgery: John Wiley & Sons, Ltd; 2015. p. 477-85.
157. Davis MR. Mammary Anatomy. In: Melvin A. Shiffman ADG, editor. Body Contouring: Art, Science, and Clinical Practice. Berlin, Heidelberg: Springer; 2010. p. 3-7.
158. Ferlay J, Soerjomataram I, Dikshit R, Eser S, Mathers C, Rebelo M, et al. Cancer incidence and mortality worldwide: Sources, methods and major patterns in GLOBOCAN 2012. International Journal of Cancer. 2015;136(5):E359-E86.
159. Song JL, Chen C, Yuan JP, Sun SR. Progress in the clinical detection of heterogeneity in breast cancer. Cancer Medicine. 2016;5(12):3475-88.
160. Navin N, Krasnitz A, Rodgers L, Cook K, Meth J, Kendall J, et al. Inferring tumor progression from genomic heterogeneity. Genome Research. 2010;20(1):68-80.
161. Marusyk A, Almendro V, Polyak K. Intra-tumour heterogeneity: a looking glass for cancer? Nature Reviews Cancer. 2012;12(5):323-34.

162. Yates LR, Gerstung M, Knappskog S, Desmedt C, Gundem G, Van Loo P, et al. Subclonal diversification of primary breast cancer revealed by multiregion sequencing. Nature medicine. 2015;21(7):751.
163. Guray M, Sahin AA. Benign Breast Diseases: Classification, Diagnosis, and Management. The Oncologist. 2006;11(5):435-49.
164. Ouyang N, Wang L. Basic Histopathological Methods and Breast Lesion Types for Research. Methods in Molecular Biology. 2016;1406:3-9.
165. Norwood SL. Fibrocystic breast disease. An update and review. Journal of Obstetric, Gynecologic, & Neonatal Nursing. 1990;19(2):116-21.
166. Santen RJ, Mansel R. Benign breast disorders. The New England Journal of Medicine. 2005;353(3):275-85.
167. Slodkowska E, Nofech-Mozes S, Xu B, Parra-Herran C, Lu F-I, Raphael S, et al. Fibroepithelial lesions of the breast: a comprehensive morphological and outcome analysis of a large series. Modern Pathology. 2018;31(7):1073-84.
168. Parker SJ, Harries SA. Phyllodes tumours. Postgraduate Medical Journal. 2001;77(909):428-35.
169. Paget J. On Disease of the Mammary Areola Preceding Cancer of the Mammary Gland. CA: A Cancer Journal for Clinicians. 1971;21(5):303-4.
170. Karakas C. Paget's disease of the breast. J Carcinog. 2011;10:31-.
171. Meisner ALW, Houman Fekrazad M, Royce ME. Breast Disease: Benign and Malignant. Medical Clinics of North America. 2008;92(5):1115-41.
172. Sharma GN, Dave R, Sanadya J, Sharma P, Sharma KK. Various types and management of breast cancer: an overview. J Adv Pharm Technol Res. 2010;1(2):109-26.
173. Branca G, Ieni A, Barresi V, Tuccari G, Caruso RA. An Updated Review of Cribriform Carcinomas with Emphasis on Histopathological Diagnosis and Prognostic Significance. Oncology Reviews. 2017;11(1):317.
174. Castellanos MR, Paramanathan K, El-Sayegh S, Forte F, Buchbinder S, Kleiner M. Breast cancer screening in women with chronic kidney disease: the unrecognized effects of metastatic soft-tissue calcification. Nature Clinical Practice Nephrology. 2008;4(6):337-41.
175. Yildiz S, Toprak H, Aydin S, Bilgin M, Oktay V, Abaci O, et al. The association of breast arterial calcification and metabolic syndrome. Clinics. 2014;69(12):841-6.
176. Wilkinson L, Thomas V, Sharma N. Microcalcification on mammography: approaches to interpretation and biopsy. The British Journal of Radiology. 2017;90(1069):20160594.
177. Nalawade Y. Evaluation of breast calcifications. Indian Journal of Radiology and Imaging. 2009;19(4):282-6.
178. Hutchinson WB, Thomas DB, Hamlin WB, Roth GJ, Peterson AV, Williams B. Risk of Breast Cancer in Women With Benign Breast Disease23. JNCI: Journal of the National Cancer Institute. 1980;65(1):13-20.
179. Haka AS, Shafer-Peltier KE, Fitzmaurice M, Crowe J, Dasari RR, Feld MS. Identifying Microcalcifications in Benign and Malignant Breast Lesions by Probing Differences in Their Chemical Composition Using Raman Spectroscopy. Cancer Research. 2002;62(18):5375-80.
180. Demetri-Lewis A, Slanetz PJ, Eisenberg RL. Breast Calcifications: The Focal Group. American Journal of Roentgenology. 2012;198(4):W325-W43.
181. Bonfiglio R, Scimeca M, Urbano N, Bonanno E, Schillaci O. Breast microcalcifications: biological and diagnostic perspectives. Future Oncology. 2018;14(30):3097-9.
182. Scimeca M, Giannini E, Antonacci C, Pistolese CA, Spagnoli LG, Bonanno E. Microcalcifications in breast cancer: an active phenomenon mediated by epithelial cells with mesenchymal characteristics. BMC Cancer. 2014;14(1):286.
183. Scott R, Stone N, Kendall C, Geraki K, Rogers K. Relationships between pathology and crystal structure in breast calcifications: an in situ X-ray diffraction study in histological sections. npj Breast Cancer. 2016;2(1):16029.

184. Kunitake J, Choi S, Nguyen KX, Lee MM, He F, Sudilovsky D, et al. Correlative imaging reveals physiochemical heterogeneity of microcalcifications in human breast carcinomas. J Struct Biol. 2018;202(1):25-34.
185. Gosling S, Scott R, Greenwood C, Bouzy P, Nallala J, Lyburn ID, et al. Calcification Microstructure Reflects Breast Tissue Microenvironment. J Mammary Gland Biol Neoplasia. 2019;24(4):333-42.
186. O'Grady S, Morgan MP. Microcalcifications in breast cancer: From pathophysiology to diagnosis and prognosis. Biochimica et Biophysica Acta - Reviews on Cancer. 2018;1869(2):310-20.
187. Qi X, Chen A, Zhang P, Zhang W, Cao X, Xiao C. Mammographic calcification can predict outcome in women with breast cancer treated with breast-conserving surgery. Oncology Letters. 2017;14(1):79-88.
188. Tabár L, Chen H-H, Duffy SW, Yen MF, Chiang CF, Dean PB, et al. A novel method for prediction of long-term outcome of women with T1a, T1b, and 10–14 mm invasive breast cancers: a prospective study. The Lancet. 2000;355(9202):429-33.
189. Büsing CM, Keppler U, Menges V. Differences in microcalcification in breast tumors. Virchows Archiv European Journal of Pathology. 1981;393(3):307-13.
190. Alarmo EL, Kallioniemi A. Bone morphogenetic proteins in breast cancer: dual role in tumourigenesis? Endocrine-Related Cancer. 2010;17(2):R123-39.
191. Bellahcène A, Castronovo V. Increased expression of osteonectin and osteopontin, two bone matrix proteins, in human breast cancer. Am J Pathol. 1995;146(1):95-100.
192. Cox RF, Jenkinson A, Pohl K, O'Brien FJ, Morgan MP. Osteomimicry of Mammary Adenocarcinoma Cells In Vitro; Increased Expression of Bone Matrix Proteins and Proliferation within a 3D Collagen Environment. PLOS one. 2012;7(7):e41679.
193. Gross anatomy of the brain. In: Clark DL, Mendez MF, Boutros NN, editors. The Brain and Behavior: An Introduction to Behavioral Neuroanatomy. 3 ed. Cambridge: Cambridge University Press; 2010. p. 4-13.
194. Jones LK. Anatomy and Brain Development. In: Russell-Chapin TAFLKJLA, editor. Neurocounseling. Alexandria: VA: American Counseling Association; 2017. p. 1-26.
195. The basal ganglia. In: Hathout GM, editor. Clinical Neuroradiology: A Case-Based Approach. Cambridge: Cambridge University Press; 2008. p. 94-136.
196. Zeng H, Sanes JR. Neuronal cell-type classification: challenges, opportunities and the path forward. Nature Reviews Neuroscience. 2017;18(9):530-46.
197. Jäkel S, Dimou L. Glial Cells and Their Function in the Adult Brain: A Journey through the History of Their Ablation. Frontiers in Cellular Neuroscience. 2017;11:24.
198. Schoenberg MR. Neuroanatomy Primer: Structure and Function of the Human Nervous System. Schoenberg MR, Scott JG, editors. Boston, MA: Boston, MA: Springer US; 2011. 59-126 p.
199. Hoogenraad CC, Wierenga C. Neurons, Overview. In: Aminoff MJ, Daroff RB, editors. Encyclopedia of the Neurological Sciences (Second Edition). Oxford: Academic Press; 2014. p. 456-8.
200. Geyer S. Brodmann's Areas. In: Aminoff MJ, Daroff RB, editors. Encyclopedia of the Neurological Sciences (Second Edition). Oxford: Academic Press; 2014. p. 550-4.
201. Sofroniew MV, Vinters HV. Astrocytes: biology and pathology. Acta Neuropathologica. 2010;119(1):7-35.
202. Streit WJ, Xue QS, Tischer J, Bechmann I. Microglial pathology. Acta Neuropathologica Communications. 2014;2:142.
203. Matej R, Tesar A, Rusina R. Alzheimer's disease and other neurodegenerative dementias in comorbidity: A clinical and neuropathological overview. Clinical Biochemistry. 2019;73:26-31.
204. Patterson C. World Alzheimer report 2018: the state of the art of dementia research: new frontiers. Alzheimer's Disease International (ADI): London, UK. 2018.

205. Bostancıklıoğlu M. An update on the interactions between Alzheimer's disease, autophagy and inflammation. Gene. 2019;705:157-66.
206. Association As. 2019 Alzheimer's disease facts and figures. Alzheimer's & Dementia. 2019;15(3):321-87.
207. Edwards FA. A Unifying Hypothesis for Alzheimer's Disease: From Plaques to Neurodegeneration. Trends in Neurosciences. 2019;42(5):310-22.
208. Madav Y, Wairkar S, Prabhakar B. Recent therapeutic strategies targeting beta amyloid and tauopathies in Alzheimer's disease. Brain Research Bulletin. 2019;146:171-84.
209. Bittner T, Burgold S, Dorostkar MM, Fuhrmann M, Wegenast-Braun BM, Schmidt B, et al. Amyloid plaque formation precedes dendritic spine loss. Acta Neuropathologica. 2012;124(6):797-807.
210. Dong S, Duan Y, Hu Y, Zhao Z. Advances in the pathogenesis of Alzheimer's disease: a re-evaluation of amyloid cascade hypothesis. Translational Neurodegeneration. 2012;1(1):18.
211. Villegas-Llerena C, Phillips A, Garcia-Reitboeck P, Hardy J, Pocock JM. Microglial genes regulating neuroinflammation in the progression of Alzheimer's disease. Current Opinion in Neurobiology. 2016;36:74-81.
212. Duan Y, Dong S, Gu F, Hu Y, Zhao Z. Advances in the Pathogenesis of Alzheimer's Disease: Focusing on Tau-Mediated Neurodegeneration. Translational Neurodegeneration. 2012;1(1):24.
213. Stoothoff WH, Johnson GVW. Tau phosphorylation: physiological and pathological consequences. Biochimica et Biophysica Acta (BBA) - Molecular Basis of Disease. 2005;1739(2):280-97.
214. Noble W, Hanger DP, Miller CCJ, Lovestone S. The importance of tau phosphorylation for neurodegenerative diseases. Front Neurol. 2013;4:83-.
215. Crowther R. Straight and paired helical filaments in Alzheimer disease have a common structural unit. Proceedings of the National Academy of Sciences. 1991;88(6):2288-92.
216. Binder LI, Guillozet-Bongaarts AL, Garcia-Sierra F, Berry RW. Tau, tangles, and Alzheimer's disease. Biochimica et Biophysica Acta (BBA) - Molecular Basis of Disease. 2005;1739(2):216-23.
217. Naseri NN, Wang H, Guo J, Sharma M, Luo W. The complexity of tau in Alzheimer's disease. Neuroscience Letters. 2019;705:183-94.
218. Braak H, Braak E. Neuropathological stageing of Alzheimer-related changes. Acta neuropathologica. 1991;82(4):239-59.
219. Braak H, Del Tredici K. Alzheimer's disease: pathogenesis and prevention. Alzheimers Dement. 2012;8(3):227-33.
220. Nirzhor SSR, Khan RI, Neelotpol S. The Biology of Glial Cells and Their Complex Roles in Alzheimer's Disease: New Opportunities in Therapy. Biomolecules. 2018;8(3).
221. Alibhai JD, Diack AB, Manson JC. Unravelling the glial response in the pathogenesis of Alzheimer's disease. The FASEB Journal. 2018;32(11):5766-77.
222. Wegiel J, Kuchna I, Wisniewski T, de Leon M, Reisberg B, Pirttila T, et al. Vascular fibrosis and calcification in the hippocampus in aging, Alzheimer disease, and Down syndrome. Acta Neuropathologica. 2002;103(4):333-43.
223. Wegiel J, Kuchna I, Wisniewski T, de Leon MJ, Reisberg B, Pirttila T, et al. Vascular fibrosis and calcification in the hippocampus in aging, Alzheimer disease, and Down syndrome. Acta Neuropathologica. 2002;103(4):333-43.
224. Töpperwien M, van der Meer F, Stadelmann C, Salditt T. Correlative x-ray phase-contrast tomography and histology of human brain tissue affected by Alzheimer's disease. NeuroImage. 2020:116523.
225. Bos D, Vernooij MW, Elias-Smale SE, Verhaaren BFJ, Vrooman HA, Hofman A, et al. Atherosclerotic calcification relates to cognitive function and to brain changes on magnetic resonance imaging. Alzheimer's & Dementia. 2012;8(5, Supplement):S104-S11.
226. Casanova MF, Araque JM. Mineralization of the basal ganglia: implications for neuropsychiatry, pathology and neuroimaging. Psychiatry research. 2003;121(1):59-87.

227. Beall SS, Patten BM, Mallette L, Jankovic J. Abnormal systemic metabolism of iron, porphyrin, and calcium in Fahr's syndrome. Annals of Neurology: Official Journal of the American Neurological Association and the Child Neurology Society. 1989;26(4):569-75.
228. Rockhill J, Mrugala M, Chamberlain MC. Intracranial meningiomas: an overview of diagnosis and treatment. Neurosurgical focus. 2007;23(4):E1.
229. Kobayashi S, Yamadori I, Miki H, Ohmori M. Idiopathic nonarteriosclerotic cerebral calcification (Fahr's disease): an electron microscopic study. Acta Neuropathol. 1987;73(1):62-6.
230. Bugnicourt J-M, Chillon J-M, Massy ZA, Canaple S, Lamy C, Deramond H, et al. High prevalence of intracranial artery calcification in stroke patients with CKD: a retrospective study. Clinical Journal of the American Society of Nephrology. 2009;4(2):284-90.
231. Oliveira JM, Oliveira M. Primary brain calcification in patients undergoing treatment with the biphosphanate alendronate. Scientific reports. 2016;6:22961.
232. Mejdoubi M, Zegermann T. Extensive brain calcification in idiopathic hypoparathyroidism. Journal of Neurology, Neurosurgery & Psychiatry. 2006;77(12):1328-.
233. Livingston JH, Stivaros S, Warren D, Crow YJ. Intracranial calcification in childhood: a review of aetiologies and recognizable phenotypes. Developmental Medicine & Child Neurology. 2014;56(7):612-26.
234. Vladár AE, Postek MT, Ming B. On the Sub-Nanometer Resolution of Scanning Electron and Helium Ion Microscopes. Microscopy Today. 2018;17(2):6-13.
235. Bogner A, Jouneau PH, Thollet G, Basset D, Gauthier C. A history of scanning electron microscopy developments: Towards “wet-STEM” imaging. Micron. 2007;38(4):390-401.
236. Heintzmann R, Ficz G. Breaking the resolution limit in light microscopy. Brief Funct Genomic Proteomic. 2006;5(4):289-301.
237. Ke X, Bittencourt C, Van Tendeloo G. Possibilities and limitations of advanced transmission electron microscopy for carbon-based nanomaterials. Beilstein Journal of Nanotechnology. 2015;6:1541-57.
238. Bazin D, Jouanneau C, Bertazzo S, Sandt C, Dessombz A, Réfrégiers M, et al. Combining field effect scanning electron microscopy, deep UV fluorescence, Raman, classical and synchrotron radiation Fourier transform Infra-Red Spectroscopy in the study of crystal-containing kidney biopsies. Comptes Rendus Chimie. 2016;19(11):1439-50.
239. Janssens K. Electron Microscopy. In: Janssens K, editor. Modern Methods for Analysing Archaeological and Historical Glass. 1: John Wiley & Sons, Ltd; 2013. p. 129-54.
240. Amelinckx S. Electron microscopy principles and fundamentals S. Amelinckx DvD, J. van Landuyt, Gustaaf van Tendeloo editor. Weinheim [Germany]: VCH, a Wiley Co.; 1997.
241. Leng Y. Transmission Electron Microscopy. Materials Characterization. Singapore: John Wiley & Sons (Asia) Pte Ltd; 2010. p. 79–119.
242. Stokes DJ. Principles and practice of variable pressure/environmental scanning electron microscopy (VP-ESEM). Rainforth M, editor. Chichester, U.K.: Wiley; 2008.
243. Stokes DJ. General Principles of VP-ESEM: Utilising a Gas. Principles and Practice of Variable Pressure/Environmental Scanning Electron Microscopy (VP-ESEM). Chichester, UK: John Wiley & Sons, Ltd; 2008. p. 63-92.
244. Leng Y. Scanning Electron Microscopy. Materials Characterization. Weinheim, Germany: Wiley-VCH Verlag GmbH & Co; 2013. p. 127-61.
245. Thomas JM, Ducati C. Transmission Electron Microscopy. In: Védrine PDMCPDJC, editor. Characterization of Solid Materials and Heterogeneous Catalysts. 2: John Wiley & Sons, Ltd; 2012. p. 655-701.
246. Lei C. Transmission Electron Microscopy. In: Wang GWPQ, editor. Nanotechnology Research Methods for Foods and Bioproducts: John Wiley & Sons, Ltd; 2012. p. 127-44.
247. Tsolaki E, Bertazzo S. Electron Microscopy for the Characterization of Soft Tissue Mineralization. In: Aikawa E, Hutcheson JD, editors. Cardiovascular Calcification and Bone Mineralization. Cham: Springer International Publishing; 2020. p. 219-34.

248. Joseph CL, Bernal S. Optical and Electron Microscopy. Modern Devices. Hoboken, NJ: John Wiley & Sons; 2016. p. 259–76

249. Watt IM. Electron–specimen interactions: processes and detectors. The Principles and Practice of Electron Microscopy. 2 ed. Cambridge: Cambridge University Press; 1997. p. 30-58.
250. Watts SW, Priestley JRC, Thompson JM. Serotonylation of Vascular Proteins Important to Contraction. PLOS one 2009;4(5):e5682.
251. Williams DB, Carter CB. Transmission Electron Microscopy. Boston, MA: Springer; 2009.
252. Polkowska A, Warmuzek M, Kalarus J, Polkowski W, Sobczak N. A comparison of various imaging modes in scanning electron microscopy during evaluation of selected Si/refractory sessile drop couples after wettability tests at ultra-high temperature. Transactions of Foundry Research Institute (Prace Instytutu Odlewnictwa). 2017;57:337-44.
253. Joy DC, Joy CS. Low voltage scanning electron microscopy. Micron. 1996;27(3-4):247-63.
254. Leng Y. Materials characterization introduction to microscopic and spectroscopic methods. Singapore, Hoboken, NJ: J. Wiley; 2008.
255. Pivovarova NB, Andrews SB. Measurement of total calcium in neurons by electron probe X-ray microanalysis. J Vis Exp. 2013(81):e50807.
256. Howat WJ, Wilson BA. Tissue fixation and the effect of molecular fixatives on downstream staining procedures. Methods. 2014;70(1):12-9.
257. Fox CH, Johnson FB, Whiting J, Roller PP. Formaldehyde fixation. Journal of Histochemistry and Cytochemistry. 1985;33(8):845-53.
258. Taqi SA, Sami SA, Sami LB, Zaki SA. A review of artifacts in histopathology. Journal of oral and maxillofacial pathology. 2018;22(2):279-.
259. Stradleigh TW, Ishida AT. Fixation strategies for retinal immunohistochemistry. Progress in Retinal and Eye Research. 2015;48:181-202.
260. Hoffman EA, Frey BL, Smith LM, Auble DT. Formaldehyde crosslinking: a tool for the study of chromatin complexes. J Biol Chem. 2015;290(44):26404-11.
261. Werner M, Chott A, Fabiano A, Battifora H. Effect of Formalin Tissue Fixation and Processing on Immunohistochemistry. The American Journal of Surgical Pathology. 2000;24(7):1016-9.
262. Pow DV, Wright LL, Vaney DI. The immunocytochemical detection of amino-acid neurotransmitters in paraformaldehyde-fixed tissues. Journal of Neuroscience Methods. 1995;56(2):115-23.
263. Pow DV. Immunocytochemical detection of amino acid neurotransmitters in paraformaldehyde-fixed tissues. Methods in Molecular Biology. 1997;72:103-23.
264. Bray D. Critical Point Drying of Biological Specimens for Scanning Electron Microscopy. In: Williams JR, Clifford AA, editors. Supercritical Fluid Methods and Protocols. Totowa, NJ: Humana Press; 2000. p. 235-43.
265. Braet F, De Zanger R, Wisse E. Drying cells for SEM, AFM and TEM by hexamethyldisilazane: a study on hepatic endothelial cells. Journal of Microscopy. 1997;186(1):84-7.
266. Thomasson SA, Thomasson JR. A Comparison of CPD (Critical Point Drying) and HMDS (Hexamethyldisilazane) in the Preparation of Corallorhiza spp. Rhizomes and Associated Mycorrhizae for SEM (Scanning Electron Microscopy). Transactions of the Kansas Academy of Science. 2011;114(2):129-34.
267. Hazrin-Chong NH, Manefield M. An alternative SEM drying method using hexamethyldisilazane (HMDS) for microbial cell attachment studies on sub-bituminous coal. Journal of Microbiological Methods. 2012;90(2):96-9.

268. Griffiths G. Biological Specimen Preparation for Transmission Electron Microscopy. Journal of Microscopy. 1999;196(3):353-4.
269. Thiéry G, Bernier J, Bergeron M. A simple technique for staining of cell membranes with imidazole and osmium tetroxide. Journal of Histochemistry & Cytochemistry. 1995;43(10):1079-84.
270. Venable JH, Coggeshall R. A Simplified Lead Citrate Stain for Use in Electron Microscopy. The Journal of Cell Biology. 1965;25(2):407-8.
271. Scarff CA, Fuller MJG, Thompson RF, Iadanza MG. Variations on Negative Stain Electron Microscopy Methods: Tools for Tackling Challenging Systems. Journal of Visualized Experiments. 2018(132).
272. Kizilyaprak C, Daraspe J, Humbel BM. Focused ion beam scanning electron microscopy in biology. Journal of Microscopy 2014;254(3):109-14.
273. Kim B, Hochella MF. Analytical Transmission Electron Microscopy and Scanning Transmission Electron Microscopy Techniques for the Characterization of Nanomaterial Composition, Phase and Crystallinity: Elsevier Science & Technology; 2015. 123-52 p.
274. Landis S. Focused Ion Beam Direct-Writing. Lithography. Hoboken, NJ USA: John Wiley & Sons, Inc.; 2013. p. 183–232.
275. Cleland TP, Voegele K, Schweitzer MH. Empirical evaluation of bone extraction protocols. PLOS one. 2012;7(2):e31443.
276. Schroeter ER, DeHart CJ, Schweitzer MH, Thomas PM, Kelleher NL. Bone protein "extractomics": comparing the efficiency of bone protein extractions of Gallus gallus in tandem mass spectrometry, with an eye towards paleoproteomics. PeerJ. 2016;4:e2603-e.
277. Cleland TP, Vashishth D. Bone protein extraction without demineralization using principles from hydroxyapatite chromatography. Analytical Biochemistry. 2015;472:62-6.
278. Jiang X, Ye M, Jiang X, Liu G, Feng S, Cui L, et al. Method Development of Efficient Protein Extraction in Bone Tissue for Proteome Analysis. Journal of Proteome Research. 2007;6(6):2287-94.
279. Idleburg C, DeLassus EN, Novack DV. Immunohistochemistry of Skeletal Tissues. In: Westendorf JJ, van Wijnen AJ, editors. Osteoporosis and Osteoarthritis. New York: Springer New York; 2015. p. 87-95.
280. Im K, Mareninov S, Diaz MFP, Yong WH. An introduction to performing immunofluorescence staining. In: Yong WH, editor. Biobanking: Methods and Protocols. 1897. New York: Springer New York; 2019. p. 299-311.
281. Drummen GP. Fluorescent probes and fluorescence (microscopy) techniques-illuminating biological and biomedical research. Molecules. 2012;17(12):14067-90.
282. Cooper M, Lummas S. Antibodies for Immunochemistry. Immunohistochemistry and Immunocytochemistry: Essential Methods: John Wiley & Sons, Ltd; 2016. p. 1-24.
283. Chen X, Cho D-B, Yang P-C. Double staining immunohistochemistry. N Am J Med Sci. 2010;2(5):241-5.
284. Roychoudhuri C, Kracklauer AF, Creath K. The Nature of Light: Bellingham, Washington : SPIE; 2017.
285. Langenick J. The Selection of Reporter Labels. Immunohistochemistry and Immunocytochemistry: John Wiley & Sons, Ltd; 2016. p. 25-33.
286. Sauer M, Hofkens J, Enderlein J. Fluorophores and Fluorescent Labels. Handbook of Fluorescence Spectroscopy and Imaging: John Wiley & Sons, Ltd; 2011. p. 31-60.
287. Chang XH, Zhang J, Wu LH, Peng YK, Yang XY, Li XL, et al. Research Progress of Near-Infrared Fluorescence Immunoassay. Micromachines (Basel). 2019;10(6).
288. Loria R, Kos W, Campbell A, Madge G. Suppression of aortic elastic tissue autofluorescence for the detection of viral antigen. Histochemistry. 1979;61(2):151-5.
289. Moreno-García A, Kun A, Calero O, Medina M, Calero M. An Overview of the Role of Lipofuscin in Age-Related Neurodegeneration. Frontiers in Neuroscience. 2018;12(464).

290. Canene-Adams K. Preparation of Formalin-fixed Paraffin-embedded Tissue for Immunohistochemistry. In: Lorsch J, editor. Methods in Enzymology. 533: Academic Press; 2013. p. 225-33.
291. Maity B, Sheff D, Fisher RA. Immunostaining: Detection of Signaling Protein Location in Tissues, Cells and Subcellular Compartments. In: Conn PM, editor. Methods in Cell Biology. 113: Academic Press; 2013. p. 81-105.
292. Shi S-R, Key ME, Kalra KL. Antigen retrieval in formalin-fixed, paraffin-embedded tissues: an enhancement method for immunohistochemical staining based on microwave oven heating of tissue sections. Journal of Histochemistry & Cytochemistry. 1991;39(6):741-8.
293. Buchwalow I, Samoilova V, Boecker W, Tiemann M. Non-specific binding of antibodies in immunohistochemistry: fallacies and facts. Scientific Reports. 2011;1:28.
294. Jackson P, Gandy M. Quality Assurance in Immunochemistry. Immunohistochemistry and Immunocytochemistry: Essential Methods: John Wiley & Sons, Ltd; 2016. p. 123-55.
295. Jamur MC, Oliver C. Permeabilization of Cell Membranes. In: Oliver C, Jamur MC, editors. Immunocytochemical Methods and Protocols. Totowa, NJ: Humana Press; 2010. p. 63-6.
296. Kapuscinski J. DAPI: a DNA-Specific Fluorescent Probe. Biotechnic & Histochemistry. 1995;70(5):220-33.
297. Kommnick C, Lepper A, Hensel M. Correlative light and scanning electron microscopy (CLSEM) for analysis of bacterial infection of polarized epithelial cells. Scientific Reports. 2019;9(1):17079.
298. van Rijnsoever C, Oorschot V, Klumperman J. Correlative light-electron microscopy (CLEM) combining live-cell imaging and immunolabeling of ultrathin cryosections. Nature Methods. 2008;5(11):973-80.
299. Kóssa G. Über die im Organismus künstlich erzeugbaren Verkalkungen. 1901.
300. Barka T, Anderson PJ. Histochemistry: theory, practice, and bibliography: Hoeber Medical Division, Harper & Row; 1963.
301. Cameron GR, Scholar G. The staining of calcium. Journal of Pathology and Bacteriology. 1930;33(4):929-55.
302. Puchtler H, Meloan SN. Demonstration of phosphates in calcium deposits: A modification of von Kossa's reaction. Histochemistry. 1978;56(3):177-85.
303. Pizzolato P. Histochemical recognition of calcium oxalate. Journal of Histochemistry & Cytochemistry. 1964;12(5):333-6.
304. Chin DD, Wang J, Mel De Fontenay M, Plotkin A, Magee GA, Chung EJ. Hydroxyapatite-binding micelles for the detection of vascular calcification in atherosclerosis. Journal of Materials Chemistry B. 2019;7(41):6449-57.
305. Felix DD, Gore JC, Yankeelov TE, Peterson TE, Barnes S, Whisenant J, et al. Detection of breast cancer microcalcification using (99m)Tc-MDP SPECT or Osteosense 750EX FMT imaging. Nuclear Medicine and Biology. 2015;42(3):269-73.
306. Pilgrim MG, Lengyel I, Lanzirotti A, Newville M, Fearn S, Emri E, et al. Subretinal Pigment Epithelial Deposition of Drusen Components Including Hydroxyapatite in a Primary Cell Culture Model. Investigative ophthalmology & visual science. 2017;58(2):708-19.
307. Zaheer A, Lenkinski RE, Mahmood A, Jones AG, Cantley LC, Frangioni JV. In vivo near-infrared fluorescence imaging of osteoblastic activity. Nature Biotechnology. 2001;19(12):1148-54.
308. Kurien BT, Scofield RH. Introduction to protein blotting. Methods in Molecular Biology. 2009;536:9-22.
309. Eidhammer I, Flikka K, Martens L, Mikalsen SO. Protein Separation – 2D Gel Electrophoresis. Computational Methods for Mass Spectrometry Proteomics. Chichester, UK: John Wiley & Sons Ltd.; 2007. p. 31-41.

310. Gwozdz T, Dorey K. Chapter 6 - Western Blot. In: Jalali M, Saldanha FYL, Jalali M, editors. Basic Science Methods for Clinical Researchers. Boston: Academic Press; 2017. p. 99-117.
311. Chevallet M, Luche S, Rabilloud T. Silver staining of proteins in polyacrylamide gels. Nat Protoc. 2006;1(4):1852-8.
312. Switzer RC, Merril CR, Shifrin S. A highly sensitive silver stain for detecting proteins and peptides in polyacrylamide gels. Analytical Biochemistry. 1979;98(1):231-7.
313. Hempelmann E, Krafts K. The mechanism of silver staining of proteins separated by SDS polyacrylamide gel electrophoresis. Biotechnic & Histochemistry. 2017;92(2):79-85.
314. Pettegrew CJ, Jayini R, Islam MR. Transfer buffer containing methanol can be reused multiple times in protein electrotransfer. Journal of biomolecular techniques. 2009;20(2):93-5.
315. Sumi S, Mathai A, Radhakrishnan VV. Dot-immunobinding assay. Methods in Molecular Biology. 2009;536:89-93.
316. Najafov A, Hoxhaj G. Special Cases. In: Najafov A, Hoxhaj G, editors. Western Blotting Guru: Academic Press; 2017. p. 51-5.
317. Reichard A, Asosingh K. Best Practices for Preparing a Single Cell Suspension from Solid Tissues for Flow Cytometry. Cytometry A. 2019;95(2):219-26.
318. Balasubramanian P, Prabhakaran MP, Sireesha M, Ramakrishna S. Collagen in Human Tissues: Structure, Function, and Biomedical Implications from a Tissue Engineering Perspective. Polymer Composites – Polyolefin Fractionation – Polymeric Peptidomimetics – Collagens. Advances in Polymer Science2012. p. 173-206.
319. Raschke S, Guan J, Iliakis G. Application of alkaline sucrose gradient centrifugation in the analysis of DNA replication after DNA damage. Methods in Molecular Biology. 2009;521:329-42.
320. Konoshenko MY, Lekchnov EA, Vlassov AV, Laktionov PP. Isolation of Extracellular Vesicles: General Methodologies and Latest Trends. BioMed Research International. 2018;2018:8545347.
321. Lyon SM, Mayampurath A, Rogers MR, Wolfgeher DJ, Fisher SM, Volchenboum SL, et al. A method for whole protein isolation from human cranial bone. Analytical biochemistry. 2016;515:33-9.
322. Gerstenfeld LC, Feng M, Gotoh Y, Glimcher MJ. Selective extractability of noncollagenous proteins from chicken bone. Calcified Tissue International. 1994;55(3):230-5.
323. Mohammadi Z, Shalavi S, Jafarzadeh H. Ethylenediaminetetraacetic acid in endodontics. The European Journal of Dentistry. 2013;7(Suppl 1):S135-S42.
324. Simpson RJ. Homogenization of mammalian tissue. Cold Spring Harbor Protocols. 2010;2010(7):pdb prot5455.
325. Bradford MM. A rapid and sensitive method for the quantitation of microgram quantities of protein utilizing the principle of protein-dye binding. Analytical Biochemistry. 1976;72(1):248-54.
326. Redmile-Gordon MA, Armenise E, White RP, Hirsch PR, Goulding KWT. A comparison of two colorimetric assays, based upon Lowry and Bradford techniques, to estimate total protein in soil extracts. Soil Biology and Biochemistry. 2013;67:166-73.
327. Zor T, Selinger Z. Linearization of the Bradford protein assay increases its sensitivity: theoretical and experimental studies. Analytical Biochemistry. 1996;236(2):302-8.
328. Bass JJ, Wilkinson DJ, Rankin D, Phillips BE, Szewczyk NJ, Smith K, et al. An overview of technical considerations for Western blotting applications to physiological research. Scand J Med Sci Sports. 2017;27(1):4-25.
329. Nießen J, Jedlitschky G, Greinacher A, Kroemer HK. Isolation of Platelet Granules. Current Protocols in Cell Biology. 2010;46(1):3.35.1-3..14.
330. Aaron JS, Taylor AB, Chew T-L. Image co-localization – co-occurrence versus correlation. Journal of Cell Science. 2018;131(3):jcs211847.

331. Dunn KW, Kamocka MM, McDonald JH. A practical guide to evaluating colocalization in biological microscopy. The American Journal of Physiology: Cell Physiology. 2011;300(4):C723-42.
332. Corder GW, Foreman DI. Nonparametric Statistics for Non-Statisticians: United States: John Wiley & Sons Inc; 2011.
333. Gopal R, Calvo C, Ito J, Sabine WK. Crystal Structure of Synthetic Mg-Whitlockite, Ca18Mg2H2(PO4)14. Canadian Journal of Chemistry. 1974;52(7):1155-64.
334. Shih Y-RV, Hwang Y, Phadke A, Kang H, Hwang NS, Caro EJ, et al. Calcium phosphate-bearing matrices induce osteogenic differentiation of stem cells through adenosine signaling. Proceedings of the National Academy of Sciences. 2014;111(3):990-5.
335. Cheng H, Chabok R, Guan X, Chawla A, Li Y, Khademhosseini A, et al. Synergistic interplay between the two major bone minerals, hydroxyapatite and whitlockite nanoparticles, for osteogenic differentiation of mesenchymal stem cells. Acta Biomaterialia. 2018;69:342-51.
336. Hortells L, Sur S, St. Hilaire C. Cell Phenotype Transitions in Cardiovascular Calcification. Frontiers in Cardiovascular Medicine. 2018;5(27).
337. Agyare E, Kandimalla K. Delivery of Polymeric Nanoparticles to Target Vascular Diseases. Journal of Biomolecular Research & Therapeutics. 2014;3(1).
338. Barua S, Mitragotri S. Challenges associated with Penetration of Nanoparticles across Cell and Tissue Barriers: A Review of Current Status and Future Prospects. Nano Today. 2014;9(2):223-43.
339. Claesson-Welsh L. Vascular permeability--the essentials. Upsala Journal of Medical Sciences. 2015;120(3):135-43.
340. Sindhwani S, Syed AM, Ngai J, Kingston BR, Maiorino L, Rothschild J, et al. The entry of nanoparticles into solid tumours. Nature Materials. 2020.
341. Gupta MK, Lee Y, Boire TC, Lee JB, Kim WS, Sung HJ. Recent strategies to design vascular theranostic nanoparticles. Nanotheranostics. 2017;1(2):166-77.
342. Akat K, Kaden JJ, Schmitz F, Ewering S, Anton A, Klomfaß S, et al. Calcium Metabolism in Adults With Severe Aortic Valve Stenosis and Preserved Renal Function. The American Journal of Cardiology. 2010;105(6):862-4.
343. Wald DS, Tsolaki E, Bestwick JP, Bertazzo S. Scanning electron microscopy for blood micro-crystals in aortic stenosis patients. PLOS one. 2018;13(8):e0202282.
344. Dhingra R, Sullivan LM, Fox CS, Wang TJ, D'Agostino RB, Sr, Gaziano JM, et al. Relations of Serum Phosphorus and Calcium Levels to the Incidence of Cardiovascular Disease in the Community. Archives of Internal Medicine. 2007;167(9):879-85.
345. Foley RN, Collins AJ, Herzog CA, Ishani A, Kalra PA. Serum Phosphorus Levels Associate with Coronary Atherosclerosis in Young Adults. Journal of the American Society of Nephrology. 2009;20(2):397-404.
346. Moe SM. Disorders involving calcium, phosphorus, and magnesium. Primary Care. 2008;35(2):215-37, v-vi.
347. Yilmaz H. Assessment of mean platelet volume (MPV) in primary hyperparathyroidism: Effects of successful parathyroidectomy on MPV levels. Endocrine regulations. 2014;48:182-8.
348. Lano G, Sallee M, Pelletier M, Bataille S, Fraisse M, Berda-Haddad Y, et al. Mean Platelet Volume Predicts Vascular Access Events in Hemodialysis Patients. Journal of Clinical Medicine. 2019;8(5).
349. Jung DH, Lee HR, Lee YJ, Kim JK, Park BJ, Shim JY. The association between coronary artery calcification and mean platelet volume in the general population. Platelets. 2011;22(8):567-71.
350. Ueno M, Kodali M, Tello-Montoliu A, Angiolillo DJ. Role of platelets and antiplatelet therapy in cardiovascular disease. Journal of Atherosclerosis and Thrombosis. 2011;18(6):431-42.

351. Gils JM, Zwaginga JJ, Hordijk PL. Molecular and functional interactions among monocytes, platelets, and endothelial cells and their relevance for cardiovascular diseases. Journal of Leukocyte Biology. 2009;85:195-204.
352. Borissoff JI, Spronk HMH, ten Cate H. The Hemostatic System as a Modulator of Atherosclerosis. New England Journal of Medicine. 2011;364(18):1746-60.
353. Italiano JE. The structure and production of blood platelets. In: Page CP, Vermylen J, Lopez JA, Gresele P, Fuster V, editors. Platelets in Hematologic and Cardiovascular Disorders: A Clinical Handbook. Cambridge: Cambridge University Press; 2007. p. 1-20.
354. Żmigrodzka M, Guzera M, Miśkiewicz A, Jagielski D, Winnicka A. The biology of extracellular vesicles with focus on platelet microparticles and their role in cancer development and progression. Tumor Biology. 2016;37(11):14391-401.
355. von Hundelshausen P, Schmitt MM. Platelets and their chemokines in atherosclerosis-clinical applications. Frontiers in Physiology. 2014;5:294.
356. Hernández-Ruiz L, Valverde F, Jimenez-Nuñez MD, Ocaña E, Sáez-Benito A, Rodríguez-Martorell J, et al. Organellar proteomics of human platelet dense granules reveals that 14-3-3ζ is a granule protein related to atherosclerosis. Journal of Proteome Research. 2007;6(11):4449-57.
357. Foresta C, Strapazzon G, De Toni L, Fabris F, Grego F, Gerosa G, et al. Platelets express and release osteocalcin and co-localize in human calcified atherosclerotic plaques. Journal of Thrombosis and Haemostasis. 2013;11(2):357-65.
358. Bouchareb R, Boulanger M-C, Tastet L, Mkannez G, Nsaibia MJ, Hadji F, et al. Activated platelets promote an osteogenic programme and the progression of calcific aortic valve stenosis. European Heart Journal. 2018;40(17):1362-73.
359. Schurgers LJ, Akbulut AC, Kaczor DM, Halder M, Koenen RR, Kramann R. Initiation and Propagation of Vascular Calcification Is Regulated by a Concert of Platelet- and Smooth Muscle Cell-Derived Extracellular Vesicles. Frontiers in Cardiovascular Medicine. 2018;5:36.
360. Vajen T, Benedikter BJ, Heinzmann ACA, Vasina EM, Henskens Y, Parsons M, et al. Platelet extracellular vesicles induce a pro-inflammatory smooth muscle cell phenotype. Journal of Extracellular Vesicles. 2017;6(1):1322454.
361. McNicol A, Israels SJ. Platelet Dense Granules: Structure, Function and Implications for Haemostasis. Thrombosis Research. 1999;95(1):1-18.
362. Bennett JS. Structure and function of the platelet integrin alphaIIbbeta3. The Journal of clinical investigation. 2005;115(12):3363-9.
363. Guo S, Shen S, Wang J, Wang H, Li M, Liu Y, et al. Detection of high-risk atherosclerotic plaques with ultrasound molecular imaging of glycoprotein IIb/IIIa receptor on activated platelets. Theranostics. 2015;5(4):418-30.
364. Woollard KJ, Chin-Dusting J. Therapeutic targeting of p-selectin in atherosclerosis. Inflammation & Allergy - Drug Targets. 2007;6(1):69-74.
365. Blann AD, Nadar SK, Lip GYH. The adhesion molecule P-selectin and cardiovascular disease. European Heart Journal. 2003;24(24):2166-79.
366. Valentijn KM, Sadler JE, Valentijn JA, Voorberg J, Eikenboom J. Functional architecture of Weibel-Palade bodies. Blood. 2011;117(19):5033-43.
367. Herr N, Bode C, Duerschmied D. The Effects of Serotonin in Immune Cells. Frontiers in Cardiovascular Medicine. 2017;4(48).
368. Machida T, Iizuka K, Hirafuji M. 5-Hydroxytryptamine and Its Receptors in Systemic Vascular Walls. Biological and Pharmaceutical Bulletin. 2013;36(9):1416-9.
369. Olumuyiwa-Akeredolu OO, Page MJ, Soma P, Pretorius E. Platelets: emerging facilitators of cellular crosstalk in rheumatoid arthritis. Nature Reviews Rheumatology. 2019;15(4):237-48.
370. Maurer-Spurej E, Pittendreigh C, Wu JK. Diagnosing platelet delta-storage pool disease in children by flow cytometry. American Journal of Clinical Pathology. 2007;127(4):626-32.

371. Brenner B, Harney JT, Ahmed BA, Jeffus BC, Unal R, Mehta JL, et al. Plasma serotonin levels and the platelet serotonin transporter. Journal of Neurochemistry. 2007;102(1):206-15.
372. Baskar K, Sur S, Selvaraj V, Agrawal DK. Functional constituents of a local serotonergic system, intrinsic to the human coronary artery smooth muscle cells. Molecular Biology Reports. 2015;42(8):1295-307.
373. Mercado CP, Kilic F. Molecular mechanisms of SERT in platelets: regulation of plasma serotonin levels. Molecular Interventions. 2010;10(4):231-41.
374. Steiner JA, Carneiro AMD, Blakely RD. Going with the Flow: Trafficking-Dependent and -Independent Regulation of Serotonin Transport. Traffic. 2008;9(9):1393-402.
375. Fraer M, Kilic F. Serotonin: a different player in hypertension-associated thrombosis. Hypertension. 2015;65(5):942-8.
376. Carneiro AM, Cook EH, Murphy DL, Blakely RD. Interactions between integrin alphaIIbbeta3 and the serotonin transporter regulate serotonin transport and platelet aggregation in mice and humans. Journal of Clinical Investigation. 2008;118(4):1544-52.
377. Israels SJ, McMillan EM, Robertson C, Singhory S, McNicol A. The lysosomal granule membrane protein, LAMP-2, is also present in platelet dense granule membranes. Thrombosis and Haemostasis. 1996;75(4):623-9.
378. Kowal J, Arras G, Colombo M, Jouve M, Morath JP, Primdal-Bengtson B, et al. Proteomic comparison defines novel markers to characterize heterogeneous populations of extracellular vesicle subtypes. Proceedings of the National Academy of Sciences of the United States of America. 2016;113(8):E968-77.
379. Deng W, Tang T, Hou Y, Zeng Q, Wang Y, Fan W, et al. Extracellular vesicles in atherosclerosis. Clinica Chimica Acta. 2019;495:109-17.
380. McNally E, Schwarcz H, Botton G, Arsenault A. A Model for the Ultrastructure of Bone Based on Electron Microscopy of Ion-Milled Sections. PLOS one. 2012;7:e29258.
381. Tzaphlidou M. Bone architecture: collagen structure and calcium/phosphorus maps. Journal of Biological Physics. 2008;34(1-2):39-49.
382. Leroyer AS, Isobe H, Lesèche G, Castier Y, Wassef M, Mallat Z, et al. Cellular Origins and Thrombogenic Activity of Microparticles Isolated From Human Atherosclerotic Plaques. Journal of the American College of Cardiology. 2007;49(7):772-7.
383. White JG. Electron opaque structures in human platelets: Which are or are not dense bodies? Platelets. 2008;19(6):455-66.
384. Ruiz FA, Lea CR, Oldfield E, Docampo R. Human platelet dense granules contain polyphosphate and are similar to acidocalcisomes of bacteria and unicellular eukaryotes. Journal of Biological Chemistry. 2004;279(43):44250-7.
385. Ambrosio AL, Di Pietro SM. Storage pool diseases illuminate platelet dense granule biogenesis. Platelets. 2017;28(2):138-46.
386. Lee J, Yang J, Kwon SG, Hyeon T. Nonclassical nucleation and growth of inorganic nanoparticles. Nature Reviews Materials. 2016;1(8):16034.
387. Mark BL, Jilkina O, Bhullar RP. Association ofRalGTP-Binding Protein with Human Platelet Dense Granules. Biochemical and Biophysical Research Communications. 1996;225(1):40-6.
388. Gerrard J, Lint D, Sims P, Wiedmer T, Fugate R, McMillan E, et al. Identification of a platelet dense granule membrane protein that is deficient in a patient with the Hermansky-Pudlak syndrome. Blood. 1991;77(1):101-12.
389. Harris JR. Megakaryocytes, Platelets, Macrophages, and Eosinophils: Springer US; 1991.
390. Chanpeng P, Svasti S, Paiboonsukwong K, Smith DR, Leecharoenkiat K. Platelet proteome reveals specific proteins associated with platelet activation and the hypercoagulable state in β-thalassmia/HbE patients. Scientific Reports. 2019;9(1):6059.
391. Petrich BG, Marchese P, Ruggeri ZM, Spiess S, Weichert RA, Ye F, et al. Talin is required for integrin-mediated platelet function in hemostasis and thrombosis. Journal of Experimental Medicine. 2007;204(13):3103-11.

392. Cohen I. The contractile system of blood platelets and its function. Methods and achievements in experimental pathology. 1979;9:40-86.
393. Bearer EL. Cytoskeletal domains in the activated platelet. Cell Motility and the Cytoskeleton. 1995;30(1):50-66.
394. Paul A, Straub A, Weber N, Ziemer G, Wendel HP. CD41 Western blotting: a new method to detect platelet adhesion to artificial surfaces used in extracorporeal circulation procedures. Journal of Materials Science: Materials in Medicine. 2008;20(1):373.
395. Moroi M, Jung SM. Platelet glycoprotein VI: its structure and function. Thrombosis Research. 2004;114(4):221-33.
396. Dmitriev AD, Factor MI, Segal OL, Pavlova EV, Massino YS, Smirnova MB, et al. Western blot analysis of human and rat serotonin transporter in platelets and brain using site-specific antibodies: Evidence that transporter undergoes endoproteolytic cleavage. Clinica Chimica Acta. 2005;356(1):76-94.
397. Merlot AM, Kalinowski DS, Richardson DR. Unraveling the mysteries of serum albumin—more than just a serum protein. Frontiers in Physiology. 2014;5(299).
398. Wentworth JK, Pula G, Poole AW. Vasodilator-stimulated phosphoprotein (VASP) is phosphorylated on Ser157 by protein kinase C-dependent and -independent mechanisms in thrombin-stimulated human platelets. Biochemical Journal. 2006;393(Pt 2):555-64.
399. Heijnen H, van der Sluijs P. Platelet secretory behaviour: as diverse as the granules … or not? Journal of Thrombosis and Haemostasis. 2015;13(12):2141-51.
400. Minai O, Dweik R, Aytekin M, Aulak K, Haserodt S, Chakravarti R. Abnormal platelet aggregation in idiopathic pulmonary arterial hypertension: Role of nitric oxide. American Journal of Physiology: Lung Cellular and Molecular Physiology. 2012;302:L512-L20.
401. Qin X, Corriere MA, Matrisian LM, Guzman RJ. Matrix metalloproteinase inhibition attenuates aortic calcification. Arteriosclerosis, Thrombosis, and Vascular Biology. 2006;26(7):1510-6.
402. Haug C, Lenz C, Diaz F, Bachem MG. Oxidized low-density lipoproteins stimulate extracellular matrix metalloproteinase Inducer (EMMPRIN) release by coronary smooth muscle cells. Arteriosclerosis, Thrombosis, and Vascular Biology. 2004;24(10):1823-9.
403. Joghetaei N, Akhyari P, Rauch BH, Cullen P, Lichtenberg A, Rudelius M, et al. Extracellular matrix metalloproteinase inducer (CD147) and membrane type 1-matrix metalloproteinase are expressed on tissue macrophages in calcific aortic stenosis and induce transmigration in an artificial valve model. The Journal of Thoracic and Cardiovascular Surgery. 2011;142(1):191-8.
404. Allahverdian S, Chehroudi AC, McManus BM, Abraham T, Francis GA. Contribution of Intimal Smooth Muscle Cells to Cholesterol Accumulation and Macrophage-Like Cells in Human Atherosclerosis. Circulation. 2014;129(15):1551-9.
405. Hanby HA, Bao J, Noh JY, Jarocha D, Poncz M, Weiss MJ, et al. Platelet dense granules begin to selectively accumulate mepacrine during proplatelet formation. Blood Advances. 2017;1(19):1478-90.
406. Mora S, Manson JE. Aspirin for Primary Prevention of Atherosclerotic Cardiovascular Disease: Advances in Diagnosis and Treatment. JAMA Internal Medicine. 2016;176(8):1195-204.
407. Naseem M, Murray J, Hilton JF, Karamchandani J, Muradali D, Faragalla H, et al. Mammographic microcalcifications and breast cancer tumorigenesis: a radiologic-pathologic analysis. BMC Cancer. 2015;15:307.
408. Morgan MP, Cooke MM, McCarthy GM. Microcalcifications Associated with Breast Cancer: An Epiphenomenon or Biologically Significant Feature of Selected Tumors? Journal of Mammary Gland Biology and Neoplasia. 2005;10(2):181-7.
409. Ferranti C. ea. Relationships between age, mammographic features and pathological tumour characteristics I non-palpable breast cancer. The British Journal of Radiology. 2000;73:698-705.

410. Wang Z, Hauser N, Singer G, Trippel M, Kubik-Huch RA, Schneider CW, et al. Non-invasive classification of microcalcifications with phase-contrast X-ray mammography. Nature Communications. 2014;5:3797.
411. O'Grady S, Morgan MP. Microcalcifications in breast cancer: From pathophysiology to diagnosis and prognosis. Biochim Biophys Acta Rev Cancer. 2018;1869(2):310-20.
412. Kim KI, Lee KH, Kim TR, Chun YS, Lee TH, Choi HY, et al. Changing patterns of microcalcification on screening mammography for prediction of breast cancer. Breast Cancer. 2016;23(3):471-8.
413. Rominger MB, Steinmetz C, Westerman R, Ramaswamy A, Albert US. Microcalcification-Associated Breast Cancer: Presentation, Successful First Excision, Long-Term Recurrence and Survival Rate. Breast Care (Basel). 2015;10(6):380-5.
414. Scott R, Stone N, Kendall C, Geraki K, Rogers K. Relationships between pathology and crystal structure in breast calcifications: an in situ X-ray diffraction study in histological sections. Npj Breast Cancer. 2016;2:16029.
415. Cox RF, Hernandez-Santana A, Ramdass S, McMahon G, Harmey JH, Morgan MP. Microcalcifications in breast cancer: novel insights into the molecular mechanism and functional consequence of mammary mineralisation. British journal of cancer. 2012;106(3):525-37.
416. Choi S, Coonrod S, Estroff L, Fischbach C. Chemical and physical properties of carbonated hydroxyapatite affect breast cancer cell behavior. Acta Biomaterialia. 2015;24:333-42.
417. Baker R, Rogers KD, Shepherd N, Stone N. New relationships between breast microcalcifications and cancer. British journal of cancer. 2010;103(7):1034-9.
418. Radenkovic S, Konjevic G, Isakovic A, Stevanovic P, Gopcevic K, Jurisic V. HER2-positive breast cancer patients: correlation between mammographic and pathological findings. Radiation Protection Dosimetry. 2014;162(1-2):125-8.
419. Scimeca M, Giannini E, Antonacci C, Pistolese CA, Spagnoli LG, Bonanno E. Microcalcifications in breast cancer: an active phenomenon mediated by epithelial cells with mesenchymal characteristics. BMC cancer. 2014;14:286.
420. Demetri-Lewis A, Slanetz PJ, Eisenberg RL. Breast calcifications: the focal group. AJR American journal of roentgenology. 2012;198(4):W325-43.
421. A. S-W. Breast cancer imaging: Mammography among women of up to 45 years. Polish Journal of Radiology. 2010;75(1):37-42.
422. Frappart L, Remy I, Lin HC, Bremond A, Raudrant D, Grousson B, et al. Different types of microcalcifications observed in breast pathology. Virchows Archiv A. 1987;410(3):179-87.
423. Haka Abigail S. S-PKE, Fitzmaurice Maryann, Crowe Joseph, Dasari Ramachandra R., Feld Michael S. Identifying Microcalcifications in Benign and Malignant Breast Lesions by Probing Differences in Their Chemical Composition Using Raman Spectroscopy. Cancer Research. 2002;61(18):5375-80.
424. Ben Lakhdar A, Daudon M, Mathieu M-C, Kellum A, Balleyguier C, Bazin D. Underlining the complexity of the structural and chemical characteristics of ectopic calcifications in breast tissues through FE-SEM and µFTIR spectroscopy. Comptes Rendus Chimie. 2016;19(11-12):1610-24.
425. Rowe AMP. One-Way Analysis of Variance (ANOVA) - Including Dunnett's and Tukey's Follow Up Tests. A Practical Approach to Using Statistics in Health Research: John Wiley & Sons, Ltd; 2018. p. 93-103.
426. Veselinović L, Karanović L, Stojanović Z, Bračko I, Marković S, Ignjatović N, et al. Crystal structure of cobalt-substituted calcium hydroxyapatite nanopowders prepared by hydrothermal processing. Journal of Applied Crystallography. 2010;43(2):320-7.
427. You AYF, Bergholt MS, St-Pierre J-P, Kit-Anan W, Pence IJ, Chester AH, et al. Raman spectroscopy imaging reveals interplay between atherosclerosis and medial calcification in the human aorta. Science Advances. 2017;3(12):e1701156.

428. Nosenko VV, Yaremko AM, Dzhagan VM, Vorona IP, Romanyuk YA, Zatovsky IV. Nature of some features in Raman spectra of hydroxyapatite-containing materials. Journal of Raman Spectroscopy. 2016;47(6):726-30.
429. Wopenka B, Pasteris JD. A mineralogical perspective on the apatite in bone. Materials Science and Engineering: C. 2005;25(2):131-43.
430. Shah F, Lee B, Tedesco J, Wexell C, Persson C, Thomsen P, et al. Micrometer-Sized Magnesium Whitlockite Crystals in Micropetrosis of Bisphosphonate-Exposed Human Alveolar Bone. Nano Letters. 2017;17.
431. Jang HL, Jin K, Lee J, Kim Y, Nahm SH, Hong KS, et al. Revisiting Whitlockite, the Second Most Abundant Biomineral in Bone: Nanocrystal Synthesis in Physiologically Relevant Conditions and Biocompatibility Evaluation. ACS Nano. 2014;8(1):634-41.
432. Scotchford CA, Vickers M, Yousuf Ali S. The isolation and characterization of magnesium whitlockite crystals from human articular cartilage. Osteoarthritis and Cartilage. 1995;3(2):79-94.
433. Yavorskyy A, Hernandez-Santana A, McCarthy G, McMahon G. Detection of calcium phosphate crystals in the joint fluid of patients with osteoarthritis - analytical approaches and challenges. Analyst. 2008;133(3):302-18.
434. Grimm KA. Cardiovascular Physiology. Veterinary Anesthesia and Analgesia. Chichester, UK: John Wiley & Sons, Ltd; 2017 p. 415–72.
435. Wang AZ. EPR or no EPR? The billion-dollar question. Science translational medicine. 2015;7(294):294ec112-294ec112.
436. Wang L, Huo M, Chen Y, Shi J. Tumor Microenvironment-Enabled Nanotherapy. Advanced Healthcare Materials. 2018;7(8):1701156.
437. Liu X, Jiang J, Meng H. Transcytosis - An effective targeting strategy that is complementary to "EPR effect" for pancreatic cancer nano drug delivery. Theranostics. 2019;9(26):8018-25.
438. Zarà M, Guidetti GF, Boselli D, Villa C, Canobbio I, Seppi C, et al. Release of Prometastatic Platelet-Derived Microparticles Induced by Breast Cancer Cells: A Novel Positive Feedback Mechanism for Metastasis. TH Open. 2017;1(2):e155-e63.
439. Li N. Platelets in cancer metastasis: To help the "villain" to do evil. International Journal of Cancer. 2016;138(9):2078-87.
440. Yan M, Jurasz P. The role of platelets in the tumor microenvironment: From solid tumors to leukemia. Biochimica et Biophysica Acta (BBA) - Molecular Cell Research. 2016;1863(3):392-400.
441. Johnson KE, Machlus KR, El-Husayni S, Kulenthirarajan R, Forward JA, Italiano JE, Jr., et al. Platelets Promote Breast Cancer Metastasis By Reprogramming Tumor Cells to Produce IL-8. Blood. 2015;126(23):2233-.
442. Schumacher D, Strilic B, Sivaraj KK, Wettschureck N, Offermanns S. Platelet-derived nucleotides promote tumor-cell transendothelial migration and metastasis via P2Y2 receptor. Cancer Cell. 2013;24(1):130-7.
443. Ducheyne P, Qiu Q. Bioactive ceramics: the effect of surface reactivity on bone formation and bone cell function. Biomaterials. 1999;20(23-24):2287-303.
444. LeGeros RZ. Properties of osteoconductive biomaterials: Calcium phosphates. Clin Orthop Rel Res. 2002(395):81-98.
445. LeGeros RZ. Calcium Phosphate-Based Osteoinductive Materials. Chemical Reviews. 2008;108(11):4742-53.
446. Engler AJ, Sen S, Sweeney HL, Discher DE. Matrix Elasticity Directs Stem Cell Lineage Specification. Cell. 2006;126(4):677-89.
447. Meena R, Kesari KK, Rani M, Paulraj R. Effects of hydroxyapatite nanoparticles on proliferation and apoptosis of human breast cancer cells (MCF-7). Journal of Nanoparticle Research. 2012;14(2):712.

448. Pathi SP, Lin DD, Dorvee JR, Estroff LA, Fischbach C. Hydroxyapatite nanoparticle-containing scaffolds for the study of breast cancer bone metastasis. Biomaterials. 2011;32(22):5112-22.
449. Kamalakar A, Bendre MS, Washam CL, Fowler TW, Carver A, Dilley JD, et al. Circulating interleukin-8 levels explain breast cancer osteolysis in mice and humans. Bone. 2014;61:176-85.
450. Whiteside TL, Gambotto A, Albers A, Stanson J, Cohen EP. Human tumor-derived genomic DNA transduced into a recipient cell induces tumor-specific immune responses Proceedings of the National Academy of Sciences. 2002;99(14):9415.
451. Khan MA, Wu VM, Ghosh S, Uskoković V. Gene delivery using calcium phosphate nanoparticles: Optimization of the transfection process and the effects of citrate and poly(l-lysine) as additives. Journal of Colloid and Interface Science. 2016;471:48-58.
452. Khoury R, Ghossoub E. Diagnostic biomarkers of Alzheimer's disease: A state-of-the-art review. Biomarkers in Neuropsychiatry. 2019;1:100005.
453. Csincsik L, MacGillivray TJ, Flynn E, Pellegrini E, Papanastasiou G, Barzegar-Befroei N, et al. Peripheral Retinal Imaging Biomarkers for Alzheimer's Disease: A Pilot Study. Ophthalmic Res. 2018;59(4):182-92.
454. Peters MEM, Kockelkoren R, de Brouwer EJM, Koek HL, Bleys RLAW, Mali WPTM, et al. Histological validation of calcifications in the human hippocampus as seen on computed tomography. PLOS one. 2018;13(5):e0197073-e.
455. Iwase T, Yoshida M, Hashizume Y, Yazawa I, Takahashi S, Ando T, et al. Intracranial vascular calcification with extensive white matter changes in an autopsy case of pseudopseudohypoparathyroidism. Neuropathology. 2019;39(1):39-46.
456. Miklossy J, Mackenzie IR, Dorovini-Zis K, Calne DB, Wszolek ZK, Klegeris A, et al. Severe vascular disturbance in a case of familial brain calcinosis. Acta Neuropathologica. 2005;109(6):643-53.
457. Kockelkoren R, De Vis JB, Stavenga M, Mali WPTM, Hendrikse J, Rozemuller AM, et al. Hippocampal calcification on brain CT: prevalence and risk factors in a cerebrovascular cohort. Eur Radiol. 2018;28(9):3811-8.
458. Braak H, Alafuzoff I, Arzberger T, Kretzschmar H, Del Tredici K. Staging of Alzheimer disease-associated neurofibrillary pathology using paraffin sections and immunocytochemistry. Acta neuropathologica. 2006;112(4):389-404.
459. Margolis HC, Kwak SY, Yamazaki H. Role of mineralization inhibitors in the regulation of hard tissue biomineralization: relevance to initial enamel formation and maturation. Frontiers in Physiology. 2014;5:339.
460. Činátl J, Šprincl L, Kouřílek K. Calcification of Cell Nuclei in Experimental Necrosis in vivo. Nature. 1967;216(5119):1011.
461. Činátl J. Initiation of structures by nuclei of dead cells. Experimental Cell Research. 1967;47(1):123-31.
462. Bubis JJ, Sandbank U, Bartov I, Dror Y, Budowski P, Wolman M. Mineralized cells: Neurons, glia or macrophages? Acta Neuropathologica. 1978;44(1):47-51.
463. Riew T-R, Shin Y-J, Kim HL, Cho JM, Pak H-J, Lee M-Y. Spatiotemporal Progression of Microcalcification in the Hippocampal CA1 Region following Transient Forebrain Ischemia in Rats: An Ultrastructural Study. PLOS one. 2016;11(7):e0159229.
464. Heiko Braak EB. Staging of alzheimer's disease-related neurofibrillary changes. Neurobiology of Aging 1995;16(3):271-8.
465. Hanna Ksiezak-Reding W-KLS-HY. Phosphate analysis and dephosphorylation of modified tau associated with paired helical filaments. Brain Research. 1992;597(2):209-319.
466. Arriagada PV, Growdon JH, Hedley-Whyte ET, Hyman BT. Neurofibrillary tangles but not senile plaques parallel duration and severity of Alzheimer's disease. Neurology. 1992;42(3 Pt 1):631-9.

467. Giannakopoulos P, Herrmann FR, Bussiere T, Bouras C, Kovari E, Perl DP, et al. Tangle and neuron numbers, but not amyloid load, predict cognitive status in Alzheimer's disease. Neurology. 2003;60(9):1495-500.
468. Gomez-Isla T, Hollister R, West H, Mui S, Growdon JH, Petersen RC, et al. Neuronal loss correlates with but exceeds neurofibrillary tangles in Alzheimer's disease. Annals of Neurology. 1997;41(1):17-24.
469. Mocanu MM, Nissen A, Eckermann K, Khlistunova I, Biernat J, Drexler D, et al. The potential for beta-structure in the repeat domain of tau protein determines aggregation, synaptic decay, neuronal loss, and coassembly with endogenous Tau in inducible mouse models of tauopathy. The Journal of Neuroscience. 2008;28(3):737-48.
470. Sydow A, Van der Jeugd A, Zheng F, Ahmed T, Balschun D, Petrova O, et al. Reversibility of Tau-related cognitive defects in a regulatable FTD mouse model. Journal of Molecular Neuroscience. 2011;45(3):432-7.
471. Sydow A, Van der Jeugd A, Zheng F, Ahmed T, Balschun D, Petrova O, et al. Tau-induced defects in synaptic plasticity, learning, and memory are reversible in transgenic mice after switching off the toxic Tau mutant. The Journal of Neuroscience. 2011;31(7):2511-25.
472. Andorfer C, Acker CM, Kress Y, Hof PR, Duff K, Davies P. Cell-cycle reentry and cell death in transgenic mice expressing nonmutant human tau isoforms. The Journal of Neuroscience. 2005;25(22):5446-54.
473. Gendron TF, Petrucelli L. The role of tau in neurodegeneration. Molecular Neurodegeneration. 2009;4:13.
474. Kimura T, Fukuda T, Sahara N, Yamashita S, Murayama M, Mizoroki T, et al. Aggregation of detergent-insoluble tau is involved in neuronal loss but not in synaptic loss. Journal of Biological Chemistry. 2010;285(49):38692-9.
475. de Calignon A, Fox LM, Pitstick R, Carlson GA, Bacskai BJ, Spires-Jones TL, et al. Caspase activation precedes and leads to tangles. Nature. 2010;464(7292):1201-4.
476. Polydoro M, Acker CM, Duff K, Castillo PE, Davies P. Age-dependent impairment of cognitive and synaptic function in the htau mouse model of tau pathology. The Journal of Neuroscience. 2009;29(34):10741-9.
477. Spires-Jones TL, Kopeikina KJ, Koffie RM, de Calignon A, Hyman BT. Are tangles as toxic as they look? Journal of Molecular Neuroscience. 2011;45(3):438-44.
478. Wittmann CW, Wszolek MF, Shulman JM, Salvaterra PM, Lewis J, Hutton M, et al. Tauopathy in Drosophila: neurodegeneration without neurofibrillary tangles. Science. 2001;293(5530):711-4.
479. Rady RM, Zinkowski RP, Binder LI. Presence of tau in isolated nuclei from human brain. Neurobiology of Aging. 1995;16(3):479-86.
480. Thurston VC, Zinkowski RP, Binder LI. Tau as a nucleolar protein in human nonneural cells in vitro and in vivo. Chromosoma. 1996;105(1):20-30.
481. Ulrich G, Salvadè A, Boersema P, Calì T, Foglieni C, Sola M, et al. Phosphorylation of nuclear Tau is modulated by distinct cellular pathways. Scientific Reports. 2018;8(1):17702.
482. Bukar Maina M, Al-Hilaly YK, Serpell LC. Nuclear Tau and Its Potential Role in Alzheimer's Disease. Biomolecules. 2016;6(1):9.
483. Greenwood JA, Johnson GV. Localization and in situ phosphorylation state of nuclear tau. Experimental Cell Research. 1995;220(2):332-7.
484. Lyck L, Dalmau I, Chemnitz J, Finsen B, Schrøder HD. Immunohistochemical markers for quantitative studies of neurons and glia in human neocortex. Journal of Histochemistry and Cytochemistry. 2008;56(3):201-21.
485. Rogalińska M. Alterations in cell nuclei during apoptosis. Cellular & Molecular Biology Letters. 2002;7(4):995-1018.
486. Hou L, Liu K, Li Y, Ma S, Ji X, Liu L. Necrotic pyknosis is a morphologically and biochemically distinct event from apoptotic pyknosis. Journal of Cell Science. 2016;129(16):3084-90.

487. Kay HH, Nelson DM, Wang Y. The placenta from development to disease Chichester, West Sussex

Hoboken, NJ : Wiley-Blackwell; 2011.
488. Huppertz B. The anatomy of the normal placenta. Journal of Clinical Pathology. 2008;61(12):1296-302.
489. Miller JM, Brown HL, Kissling GA, Gabert HA. The relationship of placental grade to fetal size and growth at term. American journal of perinatology. 1988;5(01):19-21.
490. Spirt B, Cohen W, Weinstein H. The incidence of placental calcification in normal pregnancies. Radiology. 1982;142(3):707-11.
491. Chen K, Chen L, Lee Y. Exploring the relationship between preterm placental calcification and adverse maternal and fetal outcome. Ultrasound in Obstetrics & Gynecology. 2011;37(3):328-34.
492. Salmani D, Purushothaman S, Somashekara SC, Gnanagurudasan E, Sumangaladevi K, Harikishan R, et al. Study of structural changes in placenta in pregnancy-induced hypertension. Journal of natural science, biology, and medicine. 2014;5(2):352.
493. Grannum PA, Berkowitz RL, Hobbins JC. The ultrasonic changes in the maturing placenta and their relation to fetal pulmonic maturity. American Journal of Obstetrics and Gynecology. 1979;133(8):915-22.
494. Al-Zuhair A, Ibrahim M, Mughal S. Calcium deposition on the maternal surface of the human placenta: a scanning electron microscopic study. Archives of gynecology. 1984;234(3):167-72.
495. Mirza FG, Ghulmiyyah LM, Tamim H, Makki M, Jeha D, Nassar A. To ignore or not to ignore placental calcifications on prenatal ultrasound: a systematic review and meta-analysis. The Journal of Maternal-Fetal & Neonatal Medicine. 2018;31(6):797-804.
496. Moran M, Higgins M, Zombori G, Ryan J, McAuliffe F. Computerized assessment of placental calcification post-ultrasound: a novel software tool. Ultrasound in Obstetrics & Gynecology. 2013;41(5):545-9.
497. Klesges LM, Murray DM, Brown JE, Cliver SP, Goldenberg RL. Relations of cigarette smoking and dietary antioxidants with placental calcification. American journal of epidemiology. 1998;147(2):127-35.
498. Jamal A, Moshfeghi M, Moshfeghi S, Mohammadi N, Zarean E, Jahangiri N. Is preterm placental calcification related to adverse maternal and foetal outcome? Journal of Obstetrics and Gynaecology. 2017;37(5):605-9.
499. Lu H, Guo Y-n, Liu S-n, Zhang D-c. Nanobacteria may be linked to calcification in placenta. Ultrastructural pathology. 2012;36(3):160-5.
500. Varma V, Kim K. Placental calcification: ultrastructural and X-ray microanalytic studies. Scanning electron microscopy. 1985(Pt 4):1567-72.
501. Poggi S, Bostrom K, Demer L, Skinner H, Koos B. Placental calcification: a metastatic process? Placenta. 2001;22(6):591-6.
502. Eidelman N, Boyde A, Bushby AJ, Howell PGT, Sun J, Newbury DE, et al. Microstructure and mineral composition of dystrophic calcification associated with the idiopathic inflammatory myopathies. Arthritis Research & Therapy. 2009;11(5):R159.
503. Ortlepp JR, Schmitz F, Mevissen V, Weiss S, Huster J, Dronskowski R, et al. The amount of calcium-deficient hexagonal hydroxyapatite in aortic valves is influenced by gender and associated with genetic polymorphisms in patients with severe calcific aortic stenosis. European Heart Journal. 2004;25(6):514-22.
504. Wallingford MC, Gammill HS, Giachelli CM. Slc20a2 deficiency results in fetal growth restriction and placental calcification associated with thickened basement membranes and novel CD13 and lamininα1 expressing cells. Reproductive Biology. 2016;16(1):13-26.